Droplet Dynamics on Heterogeneous Surfaces

School of Mathematics
Ysgol Mathemateg

Danny John Groves

A thesis submitted for the degree of Doctor of Philosophy

Submitted: 23rd September 2019
Revised: 25th October 2019

Summary

The motion of a liquid drop over solid surfaces is easy to visualise, yet, from a scientific standpoint is inherently challenging to study. This arises from the multi-scale nature of the governing physics, including gravity and capillarity in the macro-scale, and slip close to the contact line. This thesis studies droplets through a combined numerical and analytical approach to extract physical insights in complex scenarios. Using the lubrication approximation, the Stokes equations are combined with the appropriate boundary conditions to derive a non-linear partial differential equation for the fluid thickness. To determine how the droplet evolves in time, we develop solution methods to the full equation using a pseudospectral collocation approach in both two-, and three-dimensional settings. Using the boundary integral formulation we also develop a hybrid method which is combined with the analysis to offer an attractive compromise between the low-order models and full-scale computing. Analytical progress is made in the slow spreading and negligible gravity regime by utilising the method of matched asymptotic expansions which has been successful in related works to derive low-order approximate models that predict the solutions of the full equations. Specifically, we consider droplets spreading over flat and horizontal substrates with mass transfer that may occur at free surface, or by evaporation which is maximised close to the contact line. Extensions are also made by considering topographically varying substrates with sufficiently small amplitudes. The outcomes of the analysis are contrasted to simulations of the governing equation for a number of cases. We present convincing numerical evidence that suggest that the reduced models can replace the full model within their domain of validity, and thus mitigate considerably the associated high computational costs required for such simulations, at the same time, uncover experimentally observed phenomena, such as pinning, stick-slip, and hysteresis-type effects induced through surface features.

Acknowledgements

My time as a postgraduate student has been been one filled with memories and excellent people, some of which have now become life long friends. The acknowledgements of any thesis provide the author with the much needed space to thank the people who supported their journey, and also, to show some of their personality through a rather impersonal piece of scientific literature.

First and foremost, I would like to offer my deepest gratitude to my academic supervisor and friend Dr. Nikos Savva for your time, effort, and patience. I truly cannot express my appreciation for all that you have taught, and the guidance you have provided to make this thesis a reality. A special thanks also goes to Dr. Chris Davies and Dr. Usama Kadri for your support as my secondary supervisors. I would also like to thank the EPSRC for funding my research, and ARCCA for the use of the supercomputing systems at Cardiff University where I performed many of my computational experiments.

A special mention goes to my office colleagues, Joe bishop and Alex Safar, who have listened to my many ramblings, provided assistance on more than one occasion, and importantly, gave humorous distraction through times of academic difficulty. To Dr. Waleed Ali, thank you for all your help with my thesis, and more importantly, for your invaluable friendship. To Dr. Scott Morgan, thank you for all your assistance in SIAM activities and helping me to broaden skills and experience with outreach activities. Also for your friendship, thank you Dr. Sally Hill, Dr. Alex Mackay as well as many other postgraduate students at the Cardiff mathematics department, too many to mention here.

For all the support I have received over my life, I cannot form into words my gratitude to my family. Mum, you really are my biggest fan and I could not have done this without your support, love, and importantly, your excellent humour. Dad, you have taught me many valuable life lessons and built up my confidence so that I could follow the path you knew was

Contents

— Chapter 1 —

Introduction

The motion of a liquid over a solid surface is a process that is observed frequently, for instance, with water dew on plant leaves or the rain drops on a car windscreen (see figure 1.1 [1]). These scenarios are incredibly easy to visualise, yet, they pose challenges that are of interest, in order to both advance our fundamental understanding of these phenomena and to inform the development of the associated applications. The interplay between micro- and macro-scale physics that govern such situations also explains other phenomena, such as why it is possible for certain insects to walk on water (see Gao & Jiang [1]), or why breakfast cereals tend to clump together while floating on milk (see Vella & Mahadevan [2]). The broad range of scientific problems posed by moving contact lines have birthed decades worth of research creating a subject of study that intertwines mathematics, engineering, chemistry, physics and scientific computing. Importantly, this study has also contributed in the creation and improvement of technologies. For instance, the analysis of evaporating droplets has direct impact in DNA analysis [3], printing applications [4, 5], as well as the fabrication of display technologies [6]. Also, studying evaporation times and heat transfer from the surface to the
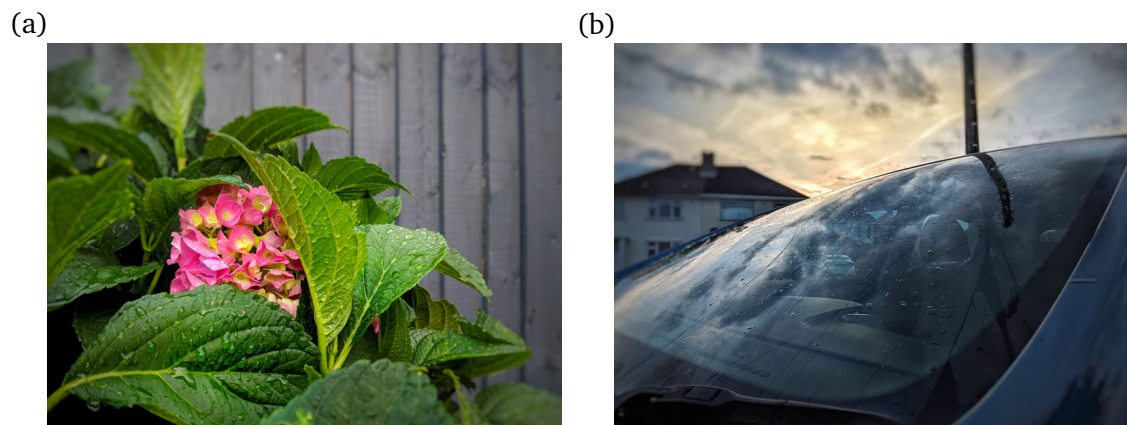
(a)   (b)

Figure 1.1: Water droplets on plant leaves (a), and a car windscreen (b).

[1]All photographs in this thesis are part of the author's private collection.

droplet can optimise spray cooling processes [7, 8], for medical [9], industrial [10], and fuel industry applications [11]. Likewise, understanding how droplets interact with surfaces decorated with chemical and/or topographical heterogeneities can assist in the development of water collecting materials [12], enhance condensation [13, 14] and give directed transport in microfluidic and lab-on-a-chip devices [15].

1.1   Wetting Hydrodynamics

Broadly, the subject of study that concerns how droplets interact with solid substrates is referred to as *wetting hydrodynamics*. Simply put, wetting considers the solid, liquid and gas phases, where the degree of how much a surface is 'wetted' is due to a force balance between cohesive and adhesive forces. This is typically classified into two regimes depending on the *contact angle* which is determined at the *contact line* where the liquid-vapour and the solid-liquid interfaces meet (see figure 1.2). In one regime cohesive forces dominate creating a case of low wettability (hydrophobic), and in the other regime the fluid base is maximised (hydrophilic). It is worth noting, however, that other cases exist, such as the perfect wetting case where the contact angle $\theta_{\mathrm{eq}} = 0°$, and the non-wetting case with $\theta_{\mathrm{eq}} = 180°$, although in reality none of these extremes are reached.

The two distinct regimes in figure 1.2 can occur due to a large variety of physical processes. For instance, changes in surface topography can create a hydrophobic surface, as observed with the famously studied *lotus effect* where lotus leaves have nanoscopic topographical structures for self-cleaning purposes (see Barthlott & Neinhuis [16]). These effects can likewise be created with chemical treatments, for example, with titanium dioxide coatings which are used on windows to break down bio-organic materials in sunlight so that the residual dirt is cleaned
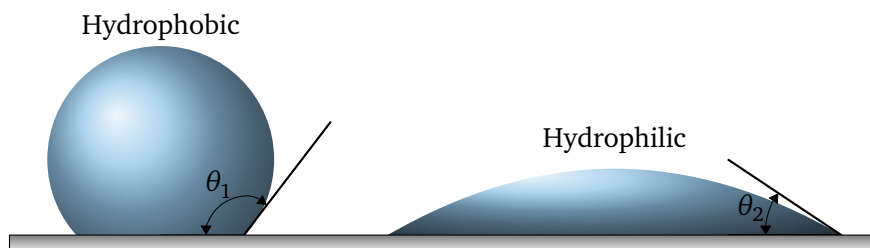

Figure 1.2: The two distinct cases of wetting for liquid droplets. The left droplet corresponds to the hydrophobic regime where the contact angle $\theta_{\mathrm{eq}} = \theta_1 \geq 90°$, and the right drop is in the hydrophilic regime where the contact angle $\theta_{\mathrm{eq}} = \theta_2 < 90°$.
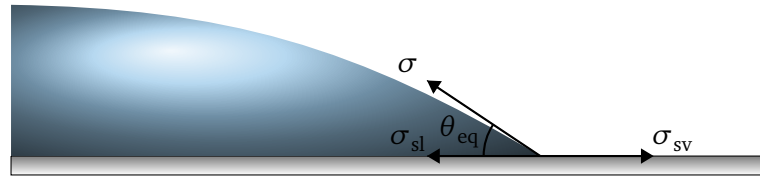
Figure 1.3: A depiction of the surface tensions used within Young's equation (1.1).

with the hydrophilic properties of the coating (see Parkin & Palgrave [17] for a review of self-cleaning coatings). Also, the use of electrical fields can cause a droplet to transition from a hydrophobic state, to a hydrophilic one (see Mugele & Baret [18] for a review), which has applications in microlenses [19], fibre optics [20] and microfluidic devices [21].

The equilibrium contact angle, θ_{eq} (the contact angle of which a droplet is no longer spreading), can be determined using Young's equation [22]

$$\sigma_{sv} = \sigma_{sl} + \sigma \cos(\theta_{eq}), \tag{1.1}$$

where σ_{sv}, σ_{sl} and σ denote the solid-vapour, solid-liquid and liquid-vapour surface tensions, respectively (see figure 1.3). Equation (1.1) is defined when the three phases are at a force balance with each other, and holds macroscopically on a scale larger than the long-ranged intermolecular forces (see Bonn *et al.* [23] for further details). Therefore in the 'ideal' setting of horizontal, perfectly flat, and clean substrates, one can in principle use (1.1) to determine θ_{eq} by knowing σ_{sv}, σ_{sl} and σ. However, in general equilibrium angle is easier to determine than the surface tensions, although both can be computed by using density functional theory (see Yatsyshin *et al.* [24]).

1.2   Ideal Surfaces

It is worth reiterating that Young's equation (1.1) relies on the ideal conditions of perfectly clean, horizontal and flat substrates. Wetting in this configuration is arguably the easiest to study theoretically, particularly in the limit when a droplet has a characteristic length L that is smaller than the capillary length

$$l_c = \sqrt{\frac{\sigma}{\rho g}}, \tag{1.2}$$

so that gravitational effects can be neglected, where ρ is the fluid density, and g is the acceleration due to gravity. In this circumstance, hydrodynamic theory predicts that spreading is due to the competition between viscous and capillary forces and the droplet radius, $r(t)$,

evolves according to the power law

$$r(t) \sim t^{1/10}, \tag{1.3}$$

for droplets sufficiently far from equilibrium. Equation (1.3) is commonly referred to as Tanner's law (see Tanner [25]), and has been confirmed experimentally by a number of studies [25–27] (although it is worth noting that this was first obtained theoretically by Voinov [28]). While Tanner's law predicts the spreading dynamics rather well, it is limited in the fact that it only captures the intermediate spreading behaviours, and thus, does not apply for long-time dynamics where the droplet will reach an equilibrium radius.

Typically any classical problem in fluid mechanics is coupled with the no-slip boundary condition which states that at the solid boundary, the fluid will have zero velocity relative to the boundary. However, Moffatt [29] first pointed out that the no-slip condition enforces infinite acceleration caused by infinite stress and pressure at the contact line, both of which are physically invalid (see Sibley *et al.* [30]). This gave birth to the so-called *moving contact line problem*, which was brought more to light by Huh & Scriven [31] who extended the work of Moffatt by introducing slip at the moving boundary, which is facilitated by using a slip condition like the one mentioned in the far earlier work of Navier [32] (see Bonn *et al.* [23] and Shikhmurzaev [33] for detailed discussions).

Although the slip condition was initially implemented as a means to alleviate the moving contact line problem, it does have some physical basis as shown in molecular dynamics simulations [34–36], and since, the slip condition has been extended with the proposition of several types of models (see Dussan [37], Haley & Miksis [38] and Ruckenstein & Dunn [39]). The moving contact line problem, likewise, can be alleviated with the *precursor film model* which says that there is a very thin constant-thickness film of fluid away from the droplet. In this sense the droplet does not have an actual contact line, but an apparent one, allowing for the no-slip boundary condition to be imposed (see de Gennes [40] and Schwartz & Eley [41]). Other mechanisms have also been proposed, including the use of evaporative fluxes [42], considering 180° contact angles [43], assuming that the free surface of the liquid is diffuse [44, 45], shear thinning rheology [46], and the so-called interface formation model [47].

In many cases, the theoretical treatment of moving contact line problems is based around negligible inertial effects and a small capillary number which is defined by

$$\mathrm{Ca} = \frac{\mu U}{\sigma}, \tag{1.4}$$
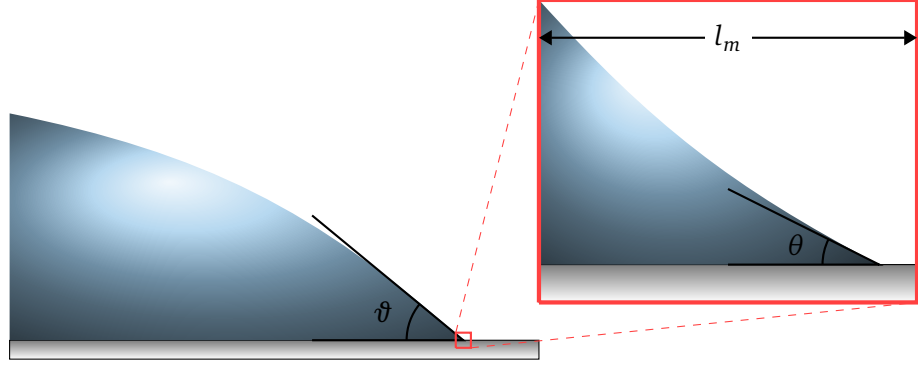
Figure 1.4: The two scales of the drop. On the left is the macro-scale with apparent contact angle ϑ, and the right depicts a zoomed in snapshot of the micro-scale of length l_m with locally varying angle θ.

where μ is the fluid's dynamic viscosity and U is the characteristic horizontal velocity. This regime is not entirely restrictive since in most spreading experiments Ca ranges between 10^{-5} and 10^{-3} (see Bonn *et al.* [23]). This leads to simplifications in the continuum description of fluid mechanics, which can be further simplified by assuming that the droplet thickness H is much smaller than its length-scale L (i.e., assuming small contact angles). This is referred to as the *lubrication*, or *long-wave approximation* and is commonly used to model thin-film flows (see O'Brien & Schwartz [48]). In this setting a coupled macro- and micro-scale investigation can be undertaken so that a broader picture of contact line dynamics can be obtained. Namely, in the macro-scale the dynamics are governed by a balance of capillary and viscous forces so that microscopic effects are negligible, whereas close to the contact line there is a small region where microscopic effects, such as slip, become crucial (the region is of width l_m which is set by the microscopic effect). In the lubrication limit Voinov [28] derived a relation that couples the details of both the micro- and macro-scales, namely

$$\left(\partial_x h(x,t)\right)^3 = \theta^3 + 9\mathrm{Ca}\ln\left(\frac{x}{l_m}\right), \tag{1.5}$$

which is often referred to as the *Cox-Voinov law*, where $h(x,t)$ denotes the droplet thickness and l_m is some length-scale arising from the microscale physics near the contact line. In equation (1.5) there is only a weak dependence on l_m, and it is far more crucial to find the microscopic contact angle θ to predict the dynamics (see figure 1.4 for a visual depiction of microscopic region). Importantly, if the contact line recedes then equation (1.5) does not hold due to the presence of a non-vanishing curvature in the governing equation [49], thus requiring a separate treatment [50, 51].

Using matched asymptotic analysis, Lacey [52] developed the first general asymptotic procedure to account for fully three-dimensional (3D) droplets, expressing the normal velocity of the contact line in non-dimensional form as

$$v \cdot \nu = \frac{\theta^3 - \vartheta^3}{3 \ln(\lambda)}. \tag{1.6}$$

Here, ν is the normal vector to the contact line (see chapter 2 for details), λ is the non-dimensional slip-length (the length of the micro-scale region, i.e. $l_m = \lambda$), and $\vartheta = -|\nabla h|_C$ is the apparent (macroscopic) contact angle which is extrapolated from the height in the bulk near the contact line. It is worth noting that (1.6) is valid in the limit where slip vanishes (i.e. as $\lambda \to 0$) meaning λ is the small parameter in the asymptotic treatment used to derive (1.6). In fact, one can use (1.6) to obtain Tanner's law for axisymmetric spreading. In this regime, the time-dependent droplet thickness is described by

$$h(x,t) = \frac{\vartheta r}{2} \left(1 - \frac{x^2}{r^2} \right), \tag{1.7}$$

for given droplet radius $r(t)$, volume v, and where

$$\vartheta = -\partial_x h(x,t)|_{x=r(t)} = \frac{8v}{r(t)^3}, \tag{1.8}$$

is the apparent contact angle (see Bonn *et al.* [23] and Savva *et al.* [53]). Thus, using (1.6) we formulate the equation

$$\dot{r}(t) = \frac{\theta^3 - \left(8v/r(t)^3 \right)^3}{3 \ln(\lambda)}, \tag{1.9}$$

which is solved for the radius evolution in time (where dots denote differentiation with respect to time). It is easy to see that far from equilibrium θ is much smaller than the apparent contact angle, which may be neglected in (1.9) to give

$$r(t) \sim \left(-\frac{5120 v^3}{3 \ln(\lambda)} \right)^{1/10} t^{1/10}, \tag{1.10}$$

which is Tanner's law, as expected. Therefore, using (1.10) with non-dimensional parameters $v = 1$, $\lambda = 10^{-4}$, and the initial condition $r(0) = 0.1$ we see in figure 1.5 that $r(t) \sim 1.69 t^{1/10}$ gives a good estimate for the spreading behaviour. However, we can readily observe that the transition to equilibrium is not captured, as previously discussed.

It is worth stressing that equation (1.6) is a leading-order approximation to the full spreading dynamics, and describes the first term in the asymptotic expansion for the normal velocity of the contact line as $\lambda \to 0$. Hocking remarked on this point in [54], saying that a two
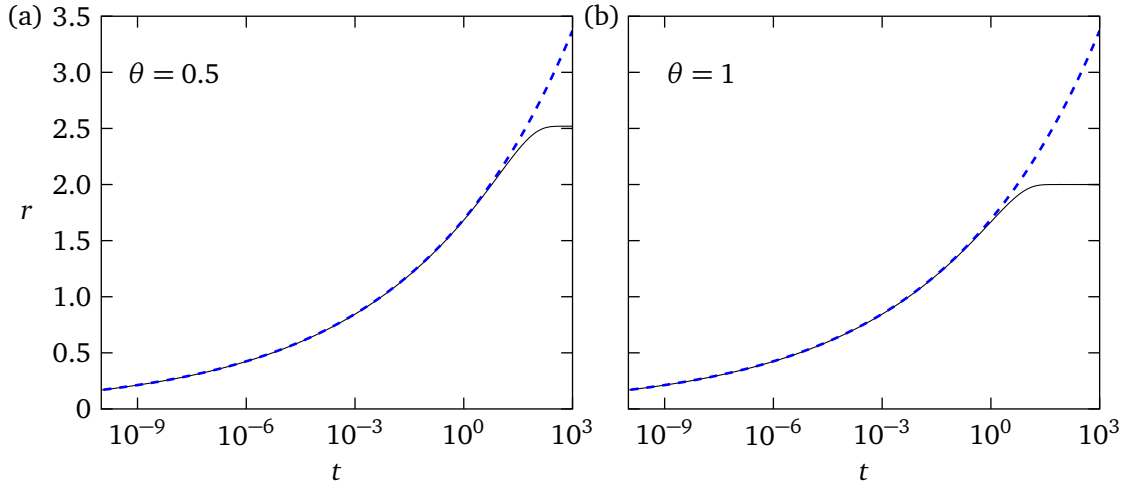
Figure 1.5: A visualisation of Tanner's law by comparing to solutions of (1.9) with non-dimensional parameters $r(0) = 0.1$, $\lambda = 10^{-4}$ and $\nu = 1$. Plots (a) and (b) depict radius evolutions for $\theta = 0.5$ and $\theta = 1$, respectively, where black curves are predictions from (1.9) and dashed blue curves are plots of Tanner's law $r(t) \sim 1.69t^{1/10}$ found from (1.10). All variables are made non-dimensional according to the scalings introduced in chapter 2.

term expansion is the minimum number of terms required to yield satisfactory results, since a single term would give the same answer if the small parameter λ was replaced by a multiple of itself. Thus, attention is given in many studies to derive the next-order correction and obtain more accurate approximations to the full governing equations. This is highlighted in [54] where the next-order correction is derived for when gravitational effects become appreciable, showing how obtaining this correction is not only important, but highly non-trivial. Therefore the analytical methodologies presented in this thesis extend the original ideas presented by Hocking [54] as well as more recent work to account for additional complexities that have not previously been considered via matched asymptotics [53, 55–61]. The outcomes of these approaches amount to obtaining the corrections to (1.6) of $O(1/|\ln(\lambda)|^2)$ as $\lambda \to 0$ which as will we show, they are essential to accurately capture solutions as compared to numerical calculations of the full equations.

1.3 Surfaces with Defects

Flat, horizontal and clean substrates are not typical and the presence of surface heterogeneities attributed to surface roughness, dust, or chemical impurities is unavoidable. This implies that non-ideal substrates have a large range of contact angles so that additional behaviours take place. Therefore, in such configurations there is a hysteresis of the contact angle across the

substrate considered [62–64], which even for carefully prepared substrates can span a few degrees, although, it is often reported to span several tens of degrees (see Johnson & Dettre [65]). This is referred to in the literature as *contact angle hysteresis* [23, 40]; presently there is no widely accepted model for hysteretic effects, and they are usually imposed in an ad hoc manner. Here we assume that there is no contact angle hysteresis *a priori*, showing how hysteresis-like effects naturally emerge due to the presence of substrate features.

Surface features unravel a broader set of interesting dynamics, such as the ability for the contact line to remain pinned upon localised defects (see Cubaud & Fermigier [63] and Bonn *et al.* [23]), or to exhibit sharp transitions across the substrate which are referred to as *stick-slip* (or *stick-jump*) motions (see Rio *et al.* [66], Chung *et al.* [67] and Kusumaatmaja & Yeomans [68]). If a droplet is positioned on an inclined slope, then the substrate defects along the surface can render the droplet immobile until the critical inclination angle is reached (i.e. contact angle hysteresis holds the droplet in place). Finding this angle is a focus for many experimental and theoretical studies, which was first studied in two dimensions (2D) by using force balance arguments [69]. Since, the main result in [69] has been generalised to account for 3D droplets and other effects [70, 71], where [69] and its variants have been confirmed experimentally by many authors (see, e.g. [69, 72–74]).

Perhaps one of the first studies into chemically heterogeneous surfaces was by Cassie [75] who used energetic and thermodynamic arguments to derive an equation for an effective contact angle, θ_c. If a substrate consists of only two materials then it was shown that

$$\cos(\theta_c) = \alpha_1 \cos(\theta_1) + \alpha_2 \cos(\theta_2), \tag{1.11}$$

where θ_1 and θ_2 are the contact angles with fractional surface area α_1 and α_2 for the substrates of materials 1, and 2, respectively. A number of experimental studies have investigated the validity of (1.11) (see, e.g. [76–78]), to find the agreement was only qualitative. Besides, Cassie's equation is derived solely on thermodynamic arguments without the use of any fluid dynamics.

Droplet equilibria on rough surfaces were first considered theoretically by Wenzel [79] who obtained an expression for the effective contact angle, θ_r, that accounts for the extra area of the drop in contact with the substrate. In the absence of contact angle hysteresis due to chemical defects, this is given as

$$\cos(\theta_r) = \tilde{r} \cos(\theta_{\text{eq}}), \tag{1.12}$$

where $\tilde{r}$ is the ratio of the real to the projected area covered by the drop. When $\theta_{eq} < 90°$ we have $\theta_r < \theta_{eq}$ since $\tilde{r}$ is always greater than 1, which implies that spreading is promoted by surface roughness. Despite a number of experimental studies confirming approximately Wenzel's law [80–82], the derivation leading to (1.12) relies on relatively simple arguments, which arguably does not reflect the true complexity of wetting over rough substrates. The theoretical studies by Savva *et al*. [83, 84] show from their numerical experiments that surface roughness in fact inhibits wetting, contradicting Wenzel's theory, which is also demonstrated experimentally by Chung *et al*. [67] for parallel grooved substrates.

Cassie and Wenzel's equations predict the contact angle and do not explain dynamic phenomena, which are arguably more interesting and challenging to study. For instance, Joanny & de Gennes investigated droplet pinning in the conceptually simpler situation of a single substrate defect to understand the balance between the pinning force and the deformation in the contact line, proposing a somewhat oversimplified model for the so-called elasticity of the contact line [85, 86]. Such considerations become unwieldy once multiple defects are considered, as highlighted in the experimental work of Cubaud *et al*. [87] (see also Cubaud & Fermigier [63]), showing that the heterogeneous defects not only trap the droplet but cause the contact line to become distorted by these defects, giving rise to stick-slip events, as reported in experiments with chemical [66, 88] and topographical heterogeneities [89–91].

For applications involving droplet transport, such as with microfluidic devices [92], directed droplet motion is desirable. This can be achieved by considering specially designed surface features (chemical and/or topographical) and different actuation mechanisms such as gravity for a droplet on an inclined plane, electric fields, and mechanical vibrations. These mechanisms aim towards overcoming the effects of hysteresis, which tend to trap the contact line. In this manner, the applied external forcing allows the droplet to overcome the energy barriers of the heterogeneities and achieve a more controllable droplet transport. For example, by carefully preparing the substrate with a linear gradient of chemical heterogeneity the droplet moves from regions of higher contact angles, to lower ones [93, 94]. Likewise, this can be performed with hydrophobic surfaces by changing the substrate topography [95–97], or applying an electrical field (see Takeda *et al*. [98]). Daniel & Chaudhury [99] and Daniel *et al*. [100] show experimentally that vibrating the substrate is an effective approach. As observed experimentally by Brunet *et al*. [101], if the vibrations are sufficiently strong then deformations in the free surface can even allow the droplet to move uphill (see also Benilov & Billingham

[102]), and the presence of heterogeneities can enhance this transport [60]. Electrowetting has also been shown as a plausible method to reduce the hysteresis in the surface by increasing the voltage applied to the droplet (see Li & Mugele [103]). For hydrophobic surfaces, voltage applied through the substrate can cause the droplet to flatten, and if the voltage is released the droplet can detach from the solid substrate through its quick contact line recession [104].

The dynamics of the contact line interacting with heterogeneities is often studied theoretically using matched asymptotic analysis. This method generally involves a detailed investigation of both the micro- and macro-scales, which are coupled together to form models which approximate the full equations. In many studies the product of this method yields Cox-Voinov type laws similar in appearance to (1.6) which are significantly easier to solve than the corresponding full equations. To simplify the analysis, many authors consider 2D geometries to study the undoubtedly complex relationship between the substrate heterogeneities and motion of the moving fronts [55, 56, 58–60, 83, 84, 105–107]. While this is more difficult to compare to experiments, it does allow for a phase-plane analysis to further elucidate the stick-slip and pinning behaviours which manifest themselves due to surface heterogeneities, in essence, highlighting the hysteresis-like behaviours that emerge through the substrate proporties (see, e.g. [55, 56, 58, 59]).

Fully 3D settings, however, have received comparatively far less attention. Greenspan [108] and Greenspan & McCay [109] provide the first analyses in the limit of weakly deformed contact lines by assuming *a priori* that the velocity of the contact line satisfies the relation

$$v = k\,(\vartheta - \theta)\,\boldsymbol{\nu}, \tag{1.13}$$

for some constant of proportionality $k > 0$. While pioneering the 3D study, Greenspan [108] and Greenspan & McCay [109] consider only the cases where the local contact angle varies linearly, and where the droplet does not move so that it can be described with a fixed polar-coordinate frame. It is also crucial to note that these studies do not base their approach around matched asymptotics, and neglect the presence of slip which is the effect responsible for contact line motion. For these reasons it is apparent that new, and more accurate models are required so that the interaction of droplets with substrates decorated with heterogeneities can be further studied, which can assist in rationalising experimental observations, and aid the development and improvement of modern technologies for the range of applications mentioned previously.

1.4 Contact Line Dynamics with Mass Transfer

Interesting behaviours also manifest themselves once a droplet is subjected to a change in its mass, which may occur due to a variety of physical processes, such as liquid imbibition through a permeable substrate [110–112], pumping liquid into the droplet [113], or mass loss through evaporation. Understanding this process of droplets growing and/or shrinking is crucial to inform developments in modern technologies, such as with hydrogen fuel cells [114, 115] which rely on sufficient transport of water within the cells for optimal conductivity. Arguably, however, the largest body of literature for mass flux processes is devoted to evaporating droplets which has recieved significant attention across a variety of disciplines (see Erbil [116], Brutin [117] and Brutin & Starov [118]) due to their relevance in industrial processes. Among the challenges in this area is mitigating the so-called *coffee stain effect* [119–121] so that the material inside the droplet can be distributed more evenly. This effect manifests itself once a particle-laden droplet remains pinned so that the suspended particles inside it are forced to concentrate near the contact line through capillary-induced flows, and mostly occurs during the initial stages of evaporation (see figure 1.6). The deposited pattern of material can be altered by adding surfactants to the liquid (see Seo *et al*. [122]), or by using electrical currents which suppresses the effect (see Eral *et al*. [123]).

Work on the theoretical aspects of mass transfer in droplet dynamics has been limited. By using matched asymptotic analysis in the 2D geometry, Oliver *et al*. [107] investigate constant mass flux over homogeneous substrates, where different distinguished time limits were considered. A recent study by Kiradjiev *et al*. [124] also considers an asymptotic approach with a variety of time limits, this time considering a form of the flux that is localised at the centre of the droplet. Both studies show that in the absence of heterogeneities, mass transfer yields a rich and complicated set of dynamics, which surely increase once heterogeneities are present. Pradas *et al*. [125] use a diffuse interface formulation to likewise investigate 2D droplets of variable mass by considering mass changes through a pore on the substrate with coupled surface heterogeneity. As shown in the bifurcation analysis of [125], the coupling between liquid flux and chemical heterogeneities gives rise to an interesting array of dynamic phenomena that are dependent on the droplet's volume, such as stick-slip and hysteresis-like behaviours.

In this thesis we also investigate the interesting interplay between fluid transfer and

(a)   (b)

(c)   (d)
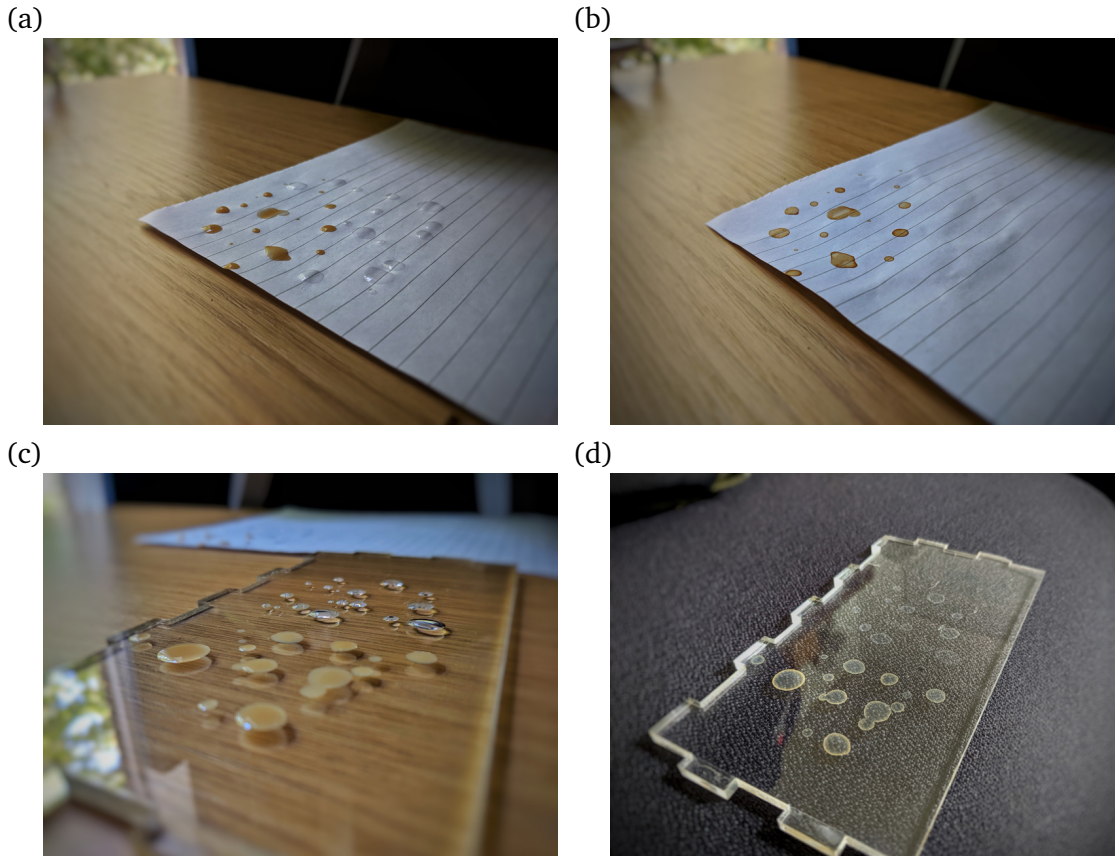
Figure 1.6: The coffee stain effect over two materials. Images (a) and (b) show droplets of coffee and tap water on paper after deposition, and evaporation, respectively. Images (c) and (d) show the same process over acrylic.

chemical heterogeneities, noting that we extend upon the asymptotic analysis of Vellingiri *et al.* [55] for 2D droplets spreading over chemically heterogeneous surfaces, including the additional terms required to account for liquid fluxes occurring through the macro-scale of the droplet. Using the 2D work as a basis of discussion, we extend upon this analysis to account for fully 3D droplets by using preliminary results of thesis for the case of constant mass which were reported in [61].

This analysis, however, is inappropriate for evaporating droplets since the flux is maximised close to the contact line, rather than through the bulk of the droplet. Analysing evaporating droplets theoretically is rather complicated due to the fact one must consider mass and energy transfer within and between the solid substrate, the liquid drop, and the surrounding gas. Typically this avenue of research is split into two main directions depending on the nature of the gas phase. If the droplet is evaporating into an inert gas such as air then the evaporation is assumed to be limited by vapour diffusion [126, 127] to study the influence of substrate conductivity [128, 129], the impact on the droplet shape [130], as well as the
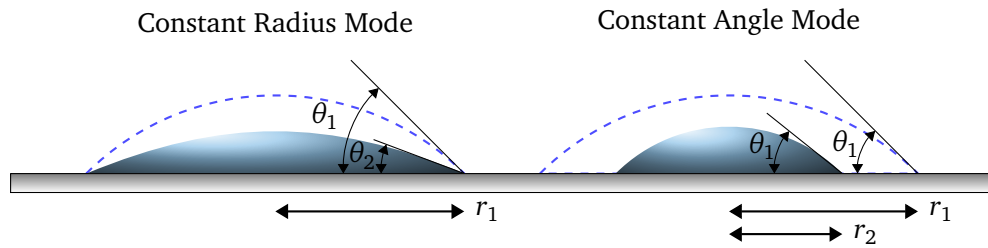
Figure 1.7: A diagram depicting the constant radius mode where the droplet remains pinned while the angle fluctuates (left), and the constant angle mode where the angle remains constant while the radius retracts (right).

flows and instabilities produced by temperature differences [131, 132]. The second direction concerns droplets that evaporate into a vapour saturated atmosphere so that the dynamics are not limited by diffusion, where phase change from liquid to gas occurs due to heating the substrate above the saturation. Experimentally this situation is more difficult to examine than evaporation into an ambient atmosphere [133–136], however, from a modelling perspective this yields simplifications in that one can decouple the dynamics of the liquid and gas phase in the so called 'one-sided' model [137] in which the assumption is that the gas phase has negligible effect on the liquid phase. Thus, avoiding a full treatment of all phases using the 'two-sided' model, which couples the Navier-Stokes equations and energy equations for the temperature, pressure and density [138]. Noteworthy also is the possibility to consider a convection free gas phase that is comprised of both an inert gas, and the liquid vapour, in the '1.5-sided' model where the thermal conductivity, density and viscosity of the gas are small compared to the liquid (see e.g. Dondlinger *et al*. [138] and Haut & Colinet [139]). Just like many other works with evaporation [53, 140–144], we likewise invoke the one-sided model alongside the lubrication approximation, adopting a similar approach like the one developed throughout this thesis.

The mass flux study allows us to investigate under which circumstances pinning and stick-slip scenarios arise. Pinning dynamics give rise to two distinct modes, the *constant-radius* and *constant-angle* modes. In the former, the contact line remains fixed in place so that the apparent contact angle changes, whereas in the latter, the apparent contact angle remains constant while the radius retracts (see figure 1.7). Understanding the creation and lifetime of these modes has become an important avenue of research for controlling droplets during the evaporation process [145–149]. Noteworthy also is a different evaporation mode reported by Wells *et al*. [150], the so-called *snapping mode*, which occurs when a droplet evaporates on

a macroscopically structured surface. In these circumstances the droplet moves to different regions of the substrate in 'snapping' transitions which occur on time-scales much longer than the harsher stick-slip events; crucially, this could provide more methodologies of controlling droplet shapes during mass loss for the aforementioned applications.

1.5   Outline of the Thesis

Throughout this thesis we will investigate the motion of liquid droplets moving over solid surfaces. As alluded to in the preceding sections, this problem is highly non-trivial, and requires the careful consideration of both the micro- and macro-scales. Specifically, this will be a combined numerical and analytical investigation which will consider a variety of physical settings, placing specific attention on when the droplet varies in mass to elucidate some of the behaviours observed in experiments.

1.5.1   Derivation of the Model

In the second chapter we review the derivation of the model that describes a thin liquid droplet moving down a inclined, rough, and chemically heterogeneous surface. Specifically, we consider viscous fluids with small contact angles so that we can invoke the lubrication approximation of the Navier-Stokes equations and derive a fourth order non-linear partial differential equation (PDE) for the droplet thickness, which is coupled with a slip condition to alleviate the moving contact line problem described previously. The appropriate boundary conditions to supplement this PDE are derived in the long-wave limit, which forms the full governing model of the thesis. To simplify the future analytical and numerical calculations, we also propose a change of variables to map the free-boundary moving contact line problem to one fixed in space.

1.5.2   Asymptotic Analysis

In the third chapter we present the analytical methodologies where progress is made in the small slip limit. This is performed by assuming that there is a separation of scales, and that the spreading of the droplet and mass changes occur sufficiently slowly so that the method of matched of matched asymptotic expansions can be used. Like the Cox-Voinov law (1.5), we aim to couple the details of the macro-scale where capillary forces dominate, and the

micro-scale close to the contact line where slip effects manifest themselves (see Lacey [52] and Hocking [54]). In previous studies this method has led to the development of reduced models for the motion of the contact line (or contact points in 2D), whose solutions typically exhibit excellent agreement with the full equations in the regime of their validity (see, for example [53, 55, 56, 58–61]).

Firstly, we limit the discussion to the 2D setting where horizontal, perfectly flat and chemically heterogeneous substrates are assumed, extending upon the analysis of Vellingiri *et al.* [55] who consider the case of constant mass. Although difficult to contrast to experimental studies, this analysis is a key stepping stone towards a greater understanding of the mechanisms responsible for many of the aforementioned effects that arise due to the interesting interplay between liquid flux and heterogeneity. Using the insights gained from the 2D study, we perform an extension to the 3D setting of the same problem by considering droplets with weakly deformed contact lines. This was achieved by considering the special case of constant mass, where the initial findings are reported in [61]. Here, we include the additional terms which account for liquid flux through the macro-scale of the drop. In both the 2D and 3D settings we describe flux as an arbitrary function, rather than assuming *a priori* a form of the flux, like, say, with evaporating droplets [53, 151]. Specifically, we focus primarily on the case when flux vanishes at the boundary of the drop to capture the main features of the dynamics without dealing with the implicit evolution equations that arise, which are similar in format to those derived by Oliver *et al.* [107] who consider the problem of constant spatial mass flux with homogeneous substrates. This assumption, however, is inappropriate in the case of evaporation since mass loss is maximised near the contact line, therefore effort is also made to extend on the analysis of Savva *et al.* [53] to include chemical heterogeneities which are neglected in [53] in favour of analytical tractability. Therefore, the contribution here is the combination of the macro-scale analysis for droplets of variable mass with a newly modified micro-scale investigation, alongside the formation of an evolution equation for the droplet volume which accounts for the deformations in the contact line. Finally, the assumption of perfectly flat surfaces will be relaxed and progress will be reported in the regime where topographical features across the substrate are sufficiently small so that the reduced model developed in the previous configurations can be used to investigate such situations.

1.5.3 Numerical Methods

In the fourth chapter the numerical methodologies we developed to establish a general framework to solve for contact line motion are described. In 2D, efforts are placed on solving the governing model using the numerical framework developed by Savva & Kalliadasis [56] which is based on the *pseudospectral collocation method* (see Trefethen [152] for a description of the pseudospectral collocation method). In 3D a new scheme is developed, noting that initial results have been reported in [61], here presenting a more general model that accounts for changes in mass flux where the substrate is inclined and includes changes in its topography.

We first develop a scheme that solves for droplet spreading with variable mass in the 2D geometry, specifically considering the case of horizontal, flat, and chemically heterogeneous substrates where gravitational forces are neglected. We also discuss the development of a general framework that solves for contact line motion with 3D droplets where gravitational effects may become appreciable, and additionally accounts for surface inclination as well as changes in surface topography and chemistry. Also explored is the development of a hybrid method that combines high-order numerical methods with low-order approximate models, such as the one developed by Lacey [52] (see equation (1.6)). This technique is based on the *boundary integral method* as presented by Glasner [153], and is used to extract the apparent contact angle to combine with the low-order models, which, as we show, works rather well against full numerical calculations of the governing equations. Once more, initial results are reported in [61]; in this thesis we generalise the boundary integral method to account for the effects of surface inclination, surface topography, and gravitational effects.

1.5.4 Simulations

In the fifth chapter, the outcomes of the analysis will be scrutinised by contrasting the solutions of the governing equations with the predictions of the models developed in chapter 3. In the mass flux cases, the balance between fluid transfer and surface heterogeneity is explored through the dynamics of simulations, where many of the interesting effects previously mentioned emerge. The additional benefit of the 2D study is that we can extract general insights by considering a bifurcation analysis similar to Pradas *et al*. [125]. Thus by treating the droplet area as a bifurcation parameter we can explore the complicated effects seen in the dynamics, such as stick-slip and hysteresis-like effects, even when the structure of the

substrate is relatively simple. In the 3D simulations we investigate similar phenomena while commenting on the qualitative comparison observed between studies concerning both droplets which vary in mass through the macro-scale features and evaporating droplets where the flux is maximised close to the contact line. The merits of the analysis are coupled with the boundary integral method where we show that it offers a more favourable alternative to full-scale computing in all presented cases, especially since full simulations require significantly more time and resources to complete than the lower-dimensional asymptotic models. This investigation is likewise extended to the case where changes in surface topography are present, where rather compelling numerical evidence suggests that the hybrid methodologies can be used in the case of small surface topographies without the need for more involved analysis.

1.5.5 Concluding Remarks

In the sixth and final chapter, the outcomes of the thesis will be summarised. As a closing section the generalised boundary integral formulation will be used alongside the derived reduced model to form preliminary explorations into the cases where surface inclination and gravitational effects are present. Specifically, contrast will be made with the low-order model (1.6) to further highlight the importance of deriving the next-order correction to accurately capture the full dynamics, and thus, motivate further study to derive a general asymptotic framework to properly account for these effects. We will also offer some brief discussions on other avenues for future work which can assist in explaining natural phenomena, as well as to develop or improve modern technologies.

— Chapter 2 —

Derivation of the Model

In this chapter we review the derivation of the governing set of equations and conditions. These derivations are based on the *long-wave* or *thin-film* approximation, which describes the flow of fluids in the case where one length scale is significantly smaller than the others. Such flows can occur in a variety of scientific problems, for example, with studying the growth of bacterial biofilms [154], gravity currents in lava flows [155], and tear films in the eye [156], to name a few (see also Oron *et al*. [157] and Craster & Matar [158]).

In this study, we consider a viscous droplet in the x-y-z Cartesian plane that moves down a slope at inclination angle α, noting the conditions of the ambient atmosphere are neglected (see figure 2.1 for a sketch of the problem considered). The substrate which supports the droplet is given by $z = \eta(x, y)$, where $\eta(x, y)$ is a differentiable function controlling the small spatial variations across the substrate. We assume that the droplet is thin so that its characteristic height-scale H is much smaller than its characteristic length-scale L, in other
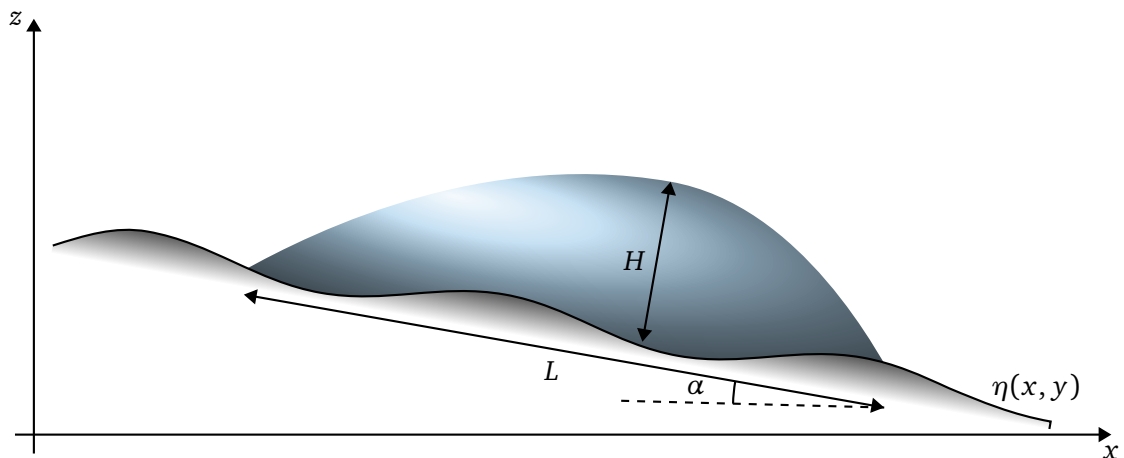

Figure 2.1: A sketch of the problem considered in the x-z plane. The droplet moves down the substrate $z = \eta(x, y)$ which is inclined at an angle α. The parameters H and L represent the characteristic height-scale, and length-scale of the droplet, respectively.

words we consider $0 < \varepsilon = H/L \ll 1$. This implies that the droplets considered have small contact angles so a long-wave approximation can be used (i.e. we consider the hydrophilic regime). Using the long-wave approximation to describe droplet spreading is a standard step for many related works (see, e.g. [54–56, 61, 107, 108]), and has the benefit that considerable simplifications to the Navier-Stokes equations and the relevant boundary conditions can be made [48], as we shall see. Importantly, the product of this step is that a single evolution equation for the droplet thickness can be derived (called the *thin-film* equation) where all velocities and pressures are eliminated.

In future sections the governing equations and conditions to form the thin-film equation are described, which are scaled according to the long-wave theory to form the non-dimensional governing PDE. This PDE is then combined with the appropriate boundary conditions that describe the liquid droplet, forming the governing model that will be used for the remainder of the thesis. To ensure that future analytical and numerical calculations are tractable, we also propose a transformation of variables which moves the system based on Cartesian variables to a more suitable coordinate system.

2.1 The Governing Equations

In this section we will highlight the equations and boundary conditions required to form the thin-film equation that describes the droplet thickness.

2.1.1 Navier-Stokes Equations

To start we consider the Navier-Stokes equations for a Newtonian fluid moving down a slope at inclination angle α with pressure p, density ρ, and dynamic viscosity μ, namely

$$\partial_t \boldsymbol{u} + (\boldsymbol{u} \cdot \boldsymbol{\nabla}) \boldsymbol{u} = -\frac{1}{\rho} \boldsymbol{\nabla} p + \frac{\mu}{\rho} \nabla^2 \boldsymbol{u} + g \sin \alpha \boldsymbol{i} - g \cos \alpha \boldsymbol{k}. \tag{2.1}$$

These equations are essentially an application of Newton's second law for fluid motion, and whose derivation, while suppressed here, can be found in many standard textbooks on fluid dynamics (see, e.g. Acheson [159]). In the above equations $\boldsymbol{u} = u\boldsymbol{i} + v\boldsymbol{j} + w\boldsymbol{k}$ is the fluid velocity where $\boldsymbol{i}$, $\boldsymbol{j}$ and $\boldsymbol{k}$ are the unit vectors denoting the downhill, transverse and normal components, respectively. In these equations, $\boldsymbol{\nabla}(\cdot) = \partial_x(\cdot)\boldsymbol{i} + \partial_y(\cdot)\boldsymbol{j} + \partial_z(\cdot)\boldsymbol{k}$, and $\nabla^2(\cdot) = \partial_x^2(\cdot) + \partial_y^2(\cdot) + \partial_z^2(\cdot)$ are the gradient and Laplacian operators in Cartesian coordinates,

respectively, and where $(\cdot)$ is the placeholder for the operand. These equations are also solved subject to the divergence free condition

$$\nabla \cdot \boldsymbol{u} = 0, \tag{2.2}$$

which implies that the density remains constant in a parcel of fluid that moves with the flow velocity, in other words, we model our flow as incompressible.

2.1.2 Boundary Conditions on the Substrate

We must supplement the Navier-Stokes equations with the necessary boundary conditions to account for the thin liquid droplets, where first we consider the conditions along the substrate (i.e. at $z = \eta(x, y)$). We have a *no-penetration condition*, which states that the fluid particles on the substrate have no normal velocity, in other words

$$\boldsymbol{u}|_{z=\eta} \cdot \boldsymbol{n}_s = 0, \tag{2.3}$$

where $\boldsymbol{n}_s$ is the unit normal substrate

$$\boldsymbol{n}_s = \frac{1}{\sqrt{1 + (\partial_x \eta)^2 + (\partial_y \eta)^2}} \begin{pmatrix} -\partial_x \eta \\ -\partial_y \eta \\ 1 \end{pmatrix}, \tag{2.4}$$

therefore, we have the condition

$$w|_{z=\eta} = \left(u \partial_x \eta + v \partial_y \eta \right)\big|_{z=\eta}. \tag{2.5}$$

As mentioned in chapter 1 we encounter the moving contact line problem, which occurs when enforcing the no-slip boundary condition at the moving contact line. To circumvent the issues of the moving contact line problem we opt for a slip condition like many related works (see e.g. [54–56, 58–61, 107]), noting that the reasons behind this choice will be further expanded on in chapter 4 where the numerical methods are discussed. This means we consider a condition of the form

$$\boldsymbol{u}|_{z=\eta} = \frac{\lambda^{3-n}}{\mu h^{n-2}} \boldsymbol{n}_s \cdot \boldsymbol{T}|_{z=\eta} \cdot \boldsymbol{t}_s, \tag{2.6}$$

where $h(x, y, t)$ is the thickness of the drop, $\boldsymbol{t}_s$ is a unit tangent vector to the surface, such as

$$\boldsymbol{t}_s = \frac{1}{\sqrt{1 + (\partial_x \eta)^2}} \begin{pmatrix} 1 \\ 0 \\ \partial_x \eta \end{pmatrix} \quad \text{or} \quad \boldsymbol{t}_s = \frac{1}{\sqrt{1 + (\partial_y \eta)^2}} \begin{pmatrix} 0 \\ 1 \\ \partial_y \eta \end{pmatrix}, \tag{2.7}$$

and $\boldsymbol{T}$ is the viscous stress tensor

$$\boldsymbol{T} = \begin{pmatrix} -p + 2\mu\partial_x u & \mu\left(\partial_y u + \partial_x v\right) & \mu\left(\partial_z u + \partial_x w\right) \\ \mu\left(\partial_y u + \partial_x v\right) & -p + 2\mu\partial_y v & \mu\left(\partial_z v + \partial_y w\right) \\ \mu\left(\partial_z u + \partial_x w\right) & \mu\left(\partial_z v + \partial_y w\right) & -p + 2\mu\partial_z w \end{pmatrix}. \tag{2.8}$$

In (2.6), λ is the dimensional parameter controlling the slip length which is assumed to be constant across the substrate, and n is a integer value which determines the type of slip condition used. If $n = 2$ we directly recover the *Navier-slip* condition which is arguably the most popular in contact line dynamics (see, e.g. [53, 54, 56–59]) and alleviates the moving contact line problem by rendering the singularity in the pressure logarithmic and the stress integrable, and thus yielding a finite force. If $n = 1$ we uncover the *inverse linear slip* boundary condition as proposed by Ruckenstein & Dunn [39] (see also Greenspan [108]), where the pressure becomes finite and therefore regularising the total shear stress, which can be implemented easier than the Navier slip model, as we shall see. However, we stress that the both slip models contain the same leading-order micro-scale asymptotics as $\lambda \to 0$, which means that the dynamics are nearly indistinguishable if the contact line variations are much longer than slip (see Savva & Kalliadasis [57]). Let us also remark about using a constant slip length across the substrate. If a more realistic spatially varying slip length was chosen, then we would not expect the underlying dynamics to be affected too drastically since previous asymptotic analyses have shown that the effect of slip is logarithmic (see, e.g. Vellingiri *et al.* [55]).

2.1.3 Boundary Conditions on the Free Surface

Alongside the conditions on the substrate we also apply conditions to the free surface of the droplet (i.e. each condition is applied at $z = h + \eta$). We allow for transfer of fluid through the free surface of the droplet through the use of the *kinematic boundary condition*, which is stated as

$$\frac{\mathrm{D}}{\mathrm{D}t}(z - h - \eta) + \frac{q}{\rho} = 0 \quad \text{at} \quad z = h + \eta, \tag{2.9}$$

where $\mathrm{D}/\mathrm{D}t$ is the convective derivative and $q(x, y, t)$ is the spatially varying mass flux function which captures fluid transfer through the free surface. Note that fluid transfer could likewise have been facilitated by relaxing the no-penetration condition on the substrate (equation (2.5)), meaning that fluid transfer would then occur through the base of the

droplet, which nevertheless leads to the same long-wave model. Here, we choose to model fluid transfer through the free surface, since in this study we investigate mass loss through evaporation in which fluid particles are transferred from the liquid to the gas phase through the free surface.

We also require no discontinuity in the hydrodynamic stress across the interface, this is expressed in the form

$$\boldsymbol{n} \cdot \boldsymbol{T} \cdot \boldsymbol{t} = 0, \quad \text{at} \quad z = h + \eta \tag{2.10}$$

where $\boldsymbol{n}$ is the unit outward normal vector to the free surface

$$\boldsymbol{n} = \frac{1}{\sqrt{1 + \left[\partial_x (h + \eta)\right]^2 + \left[\partial_y (h + \eta)\right]^2}} \begin{pmatrix} -\partial_x (h + \eta) \\ -\partial_y (h + \eta) \\ 1 \end{pmatrix}, \tag{2.11}$$

and $\boldsymbol{t}$ is any unit tangent vector, such as

$$\boldsymbol{t} = \frac{1}{\sqrt{1 + \left[\partial_x (h + \eta)\right]^2}} \begin{pmatrix} 1 \\ 0 \\ \partial_x (h + \eta) \end{pmatrix} \quad \text{or} \quad \boldsymbol{t} = \frac{1}{\sqrt{1 + \left[\partial_y (h + \eta)\right]^2}} \begin{pmatrix} 0 \\ 1 \\ \partial_y (h + \eta) \end{pmatrix}. \tag{2.12}$$

Finally, we require that the jump in the normal stress across the interface is balanced by the curvature pressure, giving the condition

$$\boldsymbol{n} \cdot \boldsymbol{T} \cdot \boldsymbol{n} = \sigma \boldsymbol{\nabla} \cdot \boldsymbol{n}. \tag{2.13}$$

2.2 Non-Dimensionalisation

Now that all equations and conditions are specified, the next step is apply a set of scalings which allow us to deduce what components of each equation are important. This will enable us to arrive with a reduced set of equations which will be used in the next section to derive the thin-film equation. The scaling laws we apply are as follows[1]:

$$x = L\tilde{x}, \quad y = L\tilde{y}, \quad z = H\tilde{z}, \quad u = U\tilde{u}, \quad v = U\tilde{v}, \quad w = W\tilde{w}, \quad t = \frac{3L}{U}\tilde{t}, \quad p = \frac{\mu U L}{H^2}\tilde{p},$$

$$h = H\tilde{h}, \quad \eta = H\tilde{\eta}, \quad \lambda = \frac{H}{3^{1/(3-n)}}\tilde{\lambda}, \quad q = \frac{\rho H U}{3L}\tilde{q}, \tag{2.14}$$

where U and W are the characteristic velocities horizontally, and vertically, and tildes correspond to dimensionless variables. Using (2.14) on the continuity equation (2.2) gives

$$\partial_{\tilde{x}}\tilde{u} + \partial_{\tilde{y}}\tilde{v} + \frac{LW}{HU}\partial_{\tilde{z}}\tilde{w} = 0, \tag{2.15}$$

---

[1]The presence of 3 in any rescaling will be justified later.

and therefore choosing $W = \varepsilon U$ so that the flow in the z direction is much slower than the x and y directions yields the non-dimensionalised equation

$$\tilde{\boldsymbol{\nabla}} \cdot \tilde{\boldsymbol{u}} = 0. \tag{2.16}$$

Similarly, applying the scalings (2.14) to the Navier-Stokes equations (2.1) gives the set of equations in non-dimensional form

$$\varepsilon^2 \mathrm{Re}\left[\frac{1}{3}\partial_{\tilde{t}}\tilde{u} + \left(\tilde{\boldsymbol{u}}\cdot\tilde{\boldsymbol{\nabla}}\right)\tilde{u}\right] = -\partial_{\tilde{x}}\tilde{p} + \varepsilon^2\left(\partial_{\tilde{x}}^2\tilde{u} + \partial_{\tilde{y}}^2\tilde{u}\right) + \partial_{\tilde{z}}^2\tilde{u} + \varepsilon^3\frac{\mathrm{Bo}}{\mathrm{Ca}}\frac{\sin\alpha}{\alpha_s}, \tag{2.17a}$$

$$\varepsilon^2 \mathrm{Re}\left[\frac{1}{3}\partial_{\tilde{t}}\tilde{v} + \left(\tilde{\boldsymbol{u}}\cdot\tilde{\boldsymbol{\nabla}}\right)\tilde{v}\right] = -\partial_{\tilde{y}}\tilde{p} + \varepsilon^2\left(\partial_{\tilde{x}}^2\tilde{v} + \partial_{\tilde{y}}^2\tilde{v}\right) + \partial_{\tilde{z}}^2\tilde{v}, \tag{2.17b}$$

$$\varepsilon^4 \mathrm{Re}\left[\frac{1}{3}\partial_{\tilde{t}}\tilde{w} + \left(\tilde{\boldsymbol{u}}\cdot\tilde{\boldsymbol{\nabla}}\right)\tilde{w}\right] = -\partial_{\tilde{z}}\tilde{p} + \varepsilon^4\left(\partial_{\tilde{x}}^2\tilde{w} + \partial_{\tilde{y}}^2\tilde{w}\right) + \varepsilon^2\partial_{\tilde{z}}^2\tilde{w} - \varepsilon^3\frac{\mathrm{Bo}}{\mathrm{Ca}}\cos\alpha. \tag{2.17c}$$

In these equations, $\mathrm{Re} = \rho U L/\mu$ is the *Reynolds number* which is a ratio between inertial and viscous forces, $\mathrm{Bo} = \rho g L^2/\sigma$ is the *Bond number* which contrasts gravitational forces to surface tension, and $\alpha_s = O(\varepsilon)$ is a small reference angle, typically taken to be the average contact angle along the substrate. Since the dynamics we wish to examine are typically slow (see also Bonn *et al.* [23]), we can neglect the inertial terms on the left hand sides of (2.17) under the assumption that viscous forces dominate. This is equivalent to saying that the Reynolds number for this scenario is small, i.e. we consider the regime where $\mathrm{Re} \ll 1$.

Across the substrate we impose the no-penetration condition (2.5) which is scaled using (2.14) to give

$$\tilde{w}|_{\tilde{z}=\tilde{\eta}} = \left(\tilde{u}\partial_{\tilde{x}}\tilde{\eta} + \tilde{v}\partial_{\tilde{y}}\tilde{\eta}\right)\big|_{\tilde{z}=\tilde{\eta}}. \tag{2.18}$$

Similarly, the slip condition (2.6) yields the two components

$$\tilde{u}|_{\tilde{z}=\tilde{\eta}} = -\frac{(\varepsilon L)^{4-2n}\tilde{\lambda}^{3-n}}{3\tilde{h}^{n-2}}\left\{\varepsilon^4\partial_{\tilde{x}}\tilde{\eta}\left(\partial_{\tilde{x}}\tilde{\eta}\partial_{\tilde{x}}\tilde{w} + \partial_{\tilde{y}}\tilde{\eta}\partial_{\tilde{y}}\tilde{w}\right) + \varepsilon^2\left[\left(\partial_{\tilde{x}}\tilde{\eta}\right)^2\partial_{\tilde{z}}\tilde{u} + \left(\partial_{\tilde{y}}\tilde{u} + \partial_{\tilde{x}}\tilde{v}\right)\partial_{\tilde{y}}\tilde{\eta}\right.$$

$$\left.\left(\partial_{\tilde{y}}\tilde{\eta}\partial_{\tilde{z}}\tilde{v} + 2\partial_{\tilde{x}}\tilde{u} - 2\partial_{\tilde{z}}\tilde{w}\right)\partial_{\tilde{x}}\tilde{\eta} - \partial_{\tilde{x}}\tilde{w}\right] - \partial_{\tilde{z}}\tilde{u}\right\}\bigg/\left\{\varepsilon^4\left[\left(\partial_{\tilde{x}}\tilde{\eta}\right)^4 + \left(\partial_{\tilde{x}}\tilde{\eta}\right)^2\left(\partial_{\tilde{y}}\tilde{\eta}\right)^2\right] + \right.$$

$$\left.\varepsilon^2\left[2\left(\partial_{\tilde{x}}\tilde{\eta}\right)^2 + \left(\partial_{\tilde{y}}\tilde{\eta}\right)^2\right] + 1\right\}^{1/2}, \tag{2.19a}$$

and

$$\tilde{v}|_{\tilde{z}=\tilde{\eta}} = -\frac{(\varepsilon L)^{4-2n}\tilde{\lambda}^{3-n}}{3\tilde{h}^{n-2}}\left\{\varepsilon^4\partial_{\tilde{y}}\tilde{\eta}\left(\partial_{\tilde{x}}\tilde{\eta}\partial_{\tilde{x}}\tilde{w} + \partial_{\tilde{y}}\tilde{\eta}\partial_{\tilde{y}}\tilde{w}\right) + \varepsilon^2\left[\left(\partial_{\tilde{y}}\tilde{\eta}\right)^2\partial_{\tilde{z}}\tilde{v} + \left(\partial_{\tilde{y}}\tilde{u} + \partial_{\tilde{x}}\tilde{v}\right)\partial_{\tilde{x}}\tilde{\eta}\right.$$

$$\left.\left(\partial_{\tilde{x}}\tilde{\eta}\partial_{\tilde{z}}\tilde{u} + 2\partial_{\tilde{y}}\tilde{v} - 2\partial_{\tilde{z}}\tilde{w}\right)\partial_{\tilde{y}}\tilde{\eta} - \partial_{\tilde{y}}\tilde{w}\right] - \partial_{\tilde{z}}\tilde{v}\right\}\bigg/\left\{\varepsilon^4\left[\left(\partial_{\tilde{y}}\tilde{\eta}\right)^4 + \left(\partial_{\tilde{x}}\tilde{\eta}\right)^2\left(\partial_{\tilde{y}}\tilde{\eta}\right)^2\right] + \right.$$

$$\varepsilon^2\left[2\left(\partial_{\tilde{y}}\tilde{\eta}\right)^2 + \left(\partial_{\tilde{x}}\tilde{\eta}\right)^2\right] + 1\Bigg\}^{1/2}, \quad (2.19\text{b})$$

in the x and y directions, respectively.

Along the free surface the scaled version of the kinematic boundary condition (2.9) is expressed as

$$\tilde{w} = \left[\frac{1}{3}\partial_{\tilde{t}}\tilde{h} + \tilde{u}\partial_{\tilde{x}}\left(\tilde{h} + \tilde{\eta}\right) + \tilde{v}\partial_{\tilde{y}}\left(\tilde{h} + \tilde{\eta}\right)\right] - \frac{\tilde{q}}{3} \quad \text{at} \quad \tilde{z} = \tilde{h} + \tilde{\eta}, \quad (2.20)$$

which is found by expanding the convective derivative $\mathrm{D}/\mathrm{D}t$ and applying (2.14). The condition (2.10) that states there is no discontinuity in the hydrodynamic stress gives the two equations

$$\partial_{\tilde{z}}\tilde{u} + \varepsilon^2\Bigg\{\partial_{\tilde{x}}\tilde{w} - \left(\partial_{\tilde{y}}\tilde{u} + \partial_{\tilde{x}}\tilde{v}\right)\left(\partial_{\tilde{y}}\tilde{h} + \partial_{\tilde{y}}\tilde{\eta}\right) - \left[\left(\partial_{\tilde{y}}\tilde{h} + \partial_{\tilde{y}}\tilde{\eta}\right)\partial_{\tilde{z}}\tilde{v} + 2\partial_{\tilde{x}}\tilde{u} - 2\partial_{\tilde{z}}\tilde{w}\right]\partial_{\tilde{x}}\tilde{h}$$

$$- \left[\left(\partial_{\tilde{x}}\tilde{h}\right)^2 + \left(\partial_{\tilde{x}}\tilde{\eta}\right)^2\right]\partial_{\tilde{z}}\tilde{u} + \left(2\partial_{\tilde{z}}\tilde{w} - 2\partial_{\tilde{x}}\tilde{u} - \partial_{\tilde{z}}\tilde{v}\partial_{\tilde{y}}\tilde{h} - 2\partial_{\tilde{x}}\tilde{h}\partial_{\tilde{z}}\tilde{u} - \partial_{\tilde{y}}\tilde{\eta}\partial_{\tilde{z}}\tilde{v}\right)\partial_{\tilde{x}}\tilde{\eta}\Bigg\}$$

$$- \varepsilon^4\left(\partial_{\tilde{x}}\tilde{h} + \partial_{\tilde{x}}\tilde{\eta}\right)\left[\partial_{\tilde{x}}\tilde{w}\left(\partial_{\tilde{x}}\tilde{\eta} + \partial_{\tilde{x}}\tilde{h}\right) + \partial_{\tilde{y}}\tilde{w}\left(\partial_{\tilde{y}}\tilde{h} + \partial_{\tilde{y}}\tilde{\eta}\right)\right] = 0, \quad (2.21\text{a})$$

and

$$\partial_{\tilde{z}}\tilde{v} + \varepsilon^2\Bigg\{\partial_{\tilde{y}}\tilde{w} - \left(\partial_{\tilde{y}}\tilde{u} + \partial_{\tilde{x}}\tilde{v}\right)\left(\partial_{\tilde{x}}\tilde{h} + \partial_{\tilde{x}}\tilde{\eta}\right) - \left[\left(\partial_{\tilde{x}}\tilde{h} + \partial_{\tilde{x}}\tilde{\eta}\right)\partial_{\tilde{z}}\tilde{u} + 2\partial_{\tilde{y}}\tilde{v} - 2\partial_{\tilde{z}}\tilde{w}\right]\partial_{\tilde{y}}\tilde{h}$$

$$- \left[\left(\partial_{\tilde{y}}\tilde{h}\right)^2 + \left(\partial_{\tilde{y}}\tilde{\eta}\right)^2\right]\partial_{\tilde{z}}\tilde{v} + \left(2\partial_{\tilde{z}}\tilde{w} - 2\partial_{\tilde{y}}\tilde{v} - \partial_{\tilde{z}}\tilde{u}\partial_{\tilde{x}}\tilde{h} - 2\partial_{\tilde{y}}\tilde{h}\partial_{\tilde{z}}\tilde{v} - \partial_{\tilde{x}}\tilde{\eta}\partial_{\tilde{z}}\tilde{u}\right)\partial_{\tilde{y}}\tilde{\eta}\Bigg\}$$

$$- \varepsilon^4\left(\partial_{\tilde{y}}\tilde{h} + \partial_{\tilde{y}}\tilde{\eta}\right)\left[\partial_{\tilde{y}}\tilde{w}\left(\partial_{\tilde{y}}\tilde{\eta} + \partial_{\tilde{y}}\tilde{h}\right) + \partial_{\tilde{x}}\tilde{w}\left(\partial_{\tilde{x}}\tilde{h} + \partial_{\tilde{x}}\tilde{\eta}\right)\right] = 0, \quad (2.21\text{b})$$

which are evaluated at the free surface (at $\tilde{z} = \tilde{h} + \tilde{\eta}$). Finally condition (2.13) is scaled according to (2.14), which gives

$$\tilde{p} + 2\varepsilon^2\left[\left(\partial_{\tilde{x}}\tilde{h} + \partial_{\tilde{x}}\tilde{\eta}\right)\partial_{\tilde{z}}\tilde{u} + \left(\partial_{\tilde{y}}\tilde{h} + \partial_{\tilde{y}}\tilde{\eta}\right)\partial_{\tilde{z}}\tilde{v} - \partial_{\tilde{z}}\tilde{w}\right] = \frac{\varepsilon^3\sigma}{\mu U}\left[\partial_{\tilde{x}}^2(\tilde{h} + \tilde{\eta}) + \partial_{\tilde{y}}^2(\tilde{h} + \tilde{\eta})\right] + O(\varepsilon^4)$$

$$(2.22)$$

and is likewise evaluated at the free surface (noting terms of $O(\varepsilon^4)$ were neglected here since the equation becomes rather unwieldy). Importantly, from (2.22) we readily deduce the scaling $\mathrm{Ca} = \mu U/\sigma \sim \varepsilon^3$ which states that the problem is surface tension dominated so that we consider the regime where $0 < \mathrm{Ca} \ll 1$, allowing us to render the spreading dynamics as quasistatic.

2.3   Derivation of the Thin-Film Equation

All previous equations and conditions can be combined into a single evolution equation for the thickness of the droplet in the limit as $\varepsilon \to 0$. Dropping the tildes, and replacing the earlier notation by defining

$$\boldsymbol{u} = u\boldsymbol{i} + v\boldsymbol{j}, \quad \boldsymbol{\nabla}(\cdot) = \partial_x(\cdot)\boldsymbol{i} + \partial_y(\cdot)\boldsymbol{j} \quad \text{and} \quad \nabla^2(\cdot) = \partial_x^2(\cdot) + \partial_y^2(\cdot), \tag{2.23}$$

equations (2.16), (2.17), (2.18), (2.19), (2.20), (2.21) and (2.22) give the following system of non-dimensional equations:

$$\boldsymbol{\nabla}p = \partial_z^2 \boldsymbol{u} + \frac{\mathrm{Bo}\sin\alpha}{\alpha_s}\boldsymbol{i}, \tag{2.24a}$$

$$\partial_z p = -\mathrm{Bo}\cos\alpha, \tag{2.24b}$$

$$\partial_z w = -\boldsymbol{\nabla}\cdot\boldsymbol{u}, \tag{2.24c}$$

$$w|_{z=\eta} = \boldsymbol{u}\cdot\boldsymbol{\nabla}\eta|_{z=\eta}, \tag{2.24d}$$

$$\boldsymbol{u}|_{z=\eta} = \frac{\lambda^{3-n}}{3h^{2-n}}\partial_z\boldsymbol{u}|_{z=\eta}, \tag{2.24e}$$

$$w|_{z=\eta+h} = \frac{1}{3}\partial_t h + \boldsymbol{u}\cdot\boldsymbol{\nabla}(h+\eta)|_{z=h+\eta} - \frac{q}{3}, \tag{2.24f}$$

$$\partial_z\boldsymbol{u}|_{z=\eta+h} = 0, \tag{2.24g}$$

$$p|_{z=\eta+h} = -\nabla^2(h+\eta). \tag{2.24h}$$

The next aim is to eliminate all velocities and pressures, and arrive with a PDE which describes the evolution of the droplet thickness $h(x,y,t)$. Firstly, we start with the incompressibility condition (2.24c) and combine with the vanishing normal velocity condition (2.24d) to obtain

$$w|_{z=\eta+h} - \boldsymbol{u}\cdot\boldsymbol{\nabla}\eta|_{z=\eta} = -\int_{\eta}^{\eta+h} \boldsymbol{\nabla}\cdot\boldsymbol{u}\,\mathrm{d}z, \tag{2.25}$$

which is appropriately modified by using the Leibniz integral rule

$$\int_{\eta}^{h+\eta} \boldsymbol{\nabla}\cdot\boldsymbol{u}\,\mathrm{d}z = \boldsymbol{\nabla}\cdot\int_{\eta}^{h+\eta} \boldsymbol{u}\,\mathrm{d}z + \boldsymbol{u}\cdot\boldsymbol{\nabla}\eta|_{z=\eta} - \boldsymbol{u}\cdot\boldsymbol{\nabla}(h+\eta)|_{z=h+\eta}, \tag{2.26}$$

and the kinematic boundary condition (2.24f), yielding

$$\frac{1}{3}\partial_t h + \boldsymbol{\nabla}\cdot\int_{\eta}^{\eta+h} \boldsymbol{u}\,\mathrm{d}z = \frac{q}{3}. \tag{2.27}$$

Using equations (2.24b) and (2.24h) we formulate the pressure as

$$p = \mathrm{Bo}\,(h+\eta-z)\cos\alpha - \nabla^2(h+\eta), \tag{2.28}$$

which is coupled with (2.24a), (2.24e) and (2.24g) to obtain the velocity[2]

$$\boldsymbol{u} = \left[\frac{(z-\eta)(\eta+2h-z)}{2} + \frac{h^{n-1}\lambda^{3-n}}{3} \right] \boldsymbol{\nabla} \left(\nabla^2(h+\eta) - \text{Bo}(h+\eta)\cos\alpha + \frac{\text{Bo}\sin\alpha}{\alpha_s}x \right).$$

(2.29)

Thus, forming the thin-film PDE on combination with equation (2.27), namely

$$\partial_t h + \boldsymbol{\nabla} \cdot \left\{ \left(h^3 + h^n \lambda^{3-n} \right) \boldsymbol{\nabla} \left[\nabla^2(h+\eta) - \text{Bo}(h+\eta)\cos\alpha + \frac{\text{Bo}\sin\alpha}{\alpha_s}x \right] \right\} = q(x,y,t), \quad (2.30)$$

which henceforth will be referred to as the governing PDE.

2.4   Derivation of the Boundary Conditions

The governing PDE (2.30) describes the height evolution of a thin liquid film. However, to study droplet spreading phenomena we must also supplement (2.30) with the appropriate boundary conditions which will form the governing model for the thesis.

2.4.1   Vanishing Thickness Condition

The first condition states that the droplet thickness vanishes as it touches the substrate, which is expressed as

$$h|_C = 0,$$

(2.31)

where $C(t)$ is the curve describing the contact line, which is made non-dimensional by scaling with the length-scale L.
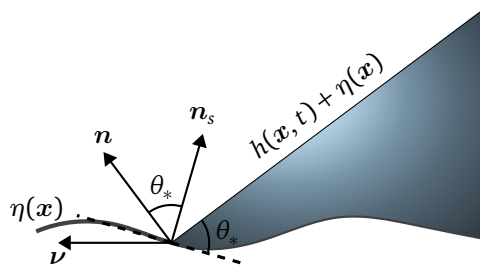
Figure 2.2: A close up of the contact line. Here $\boldsymbol{n}_s$ is the normal to the substrate (2.4), $\boldsymbol{n}$ is the normal to the droplet along the contact line (2.11), $\boldsymbol{\nu}$ is the normal to the projection of the contact line, and $\theta_* = \theta|_C$ is the contact angle around the contact line.

---

[2]The presence of 3 in the rescalings allows us to eliminate the 1/3 that arises from integrating $\boldsymbol{u}$ at the next step.

2.4.2 Contact Angle Condition

The droplet also meets the substrate at the locally varying microscopic contact angle, $\theta(\boldsymbol{x})$. In this section we will derive a condition that enforces the contact angle and complies with the long-wave theory presented previously (noting that tildes correspond to dimensionless parameters for this subsection only). The contact angle can be expressed through the equation

$$\cos\theta = \boldsymbol{n} \cdot \boldsymbol{n}_s, \tag{2.32}$$

where $\boldsymbol{n}$ is the unit normal vector along $C(t)$ (2.11), and $\boldsymbol{n}_s$ is the normal vector to the substrate (2.4) (see figure 2.2), which can be written more concisely using (2.23), namely

$$\boldsymbol{n} = \frac{\boldsymbol{k} - \boldsymbol{\nabla}(h+\eta)}{\sqrt{1 + |\boldsymbol{\nabla}(h+\eta)|^2}}, \quad \text{and} \quad \boldsymbol{n}_s = \frac{\boldsymbol{k} - \boldsymbol{\nabla}\eta}{\sqrt{1 + |\boldsymbol{\nabla}\eta|^2}}. \tag{2.33}$$

Therefore, we obtain the full boundary condition

$$\cos\theta = \frac{1 + \boldsymbol{\nabla}\eta \cdot \boldsymbol{\nabla}(h+\eta)}{\sqrt{\left(1 + |\boldsymbol{\nabla}(h+\eta)|^2\right)\left(1 + |\boldsymbol{\nabla}\eta|^2\right)}}. \tag{2.34}$$

To simplify the above statement and comply with the long-wave approximation we have used, we first start by considering $\tan^2\theta = \sec^2\theta - 1$ alongside (2.34) to arrive with

$$\tan^2\theta = \frac{\left(1 + |\boldsymbol{\nabla}(h+\eta)|^2\right)\left(1 + |\boldsymbol{\nabla}\eta|^2\right) - \left[1 + \boldsymbol{\nabla}\eta \cdot \boldsymbol{\nabla}(h+\eta)\right]^2}{\left[1 + \boldsymbol{\nabla}\eta \cdot \boldsymbol{\nabla}(h+\eta)\right]^2}, \tag{2.35}$$

which is expanded and simplified to give

$$\tan^2\theta = \frac{|\boldsymbol{\nabla}h|^2 + |\boldsymbol{\nabla}(h+\eta)|^2|\boldsymbol{\nabla}\eta|^2 - \left[\boldsymbol{\nabla}\eta \cdot \boldsymbol{\nabla}(h+\eta)\right]^2}{\left[1 + \boldsymbol{\nabla}\eta \cdot \boldsymbol{\nabla}(h+\eta)\right]^2}. \tag{2.36}$$

Using the scalings (2.14) we obtain

$$\tilde{\theta}^2 = |\tilde{\boldsymbol{\nabla}}\tilde{h}|^2 + O(\alpha_s^2), \tag{2.37}$$

after expanding $\tan\theta$ for small θ, replacing ε with the small reference angle α_s, and using $\theta = \alpha_s\tilde{\theta}$. Therefore, the above boundary condition can be used with the understanding that this condition is imposed approximately in alignment with the long-wave theory.

The normal derivative is computed using the Green's function formalism

$$\partial_\nu h = \boldsymbol{\nu} \cdot \boldsymbol{\nabla}h = \left[\boldsymbol{n}_c - (\boldsymbol{n}_c \cdot \boldsymbol{k})\,\boldsymbol{k}\right] \cdot \boldsymbol{\nabla}h = \boldsymbol{n}_c \cdot \boldsymbol{\nabla}h, \tag{2.38}$$

where $\boldsymbol{\nu}$ is the unit normal to the projection of the contact line (at $z = 0$), and $\boldsymbol{n}_c$ is a vector lying in the plane formed by $\boldsymbol{n}$ and $\boldsymbol{n}_s$, which is normal to $\boldsymbol{n}_s$, and points outwards from the contact line. Using

$$\boldsymbol{\nabla} h = \boldsymbol{n}_s \sqrt{1 + |\boldsymbol{\nabla}\eta|^2} - \boldsymbol{n}\sqrt{1 + |\boldsymbol{\nabla}(h+\eta)|^2}, \tag{2.39}$$

as deduced from the definitions (2.33), gives

$$\boldsymbol{n}_c \cdot \boldsymbol{\nabla} h = -\sin\theta \sqrt{1 + |\boldsymbol{\nabla}(h+\eta)|^2} = -\tan\theta \frac{1 + \boldsymbol{\nabla}\eta \cdot \boldsymbol{\nabla}(h+\eta)}{\sqrt{1 + |\boldsymbol{\nabla}\eta|^2}}, \tag{2.40}$$

since $\boldsymbol{n} \cdot \boldsymbol{n}_c = \cos(\pi/2 - \theta) = \sin\theta$, which yields the contact angle condition upon application of the long-wave scalings, in other words

$$-\partial_\nu \tilde{h}|_C = \tilde{\theta}|_C + O(\alpha_s). \tag{2.41}$$

2.4.3 Moving Boundary Condition

We also require an equation for the evolution of the two-dimensional contact line, $\boldsymbol{c}(\boldsymbol{x}, t)$, which can be inferred from a local expansion of the governing PDE

$$\partial_t h + \boldsymbol{\nabla} \cdot [h\boldsymbol{Q}] = q, \tag{2.42}$$

near $\boldsymbol{x} = \boldsymbol{c}$. Here $\boldsymbol{Q} = \left(h^2 + h^{n-1}\lambda^{3-n}\right)\boldsymbol{\nabla} P$ is used for notational simplicity, where P is defined by

$$P = \nabla^2(h+\eta) - \mathrm{Bo}(h+\eta)\cos\alpha + \frac{\mathrm{Bo}\sin\alpha}{\alpha_s}x. \tag{2.43}$$

Near the contact line the droplet thickness h possesses the Taylor expansion

$$h = (\boldsymbol{x} - \boldsymbol{c}) \cdot \boldsymbol{\nabla} h|_{\boldsymbol{x}=\boldsymbol{c}} + \dots, \tag{2.44}$$

where dots denote omitted higher-order corrections, which vanish as $\boldsymbol{x} \to \boldsymbol{c}$. Using this expansion we can deduce that

$$\partial_t h|_{\boldsymbol{x}=\boldsymbol{c}} = -\partial_t \boldsymbol{c} \cdot \boldsymbol{\nabla} h|_{\boldsymbol{x}=\boldsymbol{c}} + \dots, \tag{2.45}$$

which when combined with an expanded form of (2.42) gives

$$-\partial_t \boldsymbol{c} \cdot \boldsymbol{\nabla} h|_{\boldsymbol{x}=\boldsymbol{c}} + \boldsymbol{Q}|_{\boldsymbol{x}=\boldsymbol{c}} \cdot \boldsymbol{\nabla} h|_{\boldsymbol{x}=\boldsymbol{c}} + h\boldsymbol{\nabla} \cdot \boldsymbol{Q}|_{\boldsymbol{x}=\boldsymbol{c}} + \dots = q|_{\boldsymbol{x}=\boldsymbol{c}}. \tag{2.46}$$

Therefore, letting $\boldsymbol{x} = \boldsymbol{c}$ gives the equation

$$\left[(\boldsymbol{Q} - \partial_t \boldsymbol{c}) \cdot \boldsymbol{\nabla} h\right]\Big|_{\boldsymbol{x}=\boldsymbol{c}} = q|_{\boldsymbol{x}=\boldsymbol{c}}, \tag{2.47}$$

as the moving boundary condition. We can simplify this expression by using

$$\nabla h|_{\boldsymbol{x}=\boldsymbol{c}} = (\nabla h \cdot \boldsymbol{\nu})|_{\boldsymbol{x}=\boldsymbol{c}}\boldsymbol{\nu} + (\nabla h \cdot \boldsymbol{t})|_{\boldsymbol{x}=\boldsymbol{c}}\boldsymbol{\tau}, \tag{2.48}$$

where $\boldsymbol{\tau}$ is the unit tangent vector to the contact line. Since h does not change along $\boldsymbol{\tau}$ we can write

$$\nabla h|_{\boldsymbol{x}=\boldsymbol{c}} = (\nabla h \cdot \boldsymbol{\nu})|_{\boldsymbol{x}=\boldsymbol{c}}\boldsymbol{\nu} = -\theta|_{\boldsymbol{x}=\boldsymbol{c}}\boldsymbol{\nu}, \tag{2.49}$$

giving the final moving boundary condition

$$(\partial_t \boldsymbol{c} - \boldsymbol{Q}|_{\boldsymbol{x}=\boldsymbol{c}}) \cdot \boldsymbol{\nu} = \frac{q}{\theta}\bigg|_{\boldsymbol{x}=\boldsymbol{c}}. \tag{2.50}$$

2.5   The Governing Models in 2D and 3D

By dropping the tildes and taking $\alpha_s \to 0$ in the contact angle condition (2.41), we can form the governing model by combining the PDEs (2.30) and (2.50) with the vanishing height condition (2.31). Therefore we arrive with the following equations and conditions which fully determine the height of the droplet, h, and the position of the contact line, $\boldsymbol{c}$, in time

$$\partial_t h + \nabla \cdot \left[h(h^2 + \lambda^2)\nabla P\right] = q, \tag{2.51a}$$

$$\left(\partial_t \boldsymbol{c} - \lambda^2 \nabla P|_C\right) \cdot \boldsymbol{\nu} = \frac{q}{\theta}\bigg|_C, \tag{2.51b}$$

$$h|_C = 0, \tag{2.51c}$$

$$-\partial_\nu h|_C = \theta|_C. \tag{2.51d}$$

For the full model we have opted against the arguably more popular Navier slip model since it retains a logarithmic singularity in the pressure along the contact line, and it is considerably more difficult to enforce the equivalent kinematic condition (2.51b) with the $\lambda^2 \nabla P|_C$ term replaced by $\lambda h \nabla P|_C$, which both need to be finite as $h \to 0$. Using the inverse-linear slip model we eliminate the logarithmic singularity and regularise the total shear stress, simplifying the implementation. It is important to re-iterate that should we have used the Navier slip model, we would expect that the forthcoming theoretical analysis would be identical regardless of the slip model used provided that variations in the contact line occur at length scales longer than λ, and therefore, the choice in slip-scheme is not a drastic step. Since we are also interested in droplets with variable mass, we must solve alongside the condition

$$\frac{\mathrm{d}}{\mathrm{d}t}\int_{\Omega(t)} h \, \mathrm{d}\boldsymbol{x} = \int_{\Omega(t)} q \, \mathrm{d}\boldsymbol{x} = \dot{v}(t), \tag{2.51e}$$
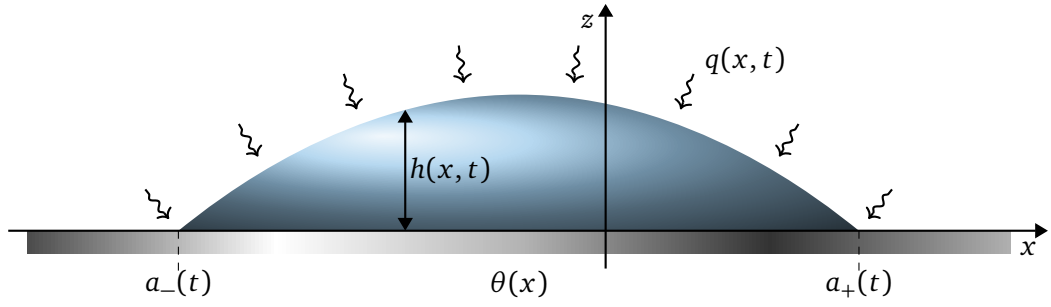
Figure 2.3: The two dimensional problem geometry. The droplet is placed over a flat and chemically heterogeneous surface provided by $\theta(x)$, where, the right and left contact points are given by $a_\pm(t)$ respectively. The droplet height is described by $h(x,t)$ and mass flux across the free surface is prescribed by $q(x,t)$.

where $\Omega(t)$ is the wetted region of the substrate, and $v(t)$ is the non-dimensional volume of the droplet (scaled with some reference volume v_s, which is usually the initial volume for cases of fluctuating mass). The condition (2.51e) can be used in two different ways. For the case where $v(t)$ is prescribed, we choose $q = \dot{v}(t)\tilde{q}$ where

$$\int_{\Omega(t)} \tilde{q}\,\mathrm{d}x = 1, \tag{2.52}$$

so that (2.51e) is automatically satisfied. However, if the functional form of q is known, like with evaporating droplets, then (2.51e) becomes an evolution equation for the droplet volume.

Solving (2.51) is a highly non-trivial problem both analytically and numerically. As a starting point one can reduce the dimensionality to the 2D setting and consider a droplet with cross sectional area $A(t)$ spreading over a horizontal ($\alpha = 0$) and flat ($\eta(x,y) = 0$) substrate (see figure 2.3 for the problem geometry in 2D). In this sense, the droplet touches the substrate at the two contact points $x = a_\pm(t)$ so that its thickness is determined in the region $a_-(t) \leq x \leq a_+(t)$ by solving the system

$$\partial_t h + \partial_x\left[h^2(h+\lambda)\partial_x^3 h\right] = q, \tag{2.53a}$$

$$\dot{a}_\pm - \lambda h \partial_x^3 h|_{x=a_\pm} = \pm \left.\frac{q}{\theta}\right|_{x=a_\pm}, \tag{2.53b}$$

$$h(a_\pm, t) = 0, \tag{2.53c}$$

$$\partial_x h|_{x=a_\pm} = \mp\theta_\pm, \tag{2.53d}$$

$$\frac{\mathrm{d}}{\mathrm{d}t}\int_{a_+}^{a_-} h\,\mathrm{d}x = \int_{a_-}^{a_+} q\,\mathrm{d}x = \dot{A}(t), \tag{2.53e}$$

where gravitational forces are neglected under the assumption that $0 < \mathrm{Bo} \ll 1$, which is equivalent to stating that the length-scale L is smaller than the capillary length l_c (which for

water at room temperature is roughly 3mm). Note that in (2.53) we have opted for the Navier slip condition as it is the predominant model in the literature (see, e.g. Savva & Kalliadasis [56] and Vellingiri *et al.* [55]), where (2.53b) has been modified from the general form (2.50) by introducing $\nu = \pm i$ at $x = a_\pm$. At the same time, it is easy to see that the treatment of the conditions (2.53b) is more non-trivial than (2.51b) which will be further expanded on in chapter 4 where numerical schemes for both slip models will be proposed. While a 2D model may be inappropriate for comparing with experimental observations, it is a key first step before tackling the fully 3D problem both numerically and analytically, which allows us to develop our understanding of the phenomenology and ultimately provide ideas into the generalisation to the 3D setting.

Both (2.51) and (2.53) are free-boundary problems where the motion of the contact line is required as part of the solution. Therefore, to simplify the future analytical and numerical calculations, in the coming sections we transform (2.51) and (2.53) to fixed domains.

2.5.1   Transformed 3D Model

For relatively weakly deformed contact lines the most suitable coordinate transformation is one based around a polar-coordinate type approach, namely we consider the change of variables

$$x = x_c(t) + ra(\phi, t)\cos\phi, \tag{2.54a}$$

$$y = y_c(t) + ra(\phi, t)\sin\phi, \tag{2.54b}$$

where $0 \leq r \leq 1$, $0 \leq \phi < 2\pi$, and $a(\phi, t)$ is the distance of a point on the contact line from the centroid $(x_c(t), y_c(t))$ (depicted in figure 2.4). In this sense, the transformation defines the droplet centroid $(x_c(t), y_c(t))$ to be the origin of the polar coordinate system, where the droplet boundary is mapped to the unit circle. Therefore, the contact line of the droplet in this coordinate system is defined at $r = 1$, and given by

$$c = \begin{pmatrix} x_c(t) + a(\phi, t)\cos\phi \\ y_c(t) + a(\phi, t)\sin\phi \end{pmatrix}. \tag{2.55}$$

An important assumption of this transformation is that we assume $a(\phi, t)$ to be a one-to-one mapping of the polar angle. Should one investigate more strongly deformed contact lines then a different parametrisation would be required, requiring e.g. $a(\phi, t)$ to be a one-to-one function of the arclength of $C(t)$. Likewise, this could also be investigated by considering a
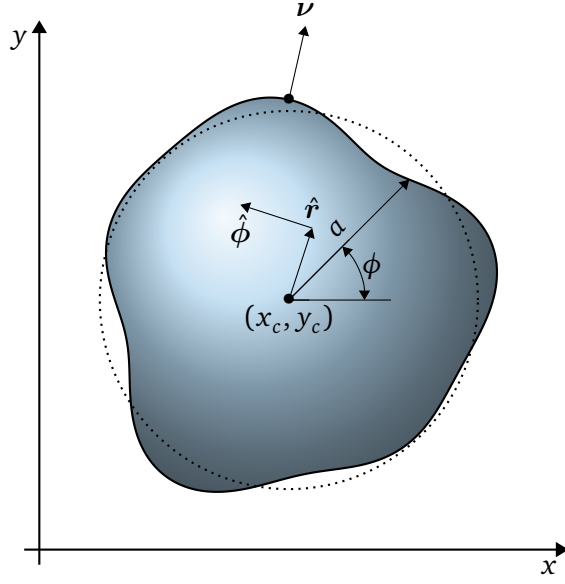
Figure 2.4: A top view of the geometry. The contact line is described by the function $a(\phi, t)$ which is the distance from the centroid $(x_c(t), y_c(t))$, and is a perturbation from the mean radius (dotted black). The vectors $\hat{r}$ and $\hat{\phi}$ represent the unit vectors radially and azimuthally, and ν denotes the unit outward normal to the contact line c.

finite element method (see Peschka [160]), or to deduce boundary-fitted curvilinear mappings (see Kang & Leal [161]). Besides, (2.54) is not too restrictive since the analysis that follows concerns droplets with weakly deformed contact lines, meaning that such flexibility is not required for our numerical scheme.

Using the transformation (2.54) the governing PDE (2.51a) becomes

$$\partial_t h - \frac{1}{a}\left[\dot{x}_c \cos\phi + \dot{y}_c \sin\phi + r\partial_t a + \frac{\partial_\phi a}{a}(\dot{x}_c \cos\phi - \dot{y}_c \sin\phi)\right]\partial_r h + \frac{\dot{x}_c \sin\phi - \dot{y}_c \cos\phi}{ar}\partial_\phi h$$
$$+ \nabla \cdot \left[h(h^2 + \lambda^2)\nabla P\right] = q(r, \phi, t), \quad (2.56a)$$

and is solved subject to the transformed conditions

$$h(1, \phi, t) = 0, \qquad (2.56b)$$

$$\partial_r h|_{r=1} = -\frac{a^2 \theta_*}{\sqrt{a^2 + (\partial_\phi a)^2}}, \qquad (2.56c)$$

where $\theta_* = \theta(x_c + a\cos\phi, y_c + a\sin\phi)$ denotes the heterogeneity evaluated at the contact line. Additionally, we are solving alongside the transformed volume constraint

$$\int_0^{2\pi}\int_0^1 ra^2\partial_t h \, dr \, d\phi = \int_0^{2\pi}\int_0^1 ra^2 q \, dr \, d\phi = \dot{v}(t). \qquad (2.56d)$$

In (2.56a) the expression for $\nabla \cdot \left[h(h^2 + \lambda^2)\nabla P\right]$ can be determined with the tensor calculus

techniques discussed in appendix A, and gives

$$\boldsymbol{\nabla} \cdot \left[h(h^2 + \lambda^2) \boldsymbol{\nabla} P \right] = \frac{1}{ra^2} \left\{ \partial_r \left[h \left(h^2 + \lambda^2 \right) G_1 \right] + \partial_\phi \left[h \left(h^2 + \lambda^2 \right) G_2 \right] \right\}, \tag{2.57}$$

where

$$G_1(r, \phi, t) = r \left[1 + \frac{(\partial_\phi a)^2}{a^2} \right] \partial_r P - \frac{\partial_\phi a}{a} \partial_\phi P, \tag{2.58a}$$

$$G_2(r, \phi, t) = \frac{1}{r} \partial_\phi P - \frac{\partial_\phi a}{a} \partial_r P. \tag{2.58b}$$

Additionally, the transformed gradient and Laplacian operators take the form

$$\boldsymbol{\nabla}(\cdot) = \hat{r} \frac{1}{a} \partial_r(\cdot) + \hat{\phi} \left[\frac{1}{ar} \partial_\phi(\cdot) - \frac{\partial_\phi a}{a^2} \partial_r(\cdot) \right], \tag{2.59}$$

$$
\begin{aligned}
\nabla^2(\cdot) = {} & \frac{1}{a^2} \left[1 + \left(\frac{\partial_\phi a}{a} \right)^2 \right] \partial_r^2(\cdot) + \frac{1}{a^2 r} \left[1 - \frac{\partial_\phi^2 a}{a} + 2 \left(\frac{\partial_\phi a}{a} \right)^2 \right] \partial_r(\cdot) \\
& - 2 \frac{\partial_\phi a}{a^3 r} \partial_\phi \partial_r(\cdot) + \frac{1}{a^2 r^2} \partial_\phi^2(\cdot),
\end{aligned}
\tag{2.60}
$$

where $\hat{r}$ and $\hat{\phi}$ denote the unit normal vectors in the radial and azimuthal directions, respectively. An equation for the contact line velocity can be found by combining the expression for the unit normal

$$\boldsymbol{\nu} = \frac{a\hat{r} - \partial_\phi a \hat{\phi}}{\sqrt{a^2 + (\partial_\phi a)^2}}, \tag{2.61}$$

and (2.51b) to yield the explicit equation

$$a(\dot{x}_c \cos \phi + \dot{y}_c \sin \phi + \partial_t a) - \partial_\phi a \left(\dot{y}_c \cos \phi - \dot{x}_c \sin \phi \right) = W(\phi, t), \tag{2.62}$$

where

$$W(\phi, t) = \lambda^2 \left\{ \left[1 + \left(\frac{\partial_\phi a}{a} \right)^2 \right] \partial_r P - \frac{\partial_\phi a}{a} \partial_\phi P \right\} \bigg|_{r=1} + \frac{q(1, \phi, t) \sqrt{a^2 + (\partial_\phi a)^2}}{\theta_*}. \tag{2.63}$$

In principle, the choice for x_c and y_c can be arbitrary as long as it is contained within $\Omega(t)$, the wetted area. As we shall see, x_c and y_c are more conveniently chosen for the analysis such that the first harmonic of $a(\phi, t)$ vanishes in the new coordinate system (see chapter 3), whereas for the numerics we chose x_c and y_c to lie at the centroid of $\Omega(t)$ which equivalently corresponds to having the first harmonic of a^3 vanish, and yields simple evolution equations for x_c and y_c. Namely this choice gives the conditions

$$\int_0^{2\pi} a^3 \cos \phi \, \mathrm{d}\phi = \int_0^{2\pi} a^3 \sin \phi \, \mathrm{d}\phi = 0, \tag{2.64}$$

which allows us to determine

$$\dot{x}_c = \frac{2\displaystyle\int_0^{2\pi} aW\cos\phi\,\mathrm{d}\phi}{\displaystyle\int_0^{2\pi} a^2\,\mathrm{d}\phi} \quad\text{and}\quad \dot{y}_c = \frac{2\displaystyle\int_0^{2\pi} aW\sin\phi\,\mathrm{d}\phi}{\displaystyle\int_0^{2\pi} a^2\,\mathrm{d}\phi}, \tag{2.65}$$

by multiplying (2.62) by $a\cos\phi$ and $a\sin\phi$, respectively, and then integrating over ϕ from 0 to 2π.

2.5.2 Transformed 2D Model

In the 2D setting we transform the free boundary problem on $a_-(t) \le x \le a_+(t)$, (2.53), to a fixed boundary problem using the change of variables

$$x = \frac{1}{2}\big[(a_+ - a_-)s + a_+ + a_-\big], \tag{2.66}$$

where $-1 \le s \le 1$. In this manner the governing PDE (2.53a) and its conditions (2.53b), (2.53c), (2.53d) and (2.53e) become

$$\partial_t h - \frac{\dot{a}_+(1+s) + \dot{a}_-(1-s)}{2d}\partial_s h + \frac{1}{d^4}\partial_s\big[h^2(h+\lambda)\partial_s^3 h\big] = q, \tag{2.67a}$$

$$\dot{a}_\pm - \frac{\lambda}{d^3}h\,\partial_s^3 h\big|_{s=\pm1} = \pm\frac{q_\pm}{\theta_\pm}, \tag{2.67b}$$

$$h(\pm1, t) = 0, \tag{2.67c}$$

$$\mp\,\partial_s h\big|_{s=\pm1} = d\theta_\pm, \tag{2.67d}$$

$$\frac{\mathrm{d}}{\mathrm{d}t}\int_{-1}^{1} h\,\mathrm{d}s = \int_{-1}^{1} q\,\mathrm{d}s = \frac{\dot{A}}{d}, \tag{2.67e}$$

where $d = (a_+ - a_-)/2$ is the droplet half-width, $\theta_\pm = \theta(a_\pm)$ and $q_\pm = q(a_\pm, t)$.

2.6 Summary

In this chapter we performed a long-wave approximation of the Navier-Stokes equations and the relevant boundary conditions, which allowed us to formulate a single evolution equation for the thickness of a thin-liquid film (2.30) by considering a slip model (2.6). To fully determine droplet spreading motion in time, the governing PDE (2.30) was combined with the appropriate boundary conditions which allowed us to deduce a generalised non-dimensional model (2.51) that accounts for the motion of the contact line by using a kinematic condition (2.50).

Simplifications to the governing model (2.51) were also proposed by reducing to the 2D setting, yielding (2.53) which is a first step in tackling the more complicated 3D problem (2.51). To simplify future numerical and analytical calculations, a change of coordinates was introduced to both (2.51) and (2.53) which moved the free-boundary problem to one of fixed intervals.

While no new results were presented in this chapter, it forms as the preliminary basis for future chapters where solution methods will be proposed to solve a variety of droplet spreading scenarios.

— Chapter 3 —

Asymptotic Analysis

The numerical stiffness of the governing systems (2.51) and (2.53) increases in the limit $\lambda \to 0$ ($\lambda \ll 1$ for macroscopically large droplets) [162] due to the difficult-to-resolve boundary layers in $\partial_y h$ near the contact line, as we have a transition from the apparent contact angle in the bulk to the prescribed angle at the contact line. In addition, imposing the moving boundary condition (2.53b) in discretised form is also non trivial and requires specialist schemes (see Savva & Kalliadasis [56] and chapter 4). Therefore, to provide an attractive alternative to full numerical calculations, as well as to offer physical insights to such a complicated multi-scale problem, we invoke the use of matched asymptotic expansions to approximate the solutions of the full models (2.51) and (2.53) (see Holmes [163] for a general description of the method). This method has been used extensively in the literature to solve a large variety of droplet spreading problems, and typically compare very favourably with solutions of the full equations in their regime of applicability (see, e.g. the 2D analyses in [55, 56, 58–60, 107, 124] , the axisymmetric analyses of [53, 54, 164] and the 3D analysis [61]).

Specifically, we aim to derive models like (1.6) that include non-trivial higher-order corrections, which will be shown in chapter 5 to be rather important in accurately capturing the full dynamics. The analysis is undertaken in the limit $\lambda \to 0$ and closely follows previous works that treated the case when there is no mass transfer, i.e. for $q \equiv 0$ (see [54–56]). This is typically split into three different parts. Firstly, we probe into the dynamics of the micro-scale where slip effects manifest themselves (called the *inner region*) to extract the behaviours of the inner region slope as the bulk is approached. Then we perform the corresponding analysis of the macro-scale where capillarity and viscous forces dominate (called the *outer region*) to extract the behaviours of the outer region slope as we approach the contact line. Finally, both slopes are combined through a set of matching criteria which allows us to couple the details of both scales, yielding a *reduced model* to approximate (2.51) (or (2.53) for 2D droplets).

This is achieved by assuming that there is sufficient separation of scales (e.g., for droplet sufficiently far from equilibrium and whose size is much larger than λ), and assuming that the dynamics is quasi-steady. This corresponds to the surface-tension dominated regime of small capillary numbers, which allows us to delay the contributions of the contact line and centroid velocities (or contact points in 2D) to the next-to-leading term. Therefore we anticipate that $|\partial_t a|, |\dot{a}_{\pm}|, |\dot{x}_c|, |\dot{y}_c| = O(1/|\ln(\lambda)|) \ll 1$ as $\lambda \to 0$ [52, 54]. For cases including arbitrary mass transfer we consider the distinguished limit where $|q|$, and consequently $|\dot{v}|$ and $|\dot{A}|$ are also $O(1/|\ln(\lambda)|)$ as $\lambda \to 0$. In this manner, the analysis remains more tractable compared to other distinguished limits, without compromising any of the qualitative features of the dynamics we wish to uncover. Should these flux terms be present at leading order, a separate treatment would be required (see Oliver *et al.* [107] for different cases for constant q and $\theta \equiv 1$). If mass loss occurs due to evaporation then we consider $|\dot{v}| = O(\lambda|\ln(\lambda)|)$ which is nevertheless much smaller than $|\partial_t a|, |\dot{x}_c|, |\dot{y}_c|$ which are $O(1/|\ln(\lambda)|)$ in this limit. Although such assumptions are necessary to perform the analysis, they are indeed physical since typical experimental settings fall in the regime of small capillary numbers [23].

Generally speaking assumptions are supplied to ensure the analysis is tractable, such as by considering axisymmetric geometries (see Hocking [54] and Savva *et al.* [53]), or homogeneous flat surfaces (see Oliver *et al.* [107] and Kiradjiev *et al.* [124]). This is simply due to the fact that the analysis is rather intricate, and grows more challenging if these assumptions are relaxed. Therefore, in the following sections we investigate different physical scenarios where the underlying assumptions of each will be stated prior to the analysis.

3.1 2D Analysis

Here we consider a 2D droplet of variable mass spreading over a horizontal ($\alpha = 0$), flat ($\eta = 0$) and chemically heterogeneous surface. We seek to extend related works in 2D on homogeneous surfaces, e.g. the work of Oliver *et al.* [107] which focused on the particular case of a constant mass flux, but, unlike here, a variety of distinguished limits were considered, or that of Kiradjiev *et al.* [124] which looked into symmetric motion when the mass flux is localised at the centre of the drop. The discussion here closely follows Vellingiri *et al.* [55] who investigated the case of constant mass, noting that here we derive the extra terms which are required to simulate for forms of q which occur in the droplet footprint.

The discussion here is limited to the 2D geometry primarily to highlight, in qualitative terms, the interesting interplay between surface heterogeneities and mass transfer, deferring the arguably more realistic 3D analysis to the following section. Despite this limitation, the work informed the approaches undertaken to tackle the generalisation to 3D by providing insights into the underlying dynamics, and also allowed us to scrutinise the dynamics by utilising a bifurcation study similar to Pradas *et al.* [125] (see chapter 5).

3.1.1 Inner Region

In the inner region, we introduce the following stretching transformation

$$h_{\text{in}} = \lambda \Upsilon_{\pm}, \quad \xi = \pm \frac{a_{\pm} - x}{\lambda} \theta_{\pm}, \tag{3.1}$$

which has the effect of zooming into the two contact points and allows us to retain the effects of slip. Hence, the governing PDE (2.53a) transforms to

$$\pm \dot{a}_{\pm} \partial_{\xi} \Upsilon_{\pm} + \theta_{\pm}^3 \partial_{\xi} \left[\Upsilon_{\pm}^2 (\Upsilon_{\pm} + 1) \partial_{\xi}^3 \Upsilon_{\pm} \right] = \frac{q_{\pm}}{\theta_{\pm}}, \tag{3.2}$$

where we dropped $O(\lambda)$ terms, assumed that q varies at length-scales longer than λ, and took $|\dot{a}_{\pm}|, |q_{\pm}| \gg \lambda$. This is a generalisation of the analysis by Vellingiri *et al.* [55] who considered the case where $q = 0$ with θ variable, and that of Oliver *et al.* [107] who treated both q and θ as constants. At $\xi = 0$ we require

$$\Upsilon_{\pm} = 0, \quad \partial_{\xi} \Upsilon_{\pm} = 1, \tag{3.3}$$

including

$$\frac{\Upsilon_{\pm}}{\xi^2} \to 0 \quad \text{as} \quad \xi \to \infty \tag{3.4}$$

to ensure compatibility with the outer region solution. Similar to the previous section, we introduce a quasistatic expansion in the form

$$\Upsilon_{\pm} = \xi + \tilde{\Upsilon}_{\pm} + \dots, \tag{3.5}$$

so that $\xi \gg \tilde{\Upsilon}$, and thus obtain the following equations for $\tilde{\Upsilon}_{\pm}$

$$\partial_{\xi}^3 \tilde{\Upsilon}_{\pm} = \frac{q_{\pm} \mp \dot{a}_{\pm} \theta_{\pm}}{\theta_{\pm}^4 \xi(\xi + 1)}. \tag{3.6}$$

Here we note that in the leading-order component we neglected q in alignment that q and $\dot{A}$ are $O(1/|\ln(\lambda)|)$ as $\lambda \to 0$. Should q terms be included at leading-order, a different approach

would be required (see e.g. section 3.3.1). Equations of the form (3.6) have previously been

encountered in other 2D studies (see [55–57, 165]) and its asymptotic structure is investigated

subject to

$$\tilde{\Upsilon}_{\pm} = \partial_{\xi}\tilde{\Upsilon}_{\pm} = 0 \quad \text{at} \quad \xi = 0, \tag{3.7}$$

as well as $\tilde{\Upsilon}_{\pm}/\xi^2 \to 0$ as $\xi \to \infty$. Equation (3.6) is easily solved subject to the above

conditions, yielding

$$\tilde{\Upsilon}_{\pm} = \frac{q_{\pm} \mp \dot{a}_{\pm}\theta_{\pm}}{\theta_{\pm}^4}\left[\frac{\xi^2}{2}\ln\left(\frac{\xi}{\xi+1}\right) + \xi\ln\left(\frac{e^{1/2}}{\xi+1}\right) - \frac{1}{2}\ln(\xi+1)\right], \tag{3.8}$$

however, we only require the leading-order behaviour as the bulk is approached so that

matching can be performed. Therefore, as $\xi \to \infty$ we arrive with

$$\partial_{\xi}\tilde{\Upsilon}_{\pm} \sim -\frac{(q_{\pm} \mp \dot{a}_{\pm}\theta_{\pm})}{\theta_{\pm}^4}\ln(e\xi), \tag{3.9}$$

from which we can write the corresponding asymptotic behaviour for the inner slopes in terms

of the original variables

$$\mp \partial_x h_{\text{in}} \sim \theta_{\pm} \pm \left(\frac{\dot{a}_{\pm}\theta_{\pm} \mp q_{\pm}}{\theta_{\pm}^3}\right)\ln\left[e\theta_{\pm}\frac{\mp(x-a_{\pm})}{\lambda}\right] \quad \text{as} \quad \frac{x-a_{\pm}}{\lambda} \to \mp\infty. \tag{3.10}$$

3.1.2   Outer Region

As $\lambda \to 0$ slip effects are negligible in the outer region and thus the slip length, λ, is dropped

from the transformed 2D PDE (2.67a). Therefore, the outer region PDE is expressed as

$$\partial_t h_{\text{out}} - \frac{\dot{a}_+(1+s) + \dot{a}_-(1-s)}{2d}\partial_s h_{\text{out}} + \frac{1}{d^4}\partial_s\left(h_{\text{out}}^3\partial_s^3 h_{\text{out}}\right) = q(s,t), \tag{3.11}$$

and is solved subject to the pertinent conditions

$$h_{\text{out}}(\pm 1, t) = 0, \quad \text{and} \quad \int_{-1}^{1} h_{\text{out}}\, ds = \frac{A}{d}. \tag{3.12}$$

In the quasistatic limit the explicit time dependence from $h_{\text{out}}(s,t)$ is dropped by

introducing the following expansion

$$h_{\text{out}}(s,t) = h_0(s, a_{\pm}(t), A(t)) + h_1(s, a_{\pm}(t), A(t), \dot{a}_{\pm}(t), \dot{A}(t)) + \ldots, \tag{3.13}$$

where $h_0 \gg h_1$ and where we assume $\dot{a}_{\pm}$ and $\dot{A}$ are small as $\lambda \to 0$ and appear linearly in h_1.

This ordering of terms is ultimately justified by rescaling time according to the slow time scale

which is $O(|\ln(\lambda)|)$ as $\lambda \to 0$ (see Oliver *et al.* [107] and Lacey [52]). At $O(1)$, we deduce the problem

$$\partial_s \left(h_0^3 \partial_s^3 h_0 \right) = 0, \tag{3.14a}$$

$$h_0(\pm 1, t) = 0, \tag{3.14b}$$

$$\int_{-1}^{1} h_0 \, \mathrm{d}s = \frac{A}{d}, \tag{3.14c}$$

which is easily solved to obtain the parabolic profile

$$h_0(s, t) = \frac{3A}{4d} \left(1 - s^2 \right), \tag{3.15}$$

and describes the quasi-static droplet thickness in the bulk. Again, we note that in the leading-order problem (3.14) q terms are neglected since they appear at $O(1/|\ln(\lambda)|)$ as $\lambda \to 0$. If q was retained here, it would contribute to differences in the droplet shape and an alternative approach would be required (see Oliver *et al.* [107]). Next, the equation for h_1 satisfies

$$\partial_t h_0 - \frac{\dot{a}_+(1+s) + \dot{a}_-(1-s)}{2d} \partial_s h_0 + \frac{1}{d^4} \partial_s \left(h_0^3 \partial_s^3 h_1 \right) = q(s, t), \tag{3.16}$$

where for notational simplicity we write q to depend directly on the s variable, rather than indirectly through x as transformed according to (2.66). Using the chain rule to write

$$\partial_t h_0 = \dot{a}_+ \partial_{a_+} h_0 + \dot{a}_- \partial_{a_-} h_0 + \dot{A} \partial_A h_0, \tag{3.17}$$

integrating (3.16), using $h_0(-1) = 0$, and after some term re-arrangement, we obtain an expression for the third derivative of h_1

$$\partial_s^3 h_1 = \frac{d^4}{h_0^3} \int_{-1}^{s} q(\tilde{s}, t) \, \mathrm{d}\tilde{s} + \frac{d^4 \vartheta}{4h_0^3} \left(f_+ \dot{a}_+ + f_- \dot{a}_- \right) + \frac{d^3 \dot{A}}{4h_0^3} (s - 2)(1 + s)^2, \tag{3.18}$$

where $f_\pm = (1 \mp s)(1 \pm s)^2$ and ϑ is the apparent contact angle as computed from the leading-order shape (3.15), namely

$$\vartheta = \mp \frac{1}{d} \partial_s h_0 |_{s=\pm 1} = \frac{3A}{2d^2}. \tag{3.19}$$

Equation (3.18) is solved subject to the conditions

$$h_1(\pm 1, t) = \int_{-1}^{1} h_1 \, \mathrm{d}s = 0, \quad \text{and} \quad \int_{-1}^{1} q \, \mathrm{d}s = \frac{\dot{A}}{d}. \tag{3.20}$$

As in related works we seek to find the behaviour of the slopes as $s \to \pm 1$, which, using (3.18), we deduce that the local expansions of the slopes of h_1 exhibit a logarithmic singularity, namely

$$\partial_s h_1 \sim -\frac{d(\vartheta \dot{a}_\pm \mp q_\pm)}{\vartheta^3} \ln(1 \mp s) - \beta_\pm \quad \text{as } s \to \pm 1, \tag{3.21}$$

where $\beta_\pm$ are time-dependent functions to be determined. To determine $\beta_\pm$, we multiply (3.18) by $f_\pm$ and integrate with respect to s over the interval $[-1+\varepsilon, 1-\varepsilon]$ for $0 < \varepsilon \ll 1$. After applying integration by parts and using the behaviours (3.21) on the left hand side we arrive with

$$(\vartheta \dot{a}_\pm \mp q_\pm)[1-\ln(\varepsilon)] - \frac{\vartheta^3 \beta_\pm}{d} = \left\{ \vartheta \dot{a}_\pm [\ln(2) - \ln(\varepsilon) - 1] + \vartheta \dot{a}_\mp \pm \frac{3\dot{A}}{2d} \mp q_\pm - \tilde{I}_\pm^\varepsilon \right\} + \dots, \tag{3.22}$$

where dots denote additional terms of $O(\varepsilon \ln(\varepsilon))$, and

$$\tilde{I}_\pm^\varepsilon = \int_{-1+\varepsilon}^{1-\varepsilon} \left[\frac{1}{2} \ln\left(\frac{1+s}{1-s} \right) \pm \frac{1}{1 \mp s} \right] q \, ds. \tag{3.23}$$

Therefore, (3.22) is straightforwardly solved to obtain

$$\beta_\pm = \frac{d}{\vartheta^2} \left[\dot{a}_\pm \ln\left(\frac{e^2}{2} \right) - \dot{a}_\mp \right] + \frac{d}{\vartheta^3} \left[\tilde{I}_\pm^\varepsilon \mp \frac{3\dot{A}}{2d} \pm q_\pm \ln(\varepsilon) \right] + O(\varepsilon \ln(\varepsilon)), \tag{3.24}$$

noting that the logarithmically diverging terms $q_\pm \ln(\varepsilon)$ are balanced with the diverging integrals $\tilde{I}_\pm^\varepsilon$ as $\varepsilon \to 0$. This is seen by rewriting $\ln(\varepsilon)$ as

$$\ln(\varepsilon) = \ln(2) - \int_{-1+\varepsilon}^{1-\varepsilon} \frac{1}{1 \mp s} \, ds, \tag{3.25}$$

and merging all integrals together to yield an integral for each contact point that does not diverge as $\varepsilon \to 0$, so that we obtain well-defined expressions for $\beta_\pm$. Hence, returning to the original time-dependent variables we deduce that as $x \to a_\pm$

$$\mp \partial_x h_{\mathrm{out}} \sim \vartheta \pm \left(\frac{\dot{a}_\pm \vartheta \mp q_\pm}{\vartheta^3} \right) \ln\left[\frac{\mp(x-a_\pm)}{2d} \right] \pm \frac{2\dot{a}_\pm - \dot{a}_\mp}{\vartheta^2} - \frac{3\dot{A}}{2d\vartheta^3} \pm \frac{I_\pm}{\vartheta^3}, \tag{3.26}$$

where

$$I_\pm = \int_{-1}^{1} \left[\frac{1}{2} \ln\left(\frac{1+s}{1-s} \right) q \pm \left(\frac{q - q_\pm}{1 \mp s} \right) \right] ds. \tag{3.27}$$

Equation (3.26) specifies how the slope of the outer region behaves as the contact points are approached, which needs to be compatibly matched with the corresponding slopes in the inner region (3.10) to yield equations for $\dot{a}_\pm$.

3.1.3   Matching

As in most problems considering the asymptotics of contact lines, we find that the x-dependent logarithmic terms of the inner (3.10), and outer (3.26) solutions cannot directly match. In many circumstances, matching is possible by considering the cubes of the slopes, which is

justified through the presence of intermediate regions between the respective inner and outer solutions (see [54–56]). For this problem, this approach fails to work due to the presence of $q_\pm$ in the singular terms in equations (3.10) and (3.26). However, matching is still possible, albeit through a much more elaborate analysis introduced by Lacey [52] for homogeneous substrates without mass transfer, which was then extended by Oliver *et al.* [107] for problems with constant q. Additionally, a recent problem-independent generalisation offered by Sibley *et al.* [166] allows us to circumvent the additional effort presented in [52] and [107]. Sibley *et al.* showed that a truncated perturbation expansion in $\dot{a}_\pm$, such as (3.10) and (3.26), at leading-order in λ leads to a breakdown of the overlap between both the inner and outer regions. Although including more terms in the $\dot{a}_\pm$ perturbation reduces the breakdown of the overlap, it was common in previous works [54, 56] to use intermediate regions as a remedy to bridge the gap between the inner and outer expansions. Sibley *et al.* determined the significant terms in the infinite $\dot{a}_\pm$ series and found an integral that gives the functional forms of the inner and outer slopes which directly match within their respective overlap regions (see also the PhD thesis of Nold [167]). Specifically this is performed by considering the integrals

$$\tilde{G}_\pm(\varphi) = \int_0^\varphi \frac{1}{\mathcal{F}_\pm(x)}\,\mathrm{d}x, \qquad (3.28)$$

for the left and right contact points, respectively, where

$$\mathcal{F}_\pm(x) = \pm\frac{\dot{a}_\pm x \mp q_\pm}{x^3 \dot{a}_\pm}, \qquad (3.29)$$

is the function characterising the overlap region (i.e. the coefficient multiplying the logarithmically diverging term in (3.26) divided by $\dot{a}_\pm$). It is clearly seen that for the special case where $q_\pm = 0$, $\tilde{G}_\pm(\varphi) = \pm\varphi^3/3$ and the usual matching of the cubes argument follows. As shown by Sibley *et al.* this allows us to specify

$$\mp\partial_x h_{\mathrm{out}} \sim \tilde{G}_\pm^{-1}\left(\dot{a}_\pm \ln\left[\frac{\mp(x-a_\pm)}{2d}\right] + \tilde{G}_\pm(\vartheta) \pm \frac{1}{\mathcal{F}_\pm(\vartheta)\vartheta^2}\left[2\dot{a}_\pm - \dot{a}_\mp \mp \frac{3\dot{A}}{2d\vartheta} + \frac{I_\pm}{\vartheta}\right]\right), \quad (3.30a)$$

$$\mp\partial_x h_{\mathrm{in}} \sim \tilde{G}_\pm^{-1}\left(\dot{a}_\pm \ln\left[\mathrm{e}\theta_\pm \frac{\mp(x-a_\pm)}{\lambda}\right] + \tilde{G}_\pm(\theta_\pm)\right), \qquad (3.30b)$$

which means that the outer and inner solutions can coincide in the overlap region through

$$\lim_{x \to a_\pm} \partial_x h_{\mathrm{out}} = \lim_{(x-a_\pm)/\lambda \to \infty} \partial_x h_{\mathrm{in}} \qquad (3.31)$$

yielding their principal matching result

$$\tilde{G}_\pm(\vartheta) - \tilde{G}_\pm(\theta_\pm) = \dot{a}_\pm\left[\ln\left(\frac{2d\mathrm{e}\theta_\pm}{\lambda}\right) \mp \frac{1}{\mathcal{F}_\pm(\vartheta)\dot{a}_\pm\vartheta^2}\left(2\dot{a}_\pm - \dot{a}_\mp \mp \frac{3\dot{A}}{2d\vartheta} + \frac{I_\pm}{\vartheta}\right)\right]. \qquad (3.32)$$

Therefore evaluating (3.28) we get

$$\tilde{G}_\pm(\varphi) = \pm\frac{\varphi^3}{3} + \frac{\varphi^2 q_\pm}{2\dot{a}_\pm} \pm \frac{\varphi q_\pm^2}{\dot{a}_\pm^2} + \frac{q_\pm^3}{\dot{a}_\pm^3}\ln\left[\frac{\mp(\dot{a}_\pm\varphi \mp q_\pm)}{q_\pm}\right], \tag{3.33}$$

so that when used in (3.33) and after some algebra, we obtain the following transcendental equations that govern the motion of the contact lines

$$\pm\frac{\vartheta^3 - \theta_\pm^3}{3} + \frac{q_\pm\left(\vartheta^2 - \theta_\pm^2\right)}{2\dot{a}_\pm} \pm \frac{q_\pm^2(\vartheta - \theta_\pm)}{\dot{a}_\pm^2} + \frac{q_\pm^3}{\dot{a}_\pm^3}\ln\left(\frac{\dot{a}_\pm\vartheta \mp q_\pm}{\dot{a}_\pm\theta_\pm \mp q_\pm}\right)$$
$$= \dot{a}_\pm\ln\left(\frac{2de\theta_\pm}{\lambda}\right) - \frac{\vartheta\dot{a}_\pm}{\vartheta\dot{a}_\pm \mp q_\pm}\left(2\dot{a}_\pm - \dot{a}_\mp \mp \frac{3\dot{A}}{2d\vartheta} + \frac{I_\pm}{\vartheta}\right), \tag{3.34}$$

determined with $O(1/|\ln(\lambda)|^3)$ error as $\lambda \to 0$. Equation (3.34) corresponds to a highly non-trivial contact line law. It is reminiscent of the equation obtained by Oliver *et al.* [107] for $q = \dot{A}/(2d)$ and $\theta(x) = 1$, and without the $O(1/|\ln(\lambda)|^2)$ terms which are included here. Based on the arguments presented by Oliver *et al.*, we anticipate that for given values of $\vartheta \neq 0$, $\theta_\pm, \dot{A}, q_\pm$ and $I_\pm$ we can solve (3.34) to uniquely determine the contact line velocities $\dot{a}_\pm$ even as $\dot{a}_\pm \to 0$. However, simulating the system (3.34) requires a more involved implementation which we chose not to undertake here, since our principal aim is uncovering the qualitative features of the dynamics. Instead, we use the explicit expressions for $\dot{a}_\pm$ obtained by requiring that $q_\pm = 0$ (i.e., no flux at $x = a_\pm$) so that matching of the cubes of the slopes becomes possible. Although having q vanish at $x = a_\pm$ is inappropriate in the case of mass loss through evaporation, as q is maximised there (see section 3.3 and [53, 164, 168]), it is appropriate for cases where the mass flux is localised somewhere within the droplet's footprint (see [124, 125]). Thus, setting $q_\pm = 0$ in (3.34) gives

$$\dot{a}_\pm = \pm\frac{\kappa_\pm\ln\left(\frac{2d\theta_\mp}{e\lambda}\right) + \kappa_\mp}{\ln\left(\frac{2d\theta_+}{e\lambda}\right)\ln\left(\frac{2d\theta_-}{e\lambda}\right) - 1}, \tag{3.35a}$$

where

$$\kappa_\pm = \frac{\vartheta^3 - \theta_\pm^3}{3} \pm \frac{I_\pm}{\vartheta} - \frac{3\dot{A}}{2d\vartheta}. \tag{3.35b}$$

The structure of this system of integrodifferential equations (IDEs) is the same as that obtained by Vellingiri *et al.* [55] in the absence of mass transfer. The reduced system (3.35) is arguably simpler to implement and easier to solve compared to the full PDE, as we shall see later on.

In the special case when

$$q = \frac{\dot{A}(t)}{A(t)}h, \tag{3.36}$$

the integrals $I_{\pm}$ evaluate to $I_{\pm} = \pm 3\dot{A}/(2d)$ at the orders we retain. In this case, the last two terms in (3.35b) cancel each other out, thus reducing (3.35a) to the same system of ordinary differential equations (ODEs) as derived by Vellingiri *et al.* [55] with mass transfer effects entering through the dependence of ϑ on A (3.19). Although this particular form for q does not correspond to a physically relevant scenario, it allows for the extraction of generic dynamics which do not depend on the particular choice of q.

We conclude the derivation of the reduced model (3.35) by acknowledging some caveats surrounding a number of subtle features of the present analysis. The first is that it relies on taking $|\dot{a}_{\pm}| \gg \lambda$, which is clearly violated as mass transfer switches from inflow to outflow, and vice versa, as it may cause a droplet front to momentarily stop moving while switching its direction of motion. This issue, however, is of a very brief duration and does not yield noticeable departures from numerical solutions of the full equations, as we shall see in chapter 5. The second caveat is that the dynamics for which $t = O(1)$, during which the free surface of the droplet evolves towards its quasistatic shape, is not properly accounted for. This limit is not analytically tractable and requires, for the most part, a numerical treatment (see, e.g. Saxton *et al.* [164] for the case of evaporating droplets). Just as in the first caveat, this relaxation towards quasisteady dynamics occurs in a short period without impacting the dynamics appreciably (see appendix C for further discussion). The final caveat is that a more complete asymptotic procedure possibly requires a separate treatment for receding droplet fronts, following, for example, the analysis by Eggers [169] for the case of a receding contact line on a plate withdrawn from a liquid bath. Given that receding fronts typically attain lower speeds than advancing ones, we chose not to pursue such analysis because these effects manifest themselves strongly only for sufficiently high recession speeds. Thus to extend the applicability of the asymptotic analysis and overcome the above-mentioned limitations, the development of a composite expansion would be required as a means to encapsulate all the pertinent scales present in the problem. This, however, appears to be a formidable task, the undertaking of which is deemed unnecessary given the generally excellent agreement we observe between solutions of the full equations and the asymptotic models (see chapter 5).

3.2   3D Analysis

In this section we generalise the analysis undertaken in the previous section to the fully 3D setting. This was achieved by firstly considering droplets with constant mass (i.e. $q = 0$), as reported in [61]. Here, we present extensions to this analysis by considering the case where q is variable, noting that the findings of [61] can be inferred from the present case rather easily by setting $\dot{v}(t)$ terms to zero. To simplify the forthcoming analysis we assume that the flux vanishes at the contact line (i.e. $q(1, \phi, t) = 0$), which in the 2D case allowed us to determine explicitly the velocities of the contact points. Besides, the results for the 2D case in chapter 5 show that the generic features can still be captured without the requirement of more specialist schemes to treat equations like (3.34), meaning for our purposes using $q(1, \phi, t) = 0$ is a reasonable assumption to make.

We additionally assume that $\partial_\phi a \ll a$ which ensures that the contact line varies at length scales that are longer than slip, and aligns with the assumption of our coordinate mapping (2.54) which requires the contact line to be a one-to-one function of the polar angle. Analytical progress becomes possible by expanding the contact line as a truncated Fourier series in which we discard the short wavelength harmonics, in other words

$$a(\phi, t) = \sum_{m=0}^{M} a_m(t) e^{im\phi}, \tag{3.37}$$

where a_m are generally complex functions of t to be determined, $M > 0$ is a large integer to be more precisely defined later, and $|a_m(t)| \ll a_0(t)$. From the motion of the moving coordinate system, uniquely defining (x_c, y_c) is always possible for all one-to-one functions $a(\phi, t)$. For the analysis we require that for any given contact line shape $a(\phi, t)$, the coordinates of (x_c, y_c) are chosen such that the first harmonic of $a(\phi, t)$ is always suppressed, namely $a_1(t) \equiv 0$. Why this choice is the natural one for the analysis will become apparent when considering the outer region dynamics. For a weakly deformed contact line, having $a_1(t) \equiv 0$ is at leading-order the same as having (x_c, y_c) at the droplet centroid since using (3.37) in (2.64) yields $\mathrm{Re}(a_1) + O(a_m^2) = 0$ and $\mathrm{Im}(a_1) + O(a_m^2) = 0$. Here, analogously to the modes of linear stability theory, all expressions containing complex exponentials are considered with their imaginary part discarded. However, we leave all time dependencies arbitrary, in contrast, the normal modes in linear stability theory are perturbations from steady states with an exponential dependence on time.

3.2.1 Inner Region

To probe into the dynamics of the inner region we use the following stretching transformation (see also Lacey [52])

$$x = c + \frac{\lambda \left(\zeta \boldsymbol{\tau} - \xi \boldsymbol{\nu}\right)}{\theta_*}, \quad h_{\text{in}} = \lambda \Upsilon \tag{3.38}$$

where ζ and ξ are measures of distance along the unit tangent vector, $\boldsymbol{\tau}$ at the contact line c, and the unit outward normal to the contact line (2.61). Up to $O(\lambda)$ we obtain the following transformed PDE

$$\left(\partial_t c \cdot \boldsymbol{\nu}\right)\partial_\xi \Upsilon + \theta_*^3 \partial_\xi \left[\Upsilon \left(\Upsilon^2 + 1\right)\partial_\xi^3 \Upsilon\right] = 0, \tag{3.39}$$

where $|\partial_t c \cdot \boldsymbol{\nu}| \gg \lambda$. Given that, by assumption, $q = 0$ at the contact line, mass flux effects contribute to the $O(\lambda)$ terms which are neglected here. Hence the analysis is identical to the inner region asymptotics for droplets of constant volume (reported in [61]). Equation (3.39) is solved alongside conditions of a similar form to those used in the 2D analysis, namely (3.3) and (3.4). To probe into the dynamics of (3.39) we introduce the quasistatic expansion $\Upsilon = \xi + \tilde{\Upsilon} + \dots$ where $\xi \gg \tilde{\Upsilon}$, and thus extract the third-order PDE for $\tilde{\Upsilon}$

$$\partial_\xi^3 \tilde{\Upsilon} = -\frac{\partial_t c \cdot \boldsymbol{\nu}}{\theta_*^3 \left(\xi^2 + 1\right)}. \tag{3.40}$$

One can see that (3.40) is of the form $\partial_\xi^3 \tilde{\Upsilon} = B/(\xi^2 + 1)$ where the numerator is independent of ξ (but are dependent on ϕ and t), which has been encountered in 2D cases [165], and whose solution is expressed as

$$\tilde{\Upsilon} = -\frac{\partial_t c \cdot \boldsymbol{\nu}}{2\theta_*^3} \left\{\xi^2 \left[\tan^{-1}(\xi) - \frac{\pi}{2}\right] + \xi \ln\left(\frac{e}{\xi + 1}\right) - \tan^{-1}(\xi)\right\}. \tag{3.41}$$

Leading from the same rationale as in the 2D analysis, we are only interested in the leading-order behaviour as the bulk is approached, giving

$$\partial_\xi \tilde{\Upsilon} \sim \frac{\partial_t c \cdot \boldsymbol{\nu}}{\theta_*^3} \ln(e\xi), \quad \text{as} \quad \xi \to \infty. \tag{3.42}$$

Although the ξ dependence of two solutions (3.8) and (3.41) are different due to the change in slip-model, their asymptotic expansions at infinity contain the same leading-order terms, and therefore as the bulk is approached (as $\xi \to \infty$) both slip models yield identical results (see figure 3.1).

Using $\partial_\nu h_{\text{in}} = -\theta_* \partial_\xi h_{\text{in}}$ allows us to express the behaviour of the normal derivative as

$$-\partial_\nu h_{\text{in}} \sim \theta_* + \frac{\partial_t c \cdot \boldsymbol{\nu}}{\theta_*^2} \ln\left[\frac{e\theta_*(c - x) \cdot \boldsymbol{\nu}}{\lambda}\right] \quad \text{as} \quad \frac{(c - x) \cdot \boldsymbol{\nu}}{\lambda} \to \infty, \tag{3.43}$$
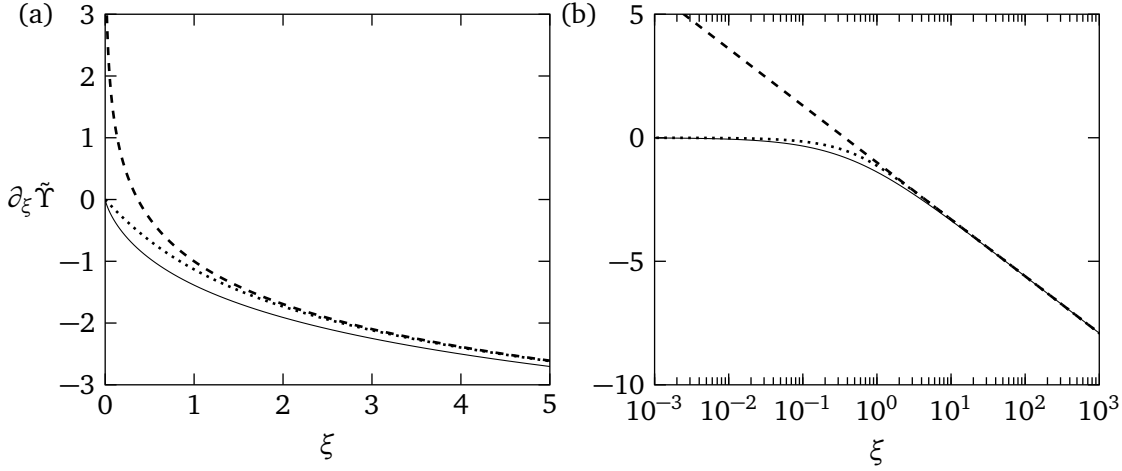
Figure 3.1: A comparison of the inner solutions in 2D (solid curves), 3D (dotted curves) and the leading-order asymptotics (dashed curves). In this example we set $(q_\pm \mp \dot{a}_\pm \theta_\pm)/\theta_\pm^4 = -(\partial_t \boldsymbol{c} \cdot \boldsymbol{\nu})/\theta_*^3 = 1$ to compare the 2D (3.8) and 3D (3.41) inner region solutions alongside the leading-order asymptotics (3.42).

which is a generalisation of the inner region behaviour obtained in the 2D geometry for when the flux vanishes at the contact line. Furthermore, assuming that the contact line is nearly circular so that only linear terms in b_m are retained we expand $\partial_t \boldsymbol{c} \cdot \boldsymbol{\nu}$ as

$$\partial_t \boldsymbol{c} \cdot \boldsymbol{\nu} = \dot{b}_0 + \left(\dot{b}_1 - \frac{b_2}{b_0}\dot{b}_1^*\right)e^{i\phi} + \left(\dot{b}_2 - \frac{3b_3}{2b_0}\dot{b}_1^*\right)e^{2i\phi} +$$

$$\sum_{m=3}^{M}\left[\dot{b}_m + \frac{(m-1)b_{m-1}}{2b_0}\dot{b}_1 - \frac{(m+1)b_{m+1}}{2b_0}\dot{b}_1^*\right]e^{im\phi} + \dots \quad (3.44)$$

where dots correspond to higher order corrections, b_1^* is the complex conjugate of b_1, $b_{M+1} = 0$, and b_m are defined through

$$b_m(t) = \begin{cases} x_c(t) - iy_c(t), & \text{for} \quad m = 1 \\ \\ a_m(t), & \text{for} \quad m \neq 1 \end{cases}. \quad (3.45)$$

It is clear that by choosing $a_1(t) \equiv 0$, the $e^{i\phi}$ terms are associated with the origin of the moving frame through $b_1(t)$. The complex conjugates in the expansion (3.44) arise from the presence of $\dot{x}_c \cos \phi - \dot{y}_c \sin \phi = (\dot{b}_1 e^{i\phi} - \dot{b}_1^* e^{-i\phi})/(2i)$ in $\partial_t \boldsymbol{c} \cdot \boldsymbol{\nu}$.

One can simplify (3.44) by neglecting terms of $O(\dot{b}_1 b_m)$ and $O(\dot{b}_1^* b_m)$ which are nevertheless smaller than those at $O(\dot{b}_m)$. Doing so yields the expansion

$$\partial_t \boldsymbol{c} \cdot \boldsymbol{\nu} = \sum_{m=1}^{M} \dot{b}_m e^{im\phi} + \dots, \quad (3.46)$$

and ultimately a simpler reduced model to implement. The additional terms in (3.44), however, contribute to corrections of the centroid motion which can become important if the

droplet undergoes long excursions (see figures 5.15 and 5.16). The 2D results in chapter 5 suggest that several periods of liquid flux can cause the droplet to move appreciably across the substrate, implying that the retained higher-order terms in (3.44) may become important here also. Therefore, retaining these terms and returning to the polar variables yields

$$-\partial_\nu h_{\mathrm{in}} \sim \theta_* + \frac{1}{\theta_*^2}\ln\left(\mathrm{e}b_0\bar{\theta}_*\frac{1-r}{\lambda}\right)\left\{\dot{b}_0 + \left(\dot{b}_1 - \frac{b_2}{b_0}\dot{b}_1^*\right)\mathrm{e}^{\mathrm{i}\phi} + \left(\dot{b}_2 - \frac{3b_3}{2b_0}\dot{b}_1^*\right)\mathrm{e}^{2\mathrm{i}\phi}\right.$$
$$\left. + \sum_{m=3}^{M}\left[\dot{b}_m + \frac{(m-1)b_{m-1}}{2b_0}\dot{b}_1 - \frac{(m+1)b_{m+1}}{2b_0}\dot{b}_1^*\right]\mathrm{e}^{\mathrm{i}m\phi}\right\} \quad \mathrm{as} \quad \frac{b_0(1-r)}{\lambda} \to \infty, \quad (3.47)$$

where barred variables henceforth are determined using

$$\bar{(\cdot)} = \frac{1}{2\pi}\int_0^{2\pi}(\cdot)\,\mathrm{d}\phi, \tag{3.48}$$

and denote the average value of the placeholder. With (3.47) determined, the next step is to investigate the macro-scale behaviours so that matching can be performed.

3.2.2 Outer Region

As in the 2D analysis, we neglect terms of $O(\lambda)$ from (2.56a) so that the solution in the outer region, h_{out}, satisfies

$$\partial_t h_{\mathrm{out}} - \frac{1}{a}\left[\dot{x}_c\cos\phi + \dot{y}_c\sin\phi + r\partial_t a + \frac{\partial_\phi a}{a}(\dot{x}_c\sin\phi - \dot{y}_c\cos\phi)\right]\partial_r h_{\mathrm{out}}$$
$$+ \frac{\dot{x}_c\sin\phi - \dot{y}_c\cos\phi}{ar}\partial_\phi h_{\mathrm{out}} + \boldsymbol{\nabla}\cdot\left(h_{\mathrm{out}}^3\boldsymbol{\nabla}\nabla^2 h_{\mathrm{out}}\right) = q(r,\phi,t), \quad (3.49)$$

with

$$h_{\mathrm{out}}(1,\phi,t) = 0, \tag{3.50a}$$

$$\frac{\mathrm{d}}{\mathrm{d}t}\int_0^{2\pi}\int_0^1 ra^2 h_{\mathrm{out}}\,\mathrm{d}r\,\mathrm{d}\phi = \int_0^{2\pi}\int_0^1 ra^2 q\,\mathrm{d}r\,\mathrm{d}\phi = \dot{v}(t), \tag{3.50b}$$

Next we introduce the quasistatic expansion

$$h_{\mathrm{out}}(r,\phi,t) = h_0(r,\phi,t) + h_1(r,\phi,t) + \dots, \tag{3.51}$$

where $h_0 \gg h_1$ and h_1 is linear in $\partial_t a$, $\dot{x}_c$, and $\dot{y}_c$ terms. The quasi-equilibrium solution h_0 is cast as

$$h_0(r,\phi,t) = h_{0,0}(r,b_0) + \sum_{m=2}^{M} b_m(t)h_{0,m}(r,b_0)\mathrm{e}^{\mathrm{i}m\phi} + \dots, \tag{3.52}$$

and describes the leading-order shape in the bulk. The functions $h_{0,0}$ and $h_{0,m}$ are determined by solving perturbatively the leading-order problem

$$\nabla^2 h_0(r, \phi, t) = \tilde{p}(t), \tag{3.53a}$$

$$h_0(1, \phi, t) = 0, \tag{3.53b}$$

$$\int_0^{2\pi} \int_0^1 r a^2 h_0 \, dr \, d\phi = v(t), \tag{3.53c}$$

where $\tilde{p}(t)$ is determined by using the volume constraint (3.53c), and noting that the flux terms do not appear in the leading-order equations since $q = O(1/|\ln(\lambda)|)$ as $\lambda \to 0$. To solve (3.53) we use the contact line expansion (3.37) and expand the Laplacian operator (2.60) to obtain

$$\nabla^2(\cdot) = \frac{1}{b_0^2 r} \partial_r[r \partial_r(\cdot)] + \frac{1}{b_0^2 r^2} \partial_\phi^2(\cdot) - \frac{1}{b_0^3 r} \sum_{m=2}^M b_m \left\{ 2 \partial_r[r \partial_r(\cdot)] - m^2 \partial_r(\cdot) \right\} e^{im\phi} + \dots, \tag{3.54}$$

and thus formulate the following ODEs for $h_{0,0}$ and $h_{0,m}$

$$P_0 h_{0,0} = \tilde{p} b_0^2, \tag{3.55a}$$

$$P_m h_{0,m} = \frac{1}{b_0 r} \partial_r \left(2 r \partial_r h_{0,0} - m^2 h_{0,0} \right), \tag{3.55b}$$

where

$$P_m(\cdot) = \frac{1}{r} \partial_r[r \partial_r(\cdot)] - \frac{m^2}{r^2}(\cdot). \tag{3.56}$$

Solving (3.53) subject to (3.53b) and (3.53c) is rather straightforward, and yields

$$h_0 = \bar{\vartheta} \left[\frac{b_0(1 - r^2)}{2} + \sum_{m=2}^M b_m \left(r^m - r^2 \right) e^{im\phi} \right] + \dots, \tag{3.57}$$

where $\bar{\vartheta} = 4v/\left(\pi b_0^3\right)$ is the average apparent contact angle, which is related to the normal derivative of (3.57)

$$\vartheta = -\partial_\nu h_0|_C = \bar{\vartheta} \left[1 + \sum_{m=2}^M \frac{b_m(1 - m)}{b_0} e^{im\phi} \right] + \dots. \tag{3.58}$$

Clearly, even if a_1 had not been zero, such terms would still not contribute to the leading-order expression (3.57). Hence the choice to associate the $e^{i\phi}$ terms with the motion of the moving coordinate system in (3.45) appears to be natural one.

The next order term, h_1, is a correction that captures the mass flux contributions as well as the centroid and contact line velocities, and is found from a solution of

$$\partial_t h_0 - \frac{1}{b_0} \left[\dot{x}_c \cos\phi + \dot{y}_c \sin\phi + r\partial_t a + \frac{\partial_\phi a}{a} (\dot{x}_c \sin\phi - \dot{y}_c \cos\phi) \right] \partial_r h_{0,0} + \nabla \cdot \left(h_{0,0}^3 \nabla \nabla^2 h_1 \right) = q, \tag{3.59}$$

subject to the conditions

$$h_1(1, \phi, t) = 0, \tag{3.60a}$$

$$\int_0^1 r h_1 \, dr = 0, \tag{3.60b}$$

$$\int_0^1 r q \, dr = \frac{\dot{v}(t)}{2\pi b_0^2}. \tag{3.60c}$$

From the inner-region solution (3.47) we anticipate that h_1 can be expanded as

$$h_1(r, \phi, t) = \sum_{m=0}^{M} \dot{b}_m h_{1,m}(r, b_0) e^{im\phi} - \frac{b_2}{b_0} \dot{b}_1^* \tilde{h}_{1,1}(r, b_0) e^{i\phi} - \frac{3b_3}{2b_0} \dot{b}_1^* \tilde{h}_{1,2}(r, b_0) e^{2i\phi}$$

$$+ \sum_{m=3}^{M} \left[\frac{(m-1) b_{m-1}}{2b_0} \dot{b}_1 - \frac{(m+1) b_{m+1}}{2b_0} \dot{b}_1^* \right] \tilde{h}_{1,m}(r, b_0) e^{im\phi} + \dots \tag{3.61}$$

To proceed, we also expand q as the truncated Fourier series

$$q(r, \phi, t) = \dot{v}(t) \sum_{m=0}^{M} q_m(r) e^{im\phi}, \tag{3.62}$$

and introduce the approximation

$$\partial_t h_0 \approx \dot{v} \partial_v h_0 + \dot{b}_0 \partial_{b_0} h_{0,0} + \sum_{m=2}^{M} \dot{b}_m h_{0,m} e^{im\phi} + \dots, \tag{3.63}$$

which gives rise to the following decoupled set of differential equations

$$\partial_r \left[r \left(1 - r^2 \right)^3 \partial_r P_0 h_{1,0} \right] + \frac{8 b_0 r \left(2 r^2 - 1 \right)}{\bar{\vartheta}^2} - \frac{\dot{v}}{\dot{b}_0} \frac{8 b_0 r}{\bar{\vartheta}^3} \left[\frac{2 \left(r^2 - 1 \right)}{b_0^2 \pi} + q_0(r) \right] = 0, \tag{3.64a}$$

$$r \partial_r \left[r \left(1 - r^2 \right)^3 \partial_r P_m h_{1,m} \right] - m^2 \left(1 - r^2 \right)^3 P_m h_{1,m} + \frac{8 b_0 r^{m+2}}{\bar{\vartheta}^2}$$
$$- \frac{\dot{v}}{\dot{b}_m} \frac{8 b_0 r^2}{\bar{\vartheta}^3} \left[\frac{4 a_m (r^2 - r^m)}{b_0^3 \pi} + q_m(r) \right] = 0, \tag{3.64b}$$

$$r \partial_r \left[r \left(1 - r^2 \right)^3 \partial_r P_m \tilde{h}_{1,m} \right] - m^2 \left(1 - r^2 \right)^3 P_m \tilde{h}_{1,m} + \frac{8 b_0 r^3}{\bar{\vartheta}^2} = 0. \tag{3.64c}$$

Unlike the corresponding inner region analysis, determining analytical solutions to (3.64) is impossible. However, as shown in the 2D analysis it suffices to find the leading order behaviour as the contact line is approached (equivalently as $r \to 1$). Therefore, using the assumption that the flux terms vanish as $r \to 1$ we determine the behaviours from (3.64) that

$$P_m h_{1,m} \sim P_m \tilde{h}_{1,m} \sim \frac{b_0}{\bar{\vartheta}^2 (1 - r)}, \quad \text{as} \quad r \to 1 \quad \text{for} \quad m \geq 0, \tag{3.65}$$

in other words

$$\partial_r h_{1,m} \sim -\frac{b_0}{\bar{\vartheta}^2} \left[\ln \left(1 - r \right) + \beta(m, t) \right] \quad \text{as} \quad r \to 1, \tag{3.66}$$

and

$$\partial_r \tilde{h}_{1,m} \sim -\frac{b_0}{\bar{\vartheta}^2} \left[\ln(1-r) + \hat{\beta}(m) \right] \quad \text{as} \quad r \to 1, \tag{3.67}$$

where $\beta(m,t)$ and $\hat{\beta}(m)$ are functions to be determined. To do this we apply a similar procedure to that used in section 3.1.2, namely, we multiply (3.64a) and (3.64b) by some functions $f_m(r)$ to be determined, and integrate over r from 0 to $1-\varepsilon$ with $0 < \varepsilon \ll 1$. To start we multiply (3.64a) by $f_0(r)$ and integrate as stated, which after integration by parts yields

$$\left[f_0(r) r \left(1-r^2\right)^3 \partial_r P_0 h_{1,0} \right]_0^{1-\varepsilon} - \int_0^{1-\varepsilon} f_0'(r) r \left(1-r^2\right)^3 \partial_r P_0 h_{1,0} \, dr$$
$$= -\frac{8b_0}{\bar{\vartheta}^2} \int_0^{1-\varepsilon} f_0(r) \left\{ r \left(2r^2-1\right) - \frac{\dot{v} r}{b_0 \bar{\vartheta}} \left[\frac{2\left(r^2-1\right)}{b_0^2 \pi} + q_0(r) \right] \right\} dr, \tag{3.68}$$

where primes denote differentiation with respect to r. From the first term in (3.68) it is clear that we must have $f_0(r)$ vanish at zero to eliminate any singular behaviours as $r \to 0$ that could arise from the $-f_0(r)(1-r^2)^3 \partial_r h_{1,0}/r$ term. To determine the functional form of $f_0(r)$ we consider the re-casting $F_0(r) = f_0'(r) r \left(1-r^2\right)^3$ to avoid the equation becoming rather unwieldy. Using this we see that the integral on the left hand side of (3.68) becomes

$$\left[F_0(r) \partial_r^2 h_{1,0} + \left(\frac{F_0(r)}{r} - F_0'(r) \right) \partial_r h_{1,0} + \left(F_0''(r) - \frac{F_0'(r)}{r} \right) h_{1,0} \right]_0^{1-\varepsilon}$$
$$- \int_0^{1-\varepsilon} \left(F_0'''(r) - \frac{F_0''(r)}{r} + \frac{F_0'(r)}{r^2} \right) h_{1,0} \, dr, \tag{3.69}$$

after performing repeated integration by parts. The integral in the above equation can be eliminated using (3.60b), provided that we require that F_0 is chosen to satisfy

$$F_0'''(r) - \frac{F_0''(r)}{r} + \frac{F_0'(r)}{r^2} = r, \tag{3.70}$$

which gives

$$F_0(r) = \frac{c_1 r^2}{4} \left[2\ln(r) - 1 \right] + \frac{c_2 r^2}{2} + c_3 + \frac{r^4}{16}. \tag{3.71}$$

The undetermined constants can be found by requiring that no singular behaviours arise in (3.69) as $\varepsilon \to 0$, and so that the behaviours near $r = 0$ are eliminated, ultimately leaving behind the behaviours of $\partial_r h_{1,0}$ near $r = 1$ so that we can determine $\beta(0,t)$. This is done by choosing $c_1 = c_3 = 0$ which eliminates behaviours near $r = 0$ up to $O(\varepsilon)$, and letting $c_2 = -1/8$ which eradicates terms of $O(1/\varepsilon)$. Therefore, we obtain

$$F_0(r) = \frac{r^2 \left(r^2-1\right)}{16}, \tag{3.72}$$

which means (3.69) yields the leading-order behaviour

$$\frac{b_0}{8\bar{\vartheta}^2}\left[\ln(\varepsilon)+\beta(0,t)-1\right]+O(\varepsilon\ln(\varepsilon)),\tag{3.73}$$

by using (3.66). The function $f_0(r)$ can be easily found by solving

$$f_0(r)'r\left(1-r^2\right)^3=\frac{r^2\left(r^2-1\right)}{16},\tag{3.74}$$

and requiring that $f_0(0)$ vanishes to eliminate the $-f_0(r)(1-r^2)^3\partial_r h_{1,0}/r$ term that arises from the first term in (3.68) when $r\to 0$, finally giving

$$f_0(r)=\frac{r^2}{32\left(r^2-1\right)}.\tag{3.75}$$

Therefore, in the limit $\varepsilon\to 0$ we see that (3.68) becomes

$$\begin{aligned}
-\frac{b_0}{8\bar{\vartheta}^2}\left[\ln(\varepsilon)+\beta(0,t)\right]=&-\frac{b_0}{8\bar{\vartheta}^2}\left[2+\ln(2)+\ln(\varepsilon)\right]\\
&-\frac{\dot{v}}{\dot{b}_0}\frac{b_0}{4\bar{\vartheta}^3}\int_0^1\frac{r^3}{(1-r^2)}\left[\frac{2\left(r^2-1\right)}{b_0^2\pi}+q_0(r)\right]dr+O(\varepsilon\ln(\varepsilon)),
\end{aligned}\tag{3.76}$$

so that

$$\beta(0,t)=\tilde{\beta}(0)+\frac{\dot{v}}{\dot{b}_0}I(0,t),\tag{3.77}$$

where

$$\tilde{\beta}(0)=2+\ln(2),\tag{3.78a}$$

$$I(0,t)=-\frac{1}{\pi b_0^2\bar{\vartheta}}+\frac{2}{\bar{\vartheta}}\int_0^1\frac{r^3 q_0(r)}{(1-r^2)}\,dr.\tag{3.78b}$$

Note that in the above formulation we arrive with precisely the same β term as derived in [61] for when $\dot{v}=0$, the difference with β term here is the contribution of the integral $I(0,t)$ which accounts for the liquid flux, and may be estimated by numerical quadrature.

Finding $\beta(m,t)$ for the azimuthal disturbances is arguably a much more delicate task. This time, after multiplying (3.64b) by $f_m(r)$ and applying integration by parts we obtain

$$\begin{aligned}
&\left[f_m(r)r^2\left(1-r^2\right)^3\partial_r P_m h_{1,m}-(f_m(r)r)'r\left(1-r^2\right)^3 P_m h_{1,m}\right]_0^{1-\varepsilon}\\
&+\int_0^{1-\varepsilon}\left\{\left[(f_m(r)r)'r\left(1-r^2\right)^3\right]'-m^2\left(1-r^2\right)^3 f_m(r)\right\}P_m h_{1,m}\,dr+\frac{8b_0}{\bar{\vartheta}^2}\int_0^{1-\varepsilon}f_m(r)r^{m+2}\,dr\\
&\qquad\qquad-\frac{\dot{v}}{\dot{b}_m}\frac{8b_0}{\bar{\vartheta}^3}\int_0^{1-\varepsilon}f_m(r)r^2\left[\frac{4a_m\left(r^2-r^m\right)}{b_0^3\pi}+q_m(r)\right]dr=0.\tag{3.79}
\end{aligned}$$

Leading from the same rationale used to determine $\beta(0, t)$ we consider the recasting

$$F_m(r) = \left[(f_m(r)r)' \, r \left(1 - r^2\right)^3 \right]' - m^2 \left(1 - r^2\right)^3 f_m(r), \tag{3.80}$$

so that we get

$$\int_0^{1-\varepsilon} F_m(r) P_m h_{1,m} \, dr = \left[F_m(r) \partial_r h_{1,m} + \left(\frac{F_m(r)}{r} - F_m'(r) \right) h_{1,m} \right]_0^{1-\varepsilon}$$
$$+ \int_0^{1-\varepsilon} \left[F_m''(r) - \frac{F_m'(r)}{r} + \frac{F_m(r)\left(1 - m^2\right)}{r^2} \right] h_{1,m} \, dr, \quad (3.81)$$

after performing repeated integration by parts. To eliminate the integral in the above equation

we set

$$F_m''(r) - \frac{F_m'(r)}{r} + \frac{F_m(r)\left(1 - m^2\right)}{r^2} = 0, \tag{3.82}$$

which is easily solved to obtain

$$F_m(r) = c_1 r^{1-m} + c_2 r^{1+m}, \tag{3.83}$$

where we choose $c_1 = 0$ to give finite solutions at $r = 0$, and where c_2 can be chosen to be any non-zero constant, which for convenience is set at $c_2 = 1$. Therefore, we solve the differential equation for $f_m(r)$

$$r^{1+m} = \left[(f_m(r)r)' \, r \left(1 - r^2\right)^3 \right]' - m^2 \left(1 - r^2\right)^3 f_m(r), \tag{3.84}$$

whose solution is obtained by requiring that $f_m(r)$ is finite for $m \geq 1$, and that $f_m \sim 1/(1-r)$ as $r \to 1$ to avoid singular terms arising in the first component of (3.79). In other words we have

$$f_m(r) = \frac{r^{m-1} \left[g_m(1) - g_m(r) \right]}{2 g_m(1)(m+4)(1 - r^2)^2}, \tag{3.85}$$

where $g_m(r)$ denotes the Gauss hypergeometric function

$$g_m(r) = {}_2F_1 \left(\frac{m - 1 - \sqrt{m^2 + 9}}{2}, \frac{m - 1 + \sqrt{m^2 + 9}}{2}; m + 1; r^2 \right). \tag{3.86}$$

Using this form for $f_m(r)$ we can use (3.79) to arrive with

$$\ln(\varepsilon) + \beta(m) = 8 \int_0^{1-\varepsilon} f_m(r) r^{m+2} \, dr - 8 \frac{\dot{v}}{b_m} \int_0^{1-\varepsilon} \frac{f_m(r) r^2}{\bar{\vartheta}} \left[\frac{4a_m(r^2 - r^m)}{b_0^3 \pi} + q_m(r) \right] dr, \tag{3.87}$$

which, solving for $\beta(m, t)$, using

$$\ln(\varepsilon) = -\int_0^{1-\varepsilon} \frac{1}{1-r} \, dr, \tag{3.88}$$

and taking the limit as $\varepsilon \to 0$ yields

$$\beta(m, t) = \tilde{\beta}(m) + \frac{\dot{v}}{b_m} I(m, t), \tag{3.89}$$

where

$$\tilde{\beta}(m) = \int_0^1 \left[8f_m(r)r^{m+2} + \frac{1}{1-r} \right] dr, \tag{3.90a}$$

$$I(m, t) = \int_0^1 \frac{8f_m(r)r^2}{\bar{\vartheta}} \left[\frac{4a_m(r^m - r^2)}{b_0^3 \pi} - q_m(r) \right] dr. \tag{3.90b}$$

As expected, we observe that the $\tilde{\beta}$ term is identical to the β term derived in [61]. Although the integral $I(m, t)$ contains time-dependent components, we can considerably reduce the computational cost associated with evaluating these integrals with numerical quadrature by calculating and storing reusable parts of the integrand.

To finalise the outer region analysis we require the functions $\hat{\beta}(m)$ which account for higher-order centroid motion corrections. Based on the analysis previously presented, these terms can be determined rather straightforwardly since $\hat{\beta}(m)$ can be determined using the functions $f_m(r)$ previously derived. Therefore using the techniques to gather $\beta(m, t)$ we obtain

$$\hat{\beta}(m) = \int_0^1 \left[8f_m(r)r^3 + \frac{1}{1-r} \right] dr, \tag{3.91}$$

which can likewise be pre-computed prior to simulations. Finding $\beta(m, t)$ and $\hat{\beta}(m)$ concludes the outer region analysis since we can now specify the slope

$$-\partial_\nu h_{\text{out}} \sim \vartheta + \frac{1}{\bar{\vartheta}^2} \left\{ \sum_{m=0}^{M} \dot{b}_m \left[\ln(1-r) + \beta(m, t) \right] e^{im\phi} - \frac{b_2}{b_0} \dot{b}_1^* \left[\ln(1-r) + \hat{\beta}(1) \right] e^{i\phi} \right.$$

$$- \frac{3b_3}{2b_0} \dot{b}_1^* \left[\ln(1-r) + \hat{\beta}(2) \right] e^{2i\phi} + \sum_{m=3}^{M} \left[\frac{(m-1)b_{m-1}}{2b_0} \dot{b}_1 - \frac{(m+1)b_{m+1}}{2b_0} \dot{b}_1^* \right] \times$$

$$\left. \left[\ln(1-r) + \hat{\beta}(m) \right] e^{im\phi} \right\}, \quad \text{as} \quad r \to 1, \tag{3.92}$$

to combine with (3.47) in the matching procedure.

3.2.3 Matching

Just like the 2D analysis with vanishing fluxes at the contact points, we can match the cubes of the inner and outer normal derivatives (3.47) and (3.92), respectively, so that they become

$$-(\partial_\nu h_{\text{in}})^3 \sim \theta_*^3 + 3\ln\left(e b_0 \bar{\theta}_* \frac{1-r}{\lambda} \right) \left\{ \dot{b}_0 + \left(\dot{b}_1 - \frac{b_2}{b_0} \dot{b}_1^* \right) e^{i\phi} + \left(\dot{b}_2 - \frac{3b_3}{2b_0} \dot{b}_1^* \right) e^{2i\phi} \right.$$

$$+ \sum_{m=3}^{M} \left[\dot{b}_m + \frac{(m-1)b_{m-1}}{2b_0} \dot{b}_1 - \frac{(m+1)b_{m+1}}{2b_0} \dot{b}_1^* \right] e^{im\phi} \Bigg\}, \quad (3.93)$$

and

$$- (\partial_\nu h_{\text{out}})^3 \sim \vartheta^3 + 3 \sum_{m=0}^{M} \dot{b}_m \left[\ln(1-r) + \beta(m,t) \right] e^{im\phi} - \frac{3b_2}{b_0} \dot{b}_1^* \left[\ln(1-r) + \hat{\beta}(1) \right] e^{i\phi}$$

$$- \frac{9b_3}{2b_0} \dot{b}_1^* \left[\ln(1-r) + \hat{\beta}(2) \right] e^{2i\phi} + 3 \sum_{m=3}^{M} \left[\frac{(m-1)b_{m-1}}{2b_0} \dot{b}_1 - \frac{(m+1)b_{m+1}}{2b_0} \dot{b}_1^* \right] \times$$

$$\left[\ln(1-r) + \hat{\beta}(m) \right] e^{im\phi}. \quad (3.94)$$

Eliminating the r-dependent logarithmic terms yields the Cox-Voinov type law (see equation (1.5))

$$\frac{\vartheta^3 - \theta^3}{3} = \sum_{m=0}^{M} \left[\dot{b}_m \tilde{\chi}_m - \dot{\nu} I(m,t) \right] e^{im\phi} - \frac{b_2}{b_0} \dot{b}_1^* \hat{\chi}_1 e^{i\phi} - \frac{3b_3}{2b_0} \dot{b}_1^* \hat{\chi}_2 e^{2i\phi}$$

$$+ \sum_{m=3}^{M} \left[\frac{(m-1)b_{m-1}}{2b_0} \dot{b}_1 - \frac{(m+1)b_{m+1}}{2b_0} \dot{b}_1^* \right] \hat{\chi}_m e^{im\phi}, \quad (3.95)$$

which is the simplified model for the motion of the contact line, where we have defined

$$\tilde{\chi}_m = \ln\left(\frac{eb_0\bar{\theta}_*}{\lambda} \right) - \tilde{\beta}(m) \quad \text{and} \quad \hat{\chi}_m = \ln\left(\frac{eb_0\bar{\theta}_*}{\lambda} \right) - \hat{\beta}(m), \quad (3.96)$$

for notational simplicity. By expanding the angles in the form

$$\vartheta_m = \frac{1}{2\pi} \int_0^1 \vartheta^3 e^{-im\phi} \, d\phi, \quad \text{and} \quad \theta_m = \frac{1}{2\pi} \int_0^1 \theta_*^3 e^{-im\phi} \, d\phi. \quad (3.97)$$

we deduce the reduced system of equations for the evolutions of b_m

$$\dot{b}_0 = w_0, \quad (3.98a)$$

$$\dot{b}_1 - \frac{\chi_1 b_2}{b_0} \dot{b}_1^* = w_1, \quad (3.98b)$$

$$\dot{b}_2 - \frac{3\chi_2 b_3}{2b_0} \dot{b}_1^* = w_2, \quad (3.98c)$$

$$\dot{b}_m + \frac{(m-1)\chi_m b_{m-1}}{2b_0} \dot{b}_1 - \frac{(m+1)\chi_m b_{m+1}}{2b_0} \dot{b}_1^* = w_m, \quad m \geq 3 \quad (3.98d)$$

where

$$w_m = \frac{\vartheta_m - \theta_m + 3\dot{\nu} I(m,t)}{3\tilde{\chi}_m}, \quad \chi_m = \frac{\hat{\chi}_m}{\tilde{\chi}_m}. \quad (3.99)$$

The reduced system of equations (3.98) describes fully the leading-order droplet spreading dynamics as $\lambda \to 0$, confirming *a posteriori* the assertion that $|\dot{b}_m| = O(1/|\ln(\lambda)|)$. These equations were reported in [61] for the special case of $\nu(t) = 2\pi$, namely for droplets of
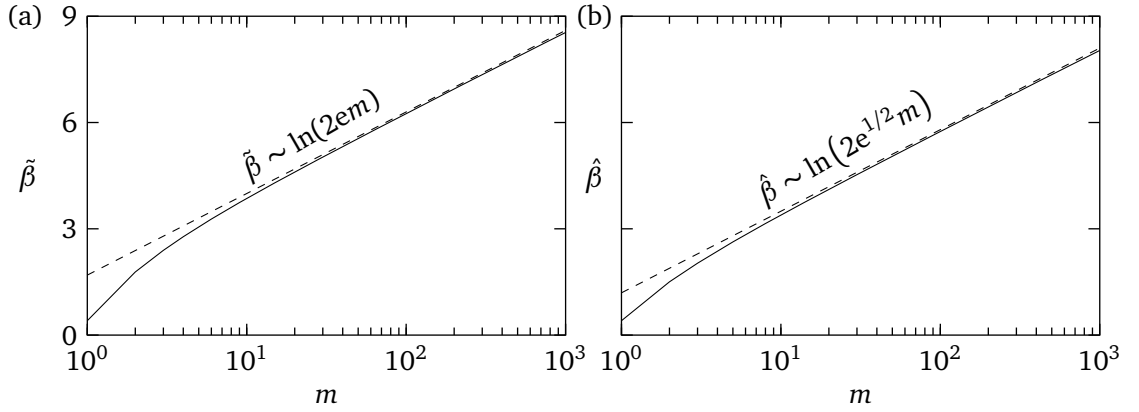
Figure 3.2: Plots of $\tilde{\beta}$ and $\hat{\beta}$ for $m \geq 1$ in (a) and (b), respectively. Both plots are on a logarithmic scale (solid curves), and include their empirically deduced asymptotics for large m (dashed curves). The discrete values in both cases are joined together for clarity.

constant mass. If $\vartheta > \theta$ then we expect that the droplet will have an advancing contact line, in the case of constant mass (i.e. $\dot{v} = 0$) we can deduce that for this to occur in (3.98) we must have

$$\ln\left(\frac{eb_0\bar{\theta}_*}{\lambda}\right) - \tilde{\beta}(m) > 0. \tag{3.100}$$

Since the above does not hold true for all values of m, it allows us to estimate on how large M can be for our analysis to hold. Therefore, taking the equilibrium radius $b_0 = 2$ for a drop of volume 2π over a perfectly homogeneous surface $\theta_* = 1$ as well as the empirically deduced asymptotics $\beta \sim \ln(2em)$ (see figure 3.2) yields $M \ll \lambda^{-1}$. However, this is not particularly restrictive since λ is always a small parameter in our analysis, and in the simulations that follow M is typically $O(100)$.

It is interesting to note that if higher harmonics are excited on a homogeneous substrate, these decay exponentially fast. This can be seen by looking at a droplet near its equilibrium for $v(t) = 2\pi$, writing

$$b_0 = 2 \quad \text{and} \quad b_m = \varepsilon e^{\tilde{\delta} t} \quad \text{for} \quad m > 1, \tag{3.101}$$

where $0 < \varepsilon \ll 1$ is a small parameter. In this regime, $\theta_m = 0$ for $m \geq 1$ and ϑ_m is estimated by using (3.58), giving

$$\vartheta_m = \frac{3(1-m)\varepsilon e^{\tilde{\delta} t}}{2}, \tag{3.102}$$

since $\bar{\vartheta} = 1$ in this configuration. By using (3.98) we obtain

$$\tilde{\delta}\varepsilon e^{\tilde{\delta} t} = \frac{\varepsilon e^{\delta t}(1-m)}{2\left[\ln\left(\frac{2e}{\lambda}\right) - \tilde{\beta}(m)\right]}, \tag{3.103}$$

which is easily solved to give the exponent

$$\tilde{\delta} = \frac{1-m}{2\left[\ln\left(\frac{2e}{\lambda}\right) - \tilde{\beta}(m)\right]}. \tag{3.104}$$

Since the denominator in the above expression is positive for $m > 1$ we have $\tilde{\delta} < 0$, implying that the higher harmonics decay exponentially at a rate which increases with m (see also Glasner [153]).

Like the 2D analysis, once q takes the specific form

$$q = \frac{\dot{v}(t)}{v(t)} h, \tag{3.105}$$

we can eliminate $\dot{v}(t)$ terms from (3.98) so that volume changes appear only through the apparent contact angle (3.58). Further simplifications can be obtained by expanding $\partial_t c \cdot \nu$ according to (3.46) which can be viewed by setting χ_m terms to zero in (3.98). However, as explained previously, we expect these terms to become of importance when considering multiple periods of flow, therefore, all test cases explored in simulations retain these terms and the complete system (3.98) is used.

3.3   Evaporative Flux

In the previous section the analysis for droplets of variable mass was considered. The analysis pertained for liquid fluxes that vanished at the contact line (i.e. $q(1, \phi, t) = 0$) where their contributions appear in the dynamics of the macro-scale. In this section we investigate droplets evaporating into their own vapour where the flux is maximised close to the contact line. Here the substrate is maintained at a constant temperature $T_s = T_0 + \Delta T$ for $\Delta T \ll T_0$ where T_0 is the saturation temperature due to the pressure in the vapour, and ΔT is the superheat. To couple thermal effects into the dynamics we consider the temperature equation [137] (noting the following variables are dimensional)

$$\partial_t T + u \cdot \nabla T = \frac{k}{\rho c_p} \nabla^2 T, \tag{3.106}$$

where k is the thermal conductivity and c_p is the specific heat capacity. Using the scalings introduced in chapter 2 it is easy to verify that the above equation reduces to

$$\partial_z^2 T = 0, \tag{3.107}$$

in the long-wave limit, where solutions are determined subject to the conditions

$$T|_{z=0} = T_s, \quad \text{and} \quad \partial_z T|_{z=h} + \frac{\bar{L}}{k}q = 0. \tag{3.108}$$

Here, $\bar{L}$ is the latent heat of vaporisation which is defined as the energy required to convert a unit amount of the material from the liquid phase to the gas phase, and therefore, using (3.107) alongside (3.108) leads to the solution

$$T = T_s - \frac{\bar{L}z}{k}q. \tag{3.109}$$

To couple the kinematic boundary condition (2.9) with the above equation, we make use of a relation arising from kinetic theory [170] that says the deviations of the interfacial temperature from T_0 are proportional to the mass loss through (see [53, 140, 171–173])

$$q = \frac{\tilde{\rho} f_a \bar{L} (T_{z=h} - T_0)}{(2 - f_a)} \sqrt{\frac{2M_w}{\pi R_g T_0^3}}. \tag{3.110}$$

In the above $\tilde{\rho}$ is the density of the vapour, M_w is the molecular weight, R_g is the gas constant and $0 < f_a \ll 1$ is the accommodation coefficient which can be viewed as the probability that a liquid particle moves from the liquid-vapour phase into the bulk vapour phase (for water this can take the large range of $0.01 < f_a < 1$, see e.g. [174, 175]).

The final step to obtain the evaporative flux model is to combine (3.109) and (3.110) to give

$$q = \frac{k\Delta T}{\bar{L}(\mathcal{S} + h)}, \tag{3.111}$$

as the dimensional version of the flux, where

$$\mathcal{S} = \frac{k(2 - f_a)}{\tilde{\rho} f_a \bar{L}^2} \sqrt{\frac{T_0^3 \pi R_g}{2M_w}}, \tag{3.112}$$

is a length-scale where smaller values denote more important kinetic effects (see Savva *et al.* [53] for a more detailed explanation on this parameter). By appropriately non-dimensionalising h using the scalings introduced in chapter 2, we combine with the kinematic boundary condition (2.9) to obtain

$$q = -\frac{\mathcal{E}}{h + \mathcal{K}}, \tag{3.113}$$

in non-dimensional form, where

$$\mathcal{E} = \frac{3k\Delta T}{\bar{L}\alpha_s^2 L\rho U}, \quad \text{and} \quad \mathcal{K} = \frac{\mathcal{S}}{\alpha_s L}. \tag{3.114}$$

	Water	Ethanol	Ammonia	FC-72
T_0 (K)	373	352	300	305
ρ (kg/m^3)	960	727	600	1665
$\tilde{\rho}$ (kg/m^3)	0.6	1.6	9.0	5.7
σ (N/m)	0.059	0.020	0.020	0.010
$\bar{L}$ ($\times 10^6$ J/kg)	2.3	0.88	1.2	0.091
M_w (kg/mol)	0.018	0.046	0.017	0.338
k (W/(mK))	0.68	0.17	0.48	0.06
μ ($\times 10^{-4}$ Pas)	2.8	4.4	1.3	5.9
S (nm)	41.6	15.3	5.3	42.1

Table 3.1: Table for the properties of fluids as seen in [53]. See references therein for the locations of the gathered data.

In the above $\mathcal{E} > 0$ is the *evaporation number*, which can be thought of as the ratio between the time-scale of capillary action and the time-scale of evaporation; and $\mathcal{K} > 0$ is the *kinetic resistance* which compares the length-scale of kinetic effects with the macroscopic length-scale L. We emphasise that this model is a first step to introducing an evaporative flux model, since it neglects the presence of effects such as thermocapillarity and heat loss to the gas phase above the free surface of the drop.

To gather a sense of the parameter regimes of interest we consider the sample fluids seen within table 3.1 as taken from Savva *et al.* [53] who cite the various sources of the data. This table is used by replacing the time-dependent rate of spreading U by using the capillary number (i.e. $U \sim \alpha_s^3 \sigma / \mu$) inside the definition of $\mathcal{E}$, noting that the static angle α_s has replaced the small parameter ε from section 2.2. If we consider small drops so that $\alpha_s = 10°$, $L = 1$ mm, $\Delta T = 1$ K and $f_a = 1$ we obtain approximately for $(\mathcal{E}, \mathcal{K})$ the pairs: $(2.71 \times 10^{-5}, 23.8 \times 10^{-5})$ for water, $(10.8 \times 10^{-5}, 8.77 \times 10^{-5})$ for ethanol, $(8.03 \times 10^{-5}, 3.04 \times 10^{-5})$ for ammonia and $(43.2 \times 10^{-5}, 24.1 \times 10^{-5})$ for perfluorohexane (FC-72). By decreasing the value of α_s to $5°$ the values of $\mathcal{E}$ become 32 times larger, whereas the values of $\mathcal{K}$ become twice as large. The slip-length typically ranges between the values $b \approx 1$ nm$-1\,\mu$m (see Lauga *et al.* [162]), which means by considering the Navier-slip model introduced in section 2.1.2 and $\alpha_s = 10°$ we have the range $\lambda \approx 1.72 \times 10^{-5} - 1.72 \times 10^{-3}$, which grows twice as large for $\alpha_s = 5°$.

It should be emphasised that the above discussion is merely to offer an indication of the relative sizes of the parameters considered. Especially since some parameters can take a wide range of values, such as S due to the associated difficulty of extracting the parameter f_a. For example, the presence of contaminants, the difficulties in measuring temperature differences between the liquid-vapour interface and the sensitivity of f_a on

temperature/pressure variations can cause issues in its experimental extraction. However, the key observation is that the parameters $\mathcal{E}$, $\mathcal{K}$ and λ are small so that a matched asymptotic analysis can be leveraged, specifically investigating evaporation times that occur on time-scales longer than that of capillary action. To ensure that the analysis is based around the expansion of a single small parameter, we introduce the change of variables $\mathcal{E} = \lambda E$ and $\mathcal{K} = \lambda K$. Due to the computational difficulties of numerically solving the full problem for values of λ that are small, we retain $\lambda = 10^{-3}$ in most of our investigative cases, and hence modify E and K accordingly to investigate realistic values of $\mathcal{E}$ and $\mathcal{K}$ based on the discussion previously presented.

Evaporating droplets typically undergo a four stage process each with their own distinct time-scales. The first stage where $t = O(1)$ is rather brief and occurs upon droplet deposition where the droplet profile will relax to the quasistatic one. As mentioned previously, this stage is rather brief and therefore we did not consider its investigation necessary. During the second, or spreading stage, the droplet either advances or recedes so that the microscopic contact angle roughly equals the apparent contact angle. During this stage, as argued by Savva *et al.* [53] and Saxton *et al.* [164], there is no appreciable mass loss due to evaporation and therefore it is reasonable to assume that this time-scale occurs on the same spreading scale as for cases of constant mass, namely $t = O(|\ln(\lambda)|)$ as $\lambda \to 0$. During the third stage, the droplet loses an order unity volume due to evaporation on the much longer time-scale $t = O(1/(\lambda|\ln(\lambda)|))$. Therefore in this stage we expect that the motion of the contact line is slow process so that $\dot{b}_m \approx 0$, meaning that the microscopic contact angle roughly equals the apparent one. Finally, during the fourth stage the droplet approaches extinction where $v(t) < \lambda$ so that there is no longer a clear separation of scales, meaning an asymptotic approach here is no longer applicable.

Consistently with Savva *et al.* [53] we base our analysis on the time-scale of the second stage with the assumption this can be used to approximate the dynamics in the first three stages. While strictly speaking from an asymptotic point of view this does not hold, later we will argue with rather compelling numerical evidence that such an assumption can be made without impacting the rather excellent agreement with simulations of the governing equations. Thus, by considering this time-scale we can avoid the intricacies of forming a composite expansion that encapsulates all scales. The forthcoming analysis is built upon the foundations of Savva *et al.* [53] where the key addition to the present case is that heterogeneous terms are

retained so that the axisymmetry constraint imposed by Savva *et al.* [53] is broken. Also, we note that a change from the Navier slip model used by Savva *et al.* [53] has been proposed so that numerical simulations for fully 3D droplets is considerably easier (see chapter 4). The analytical descriptions henceforth will use framework developed in the previous section to explore evaporating droplets, noting that the predominant focus will be modifying the inner region analysis to account for evaporation in the micro-scale.

3.3.1   Evolution of the Contact Line

To determine the equations for the evolution of the contact line for evaporating droplets, we build upon the analysis presented in section 3.2. In the outer region we anticipate that, as $\lambda \to 0$, we have $\dot{v}(t) = O(\lambda|\ln(\lambda)|)$ (as follows from the analysis of (3.131)). This means that in the outer-region, $\dot{v}(t)$ terms do not appear at the orders we consider, which is equivalent to setting the integral terms (3.78b) and (3.90b) in (3.92) to zero. Therefore, the outer region analysis for evaporating droplets is identical to that performed previously, noting that volume changes appear only through the apparent contact angle (3.58).

The main focus is to modify the inner region dynamics from section 3.2.1 to include evaporative flux terms, since, in section 3.2.1 the flux terms are neglected under the assumption that q vanishes at the contact line. On the contrary, here the flux is maximised close to the contact line, meaning a separate treatment is required. To probe into the dynamics of the inner region, we use the transformation of variables (3.38) to obtain the following separable PDE up to $O(\lambda)$

$$\frac{\partial_t \boldsymbol{c} \cdot \boldsymbol{\nu}}{\theta_*^3} \partial_\xi \Upsilon + \partial_\xi \left[\Upsilon(\Upsilon^2 + 1)\partial_\xi^3 \Upsilon \right] = -\frac{E}{\theta_*^4(\Upsilon + K)}, \qquad (3.115)$$

where the right hand side differs from (3.39) to include evaporative flux using (3.113). Just like the previous inner region analysis, we are solving the PDE (3.115) subject to the conditions of the form (3.3) at $\xi = 0$. To proceed with investigating the inner region we introduce a quasistatic expansion of the form

$$\Upsilon \sim \Upsilon_0 + (\partial_t \boldsymbol{c} \cdot \boldsymbol{\nu})\Upsilon_1 + \dots, \qquad (3.116)$$

where $\Upsilon_0 \gg \Upsilon_1$. This expansion when substituted into (3.115) yields the following equation at leading order

$$\partial_\xi \left[\Upsilon_0(\Upsilon_0^2 + 1)\partial_\xi^3 \Upsilon_0 \right] = -\frac{E}{\theta_*^4(\Upsilon_0 + K)}, \qquad (3.117)$$

which is solved for $\xi > 0$ subject to

$$\Upsilon_0|_{\xi=0} = 0, \tag{3.118a}$$

$$\partial_\xi \Upsilon_0|_{\xi=0} = 1, \tag{3.118b}$$

as well as the requirement that the behaviour of Υ_0 is linear as the bulk is approached, in other words

$$\Upsilon_0 \sim \frac{\theta_e}{\theta_*}\xi, \quad \text{as} \quad \xi \to \infty. \tag{3.119}$$

Contrary to the previous analysis where the flux is neglected from the leading-order equations, here, the flux term appears in (3.117) since E can be $O(1)$. In (3.119) we have introduced θ_e, which is the macroscopic Young's angle modified by evaporative flux (made non-dimensional by the reference angle α_s) and is obtained for given E, K, and θ_* by solving (3.117) alongside the conditions (3.118). The procedure to determine θ_e is based on similar ideas as in [53], which is nevertheless tailored for the slip model considered here and accounts for the presence of substrate heterogeneities (see appendix B for more details).

At the next order we obtain the equation

$$\frac{1}{\theta_*^3}\partial_\xi \Upsilon_0 + \partial_\xi \left[\Upsilon_0(\Upsilon_0^2 + 1)\partial_\xi^3 \Upsilon_1 + \Upsilon_1 \left(3\Upsilon_0^2 + 1\right)\partial_\xi^3 \Upsilon_0\right] = \frac{E\Upsilon_1}{\theta_*^4(\Upsilon_0 + K)^2}, \tag{3.120}$$

which is solved with

$$\Upsilon_1|_{\xi=0} = 0, \tag{3.121a}$$

$$\partial_\xi \Upsilon_1|_{\xi=0} = 0, \tag{3.121b}$$

as well as requiring that $\partial_\xi \Upsilon_1$ is no more than logarithmically large in the far field

$$\partial_\xi \Upsilon_1 \sim \frac{1}{\theta_e^2 \theta_*}\ln(\beta_{\text{in}}\xi), \quad \text{as} \quad \xi \to \infty. \tag{3.122}$$

Here β_{in} is a degree of freedom which, just as θ_e, is determined numerically for given E, K, and θ_* (see appendix B).

In the limit of weak evaporative effects the modified angle θ_e is only weakly modified from the locally varying Young's angle θ, therefore we can make progress analytically by neglecting the presence of the flux in the leading-order equation (3.117). For this circumstance the modified angle takes the form

$$\theta_e = \theta_* + \tilde{\kappa}E \quad \text{for} \quad \tilde{\kappa} \ll 1, \tag{3.123}$$

where the leading order shape is a wedge, i.e. $\Upsilon_0 = \xi$ as used in the previous 3D analysis. Hence, the parameters $\tilde{\kappa}$ and β_{in} are found by introducing the quasistatic expansion $\Upsilon \sim \xi + \tilde{\Upsilon} + \dots$ into (3.115), yielding

$$\frac{\partial_t \boldsymbol{c} \cdot \boldsymbol{\nu}}{\theta_*^3} + \partial_\xi \left[\xi \left(\xi^2 + 1 \right) \partial_\xi^3 \tilde{\Upsilon} \right] = -\frac{E}{\theta_*^4 (\xi + K)}, \tag{3.124}$$

which is solved subject to the homogeneous conditions $\tilde{\Upsilon} = \partial_\xi \tilde{\Upsilon} = 0$ at $\xi = 0$, and where $\tilde{\Upsilon}$ possesses the asymptotic behaviour

$$\partial_\xi \tilde{\Upsilon} \sim \frac{\tilde{\kappa} E}{\theta_*} + \frac{\partial_t \boldsymbol{c} \cdot \boldsymbol{\nu}}{\theta_*^3} \ln(\beta_{\text{in}} \xi) \quad \text{as} \quad \xi \to \infty. \tag{3.125}$$

Integrating (3.124) and requiring that both sides vanish as $\xi \to 0$ yields

$$\xi \partial_\xi^3 \tilde{\Upsilon} = \frac{E}{\theta_*^4 (1 + \xi^2)} \ln \left(\frac{K}{\xi + K} \right) - \frac{\xi (\partial_t \boldsymbol{c} \cdot \boldsymbol{\nu})}{\theta_*^3 (1 + \xi^2)}, \tag{3.126}$$

which is integrated once more to arrive with

$$\left[\xi \partial_\xi^2 \tilde{\Upsilon} - \partial_\xi \tilde{\Upsilon} \right]_0^l + \frac{\partial_t \boldsymbol{c} \cdot \boldsymbol{\nu}}{\theta_*^3} \ln(l) = \frac{E}{\theta_*^4} \int_0^l \frac{1}{1 + \xi^2} \ln \left(\frac{K}{\xi + K} \right) d\xi, \tag{3.127}$$

where $l \gg 1$. Using the conditions for $\tilde{\Upsilon}$ it is easy to see that as $l \to \infty$ we have

$$\tilde{\kappa} = \frac{1}{\theta_*^3} \int_0^\infty \frac{1}{1 + \xi^2} \ln \left(\frac{\xi + K}{K} \right) d\xi, \tag{3.128a}$$

$$\beta_{\text{in}} = \mathrm{e}, \tag{3.128b}$$

where the above integral is determined numerically via quadrature, noting that it may be expressed in terms of the Lerch Phi function. The case of the Navier slip model can be found in appendix A of Savva *et al.* [53]. The approximation (3.123) is valid in the limit of large K or small E, providing an acceptable approximation to θ_e in the range that $E \ll K \theta_*^3 / [1 + \ln(K)]$, allowing us to avoid the more specialised numerical treatment in this limit.

In figure 3.3 we plot the numerically generated angles θ_e for varying values of θ alongside the corresponding weakly modified angle predictions. It is easy to see that the weakly modified angle (3.123) becomes more acceptable as an approximation if θ takes larger values, or if the effect evaporation has on the inner region dynamics is weak. It is therefore reasonable to expect that if evaporation is sufficiently weak then the heterogeneity of the surface will play a larger role in the dynamics. For E fixed and K decreasing (figure 3.3(a)) we observe that the dynamics becomes less dominated by heterogeneity as kinetic resistance effects decrease, noting that the weakly modified angle approximation provides acceptable results
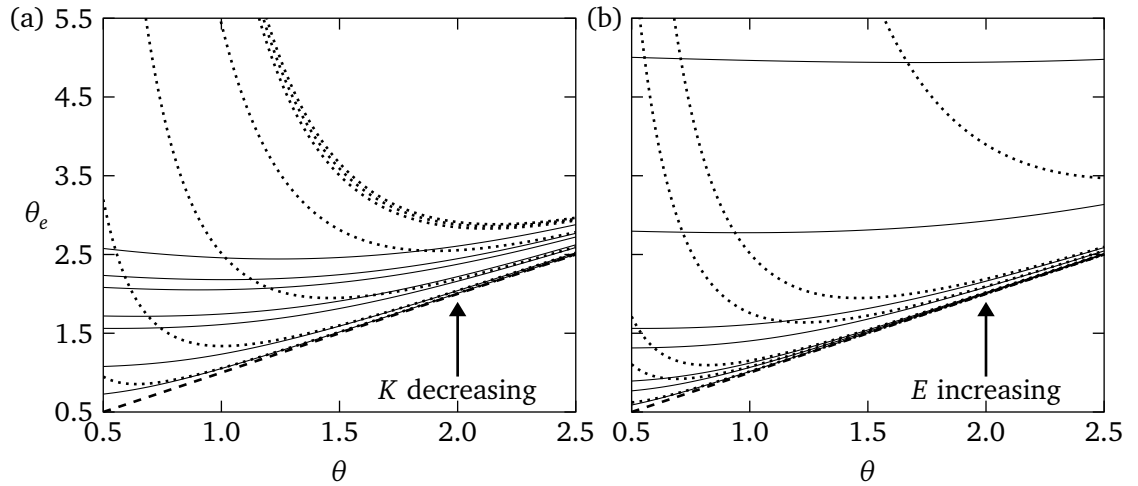
Figure 3.3: The effect of θ on the modified angle θ_e for $E = 1$ and $K = 0.01, 0.05, 0.1, 0.5, 1$, 10 and 100 in (a), and with the values of E and K swapped in (b). In both plots solid curves are the numerically determined angles through the methods in appendix B, dotted curves are the weak angle approximation (3.123) and the dashed curve plots θ against θ.
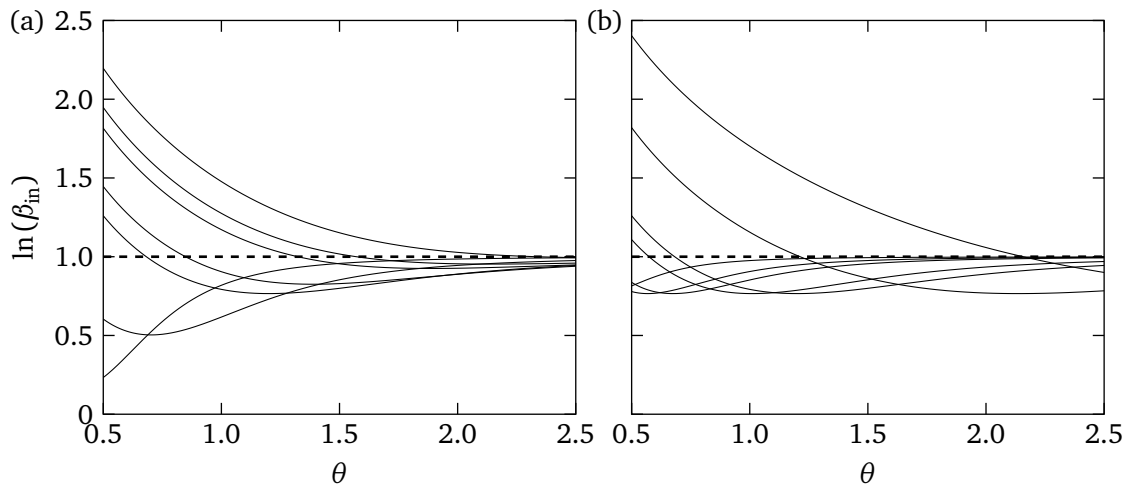

Figure 3.4: Plots of $\ln(\beta_{in})$ for varying θ. The chosen values of E and K are the same as figure 3.3. The faster convergence to 1 in (a) corresponds to increasing K, and in (b) corresponds to decreasing E.

in circumstances with higher K. However, increasing E (figure 3.3(b)) along the same orders of magnitude has a much greater effect, since for higher values of E we see that θ_e has a much larger departure from θ than in the cases of low K. The convergence to the weakly modified angle approximation can also be observed in figure 3.4 by plotting values of $\ln(\beta_{in})$, in which we again see that as θ grows we obtain convergence to $\ln(\beta_{in}) = 1$ (i.e. $\beta_{in} = e$ as found from (3.128b)), although, similarly to figure 3.3 this is achieved faster by using a low value of E and increasing K.

Using the techniques discussed in section 3.2.1 we express the inner region slope as

$$-\partial_\nu h_{\text{in}} \sim \theta_e + \frac{1}{\theta_e^2} \ln\left(\bar{\beta}_{\text{in}} b_0 \bar{\theta}_* \frac{1-r}{\lambda}\right) \left\{ b_0 + \left(b_1 - \frac{b_2}{b_0} b_1^* \right) e^{\text{i}\phi} + \left(b_2 - \frac{3b_3}{2b_0} b_1^* \right) e^{2\text{i}\phi} \right.$$

$$\left. + \sum_{m=3}^{M} \left[b_m + \frac{(m-1)b_{m-1}}{2b_0} b_1 - \frac{(m+1)b_{m+1}}{2b_0} b_1^* \right] e^{\text{i}m\phi} \right\} \quad \text{as} \quad \frac{b_0(1-r)}{\lambda} \to \infty, \quad (3.129)$$

which is matched with the outer region slope (3.92) (with $\dot{v}(t)$ terms set to zero) in the matching process as described in section 3.2.3. Therefore, taking the cubes of the slopes (3.129) and (3.92) we determine the evolution equations (3.98) for b_m, noting that we re-define

$$w_m = \frac{\vartheta_m - \theta_{e,m}}{3\left[\ln\left(\frac{\bar{\beta}_{\text{in}} b_0 \bar{\theta}_*}{\lambda} \right) - \tilde{\beta}(m) \right]}, \quad \theta_{e,m} = \frac{1}{2\pi} \int_0^{2\pi} \theta_e^3 e^{-\text{i}m\phi} \, \mathrm{d}\phi, \quad (3.130)$$

where ϑ_m is determined using (3.97). Noteworthy is that the reduced model for evaporating droplets shares close resemblance with (3.98), its key difference appears through calculation of the modified angle θ_e, rather than say, β_{in} which appears in the equations logarithmically.

3.3.2 Evolution of the Droplet Volume

Using (3.98) we can determine the contact line and centroid velocities at time t, however, these equations rely on the droplet volume which appears in the dynamics through the apparent contact angle. Therefore, to close the system and fully determine the motion of evaporating droplets we require an evolution equation for $v(t)$ found from the flux condition

$$\dot{v}(t) = -\int_0^{2\pi} \int_0^1 \frac{ra^2 \mathcal{E}}{h + \mathcal{K}} \, \mathrm{d}r \, \mathrm{d}\phi, \quad (3.131)$$

which describes the evolution of the droplet volume in time. As a starting point, one may consider using the leading-order profile (3.57) as a replacement for the droplet thickness within (3.131), which yields the approximation

$$\dot{v}(t) = -\frac{2\pi a_0 \mathcal{E}}{\bar{\vartheta}} \ln\left(\frac{\bar{\vartheta} a_0}{2\mathcal{K}} + 1 \right) - 4\mathcal{E} \int_0^{2\pi} \sum_{m=2}^{M} \left\{ a_0 a_m \int_0^1 \frac{r \left[2\mathcal{K} + \bar{\vartheta} a_0 (1 - r^m) \right]}{\left[2\mathcal{K} + \bar{\vartheta} a_0 (1 - r^2) \right]^2} \, \mathrm{d}r \right\} e^{\text{i}m\phi} \, \mathrm{d}\phi,$$

$$(3.132)$$

as $\lambda \to 0$. Therefore, under the restrictions put forth in the analysis we see that azimuthal corrections vanish by integrating $e^{\text{i}m\phi}$ over its period, leaving

$$\dot{v}(t) = -\frac{2\pi a_0 \mathcal{E}}{\bar{\vartheta}} \ln\left(\frac{\bar{\vartheta} a_0}{2\mathcal{K}} + 1 \right), \quad (3.133)$$

as the leading-order approximation, to which we can deduce that $\dot{v}(t) = O(\lambda |\ln(\lambda)|)$ as $\lambda \to 0$. This equation is reminiscent of that derived by Savva *et al.* [53] in the case of homogeneous

substrates (i.e. $\theta = 1$) and negligible gravitational effects, where it is concluded that such a formula can serve as a good approximation in the large K limit. However, this formula neglects the presence of the finer details entering through the microscopic features since (3.57) describes the thickness in the bulk. Therefore, a more elaborate analysis is required to couple these finer effects entering through the micro-scale with the corresponding macro-scale counterpart. To proceed, we follow the framework presented by Savva *et al.* [53] and develop an evolution equation for $\dot{v}(t)$ based on the assumption that the mean droplet radius is much larger than $\mathcal{K}$ and λ, noting that in the current analysis we only consider the presence of the inner and outer regions, contrary to [53] who included the analysis of the intermediate region as well. As previously highlighted, during the third stage of evaporation the evolution of the contact line is slaved as a slow process so that $\dot{b}_m \approx 0$. Using the reduced model for evaporating droplets (3.98) we see that this occurs once $\theta_e \approx \vartheta$ so that $\dot{b}_0 \approx \left[4/(9\pi\bar{\theta}_e v^2)\right]^{1/3} \dot{v}(t)$ at the axisymmetric component (noting a similar equation can be deduced for the $\dot{b}_m$ terms). This means that at the start of the third stage we have $v = O(1)$ with $\dot{v}(t)$ and $\dot{b}_0(t)$ of the same order so that $\dot{b}_0(t)$ ceases to be the greatest of small parameters, and therefore, one can neglect its role when evaporative effects dominate. However, as the volume diminishes we have $\dot{b}_0 \gg \dot{v}(t)$, meaning the approximation $\theta_e \approx \vartheta$ no longer holds. As the droplet transitions to the evaporation stage the effects of the intermediate region diminish, and since this occurs on a comparatively faster time-scale than the evaporation stage we can use $\theta_e \approx \vartheta$ to approximate the evaporation dynamics here also. Considering all three regions will supply a more complete analysis, however, using $\theta_e \approx \vartheta$ allows allows for a simplification of the analysis without impacting the agreement between calculations of the governing equations, as highlighted by the results in [53]. Besides, after the rather brief second stage $v(t)$ is not appreciably altered. In consequence, we split $\dot{v}(t)$ into contributions from both the inner and outer regions, namely

$$\dot{v}(t) = -(q_{\text{in}} + q_{\text{out}}), \tag{3.134}$$

where we consider separately the integrals

$$q_{\text{in}} = \int_0^{2\pi}\int_{r_*}^1 \frac{ra^2\mathcal{E}}{h_{\text{in}} + \mathcal{K}}\, dr\, d\phi, \quad \text{and} \quad q_{\text{out}} = \int_0^{2\pi}\int_0^{r_*} \frac{ra^2\mathcal{E}}{h_{\text{out}} + \mathcal{K}}\, dr\, d\phi, \tag{3.135}$$

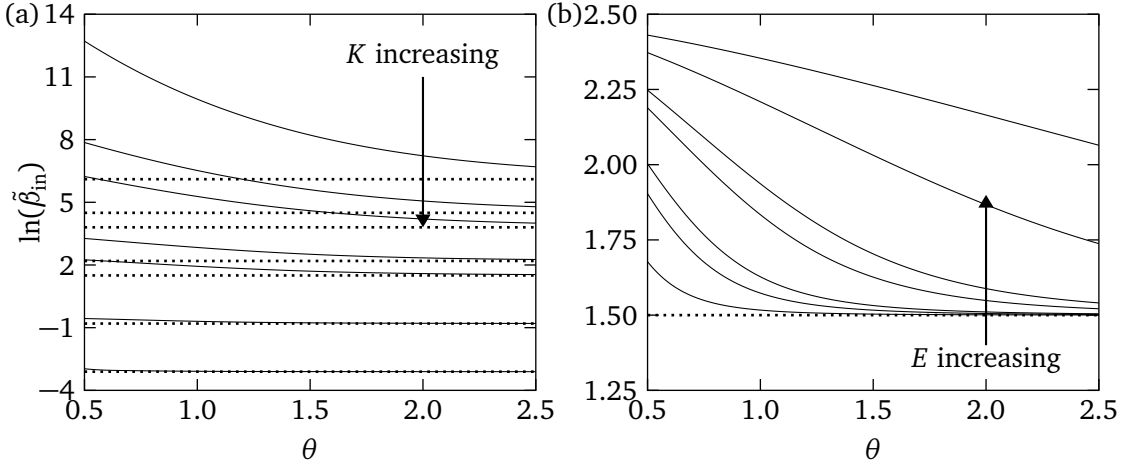for r_* being some radius where the inner region matches with the outer region.

Figure 3.5: Plots of $\ln(\tilde{\beta}_{\text{in}})$ using the same values of E and K as figure 3.4. Dotted lines are plots of $\ln\left(e^{3/2}/K\right)$.

The inner region integral is analysed by transforming the variables using (3.38), giving

$$q_{\text{in}} \sim \int_0^{2\pi}\int_0^{\xi_*} \frac{\sqrt{a^2+(\partial_\phi a)^2}}{\theta_*}\frac{\mathcal{E}}{\Upsilon_0+K}\,\mathrm{d}\xi\,\mathrm{d}\phi \quad \text{as} \quad \lambda \to 0, \tag{3.136}$$

where $h_{\text{in}} = \lambda\Upsilon_0$ is used as a leading-order approximation, and

$$\xi_* = \frac{a^2\theta_*(1-r_*)}{\lambda\sqrt{a^2+(\partial_\phi a)^2}} \gg 1 \quad \text{as} \quad \lambda \to 0. \tag{3.137}$$

Using the far field asymptotics of (3.117) we obtain the behaviour

$$\partial_\xi\Upsilon_0 \sim \frac{\theta_e}{\theta_*} - \frac{E}{2\theta_e^4\xi}\ln\left(\frac{\theta_e\tilde{\beta}_{\text{in}}\xi}{\theta_*}\right) \quad \text{as} \quad \xi \to \infty, \tag{3.138}$$

where $\tilde{\beta}_{\text{in}}$ is a parameter appearing in the next-order term in the asymptotic expansion of $\partial_\xi\Upsilon_0$, and is determined numerically using the methods presented in appendix B. Utilising this behaviour, we integrate the PDE (3.117) to yield

$$\int_0^{\xi_*} \frac{\mathcal{E}}{\Upsilon_0+K}\,\mathrm{d}\xi \sim \frac{\mathcal{E}\theta_*}{\theta_e}\ln\left(\frac{\theta_e\tilde{\beta}_{\text{in}}\xi_*}{\theta_*e^{3/2}}\right) \quad \text{as} \quad \xi_* \to \infty, \tag{3.139}$$

and therefore, transforming back to the polar variables we have the integral

$$q_{\text{in}} \sim \int_0^{2\pi} \frac{\mathcal{E}\sqrt{a^2+(\partial_\phi a)^2}}{\theta_e}\ln\left[\frac{\theta_e a^2\tilde{\beta}_{\text{in}}(1-r_*)}{\lambda e^{3/2}\sqrt{a^2+(\partial_\phi a)^2}}\right]\mathrm{d}\phi, \tag{3.140}$$

which is to be combined with the corresponding outer region contribution. Had we used the far field behaviour $\Upsilon_0 = \theta_e\xi/\theta_*$ as $\xi \to \infty$ (i.e., the leading-order behaviour as we approach the outer region) as a replacement in (3.136) we obtain $\tilde{\beta}_{\text{in}} = e^{3/2}/K$, which is expected to serve as an approximation once the dynamics are weakly modified by evaporative flux. Figure

3.5 shows a comparison between plots of $\ln(\tilde{\beta}_{in})$ and $\ln(e^{3/2}/K)$ for varying θ, suggesting that in the strong heterogeneity or weak evaporation limit we can see that indeed $e^{3/2}/K$ approximates the value of $\tilde{\beta}_{in}$.

To formulate an outer region integral that can be easily combined with (3.140), we recast the leading-order solution (3.57) in the form

$$h_0 = \frac{\vartheta a^2}{\sqrt{a^2 + (\partial_\phi a)^2}} \left\{ \frac{1-r^2}{2} + \frac{1}{2} \sum_{m=2}^{M} \frac{a_m}{a_0} \left[m\left(1-r^2\right) - 2\left(1-r^m\right) \right] e^{im\phi} \right\}, \qquad (3.141)$$

which in turn gives us the modified outer region integral

$$q_{out} \sim \int_0^{2\pi} \frac{\mathcal{E}\sqrt{a^2 + (\partial_\phi a)^2}}{\vartheta} \int_0^{r_*} \left\{ \frac{2r}{1-r^2} + \frac{2r}{a_0(1-r^2)^2} \sum_{m=2}^{M} a_m \left[m\left(r^2-1\right) \right. \right.$$
$$\left. \left. - 2\left(r^m-1\right) \right] e^{im\phi} \right\} dr\, d\phi, \quad (3.142)$$

where kinetic resistance effects have been neglected, which is an acceptable approximation for $K \ll 1$. To proceed, we evaluate the integral of the leading order component, and take the limit $r_* \to 1$ which yields the final outer region contribution

$$q_{out} \sim \int_0^{2\pi} \frac{\mathcal{E}\sqrt{a^2 + (\partial_\phi a)^2}}{\vartheta} \left\{ \ln\left[\frac{1}{2(1-r_*)} \right] + 2 \sum_{m=2}^{M} \frac{a_m}{a_0} \times \right.$$
$$\left. \int_0^1 \frac{mr\left(r^2-1\right) - 2r\left(r^m-1\right)}{(1-r^2)^2} dr\, e^{im\phi} \right\} d\phi. \quad (3.143)$$

The final step to determine the evolution equation of $\dot{v}(t)$ is to add both the contributions from the inner (3.140) and outer (3.143) region integrals by assuming that $\vartheta \approx \theta_e$. By doing so, the logarithmically singular portions of each contribution cancel each other out, leaving

$$\dot{v}(t) = -\int_0^{2\pi} \frac{\mathcal{E}\sqrt{a^2 + (\partial_\phi a)^2}}{\vartheta} \left[\ln\left(\frac{\vartheta a^2 \tilde{\beta}_{in}}{2\lambda e^{3/2}\sqrt{a^2 + (\partial_\phi a)^2}} \right) - 2 \sum_{m=2}^{M} \frac{a_m}{a_0} I_e(m) e^{im\phi} \right] d\phi,$$
$$(3.144)$$

where

$$I_e(m) = -\int_0^1 \frac{mr\left(r^2-1\right) - 2r\left(r^m-1\right)}{(1-r^2)^2} dr, \qquad (3.145)$$

which can be evaluated to give

$$I_e(m) = 1 + \frac{m}{2} \left[\Psi\left(\frac{m}{2} \right) + \gamma - 1 \right], \qquad (3.146)$$

where Ψ denotes the diagamma function, and $\gamma = 0.57722$ is the Euler-Mascheroni constant. Note that in (3.144) no efforts have been made to expand the contact line, apparent contact
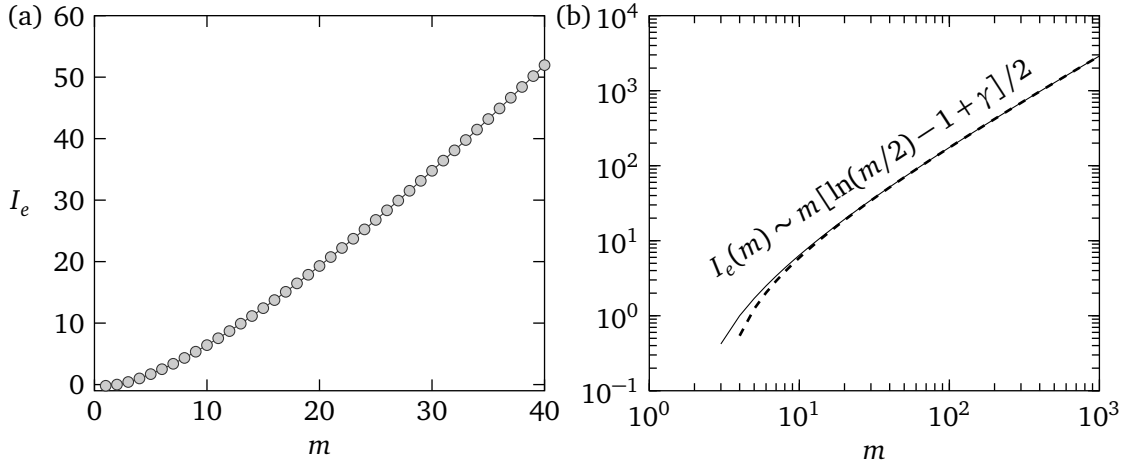
Figure 3.6: Plots of the integrals (3.145) for varying m. (a) The value of I_e for the first 40 harmonics. (b) The large m behaviour of I_e (solid curves) alongside the asymptotics of I_e (dashed curves) where γ is the Euler-Mascheroni constant.

angle, or $\tilde{\beta}_{\text{in}}$ term. Had we done so, the resultant integrals containing terms multiplying $e^{im\phi}$ terms would vanish, rendering the above formulation in the simpler format

$$\dot{v}(t) = -\frac{2\pi\mathcal{E}a_0}{\bar{\vartheta}} \ln\left(\frac{\bar{\vartheta}a_0\tilde{\beta}_{\text{in}}}{2\lambda e^{3/2}}\right), \tag{3.147}$$

which again is reminiscent of the formula derived by Savva *et al.* [53] for negligible gravitational effects. In the regime of weakly perturbed contact lines we expect that (3.147) will provide an acceptable approximation to the full dynamics, however, as we shall see, once evaporation becomes weaker the surface heterogeneity causes larger contact line deformations to emerge, rendering the predictions from (3.147) inaccurate. To remedy this issue one in principle can solve the non-expanded expression (3.144), although, this violates the assumptions put forth in the analysis which relies around perturbations from a nearly circular contact line. Later we will highlight from rather convincing numerical evidence that the full equation (3.144) can indeed be used to predict the dynamics rather well in the the regime that (3.147) fails. Besides the more complicated appearance of (3.144), its implementation is rather straightforward, since the integrals in $I_e(m)$ can be calculated *a-priori* and stored. Figure 3.6 plots values of $I_e(m)$ showing that it grows logarithmically large as m increases. Although the value of I_e grows rather large for higher values of m, we note that this will not impact the dynamics too appreciably since they appear in (3.144) multiplying a_m terms which generally are small.

It is clear, however, that (3.147) will fail when a_0 tends to the critical value

$$a_c = \frac{2\lambda e^{3/2}}{\bar{\vartheta}\bar{\bar{\beta}}_{\text{in}}} = O(\mathcal{K}),$$

(3.148)

in other words, the mean droplet radius is comparable to the kinetic length scale. In this limit (3.144) and (3.147) incorrectly predict that the droplet volume diminishes, meaning these equations are valid for when $\mathcal{K} \ll a_0$. Noteworthy from the evaporation formulas (3.144) and (3.147) is that heterogeneous terms do not appear explicitly, their contributions manifest themselves during the calculation of the inner region variable $\bar{\bar{\beta}}_{\text{in}}$ (or equivalently θ_e if used in replacement of ϑ). Therefore, it is of interest to understand how surface heterogeneity impacts the overall evaporation time for varying strengths of evaporative flux. To extract some insights we allow for surface heterogeneity to remain constant so that we can approximate the dynamics with azimuthal disturbances set to zero. By doing so, we can decouple the equations for $\dot{b}_0(t)$ and $\dot{v}(t)$ to uncover theoretical estimates for the total evaporation time. Using $a_0 = [4v/(\pi\theta_e)]^{1/3}$ in (3.147) allows us to separate the variables into the integral equation

$$t_e = \frac{\bar{\vartheta}^{4/3}}{2(2\pi)^{2/3}\mathcal{E}} \int_0^{v_0} \left\{ v^{1/3} \ln\left[\frac{\bar{\bar{\beta}}_{\text{in}}\bar{\vartheta}^{2/3}v^{1/3}}{\lambda e^{3/2}(2\pi)^{1/3}} \right] \right\}^{-1} dv,$$

(3.149)

where $v_0 = v(0)$ is the initial volume. Since the analysis partaken does not consider the extinction stage, the above integral is considered in the Cauchy principal value sense, and therefore, t_e is merely an estimate of the total evaporation time that holds until the condition that $v(t) < \lambda$ is broken. The integral on the right hand side can be evaluated analytically to obtain

$$t_e = \frac{3\lambda^2 e^3}{2\bar{\bar{\beta}}_{\text{in}}^2 \mathcal{E}} \text{Ei}\left\{ \ln\left[\frac{\bar{\bar{\beta}}_{\text{in}}^2 \bar{\vartheta}^{4/3}v_0^{2/3}}{(2\pi)^{2/3}\lambda^2 e^3} \right] \right\},$$

(3.150)

where

$$\text{Ei}(x) = -\int_{-x}^{\infty} \frac{e^{-y}}{y} dy, \quad x > 0,$$

(3.151)

is the exponential integral. Although (3.150) can be calculated numerically, further progress can be made analytically by using the large argument expansion of the exponential integral $\text{Ei}(x) = e^x/(x-1) + O(e^x x^{-3})$ to give

$$t_e = \frac{3\bar{\vartheta}^{4/3}v_0^{2/3}}{4(2\pi)^{2/3}\mathcal{E}} \ln\left[\frac{\bar{\bar{\beta}}_{\text{in}}\bar{\vartheta}^{2/3}v_0^{1/3}}{(2\pi)^{1/3}\lambda e^2} \right]^{-1},$$

(3.152)
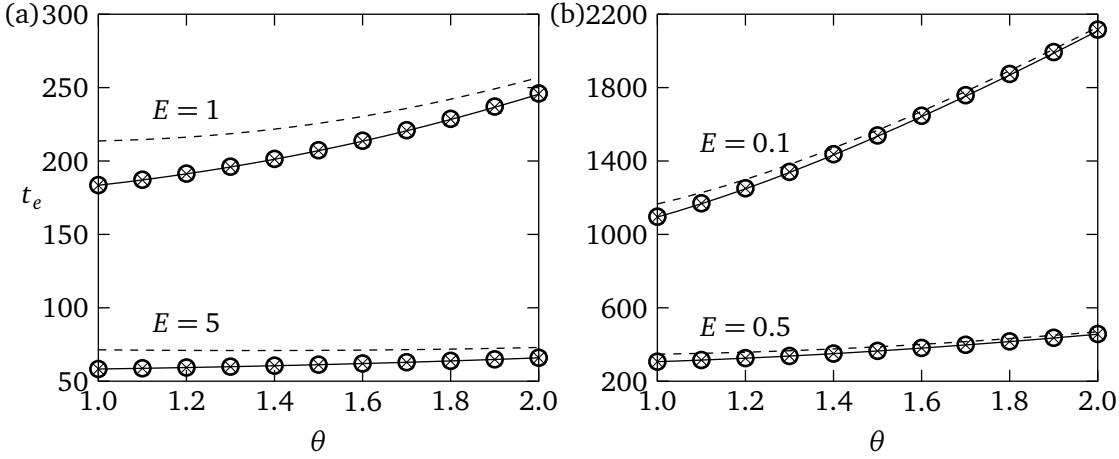
Figure 3.7: Plots of the evaporation time for varying surface heterogeneity when $\lambda = 10^{-3}$, $K = 0.1$, and for values of E exhibited inside the plots. The droplets considered had initial volume $v(0) = 2\pi$ and radius $a(\phi, 0) = 1$. In both cases crosses denote solutions of the full problem, circles are solutions of (3.98) with (3.147), and solid lines and dashed lines are the theoretical predictions (3.152) and (3.154), respectively.

as the estimate of the evaporation time. Applying similar steps we can obtain an estimate of the evaporation time from (3.133) which neglects the presence of the micro-scale details, namely

$$t_e = \frac{3\mathcal{K}^2}{2\mathcal{E}} \left(\text{Ei} \left\{ 2\ln \left[\frac{\bar{\vartheta}^{2/3} v_0^{1/3}}{(2\pi)^{1/3} \mathcal{K}} + 1 \right] \right\} - \text{Ei} \left\{ \ln \left[\frac{\bar{\vartheta}^{2/3} v_0^{1/3}}{(2\pi)^{1/3} \mathcal{K}} + 1 \right] \right\} - \ln(2) \right), \qquad (3.153)$$

which after the large argument expansion becomes

$$t_e = \frac{3\bar{\vartheta}^{4/3} v_0^{2/3}}{4(2\pi)^{2/3} \mathcal{E}} \ln \left[\frac{\bar{\vartheta}^{2/3} v_0^{1/3}}{(2\pi)^{1/3} \mathcal{K} e^{1/2}} \right]^{-1}, \qquad (3.154)$$

in the limit as $\lambda \to 0$.

By solving the full equations (2.51), and the reduced model ((3.98) with (3.147)) we compare to predictions offered by the theoretical predictions (3.152) and (3.154). The result of the computation is displayed in figure 3.7 where ten solutions of the full and reduced problem are compared for values of surface heterogeneity varying between $\theta = 1$ and $\theta = 2$. As heterogeneity increases we observe that the droplet evaporates at slower rates, which can be physically expected since for increasing θ the droplet will admit smaller radii. For smaller values of θ the droplet radius will expand further, and consequently enlarge the area of the free surface, which allows more molecules per unit area of volume to escape than for droplets of smaller radii. For lower values of E the effects of evaporative flux on the inner region dynamics become weaker (see figure 3.3), and therefore heterogeneity plays a more predominant role.
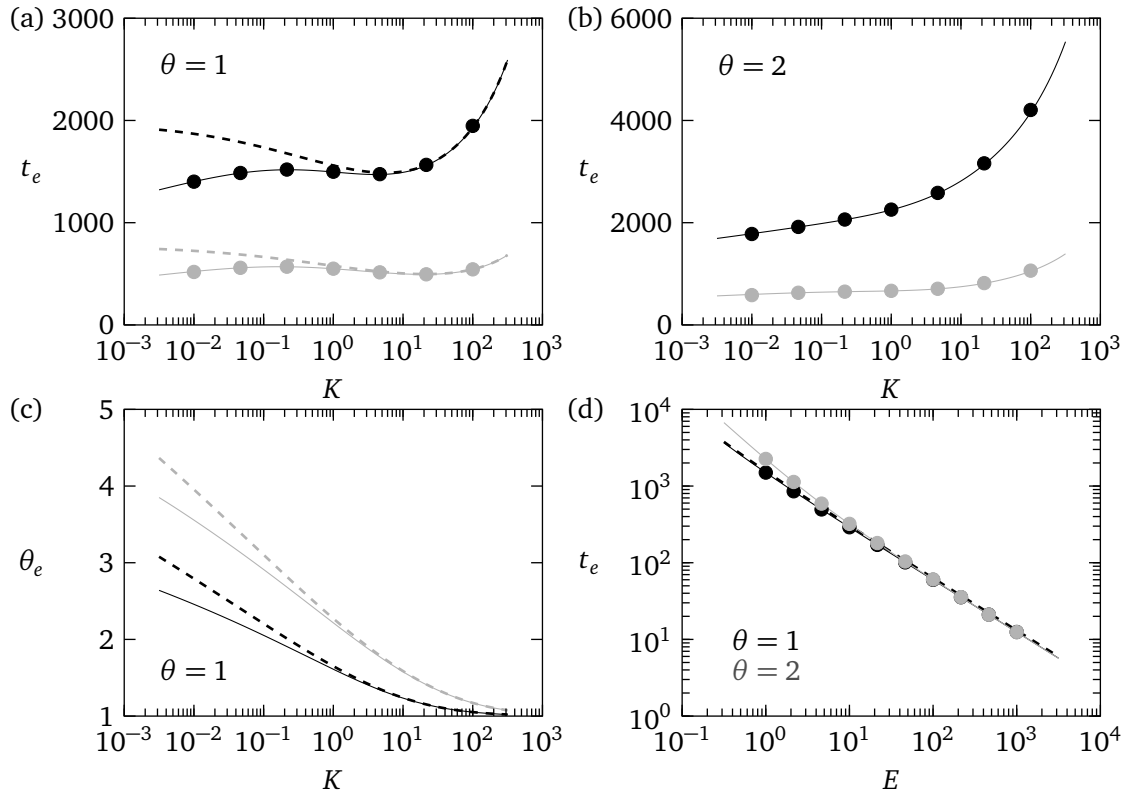
Figure 3.8: Influence of E and K on the evaporation time t_e when $\lambda = 10^{-4}$, $a(\phi, 0) = 1$ and $v(0) = 2\pi$ where in all plots dashed curves show solutions obtained from the Navier slip model (used in [53]), and solid curves are solutions from the slip model considered here. Plots (a) and (b) show t_e for varying K when $\theta = 1$ and $\theta = 2$, respectively, for $E = 1$ (black) and $E = 4$ (grey). The curves correspond to the prediction (3.152), and the circles denote the solution of the full model when $K = 10^{-2n/3}$, for $n = 0, \pm 1, \pm 2$ and ± 3. (c) Plots of the modified angle θ_e for varying K in the same style as (a) and (b). (d) The evaporation time t_e for increasing E where black and grey plots denote $\theta = 1$ and $\theta = 2$, respectively, noting circles denote solutions to the full model with $E = 10^{n/3}$ for $n = 0, 1, 2 \ldots, 9$.

For this reason the total evaporation times can drastically change by varying E and θ. For instance, when $E = 5$ the evaporation time changes by only 13% between $\theta = 1$ and $\theta = 2$, whereas for $E = 0.1$, this jumps to a 93% difference. Noteworthy also from this calculation is the rather excellent agreement between the theoretical prediction (3.152) and the predictions from the full and reduced problems, in contrast, the formulation (3.154) which neglects the inner region contributions performs rather poorly throughout.

Let us also remark on the influence that the parameters E and K have on the total evaporation time. The effect that E has on t_e is rather straightforward, showing a monotonic decrease in t_e as E grows large (see figure 3.8(d)). This is to be expected since for higher superheats the evaporation is enhanced. The effect of K is not particularly intuitive, especially for small K. In the regime of higher K we find that the evaporation times increase, which

can be directly inferred from (3.113) since as $K \to \infty$ we move towards the non-volatile case where $q = 0$. However, t_e does not always increase monotonically (compare, e.g. figures 3.8(a) and (b)), particularly for small values of K. Taking $K \to 0$ is a singular limit for the PDE model we consider, because the resulting singularity in q at the contact line is non-integrable. Thus, a non-vanishing value for K is required, analogously to requiring that $\lambda \neq 0$ to avoid the divergence in the stress. As K becomes smaller, we typically see an increase in the evaporation-modified angles (see figure 3.8(c)). This causes the droplet to spread less, thus making the heat transfer from the substrate to the droplet less efficient. At the same time, reducing K means that the kinetic resistance to evaporation also decreases, which, in principle, should promote evaporation. Hence, it is the competition of these two effects that dictate the dynamics for small K and the extent at which evaporation is enhanced or inhibited is dependent on the model under consideration, as well as other system parameters, e.g. θ (see figures 3.8(a) and (b)).

For example, it appears that for the Navier slip model, where θ_e is more strongly enhanced for smaller K (see figure 3.8(c)), evaporation times increase compared to the model considered here which predicts a slight decrease in t_e (compare the solid and dashed curves in figures 3.8(a) and (c)). For larger values of K, however, both models converge towards the same values of t_e. This model-dependent effect of K for values of K up to $O(1)$ has not been previously reported in the literature and it will be interesting to pursue this experimentally as a means to identify the most appropriate slip model for the dynamics. At the same time, we need to acknowledge the difficulty in performing such an experiment, as this would correspond to changing the substrate and/or the liquid used, and, as a result, other effects may come into prominence.

The derivation of the evolution equation for $v(t)$ concludes the analysis for evaporating droplets. Strictly speaking from an asymptotic point of view, the analysis we have undertaken only pertains for the spreading stage, meaning a composite expansion would have been required to include all relevant time-scales, like mentioned in section 3.1.3 (see Saxton *et al.* [164]). Later, in chapter 5, we argue that such an analysis can be avoided by presenting rather compelling numerical evidence to support our assumptions, including those that led to the derivation of (3.144).

3.4   Surface Roughness

To ensure analytical tractability, previously explored cases in this thesis considered substrates that were perfectly flat ($\eta(x,y) = 0$) so that the contact line became distorted due to chemical heterogeneities only. In 2D, Savva & Kalliadasis [56] included substrate topographies in their asymptotic analysis. Throughout this section we will form the preliminary basis of including the effects of substrate topography for fully 3D droplets.

The asymptotic treatment herein presented assumes that $\eta(x,y)$ is sufficiently weakly varying to avoid the substrate features perforating the free surface of the droplet, and occur at length-scales much longer than slip, meaning that their presence can be neglected from the inner region calculations (see also Savva & Kalliadasis [56]). This implies that the inner region analysis presented in section 3.2 can be reused provided that we maintain the quasistatic assumptions of slow moving contact lines and centroid motions. Therefore, the task is to modify the outer region dynamics accordingly to incorporate $\eta(x,y)$ into the analysis, which, is to be combined with the inner region slope (3.47) through the matching criteria previously presented.

To perform preliminary progress into a rather algebraically cumbersome problem, we use the simplification that surface roughness terms appear in the leading-order equations only. In essence, this renders the derivations for the corrections of the azimuthal disturbances identical to the outer region analysis in 3.2.2. This allows us to admit significant simplifications to the analysis, meaning we only need to consider finding h_0, and the corresponding apparent contact angle ϑ, so that (3.98) can be used as the reduced model in this circumstance. In principle, a full asymptotic treatment would require the surface roughness terms to be retained in the next-to-leading-order equations, however, later we will argue with numerical comparisons to the full equations that such an assumption can be made. Therefore, forming the basis of future study which will retain the additional terms.

In the outer region we deduce the following leading-order problem

$$\nabla^2 \left[h_0(r,\phi,t) + \eta(r,\phi,t) \right] = \tilde{p}(t), \tag{3.155a}$$

$$h_0(1,\phi,t) = 0, \tag{3.155b}$$

$$\int_0^{2\pi} \int_0^1 r a^2 h_0 \, \mathrm{d}r \, \mathrm{d}\phi = v(t), \tag{3.155c}$$

where $\tilde{p}(t)$ is found through the volume constraint. To facilitate the development of a

perturbative series solution we consider the recasting $\tilde{h}_0 = h_0 + \eta$ which yields the modified system

$$\nabla^2 \tilde{h}_0(r, \phi, t) = \check{p}(t), \tag{3.156a}$$

$$\tilde{h}_0(1, \phi, t) = \eta(1, \phi, t), \tag{3.156b}$$

$$\int_0^{2\pi} \int_0^1 r a^2 \tilde{h}_0 \, dr \, d\phi = v(t) + \tilde{v}(t), \tag{3.156c}$$

where

$$\tilde{v}(t) = \int_{\Omega(t)} \eta(\boldsymbol{x}) \, d\boldsymbol{x}, \tag{3.157}$$

is the volume under the surface inside the wetted region. Therefore considering the expansions

$$\tilde{h}_0(r, \phi, t) = \sum_{m=0}^{M} \tilde{h}_{0,m}(r, t) e^{im\phi}, \tag{3.158}$$

$$\eta(r, \phi, t) = \sum_{m=0}^{M} \eta_m(r, t) e^{im\phi}, \tag{3.159}$$

we formulate the two differential equations

$$P_0 \tilde{h}_{0,0} = b_0^2 \check{p}(t), \tag{3.160}$$

$$P_m \tilde{h}_{0,m} = \frac{1}{b_0 r} \partial_r \left(2 r \partial_r \tilde{h}_{0,0} - m^2 h_{0,0} \right), \tag{3.161}$$

which are easily solved to obtain

$$h_0(r, \phi, t) = \hat{p} \left(r^2 - 1 \right) + \eta_0(1) - \eta_0(r) + \sum_{m=1}^{M} \left[\frac{2 a_m \hat{p} \left(r^2 - r^m \right)}{b_0} + r^m \eta_m(1) - \eta_m(r) \right] e^{im\phi}, \tag{3.162a}$$

where

$$\hat{p} = \frac{2 \left[\pi \eta_0(1) b_0^2 - \tilde{v} - v \right]}{\pi b_0^2}, \tag{3.162b}$$

and noting that the time dependence has been dropped for notational simplicity. Also, it is easy to see that in (3.162a) we can directly recover the leading-order solution (3.57) by substituting $\eta_m = 0$ and $\tilde{v} = 0$, as expected. The apparent contact angle is determined by taking the normal derivative of (3.162a), yielding

$$\vartheta = -\frac{2\hat{p}}{b_0} + c_0(1) + \sum_{m=1}^{M} \left[\frac{2 a_m \hat{p} \, (m-1)}{b_0^2} - \frac{m \eta_m(1)}{b_0} + c_m(1) \right] e^{im\phi}, \tag{3.163}$$

where

$$\sum_{m=0}^{M} c_m(1) e^{im\phi} = \frac{1}{a} \left. \partial_r \eta \right|_{r=1} = \left. \left(\partial_x \eta \cos \phi + \partial_y \eta \sin \phi \right) \right|_{r=1}. \tag{3.164}$$

From (3.162a) one can see that from the next-order equation

$$\nabla \cdot \left(h_{0,0}^3 \nabla \nabla^2 h_1 \right) = q + \frac{1}{b_0} \left[\mathrm{Re}\left(\dot{b}_1 \mathrm{e}^{\mathrm{i}\phi} \right) + r \partial_t a \right] \partial_r h_{0,0} - \partial_t h_0, \qquad (3.165)$$

terms of $O(\dot{a}_0 \eta_m)$ and $O(\dot{a}_0 c_m)$ arise from the right hand side. The inclusion of such terms grows rather unwieldy, therefore, to justify their omission we assume that they are smaller than the $O(\dot{a}_m)$ terms. As explained previously, this eliminates all surface roughness terms from the treatment of (3.165) meaning the dynamics of η appear through the apparent contact angle alone. In calculation of the reduced model (3.98) one can either use the analytically determined angle (3.163), or ϑ can be determined using the boundary integral method as explained in chapter 4. In future chapters the merits of both approaches to finding ϑ will be explained in more detail, and more importantly, the numerical evidence to support the assumptions made here will be presented.

3.5 Summary

In the limit of vanishingly small slip lengths, small contact line velocities and slow mass transfer rates, the method of matched asymptotic expansions was utilised to develop lower-dimensional models which determine approximate solutions of their corresponding full systems in a number of settings. The models obtained here bear resemblance to (1.6) noting that we derive corrections to this equation of $O(1/|\ln(\lambda)|^2)$ as $\lambda \to 0$.

The investigation was initialised with 2D droplets spreading over horizontal and flat substrates where gravitational effects are negligible. Here, the outcome of the analysis was a pair of evolution equations to approximate (2.53), and holds for $\dot{a}_{\pm} = O(1/|\ln(\lambda)|)$ as $\lambda \to 0$. This analysis was extended to the 3D geometry by considering contact lines that are weakly perturbed so that evolution equations for the Fourier coefficients of the contact line could be determined. By appropriately modifying the analysis of the micro-scale region and determining an evolution equation for the droplet volume, we extended the discussion to include mass loss by evaporation where the droplet evaporates into its own vapour. Finally, preliminary progress was made into substrates with topographical changes by appropriately modifying the leading-order behaviours and limiting the model to cases where additional surface roughness terms can be treated as higher-order corrections to the dynamics.

— Chapter 4 —

Numerical Methods

As highlighted in chapter 1, a large number of numerical methods have been employed in the literature to study the motion of the contact line. Being a coupled macro-/micro-scale problem renders this task highly non-trivial, as one typically has to account for both scales when performing numerical simulations. Molecular dynamics simulations are becoming a promising avenue of numerical methodologies which are primarily used to understand the microscopic details of fluid motion, however, it is apparent that such techniques are rather expensive for macroscopic simulations [176]. Hybrid methodologies have been proposed in which molecular dynamics are used in the micro-scale, and a continuum model in the macro-scale where information between the two scales is interchanged through an overlap region [177, 178].

Many other common numerical methods to study fluid motion have also been used, such as finite element methods [179–181] and finite difference methods [182, 183] (see also the review by Sui *et al.* [184]). Volume-of-fluid methods that consider direct numerical simulation of the Navier-Stokes equations have also been employed [185–187]. Although no-slip is assumed in this method, the stress singularity of the moving contact line is alleviated through the means of numerical slip which scales with the size of the mesh spacing (usually up to $O(10^{-3})$). This method conserves mass and allows for topological changes in a very natural way, however, it typically requires adaptive mesh refinement to accurately capture solutions [188]. Lattice Boltzmann methods are becoming increasingly popular in the literature to describe droplet dynamics due to their flexibility in describing complex geometries [189, 190], such as considering droplets in T-shape micro-channels [191]. Although expensive computationally, this method is highly parallelisable on supercomputing clusters and has been used to describe a large array of situations, such as droplets interacting with striped substrates [192, 193], droplets evaporating on sinusoidally varying topographical substrates [150], and

droplet collision dynamics [194]. Current computing capabilities limit lattice Boltzmann methods to mesoscale dynamics and typically resolve length-scales up to $O(10^{-2})$, meaning that the microscopic details may not be sufficiently accounted for.

Long-wave models, such as the ones employed here, generally show favourable agreement with the Navier-Stokes equations within their regime of applicability [195], and have been used to solve for a variety of situations [23, 157, 158]. While typically in the literature length-scales are resolved up to $O(10^{-3})$, there are cases where this may become computationally difficult, for instance, when considering simulations of multiple droplets [196, 197]. Although these models are beneficial since it involves solving a single evolution equation rather than directly simulating the Navier-Stokes equations, it is limited in the sense that the liquid considered is thin, meaning wetting on hydrophobic substrates cannot be captured. In addition, due to the long-wave approximation, the true thermodynamic equilibrium is only approximately captured [198].

Perhaps the motion of the contact line is most conveniently treated numerically by using the precursor film model, which assumes that there is no actual contact line, but rather a very thin layer of fluid ahead of the contact line front [40]. Precursor film models can naturally describe a range of phenomena, such as arbitrarily distorted contact lines and droplet coalescence/splitting. However, precursor film models are typically computed on uniform meshes, meaning that it is not easy to capture the dynamics across multiple scales. This can be alleviated by using an adaptive meshing technique, however, this renders the implementation rather non-trivial (see Savva & Kalliadasis [57]). Numerically implementing problems with actual contact lines and a slip model is different in nature to the precursor film model as we have a free boundary problem. Resolving the finer details near the contact line also requires the use of dense meshes, but they are easier to implement than the adaptive one required for the precursor film model, since, as we shall see, they can be captured by a non-moving spatial grid. We note, however, that slip models suffer in the sense that topological changes cannot be captured with the implementation herein presented. Here, we opt for a slip model solely to avoid the numerical intricacies of the precursor film model, noting that the analysis we derived in the previous chapter likewise apply to the precursor film model, should a change in the slip-length to a parameter related to the film thickness be introduced (as shown by Savva & Kalliadasis [57]). The numerical methods in this thesis are primarily used to assess the validity of the theory, therefore the choice of considering a slip model is not a drastic one.

The approach we follow here closely follows the appendix of Savva & Kalliadasis [56] who consider 2D droplets, noting we extend upon this study to include droplets of variable mass. Savva & Kalliadasis describe how to treat the moving boundary condition (2.53b) and at the same time resolve the sharp boundary layers in $\partial_y h$ as $\lambda \to 0$. These methodologies adopt the *pseudospectral collocation method* which is described by Trefethen [152] and is primarily used to avoid the Runge phenomenon which occurs when fitting a polynomial through the values of a smooth function defined on the interval $[-1, 1]$ with an equally spaced grid; thus allowing us to obtain spectrally accurate solutions throughout the entire computational domain with a small number of collocation points. The second advantage of this approach is the natural clustering of collocation points near the contact line of the droplet, allowing us to pick up finer details in this region with a smaller number of collocation points than, say, a equispaced grid with a finite difference approach. This method has previously been successful in a large number of studies to describe droplet spreading in the 2D setting (see, e.g. [56–60]). These methods are extended here to solve the 3D model (2.51) which considers the inverse linear slip model, rather than the Navier-slip model considered by Savva & Kalliadasis [56]. The development of this scheme has been reported in [61] for droplets of constant mass spreading on horizontal, flat and chemically heterogeneous substrates, however, here we describe the generalised scheme to account for the case when additional effects are included.

We also describe a *hybrid method* which follows the framework presented by Glasner [153] to provide an attractive compromise between the low-order theory derived in the previous chapter, and full-scale simulations. The method relies on an evolution equation for the contact line which depends on the apparent contact angle, which is computed by using the boundary integral method. However, unlike Glasner, we will be utilising the asymptotic models of chapter 3 instead of some expression imposed in an ad hoc manner. As we shall see in chapter 5, an accurate extraction of this angle is highly desirable both to improve the accuracy of the theoretical predictions and to explore configurations where progress with purely theoretical tools proves to be difficult. The boundary integral method is arguably the most appropriate to use, since the solution of Laplace's equation is reduced to solving integral equations along the domain boundary, the contact line, which can then be straightforwardly used to obtain the solution across the entire wetted region. This results in a considerably smaller system compared to discretising the whole domain. Another advantage is that the output of the method is directly the apparent contact angle, which can be used to evaluate the velocity of

the contact line using, e.g. (1.6). We presented some preliminary work with this approach in [61] where it was shown that the hybrid approach enhanced the accuracy of the low-order theory for a small computational overhead.

4.1 Numerically Solving the Governing Models

As highlighted previously, numerically solving the models (2.51) and (2.53) is highly non-trivial, and requires careful consideration to formulate the appropriate numerical methodologies and ensure accurate computations. Throughout this section, we present methods to solve the 2D model (2.53), and the 3D model (2.51), which are later to be contrasted in chapter 5 with the predictions from the theoretical methods shown in chapter 3.

4.1.1 2D Geometries

To treat the free boundary problem in 2D, we introduce a series of transformations to yield a fixed boundary problem. The change of variables (2.66) leads to (2.67), including the difficult to impose moving boundary condition (2.67b). From observing this condition it is clear that $\partial_s^3 h$ must be singular as the contact points are approached so that $h \partial_s^3 h$ is finite. Therefore, to remedy the inability of conventional discretisation schemes to discretise (2.53b) as the contact points are approached (as $s \to \pm 1$) we integrate the transformed PDE (2.67a) once with respect to s, calling

$$H_n(s,t) = \int_{-1}^{s} h(\tilde{s},t)\,\mathrm{d}\tilde{s}. \tag{4.1}$$

Therefore, we recast the system (2.67) from a problem in $h(s,t)$ to one in $H_n(s,t)$

$$\partial_t H_n + \frac{\dot{d}}{d} H_n - \frac{\dot{a}_+(1+s) + \dot{a}_-(1-s)}{2d} \partial_s H_n$$
$$+ \frac{1}{d^4}\left[(\partial_s H_n)^2 (\partial_s H_n + \lambda)\,\partial_s^4 H_n\right] = \int_{-1}^{s} q(\tilde{s},t)\,\mathrm{d}\tilde{s}, \tag{4.2a}$$

$$H_n(1,t) = \frac{A}{d}, \tag{4.2b}$$

$$H_n(-1,t) = 0, \tag{4.2c}$$

$$\partial_s H_n\big|_{s=\pm 1} = 0, \tag{4.2d}$$

$$\mp \partial_s^2 H_n\big|_{s=\pm 1} = d\theta_{\pm}. \tag{4.2e}$$

Note that with this formulation we circumvent the requirement of conditions (2.53b) since using the integral constraint (2.67e) gives two new conditions on $H_n(s,t)$, namely (4.2b) and

(4.2c). This recasting also allows us to avoid the direct evaluation of $h\partial_s^3 h$ which becomes singular as $s \to \pm 1$, and additionally has the advantage that mass is exactly conserved since it enters the problem through the boundary conditions.

Chapter 14 of Trefethen [152] describes how to solve fourth-order problems with homogeneous boundary conditions. Therefore, in order to develop a spatial scheme consistent with the methods presented in [152], we cast our problem in the form $H_n = H_h + H_p$, where H_h satisfies homogeneous boundary conditions and H_p is a polynomial which satisfies conditions (4.2b), (4.2c) and (4.2d). A polynomial that satisfies these conditions takes the form

$$H_p = \frac{A}{4d}\left(2 + 3s - s^3\right), \tag{4.3}$$

which transforms the PDE (4.2a) in H_n to one in H_h

$$\partial_t H_h + \frac{\dot{a}_+}{2d}\left[H_h - (1+s)\partial_s\left(H_h + H_p\right)\right] - \frac{\dot{a}_-}{2d}\left[H_h + (1-s)\partial_s\left(H_h + H_p\right)\right]$$
$$= \int_{-1}^{s} q(\tilde{s}, t)\,\mathrm{d}\tilde{s} - \frac{\dot{A}H_p}{A} - \frac{1}{d^4}\left[\partial_s\left(H_h + H_p\right)\right]^2\left[\partial_s\left(H_h + H_p\right) + \lambda\right]\partial_s^4 H_n, \quad (4.4)$$

which is in an appropriate form for spatial discretisation using a Chebyshev collocation approach.

4.1.1.1 Numerical Scheme

To solve (4.4) we discretise spatially using $N_s + 1$ Chebyshev collocation points defined according to

$$s_j = \cos\left(\frac{j\pi}{N_s}\right), \tag{4.5}$$

which lie in the interval $[-1, 1]$ with natural clustering towards ± 1, and resolve the boundary layers in $\partial_x h$. As $\lambda \to 0$ the boundary layers in $\partial_x h$ become increasingly narrow, and thus, the points (4.5) fail to resolve these boundary layers unless N_s is sufficiently large, which in turn results in slower computations. Instead of doing this, we resolve these layers whilst maintaining a small number of points by introducing the mapping

$$\bar{s} = \frac{\sin\left[(\pi - \tilde{\alpha})s/2\right]}{\cos\left(\tilde{\alpha}/2\right)}, \tag{4.6}$$

which accumulates more collocation points towards $s = \pm 1$ depending on the smallness of the constant $0 < \tilde{\alpha} \ll 1$ (see figure 4.1 for a visualisation). As a consequence of this mapping the features in the rest of the spatial domain are resolved less, although, we expect that the
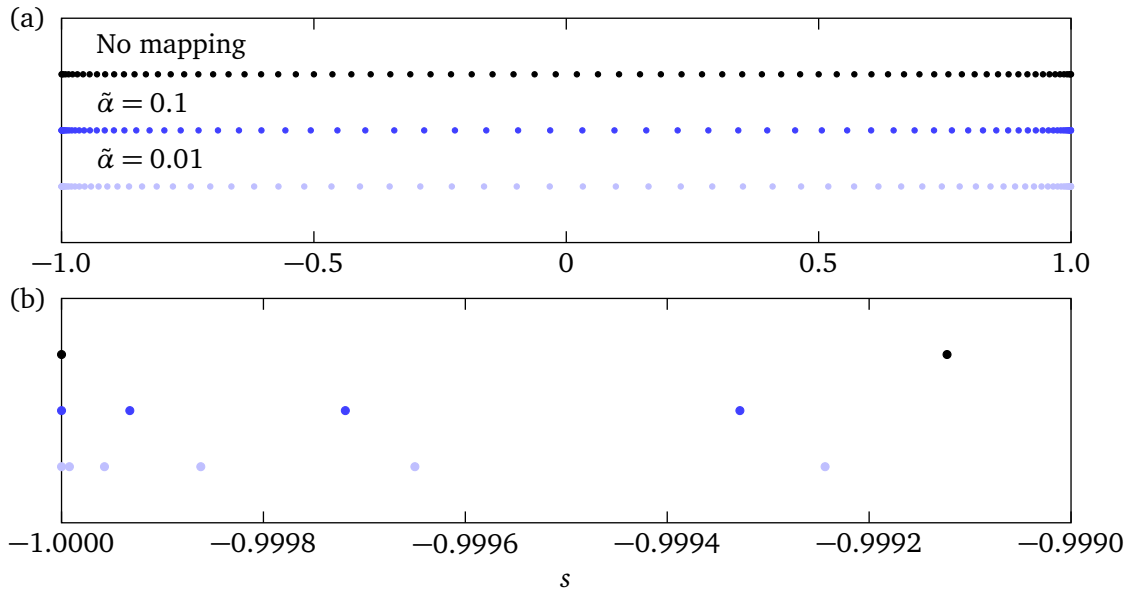
Figure 4.1: Two plots displaying the effect of the collocation point mapping (4.6) through three different cases: no mapping, $\tilde{\alpha} = 0.1$, and $\tilde{\alpha} = 0.01$. (a) Highlights the full range of $s \in [-1, 1]$ and (b) shows a zoomed in portion near $s = -1$. In each case $N_s = 75$ points were used.

droplet shape will generally remain parabolic and will not require many collocation points to be adequately captured. If, however, localised variations across the free surface are to be expected, we have the flexibility to either increase N_s or slightly increase $\tilde{\alpha}$ to better resolve the features in the bulk.

For fixed N_s we can approximate $f(s)$ as a polynomial $P_{N_s}^{2D}(s)$ of degree N_s using the following series representation

$$P_{N_s}^{2D}(s) = \sum_{j=0}^{N_s} f(s_j) l_j(s), \tag{4.7}$$

where $l_j(s)$ are Lagrange polynomials of degree N_s defined as

$$l_j(s) = \frac{\displaystyle\prod_{n=0, n \neq j}^{N_s} (s - s_n)}{\displaystyle\prod_{n=0, n \neq j}^{N_s} (s_j - s_n)}, \tag{4.8}$$

with the property that $l_j(s_n) = \delta_{jn}$ where δ_{jn} is the Kronecker delta. It is known, however, that calculations with Lagrange polynomials are both costly and numerically unstable. To circumvent these issues, $P_{N_s}^{2D}$ can alternatively be written in terms of the barycentric formula

(see Baltensperger *et al.* [199] and Berrut & Trefethen [200])

$$p_{N_s}^{2D}(s) = \frac{\displaystyle\sum_{j=0}^{N_s} \frac{\omega_j}{s-s_j} f(s_j)}{\displaystyle\sum_{j=0}^{N_s} \frac{\omega_j}{s-s_j}}. \tag{4.9}$$

Here ω_j are the barycentric weights which are grid dependent, and are given for the points (4.5) as

$$\omega_j = (-1)^j \tilde{\omega}_j, \quad \text{where} \quad \tilde{\omega}_j = \begin{cases} \dfrac{1}{2}, & j=0 \text{ and } j=N_s, \\[2mm] 1, & j=1,2,\ldots,N_s-1, \end{cases} \tag{4.10}$$

Knowing these weights we can use (4.9) to compute the values of $p_{N_s}^{2D}(s)$ everywhere in the domain, as well as the associated differentiation matrices.

To compute the derivatives of h with respect to s we follow the methods presented in chapter 14 of [152], in other words we use $\tilde{p}_{N_s}^{2D}(s)$ as a polynomial interpolant approximating h with $N_s + 1$ discrete mesh points in the form

$$\tilde{p}_{N_s}^{2D}(s) = \sum_{j=0}^{N_s} \frac{1-s^2}{1-s_j^2} l_j(s) H_h(s_j,t), \tag{4.11}$$

which satisfies the homogeneous boundary conditions on H_h. Therefore the differentiation matrices are formed by differentiating (4.11), and using the differentiation matrices based on (4.9) for the derivatives of $l_j(s)$.

The choice of polynomial interpolant automatically satisfies the boundary conditions (4.2b), (4.2c) and (4.2d). Hence, the PDE (4.4) and contact angle conditions (4.2e) are implemented by casting them in the form

$$A\frac{\mathrm{d}U}{\mathrm{d}t} = F(U,t), \tag{4.12}$$

where U is a column vector containing the unknown values of $H_h(s_j,t)$ and $a_{\pm}$, and A is a mass matrix formed from discretising the left hand side of (4.4), which is singular as it includes two zero rows due to the implementation of (4.2e) (which do not depend on $\dot{a}_{\pm}$). The right hand side, F, is the discretised form of the right hand side of (4.4) at the interior points, noting that the last two components are used to implement (4.2e). Time-stepping is performed by using the stiff ODE solver `ode15s` in MATLAB, where the singularity in the mass matrix A is accounted for by treating the resulting system as a differential algebraic equation.

4.1.1.2   Initial Condition

To initialise the PDE solver for given contact points, area, and local contact angles we require a shape for $h(s,0)$, and consequently $H_h(s,0)$. We wish for $h(s,0)$ to resemble the parabolic shape (3.15) which describes the quasi-static thickness in the bulk, whilst satisfying the contact angle constraint (2.67d) which (3.15) does not satisfy. Therefore, we use the modified shape

$$h(s,0) = \left[\chi + \frac{\psi_+(1-s) + \psi_-(1+s)}{1 + \epsilon^{-1}(1-s^2)} \right] h_0(s,0), \tag{4.13}$$

where $0 < \epsilon \ll 1$, $\psi_\pm$ are to be determined through use of the contact angle constraint (2.67d), and $\chi \approx 1$ is found using the area constraint (2.67e). In this manner, (4.13) has boundary layers of width $O(\epsilon)$ that allows the transition from the equilibrium angle at the contact points to the parabolic shape in the bulk. Strictly speaking, another form of the initial condition could be used since the relaxation times to quasi-steady dynamics occurs within $t = O(10^{-1})$, which is much shorter than the average simulation length (see appendix C). However, we choose the shape (4.13) simply because it provides a fair comparison to the theory presented in chapter 3.

Using the leading-order shape (3.15) alongside conditions (2.67d) yields

$$\psi_\pm = \frac{2d(0)^2 \theta_\mp - 3A(0)\chi}{6A(0)}. \tag{4.14}$$

To determine the constant χ we use (2.67e), which after solving a linear equation gives

$$\chi = \frac{1 + \dfrac{3\epsilon(\theta_+ + \theta_-)}{4\vartheta} \left[\dfrac{\epsilon}{\sqrt{1+\epsilon}} \tanh^{-1}\left(\dfrac{1}{\sqrt{1+\epsilon}} \right) - 1 \right]}{1 + \dfrac{3\epsilon}{2}\left[\dfrac{\epsilon}{\sqrt{1+\epsilon}} \tanh^{-1}\left(\dfrac{1}{\sqrt{1+\epsilon}} \right) - 1 \right]}. \tag{4.15}$$

Therefore, to formulate the final initial condition for the solver we consider the form

$$H_h(s,0) = \int_{-1}^{s} h(\tilde{s},0)\,d\tilde{s} - \frac{A(0)}{4d(0)}\left(2 + 3s - s^3 \right), \tag{4.16}$$

where the above integral can be determined analytically to give

$$\begin{aligned}
\int_{-1}^{s} h(\tilde{s},0)\,d\tilde{s} = {} & \frac{d\vartheta(1+s)}{12}\left\{ 3\epsilon\left[(\psi_- - \psi_+)s + 3\psi_+ + \psi_- \right] + 2\chi(1+s)(2-s) \right\} \\
& - \frac{\epsilon^2 d\vartheta(\psi_+ + \psi_-)}{2\sqrt{1+\epsilon}}\left[\tanh^{-1}\left(\frac{s}{\sqrt{1+\epsilon}} \right) + \tanh^{-1}\left(\frac{1}{\sqrt{1+\epsilon}} \right) \right] \\
& \qquad\qquad - \frac{\epsilon^2 d\vartheta(\psi_+ - \psi_-)}{4}\ln\left(\frac{1+\epsilon-s^2}{\epsilon} \right), \quad (4.17)
\end{aligned}$$

where d and ϑ are taken at time $t = 0$. Figure 4.2 presents a few initial conditions for varying ϵ, showing the gradual decay to the parabolic formulation (4.13) as $\epsilon \to 0$, in other words $h(x,0) \to h_0(x,0)$. For the purpose of our simulations we use the value $\epsilon = 0.01$.
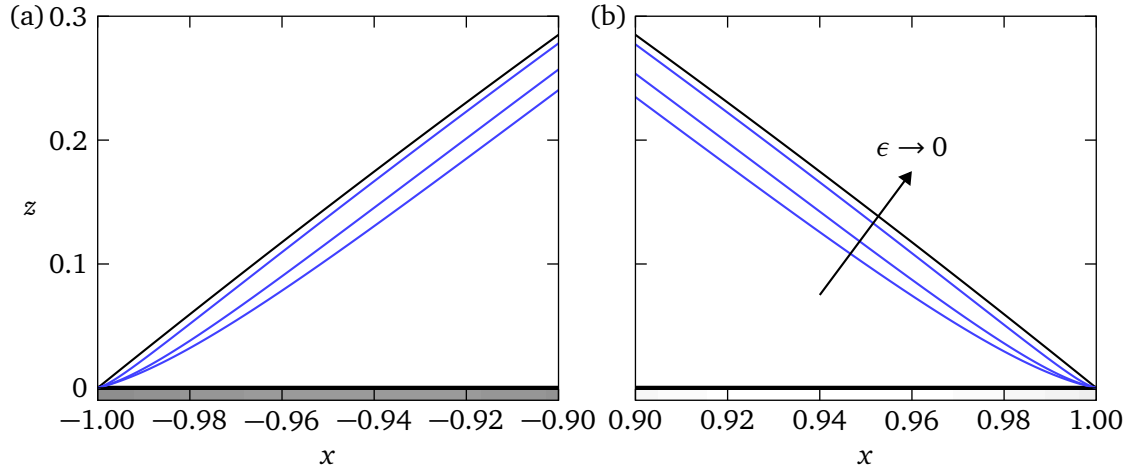
Figure 4.2: Two plots highlighting different initial conditions using equation (4.13) with $a_\pm(0) = \pm 1$ and $A(0) = 2$. The substrate is shaded according to $\theta(x) = 1 + 0.2\cos(10x) + 0.1\sin(5x)$ where darker values correspond to higher contact angles. Plots (a) and (b) represent zoomed in snapshots of the left and right contact points, respectively, where blue curves represent the initial conditions with $\epsilon = 0.1, 0.05, 0.01$, and the black curves depict the parabolic shape (3.15).

4.1.2 3D Geometries

The approach presented in the previous section cannot be easily generalised to the 3D case if the Navier slip model is used. For this reason, we used the inverse linear slip model to get the problem (2.56). During the implementation phase of (2.56) we found that the direct collocation scheme caused some issues with mass conservation where the droplet would lose or gain 1% in its total volume by the time equilibrium was reached. To mitigate this issue we multiplied (2.56a) by r, and integrated over the radial direction which yields the transformed equation

$$\int_0^r \tilde{r}\partial_t h \, d\tilde{r} - \frac{1}{a}\int_0^r \tilde{r}\left[\dot{x}_c \cos\phi + \dot{y}_c \sin\phi + \tilde{r}\partial_t a + \frac{\partial_\phi a}{a}(\dot{x}_c \cos\phi - \dot{y}_c \sin\phi)\right]\partial_{\tilde{r}}h \, d\tilde{r}$$
$$+ \frac{\dot{x}_c \sin\phi - \dot{y}_c \cos\phi}{a}\int_0^r \partial_\phi h \, d\tilde{r} + \frac{1}{a^2}\int_0^r \partial_\phi\left[h\left(h^2 + \lambda^2\right)G_2\right]d\tilde{r}$$
$$+ \frac{1}{a^2}h\left(h^2 + \lambda^2\right)G_1 = \int_0^r \tilde{r}q \, dr, \quad (4.18)$$

noting that the problem is now third order in r. By applying this modification we reduced the mass losses/gains between the more acceptable range of 0.003% to 0.01%.

Hence, we are solving a coupled PDE problem for $h(r,\phi,t)$, $a(\phi,t)$, $x_c(t)$ and $y_c(t)$ which are determined through a solution of equations (4.18), (2.62) and (2.65) subject to the conditions (2.56b) and (2.56c), noting that in the case of undetermined fluxes we must

supply an additional ODE for droplet volume, $v(t)$, by using (2.56d).

4.1.2.1   Numerical Scheme

To formulate the numerical scheme for 3D droplets we base our approach on the methods presented in section 4.1.1.1. Namely, we solve spatially using the pseudospectral collocation method, where here we discretise on the polar domain $0 \leq r \leq 1$ and $0 \leq \phi < 2\pi$ using the tensor product grid, which is created by using one-dimensional grids in each direction.

The azimuthal coordinates are discretised using a Fourier collocation method which defines equispaced points according to

$$\phi_j = \frac{2\pi j}{N_\phi}, \quad j = 0, 1, \ldots, N_\phi - 1, \tag{4.19}$$

where N_ϕ is an even number typically of $O(100)$ to account for sharply varying heterogeneities present across the substrate (either chemical or topographical). The differentiation matrices for this mesh can be deduced using the descriptions presented by Trefethen [152]. Quadrature azimuthally is performed using periodic trapezoidal rule which for smooth periodic functions converges exponentially (see Davis & Rabinowitz [201]).

The spatial discretisation in the radial direction deserves special attention due to the narrow boundary layers in $\partial_r h$ near the contact line and the presence of $1/r$ and $1/r^2$ terms in the Laplacian operator (2.60) which results in singularities when discretising at the origin (at $r = 0$). This issue can be alleviated through pole conditions which are obtained from the asymptotics of the solution as $r \to 0$, and generally are problem dependent (see, e.g. Gottlieb & Orszag [202], Huang & Sloan [203]). To avoid such conditions we utilise a spectral collocation approach based on the Chebyshev-Gauss-Radau points which bypasses including a node at the origin, and defines N_r nodes in the interval $(-1, 1]$ using

$$x_j = \cos\left(\frac{2\pi j}{2N_r - 1}\right), \quad j = 0, 1, \ldots, N_r - 1. \tag{4.20}$$

Similar to the discretisation in 2D we map more points towards the contact line using

$$\bar{x}_j = \frac{(1 - \tilde{\alpha})\left(1 - x_j^2\right)}{2} + x_j, \tag{4.21}$$

where the smaller values of $0 < \tilde{\alpha} \ll 1$ push more points towards $x_j = 1$ (i.e. the contact line of the drop). Finally, these points are mapped to the interval $(0, 1]$ using $r_j = (\bar{x}_j + 1)/2$ to form the radial discretisation. Typically we find that using $N_r = 40$ and $\tilde{\alpha} = 0.01$ is satisfactory

for capturing accurate simulations with slip length $\lambda = 10^{-4}$ or longer. For fixed N_r we use the following series representation

$$p_{N_r}^{3D}(x) = \sum_{j=0}^{N_r-1} f(x_j) l_j(x), \tag{4.22}$$

which approximates the smooth function $f(x)$ as a polynomial, noting the barycentric weights ω_j in (4.9) now change to

$$\omega_j = \begin{cases} \dfrac{1}{2}, & j = 0 \\ (-1)^j \cos\left(\dfrac{\pi j}{2N_r - 1}\right), & j = 1, 2, \ldots, N_r - 1 \end{cases}, \tag{4.23}$$

which are calculated using the method introduced by Wang *et al*. [204]. Thus, knowing these weights we can use (4.9) to compute the values of $P_{N_r}^{3D}(x)$ everywhere in the domain, as well as the associated differentiation matrices (see Baltensperger *et al*. [199]).

The differentiation matrices based on (4.9) are utilised when computing directly the derivatives of P with respect to r. To compute the derivatives of h with respect to r, we constructed specialised differentiation matrices that explicitly account for the boundary conditions of the problem, (2.56b) and (2.56c). Working on the domain $(-1, 1]$, assuming that $h'(1)$ is known and that $h(1) = 0$ (note that we have suppressed the dependence on ϕ and t for notational simplicity; primes denote differentiation with respect to x), we can utilise $\tilde{p}_{N_r}^{3D}(x)$ as a polynomial interpolant approximating h with N_r discrete mesh points in the form

$$\tilde{p}_{N_r}(x) = l_0(x)(x-1)h'(1) + \sum_{j=1}^{N_r-1} \frac{1-x}{1-x_j} l_j(x) h(x_j). \tag{4.24}$$

The derivatives of h with respect to x (which are essentially simple rescalings of the derivative with respect to r) are computed as a sum of two terms. The first matrix is a matrix-vector product arising from the last term in (4.24), with the matrix being obtained straightforwardly from the differentiation matrices corresponding to (4.22). The second term is a vector arising from the contribution of the boundary condition $h'(1)$ to the derivative at each node of the domain.

With the problem appropriately discretised in space, we cast out problem in the discrete form

$$A\frac{\mathrm{d}U}{\mathrm{d}t} = F(U, t), \tag{4.25}$$

where A is a constant mass matrix, U is a vector containing the unknown values of $h(r, \phi, t)$, $a(\phi, t)$, $x_c(t)$, and $y_c(t)$ (and $v(t)$ for evaporating droplets), and F is a vector containing

the discretised versions of (4.18), (2.62), (2.65) and (2.56d). Thus, (4.25) is integrated over time using MATLAB's stiff ODE solver `ode15s`, where computations are sped up dramatically by parallelising the computation of the Jacobian, which is arguably the most costly component of the simulations.

4.1.2.2   Initial Condition

To initialise the solver for given volume, contact line and contact angles, we require an initial estimate of the droplet thickness $h(r, \phi, 0)$. Leading from the same rationale as in the 2D setting, we use the formulation

$$h(r, \phi, 0) = \left[\chi + \frac{r^2(\psi - \chi)}{1 + \epsilon^{-1}(1 - r)} \right] h_0(r, \phi, 0), \qquad (4.26)$$

which is a good compromise between implementing the required conditions and satisfying the quasistatic shape in the bulk. Here ψ is a term which implements the contact angle constraint, $\chi \approx 1$ is determined through the volume constraint (2.56d), and $0 < \epsilon \ll 1$ is a parameter than once lowered pushes the initial condition shape towards h_0 which is determined numerically at $t = 0$ from the problem

$$\nabla^2 [h_0(\boldsymbol{x}, t) + \eta(\boldsymbol{x})] - B [h_0(\boldsymbol{x}, t) + \eta(\boldsymbol{x})] - B \hat{\alpha} x = \tilde{p}(t), \quad \text{for} \quad \boldsymbol{x} \in \Omega(t) \qquad (4.27a)$$

$$h_0(\boldsymbol{x}, t) = 0, \qquad \text{for} \quad \boldsymbol{x} \in C(t) \qquad (4.27b)$$

$$\int_{\Omega(t)} h_0(\boldsymbol{x}, t) \, d\boldsymbol{x} = v(t), \qquad (4.27c)$$

where $B = \mathrm{Bo} \cos \alpha$ and $\hat{\alpha} = \tan \alpha / \alpha_s$.

Firstly, using the normal derivative condition (2.56c) we find that the parameter ψ takes the form

$$\psi = -\frac{a^2 \theta_*}{\partial_r h_0|_{r=1} \sqrt{a^2 + (\partial_\phi a)^2}}, \qquad (4.28)$$

and similarly χ is determined through the volume constraint (2.56d), namely

$$\chi = \frac{v(0) - \displaystyle\int_0^{2\pi} \int_0^1 \frac{\psi r^3 a^2 h_0}{1 + \epsilon^{-1}(1 - r)} \, dr \, d\phi}{\displaystyle\int_0^{2\pi} \int_0^1 \left[1 - \frac{r^2}{1 + \epsilon^{-1}(1 - r)} \right] r a^2 h_0 \, dr \, d\phi}, \qquad (4.29)$$

which is determined by numerical quadrature.

Therefore, using (4.26) with typical parameter $\epsilon = 0.1$ suffices as a satisfactory initial droplet shape to mitigate any transient dynamics in relaxing to the quasistatic shape.

4.2 Numerically Solving the Reduced Equations

The reduced equations derived in chapter 3 are significantly easier to solve than the full equations (2.51) and (2.53) and can be implemented in any standard ODE solver (such as `ode45` or `ode15s` in MATLAB). In this section, we describe some of the numerical intricacies that arose through the asymptotic analysis, as well as a brief description on how the reduced models are implemented.

4.2.1 2D Equations

In 2D we are solving the IDE system (3.35) to yield the contact point positions. If we consider a spatially varying mass flux function q that occurs in the droplet footprint and vanishes at the contact points, then we additionally need to compute the integrals $I_\pm$ (3.27). Although the integrands are continuous everywhere in the domain of integration, their evaluation is problematic near the droplet boundary, and for this reason we use the Legendre-Gauss quadrature scheme (see, section 25.4 in Abramowitz & Stegun [205]), because the endpoints are no longer included among the collocation points.

4.2.2 3D Equations

The reduced model (3.98) in generally a set of non-stiff IDEs, and although complicated in appearance, their implementation is rather straightforward. Typically the system is decomposed into 101 unknowns which include one axisymmetric component and 50 Fourier sine and cosine modes for the $b_m(t)$ terms (for $m > 0$). At each time step the input is the location of the centroid $(x_c(t), y_c(t))$ and the contact line $a(\phi, t)$ so that θ_m and ϑ_m can be found using (3.97). This involves moving back and forth the Fourier space with the fast Fourier transform.

The equations (3.98) require numerical quadrature for the integrals (3.78b), (3.90a), (3.90b), and (3.91). To determine these integrals we consider the alternate forms

$$I(0,t) = -\frac{1}{\pi b_0^2 \bar{\vartheta}} + \frac{1}{\bar{\vartheta}} \int_0^1 \frac{r^{5/2} q_0(\sqrt{r})}{1-r} \, \mathrm{d}r, \tag{4.30}$$

$$I(m,t) = \int_0^1 \frac{2r^{m/2}[g_m(1) - g_m(\sqrt{r})]}{\bar{\vartheta} g_m(1)(m+4)(1-r)^2} \left[\frac{4a_m(r^{m/2}-r)}{b_0^3 \pi} - q_m(\sqrt{r}) \right] \mathrm{d}r, \tag{4.31}$$

$$\tilde{\beta}(m) = \int_0^1 \left\{ \frac{1}{1-r} + \frac{2r^m}{(m+4)(1-r)^2} \left[1 - \frac{g_m(\sqrt{r})}{g_m(1)} \right] \right\} \mathrm{d}r + \ln(2), \tag{4.32}$$

$$\hat{\beta}(m) = \int_0^1 \left\{ \frac{1}{1-r} + \frac{2r^{(m+1)/2}}{(m+4)(1-r)^2} \left[1 - \frac{g_m(\sqrt{r})}{g_m(1)} \right] \right\} \, dr + \ln(2), \tag{4.33}$$

where the last three integrals are calculated for $m \geq 1$. To determine the Gauss hypergeometric functions $g_m(r)$ (3.86) we consider the governing differential equation for $g_m(r)$

$$r(1-r)g_m'' + (1+m-rm)g_m' + \left(\frac{m}{2} + 2 \right) g_m = 0, \tag{4.34}$$

where primes denote differentiation with respect to r. Rather than solving directly for $g_m(r)$ we consider the recasting $\tilde{g}_m(r) = g_m(r)/g_m(1)$ which satisfies the same equation, and is solved subject to the conditions that

$$\tilde{g}_m(1) = 1 \quad \text{and} \quad \tilde{g}_m'(1) = -\frac{m}{2} - 2, \tag{4.35}$$

in which the last condition arises from considering the asymptotics of g_m' near $r = 1$. Therefore, the linear differential equation (4.34) is solved numerically with the pseudospectral collocation method by matrix inversion, where the boundary conditions at $r = 1$ are built into the matrices. Once $g_m(r)$ are determined at the collocation points we use the barycentric formula to interpolate to the Legendre-Gauss quadrature mesh, which allows us to bypass evaluating the integrand at $r = 1$.

To avoid repeating calculations during simulations of the reduced models, the values of $\tilde{\beta}(m)$ and $\hat{\beta}(m)$ are calculated once and stored. The integrals $I(m, t)$ include time-dependent variables and thus require evaluation during simulations. Therefore, to mitigate the computational time required to determine $I(m, t)$ we store and retrieve the values of $g_m(r)$ whenever these are required.

In some simulations we compare solutions of (3.98) to those obtained from the leading-order formula (1.6). To perform simulations using (1.6), equations (2.62) and (2.65) are used with

$$W(\phi, t) = \frac{\left(\theta_*^3 - \vartheta^3 \right) \sqrt{a^2 + (\partial_\phi a)^2}}{3 \ln(\lambda)}, \tag{4.36}$$

in which ϑ is obtained using the boundary integral approach described in section 4.3. The reason for this is primarily to assess the importance of the additional next-order correction terms derived in the analysis presented here, since, (1.6) describes only the leading-order term in the asymptotic expansion for the normal velocity of the contact line.

4.3 The Hybrid Method

The hybrid method leverages the results of the asymptotic analysis undertaken in chapter 3 so that for given contact line shape, the apparent contact angle ϑ is computed, which can be fed into some contact line law which will govern the evolution of the contact line. By doing so, we offer an attractive alternative to simulating the full model, combining improved accuracy compared to using the estimates of (3.58) (and (3.163) for rough substrates), with computational efficiency. Essentially, we are interested in solving the leading-order problem (4.27) which describes the quasi-static thickness in the bulk, so that the apparent contact angle can be found. Rather than obtaining the droplet thickness everywhere in the wetted region $\Omega(t)$, we use the boundary integral method like Glasner [153] which allows us to only determine the required apparent contact angle. One of the differences between the present work and that of Glasner is the choice of parametrisation, here we consider the polar angle (4.19), whereas Glasner parameterises by arc length. Another notable difference is that we consider substrates that are topographically rough, on the contrary, Glasner considers flat substrates only.

Throughout the following sections we will consider two distinct cases, one with gravitational effects included, and one without. As we shall see, both cases are formulated and implemented differently, although the key ideas are common for both.

4.3.1 Horizontal Substrates Without Gravity

Here we neglect gravity and seek an expression for the apparent contact angle derived from the linear elliptic problem

$$-\nabla^2 \left[h_0(\boldsymbol{x}, t) + \eta(\boldsymbol{x}) \right] = \tilde{p}(t), \quad \text{for} \quad \boldsymbol{x} \in \Omega(t) \tag{4.37a}$$

$$h_0(\boldsymbol{x}, t) = 0, \quad \text{for} \quad \boldsymbol{x} \in C(t) \tag{4.37b}$$

$$\int_{\Omega(t)} h_0(\boldsymbol{x}, t) \, \mathrm{d}\boldsymbol{x} = v(t), \tag{4.37c}$$

for $\boldsymbol{x} = (x, y)$, and where $\tilde{p}(t)$ is to be found using the volume constraint ((4.37) can be deduced by setting $\mathrm{Bo} = 0$ in (4.27)).

Central to any discussion on the boundary integral formulation is the free-space Green's function

$$G(\boldsymbol{x}, \boldsymbol{x}_0) = -\frac{1}{2\pi} \ln |\boldsymbol{x} - \boldsymbol{x}_0|, \tag{4.38}$$

which is defined as the radially symmetric solution to

$$-\nabla^2 G(x, x_0) = \delta(x - x_0), \quad \text{for} \quad x, x_0 \in \mathbb{R}^2, \tag{4.39}$$

where δ denotes the Dirac delta function. To remove the unknown $\tilde{p}(t)$ from (4.37) we consider the variable

$$w(x, t) = \frac{h_0(x, t) + \eta(x)}{\tilde{p}(t)} + \frac{|x|^2}{4}, \tag{4.40}$$

which satisfies Laplace's equation with inhomogeneous boundary conditions, namely

$$\nabla^2 w(x, t) = 0, \qquad \text{for} \quad x \in \Omega(t), \tag{4.41a}$$

$$w(x, t) = \frac{\eta(x)}{\tilde{p}(t)} + \frac{|x|^2}{4}, \quad \text{for} \quad x \in C(t). \tag{4.41b}$$

The problem for $w(x, t)$, (4.41), cannot be solved because the unknown $\tilde{p}(t)$ is in the boundary condition (4.41b). Using the principle of superposition we write $w(x, t) = w_0(x, t)/\tilde{p}(t) + w_1(x, t)$, formulating the two independent problems for $w_0(x, t)$

$$\nabla^2 w_0(x, t) = 0, \qquad \text{for} \quad x \in \Omega(t), \tag{4.42a}$$

$$w_0(x, t) = \eta(x), \quad \text{for} \quad x \in C(t), \tag{4.42b}$$

and $w_1(x, t)$

$$\nabla^2 w_1(x, t) = 0, \qquad \text{for} \quad x \in \Omega(t), \tag{4.43a}$$

$$w_1(x, t) = \frac{|x|^2}{4} \quad \text{for} \quad x \in C(t), \tag{4.43b}$$

which, once solved for their normal derivatives, we can determine the macroscopic contact angle

$$\vartheta = -\partial_\nu h_0(x, t) = \partial_\nu \eta(x) - \partial_\nu w_0(x, t) + \tilde{p}(t) \left[\frac{x \cdot \nu}{2} - \partial_\nu w_1(x, t) \right], \tag{4.44}$$

along the contact line.

To determine the unknown normal derivatives we multiply equations (4.42a) and (4.43a) by (4.38) and apply Green's second integral identity to yield the boundary integral equations

$$\int_{C(t)} G(x, x_0) \partial_\nu w_0(x, t) \, ds(x) = \frac{\eta(x_0)}{2} + \int_{C(t)} \eta(x) \partial_\nu G(x, x_0) \, ds(x), \tag{4.45a}$$

$$\int_{C(t)} G(x, x_0) \partial_\nu w_1(x, t) \, ds(x) = \frac{|x_0|^2}{8} + \frac{1}{4} \int_{C(t)} |x|^2 \partial_\nu G(x, x_0) \, ds(x), \tag{4.45b}$$

for $x_0 \in C(t)$, which are cast into dense linear systems for the unknowns $\partial_\nu w_0(x, t)$ and $\partial_\nu w_1(x, t)$. The unknown function $\tilde{p}(t)$ which appears in (4.44) is determined from the volume constraint (4.27c), which is equivalently written as

$$v(t) = \frac{1}{4} \int_{\Omega(t)} h_0(x, t) \nabla^2 |x|^2 \, dx. \tag{4.46}$$

Using Green's second integral identity followed by $\nabla \cdot \left(|x|^2 x \right) = 4|x|^2$ and the divergence theorem yields

$$\tilde{p}(t) = \frac{v(t) + \tilde{v}(t) - \int_{C(t)} \left[\frac{\eta(x)(x \cdot \nu)}{2} - \frac{|x|^2}{4} \partial_\nu w_0(x, t) \right] ds(x)}{\int_{C(t)} \frac{|x|^2}{4} \left[\frac{x \cdot \nu}{4} - \partial_\nu w_1(x, t) \right] ds(x)}, \tag{4.47}$$

where $\tilde{v}(t)$ is defined in (3.157).

Hence, given the contact line shape $a(\phi, t)$ and centroid locations $(x_c(t), y_c(t))$, we solve (4.45a) and (4.45b) for the normal derivatives of $w_0(x, t)$ and $w_1(x, t)$ which are used within (4.47) to determine $\tilde{p}(t)$, which are all combined in (4.44) to yield the macroscopic angle ϑ. In the case where the substrate is flat so that $\eta(x) = 0$, the problem is reduced to solving one integral equation for w_1, noting that (4.47) and (4.44) are modified by removing $\tilde{v}(t)$, $\partial_\nu w_0(x, t)$, and $\eta(x)$ terms.

4.3.1.1 Implementation Aspects

The boundary integral equations we need to solve can be cast in the form

$$\int_{C(t)} G(x, x_0) \partial_\nu w(x, t) \, ds(x) = \hat{w}_1(x_0) + \int_{C(t)} \hat{w}_2(x) \partial_\nu G(x, x_0) \, ds(x), \quad x_0 \in C(t) \tag{4.48}$$

where $\partial_\nu w(x, t)$ is the unknown function to be determined and $\hat{w}_{1,2}(x_0)$ are given. Using (2.54) to write the integrals in terms of the polar angle of the moving frame ϕ, we write the line element as $ds(x) = D(\phi) d\phi$ where

$$D(\phi) = \sqrt{a(\phi)^2 + \left[\partial_\phi a(\phi) \right]^2}, \tag{4.49}$$

noting that we consider the points x and x_0 to lie on the contact line $C(t)$ with polar angles ϕ and ϕ_0, respectively (where the time variable t has been suppressed for notational simplicity). To form the boundary integral equations (4.45a) and (4.45b) we require $|x|^2$, $G(x, x_0)$ and $\partial_\nu G(x, x_0)$ which are given in the polar variables as

$$|x|^2 = x_c^2 + y_c^2 + a(\phi)^2 + 2a(\phi)(x_c \cos \phi + y_c \sin \phi), \tag{4.50}$$

$$G(\boldsymbol{x}, \boldsymbol{x}_0) = -\frac{1}{2\pi} \ln[R(\phi, \phi_0)], \tag{4.51}$$

$$\partial_\nu G(\boldsymbol{x}, \boldsymbol{x}_0) = -\frac{F(\phi, \phi_0)}{2\pi R^2(\phi, \phi_0)}. \tag{4.52}$$

where

$$R(\phi, \phi_0) = \sqrt{[a(\phi) - a(\phi_0)]^2 + 4a(\phi)a(\phi_0)\sin^2\left(\frac{\phi - \phi_0}{2}\right)}, \tag{4.53}$$

$$F(\phi, \phi_0) = \frac{a(\phi)^2 - a(\phi)a(\phi_0)\cos(\phi - \phi_0) - \partial_\phi a(\phi)a(\phi_0)\sin(\phi - \phi_0)}{D(\phi)}. \tag{4.54}$$

Clearly, $G(\boldsymbol{x}, \boldsymbol{x}_0)$ is logarithmically singular as $\phi \to \phi_0$. Hence, to accurately perform the quadrature on the left hand side of (4.48) we proceed as highlighted in related works (see Glasner [153] and Hao *et al.* [206]). This involves splitting the logarithmically singular kernel into singular (denoted $\check{G}(\boldsymbol{x}, \boldsymbol{x}_0)$) and non-singular parts (denoted $\hat{G}(\boldsymbol{x}, \boldsymbol{x}_0)$), where the singular part is integrated with a high-order quadrature scheme which is tailored to account for the singularity as $\phi \to \phi_0$ (see Kress *et al.* [207] and Kress [208]). Such a scheme allows us to compute integrals of the form

$$\int_0^{2\pi} \ln\left[4\sin^2\left(\frac{\phi - \phi_0}{2}\right)\right] f(\phi)\,\mathrm{d}\phi, \tag{4.55}$$

according to the quadrature rule

$$\sum_{j=0}^{N_\phi - 1} \tilde{w}_{|i-j|} f(\phi_j), \tag{4.56}$$

with spectral accuracy if $f(\phi)$ is smooth, where ϕ_j are given by (4.19) and $\tilde{w}_j$ are the quadrature weights

$$\tilde{w}_j = -\frac{4\pi(-1)^j}{N_\phi^2} - \frac{4\pi}{N_\phi} \sum_{m=1}^{N_\phi/2 - 1} \frac{1}{m} \cos\left(\frac{2mj\pi}{N_\phi}\right). \tag{4.57}$$

One could alternatively form the integration matrix using a different high-order quadrature rule which accounts for the logarithmic singularity as $\phi \to \phi_0$, such as the rule developed by Alpert [209], however, we opt for implementation using this method of quadrature due to the faster convergence rates shown by Hao *et al.* [206].

Therefore we split $G(\boldsymbol{x}, \boldsymbol{x}_0)$ into the parts

$$\hat{G}(\boldsymbol{x}, \boldsymbol{x}_0) = \begin{cases} -\dfrac{1}{4\pi} \ln\left\{ \dfrac{[a(\phi) - a(\phi_0)]^2 + 4a(\phi)a(\phi_0)\sin^2\left(\frac{\phi - \phi_0}{2}\right)}{4\sin^2\left(\frac{\phi - \phi_0}{2}\right)} \right\}, & \text{for } \phi \neq \phi_0 \\[4ex] -\dfrac{1}{2\pi} \ln[D(\phi)], & \text{for } \phi = \phi_0 \end{cases} \tag{4.58}$$

and

$$\check{G}(\boldsymbol{x}, \boldsymbol{x}_0) = -\frac{1}{4\pi} \ln\left[4\sin^2\left(\frac{\phi - \phi_0}{2}\right)\right], \tag{4.59}$$

where all other integrals in the ϕ variable are implemented straightforwardly using the periodic trapezoidal rule, noting that $\partial_\nu G(\boldsymbol{x}, \boldsymbol{x}_0)$ is continuous as $\phi \to \phi_0$, in other words

$$\partial_\nu G(\boldsymbol{x}_0, \boldsymbol{x}_0) = -\frac{a(\phi)^2 + 2\left[\partial_\phi a(\phi)\right]^2 - a(\phi)\partial_\phi^2 a(\phi)}{4\pi D(\phi)^3}. \tag{4.60}$$

We also require use of the expressions

$$\boldsymbol{x} \cdot \boldsymbol{\nu} = \frac{a(\phi)^2 + x_c\left[a(\phi)\cos\phi + \partial_\phi a(\phi)\sin\phi\right] + y_c\left[a(\phi)\sin\phi - \partial_\phi a(\phi)\cos\phi\right]}{D(\phi)}, \tag{4.61}$$

$$\partial_\nu \eta(\boldsymbol{x}) = \frac{\left[a(\phi)\cos\phi + \partial_\phi a(\phi)\sin\phi\right]\partial_x \eta(\boldsymbol{x}) + \left[a(\phi)\sin\phi - \partial_\phi a(\phi)\cos\phi\right]\partial_y \eta(\boldsymbol{x})}{D(\phi)},$$

$$\tag{4.62}$$

as well as the integral

$$\tilde{v}(t) = \int_0^{2\pi} \int_0^1 r a^2 \eta(r, \phi, t)\, dr\, d\phi, \tag{4.63}$$

where radial quadrature is performed using the Clenshaw-Curtis quadrature weights (see Clenshaw & Curtis [210] and Trefethen [211]). For the most part $\partial_x \eta(\boldsymbol{x})$ and $\partial_y \eta(\boldsymbol{x})$ can be calculated analytically since the functional form of $\eta(\boldsymbol{x})$ is known. However, should the substrate features be generated numerically then $\partial_x \eta(\boldsymbol{x})$ and $\partial_y \eta(\boldsymbol{x})$ will require numerical differentiation accompanied by the appropriate interpolation to find their values along the contact line.

With all the necessary components in place, we can accurately discretise the integral equations (4.45a) and (4.45b) into dense linear systems to solve for the unknowns $\partial_\nu w_0(\phi_i)$ and $\partial_\nu w_1(\phi_i)$, which can then be combined with (4.47) and (4.44) to determine the macroscopic contact angle across the discrete points. It is worth noting that splitting up the Green's function and using Kress quadrature yields a method that is not amenable to speed-up using the fast multipole method (see Greengard & Rokhlin [212]). Therefore, for very large N_ϕ this method can become inefficient due to the matrix inversions required for the large dense matrices. This can be bypassed by using the aforementioned Alpert quadrature rule [209] which is compatible with the fast multipole method, however, since we consider regimes where N_ϕ is only moderate in size we did not deem necessary to pursue this avenue further.

To gather a sense of the rate of convergence of this method we show two simple convergence tests in figure 4.3, where we compare boundary integral simulations for varying
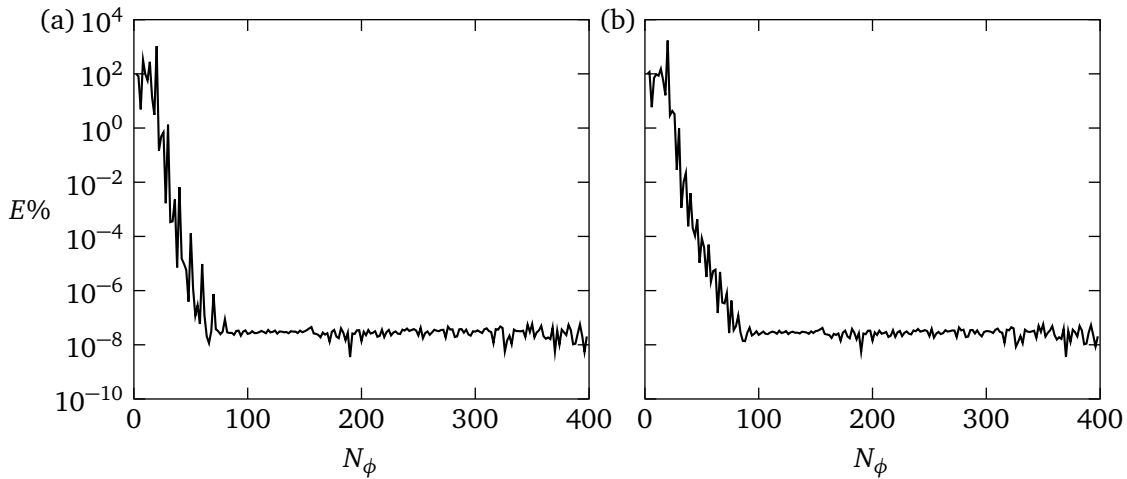
Figure 4.3: Convergence tests for the boundary integral method (see text for a description of the test performed). (a) The percentage error when $a(\phi) = 1 + 0.1\cos(5\phi)$ and $\eta(x,y) = 0.15\sin(2x) + 0.1\cos(3y)$. (b) The same calculation for $a(\phi) = 1 + 0.1\cos(5\phi) + 0.05\sin(3\phi)$ and $\eta(x,y) = 0.05\sin(5x) + 0.15\cos(2y)$. In both cases $v = 2\pi$, $x_c = -2$ and $y_c = 5$.

N_ϕ against one calculated at $N_\phi = 400$ by using the percentage error

$$E\% = 100\left|\frac{\tilde{\vartheta} - \bar{\vartheta}}{\bar{\vartheta}}\right|, \tag{4.64}$$

where $\tilde{\vartheta}$ denotes the mean angles obtained for varying N_ϕ, and $\bar{\vartheta}$ is the mean angle calculated at $N_\phi = 400$. It is easy to see from figure 4.3 that the boundary integral calculations converge in a reasonable number of collocation points, showing how $N_\phi = 100$ points typically suffices for satisfactory accuracy. Perhaps the best benefit of this approach is the time difference required to calculate the apparent contact as compared to one found with a pseudospectral collocation approach. By using $N_\phi = 200$ and $N_r = 40$ (8000 unknowns) the spectral method answer is obtained in around 16 seconds, whereas the boundary integral simulation with $N_\phi = 200$ takes 0.01 seconds or less (calculations performed on a mid of the range PC).

4.3.2   Gravitational Effects

When gravity is important and for inclined substrates we need to consider the full equations (4.27). The derivations here follow the same format as seen previously, noting that we adopt the same notation as before, and that any additional changes to the formulation will be highlighted as appropriate.

As in the zero-gravity case (4.27a) is homogenised by introducing the new variable $w(\boldsymbol{x}, t)$, namely

$$w(\boldsymbol{x}, t) = h_0(\boldsymbol{x}, t) + \eta(\boldsymbol{x}) + \frac{\tilde{p}(t)}{B} + \hat{\alpha}x, \tag{4.65}$$

which yields the Dirichlet problem governed by the homogeneous modified Helmholtz equation

$$\nabla^2 w(\boldsymbol{x}, t) - B w(\boldsymbol{x}, t) = 0 \quad \text{for} \quad \boldsymbol{x} \in \Omega(t), \tag{4.66a}$$

$$w(\boldsymbol{x}, t) - \left[\eta(\boldsymbol{x}) + \frac{\tilde{p}(t)}{B} + \hat{\alpha}x \right] = 0 \quad \text{for} \quad \boldsymbol{x} \in C(t). \tag{4.66b}$$

Unlike previous studies of the modified Helmholtz equation with the boundary integral method (see Kropinski & Quaife [213] and Quaife [214]), the unknown $\tilde{p}(t)$ is present in the boundary condition. Again, by a superposition of solutions of the form

$$w(\boldsymbol{x}, t) = w_0(\boldsymbol{x}, t) + \tilde{p}(t) w_1(\boldsymbol{x}, t), \tag{4.67}$$

we formulate two independent problems for $w_0(\boldsymbol{x}, t)$

$$\nabla^2 w_0(\boldsymbol{x}, t) - B w_0(\boldsymbol{x}, t) = 0 \qquad \text{for} \quad \boldsymbol{x} \in \Omega(t), \tag{4.68a}$$

$$w_0(\boldsymbol{x}, t) = \eta(\boldsymbol{x}) + \hat{\alpha}x \quad \text{for} \quad \boldsymbol{x} \in C(t), \tag{4.68b}$$

and $w_1(\boldsymbol{x}, t)$

$$\nabla^2 w_1(\boldsymbol{x}, t) - B w_1(\boldsymbol{x}, t) = 0 \quad \text{for} \quad \boldsymbol{x} \in \Omega(t), \tag{4.69a}$$

$$w_1(\boldsymbol{x}, t) = \frac{1}{B} \quad \text{for} \quad \boldsymbol{x} \in C(t). \tag{4.69b}$$

Using the techniques highlighted previously, we arrive with the following boundary integral equations to solve for $\partial_\nu w_0(\boldsymbol{x}, t)$ and $\partial_\nu w_1(\boldsymbol{x}, t)$ for $x_0 \in C(t)$:

$$\int_{C(t)} G(\boldsymbol{x}, \boldsymbol{x}_0) \partial_\nu w_0(\boldsymbol{x}, t) \, \mathrm{d}s(\boldsymbol{x}) = -\frac{\eta(\boldsymbol{x}_0) + \hat{\alpha}x}{2} + \int_{C(t)} \left[\eta(\boldsymbol{x}) + \hat{\alpha}x \right] \partial_\nu G(\boldsymbol{x}, \boldsymbol{x}_0) \, \mathrm{d}s(\boldsymbol{x}),$$

$$\tag{4.70a}$$

$$\int_{C(t)} G(\boldsymbol{x}, \boldsymbol{x}_0) \partial_\nu w_1(\boldsymbol{x}, t) \, \mathrm{d}s(\boldsymbol{x}) = -\frac{1}{2B} + \frac{1}{B} \int_{C(t)} \partial_\nu G(\boldsymbol{x}, \boldsymbol{x}_0) \, \mathrm{d}s(\boldsymbol{x}), \tag{4.70b}$$

where $G(\boldsymbol{x}, \boldsymbol{x}_0)$ is the free-space Green's function for the modified Helmholtz equation

$$G(\boldsymbol{x}, \boldsymbol{x}_0) = -\frac{1}{2\pi} K_0 \left(\sqrt{B} |\boldsymbol{x} - \boldsymbol{x}_0| \right), \tag{4.71}$$

which is the radially symmetric solution to

$$\nabla^2 G(\boldsymbol{x}, \boldsymbol{x}_0) - B G(\boldsymbol{x}, \boldsymbol{x}_0) = \delta(\boldsymbol{x} - \boldsymbol{x}_0), \tag{4.72}$$

where K_0 denotes the modified Bessel function of the second kind of order zero.

Next we use the volume constraint (4.27c) to determine $\tilde{p}(t)$, therefore, after applying the transformation (4.65) we obtain

$$v + \int_{\Omega(t)} \eta(x)\,dx = \int_{\Omega(t)} [w_0(x,t) - vx]\,dx + \tilde{p}(t)\int_{\Omega(t)} \left[w_1(x,t) - \frac{1}{B}\right]dx, \qquad (4.73)$$

which is changed to

$$v + \tilde{v} = \int_{\Omega(t)} \left[\frac{\nabla^2 w_0(x,t)}{B} - \hat{\alpha}x\right]dx + \frac{\tilde{p}(t)}{B}\int_{\Omega(t)} \left[\nabla^2 w_1(x,t) - 1\right]dx, \qquad (4.74)$$

by using the equations (4.68a), (4.69a), and the definition (3.157). To change the volume integrals to line integrals, we apply the substitution

$$\hat{\alpha}x = \frac{1}{B}\nabla \cdot \frac{B\hat{\alpha}x^2}{2}i, \qquad (4.75)$$

so that the divergence theorem can be applied, and therefore, after some re-arranging arrive at

$$\tilde{p}(t) = \frac{B(v + \tilde{v}) - \displaystyle\int_{C(t)} \left[\partial_\nu w_0(x,t) - \frac{B\hat{\alpha}x^2}{2}i \cdot \nu\right]ds(x)}{\displaystyle\int_{C(t)} \left[\partial_\nu w_1(x,t) - \frac{x \cdot \nu}{2}\right]ds(x)}. \qquad (4.76)$$

Finally, the boundary integral formulation is as follows; we solve (4.70a) and (4.70b) for the normal derivatives of $w_0(x,t)$ and $w_1(x,t)$, which are then utilised within (4.76) to determine $\tilde{p}(t)$, all of which are combined to yield the apparent contact angle

$$-\vartheta = \partial_\nu h_0(x,t) = \partial_\nu w_0(x,t) + \tilde{p}(t)\partial_\nu w_1(x,t) - \partial_\nu \eta(x) - \hat{\alpha}i \cdot \nu, \qquad (4.77)$$

therefore completing the derivation of the generalised boundary integral formulation.

4.3.2.1 Implementation Aspects

Here we note that the boundary integral equations we wish to solve, (4.70a) and (4.70b), are in the same format as (4.48), therefore the discussion here closely follows the previous implementation. In this case the free-space Green's function and corresponding normal derivative are expressed as

$$G(x, x_0) = -\frac{1}{2\pi}K_0\left[\sqrt{B}R(\phi, \phi_0)\right], \qquad (4.78)$$

and

$$\partial_\nu G(x, x_0) = \frac{\sqrt{B}F(\phi, \phi_0)}{2\pi R(\phi, \phi_0)}K_1\left[\sqrt{B}R(\phi, \phi_0)\right]. \qquad (4.79)$$

The implementation of $G(\boldsymbol{x}, \boldsymbol{x}_0)$ and $\partial_\nu G(\boldsymbol{x}, \boldsymbol{x}_0)$ follow the same ideas as before, splitting the free-space Green's function into the non-singular part,

$$
\hat{G}(\boldsymbol{x}, \boldsymbol{x}_0) = \begin{cases} -\dfrac{K_0\big[\sqrt{B}R(\phi, \phi_0)\big]}{2\pi} + \dfrac{1}{4\pi} I_0\big[\sqrt{B}R(\phi, \phi_0)\big] \ln\left[\sin^2\left(\dfrac{\phi - \phi_0}{2}\right)\right], & \text{for} \quad \phi \neq \phi_0 \\[4mm] \dfrac{1}{2\pi}\left[\gamma + \ln\left(\dfrac{\sqrt{B}D(\phi)}{2}\right)\right], & \text{for} \quad \phi = \phi_0 \end{cases}
$$

$$\text{(4.80a)}$$

and the singular part

$$
\check{G}(\boldsymbol{x}, \boldsymbol{x}_0) = \frac{1}{4\pi} I_0\big[\sqrt{B}R(\phi, \phi_0)\big] \ln\left[\sin^2\left(\frac{\phi - \phi_0}{2}\right)\right]. \tag{4.80b}
$$

Here I_0 denotes the modified Bessel function of the first kind of order zero. In this sense, the non-singular part $\hat{G}(\boldsymbol{x}, \boldsymbol{x}_0)$ is evaluated using the periodic trapezoidal rule and the singular part is once again dealt with by the high-order quadrature scheme described earlier.

However, the normal derivative $\partial_\nu G(\boldsymbol{x}, \boldsymbol{x}_0)$ must be treated with caution. Although it is non-singular in the limit as $\phi \to \phi_0$ a naïve implementation of the trapezoidal rule results in slower convergence than expected. This is because the error of the trapezoidal rule decays at the same rate as the Fourier coefficients of the integrand (see Quaife [214]), and since the Fourier coefficients of the Bessel function K_1 decay slowly, a more appropriate quadrature scheme is required. To alleviate this issue a large variety of higher-order quadrature schemes may be utilised, such as the aforementioned Alpert quadrature scheme (see Alpert [209]), or the Kapur-Rokhlin quadrature rule (see Kapur & Rokhlin [215]), which are both higher-order modified versions of the trapezoidal rule. In the PhD thesis by Quaife [214] the Alpert quadrature rule is used to evaluate the integrals including the normal derivative $\partial_\nu G(\boldsymbol{x}, \boldsymbol{x}_0)$ which they show results in satisfactory accuracy, and has the additional benefit that the method is fast multipole compatible. The aforementioned schemes, including the Alpert method, are also discussed at length by Hao *et al.* [206] to treat logarithmically singular kernals where it is concluded that Kress quadrature outperforms these rules for the cases they consider. Here we treat the integrals involving $\partial_\nu G(\boldsymbol{x}, \boldsymbol{x}_0)$ with Kress quadrature for this reason since we desire fast convergence, and do not need to consider speed-up with the fast mutltipole method since N_ϕ is only moderate in size for the cases we consider.

To implement the Kress quadrature scheme for the normal derivative $\partial_\nu G(\boldsymbol{x}, \boldsymbol{x}_0)$ we must
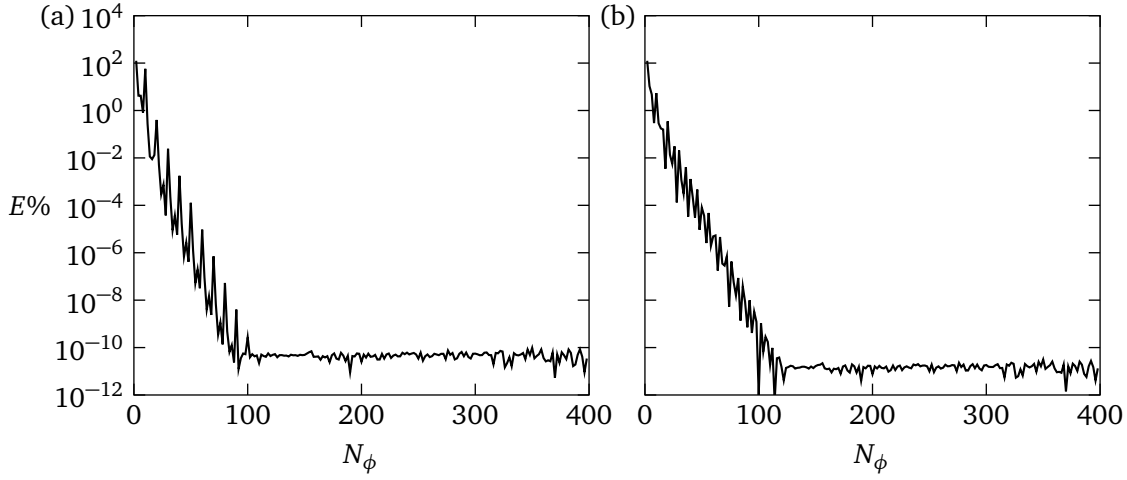
Figure 4.4: Repetition of the calculations in figure 4.3 where in (a) Bo $= 0.75$, $\alpha = 5°$ and (b) Bo $= 2$, $\alpha = 10°$ with $\alpha_s = 15°$ in both cases.

split it into two parts, involving a part evaluated by the periodic trapezoidal rule

$$\widehat{\partial_\nu G}(x, x_0) = \frac{\sqrt{B}F(\phi, \phi_0)}{2\pi R(\phi, \phi_0)} \left\{ K_1 \left[\sqrt{B}R(\phi, \phi_0) \right] - \frac{1}{2} I_1 \left[\sqrt{B}R(\phi, \phi_0) \right] \ln \left[\sin^2 \left(\frac{\phi - \phi_0}{2} \right) \right] \right\}$$
(4.81)

and a portion evaluated by Kress quadrature

$$\widetilde{\partial_\nu G}(x, x_0) = \frac{\sqrt{B}F(\phi, \phi_0)}{4\pi R(\phi, \phi_0)} I_1 \left[\sqrt{B}R(\phi, \phi_0) \right] \ln \left[\sin^2 \left(\frac{\phi - \phi_0}{2} \right) \right],$$
(4.82)

where $\phi \neq \phi_0$. In the limit as $\phi \to \phi_0$ we have

$$\widehat{\partial_\nu G}(x_0, x_0) = \frac{a(\phi)^2 + 2 \left[\partial_\phi a(\phi) \right]^2 - a(\phi) \partial_\phi^2 a(\phi)}{4\pi D(\phi)^3},$$
(4.83a)

$$\widetilde{\partial_\nu G}(x_0, x_0) = 0.$$
(4.83b)

Finally, to complete all the ingredients needed to implement the boundary integral method in order to extract (4.77), we also require

$$\frac{B\hat{\alpha}x^2}{2} i \cdot \nu = \frac{B\hat{\alpha} \left[a(\phi) \cos \phi + \partial_\phi a(\phi) \sin \phi \right] \left[x_c(t) + a(\phi) \cos \phi \right]^2}{2D(\phi)},$$
(4.84)

and

$$\hat{\alpha} i \cdot \nu = \hat{\alpha} \frac{a(\phi) \cos \phi + \partial_\phi a(\phi) \sin \phi}{D(\phi)},$$
(4.85)

alongside the expression for $x \cdot \nu$ (4.61) and $\partial_\nu \eta(x)$ (4.62).

To assess the convergence of this approach we use the error checking methods presented in the gravity-free case to yield the convergence plots of figure 4.4. Just like figure 4.3 we observe that satisfactory convergence rates are achieved, noting that choosing $N_\phi = 100$ is more than adequate in obtaining accurate solutions.

4.4 Summary

In this chapter we presented the numerical methods used to solve the governing PDE (2.30) for cases involving 2D and 3D droplets. The developed numerical schemes used the Chebyshev collocation method for spatial discretisation, and time integration using the method of lines. Although the approach in 2D was limited to perfectly flat, and horizontal surfaces with negligible gravitational effects, the 3D scheme was generalised to handle all these scenarios.

The 2D implementation extended related implementations that appeared previously in the literature, whereas the 3D extension is the key contribution of the present thesis which has been reported for the first time in [61]. In addition, a hybrid method has been developed to accompany the analysis undertaken. It was based on the ideas presented by Glasner [153], but, unlike here he imposed ad hoc the contact line velocities. Crucially, the boundary integral method developed was extended to account for surface roughness with the aim to be used in related studies that extend beyond the present thesis.

Besides the convergence tests in figures 4.3 and 4.4, simulations using the methods presented in this chapter are deferred to chapter 5 where comparisons are made with the outcomes of the analysis performed in chapter 3.

— Chapter 5 —

Simulations

Throughout this chapter we assess how well the analytical methods presented in chapter 3 compare to the numerical methods presented in chapter 4, and elucidate some of the interesting phenomena that arise from experimental settings. Here we structure the sections according to each physical setting considered in chapter 3, paying specific attention to where the droplet mass is variable to develop some insights on the interplay between liquid flux and chemical heterogeneity.

In what follows, the *full model* refers to direct numerical simulations of the governing PDEs (2.51) in 3D and (2.53) in 2D, as discussed in chapter 4. The *reduced model* corresponds to solving the simplified systems of equations derived in chapter 3. Finally, the *hybrid model* combines the boundary integral formulation derived in chapter 4 with the outcomes of the analysis in chapter 3.

5.1 2D Prescribed Variable Mass

We begin by considering the 2D setting where flat and horizontal substrates are assumed. Here, the reduced model corresponds to solving (3.35) for the positions of the contact points. Unless otherwise stated in the results that follow, we fix $a_\pm(0) = \pm 1$, $\lambda = 10^{-4}$ and plot solutions of the full and reduced models by solid and dashed lines, respectively.

Whenever periodic variations of the cross sectional area are required, they are prescribed with the $\mathcal{P}$-periodic function

$$A(t) = \mathcal{A} + \frac{\tilde{\mathcal{A}}}{\tan^{-1} \mathcal{M}} \tan^{-1}\left[\frac{\mathcal{M}\sin(2\pi t/\mathcal{P})}{\sqrt{1 + \mathcal{M}^2 \cos^2(2\pi t/\mathcal{P})}} \right], \tag{5.1}$$

which describes oscillations of amplitude $\tilde{\mathcal{A}}$ away from the mean value $\mathcal{A}$. For finite values of the parameter $\mathcal{M}$, equation (5.1) is everywhere smooth, tending to $\mathcal{A} + \tilde{\mathcal{A}}\sin(2\pi t/\mathcal{P})$ in the limit $\mathcal{M} \to 0$. In the opposite limit, as $\mathcal{M} \to \infty$, $A(t)$ tends to a piecewise linear
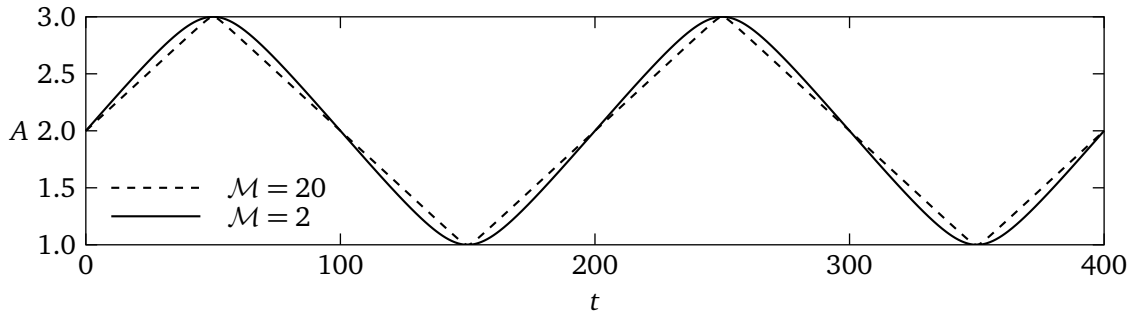
Figure 5.1: The area function (5.1) for two different values of $\mathcal{M}$ alongside using $\mathcal{A} = 2$, $\bar{\mathcal{A}} = 1$ and $\mathcal{P} = 200$ in both cases.

$\mathcal{P}$-periodic sawtooth function. Although the jump discontinuities in the first derivative of a sawtooth function are generally harmless and do not pose additional challenges in simulations, equation (5.1) avoids these discontinuities altogether while simulating nearly piecewise linear inflow/outflow scenarios for sufficiently large $\mathcal{M}$. In all simulations performed, we fix $\mathcal{M} = 20$ (see figure 5.1).

5.1.1   Hysteresis Behaviours

In the first set of examples, we assume that q is given by equation (3.36) which, as previously mentioned, reduces (3.35) to a simpler system of ODEs. For the corresponding numerical solution to the PDE problem, such form also avoids the use of dense meshes that would be required to accurately capture highly localised fluxes. In these test cases we consider simple heterogeneity profiles that describe alternating patches of nearly constant wettability, in order to highlight some complex behaviours that arise. These include the pinning of the droplet fronts, which typically occurs in regions where $\theta(x)$ changes abruptly and points to substrate-induced hysteresis-like effects, as well as the constant-radius and constant-angle modes, previously discussed in chapter 1. Indeed, for area changes following (5.1) and suitably chosen parameters $\mathcal{A}$, $\tilde{\mathcal{A}}$, $\mathcal{P}$ and profiles $\theta(x)$, the dynamics can be made to alternate between these two modes as shown in figure 5.2, noting also the excellent agreement between the full and reduced models. Previously, studies such as Amini & Homsy for ideal [147] and structured substrates [148] have treated these modes separately. However, we observe that both of these modes can arise in a single simulation, like Pham & Kumar [149] who consider a numerical investigation of a droplet evaporating over a single topographical defect

On the other hand, it is important to emphasise that this behaviour is not particularly
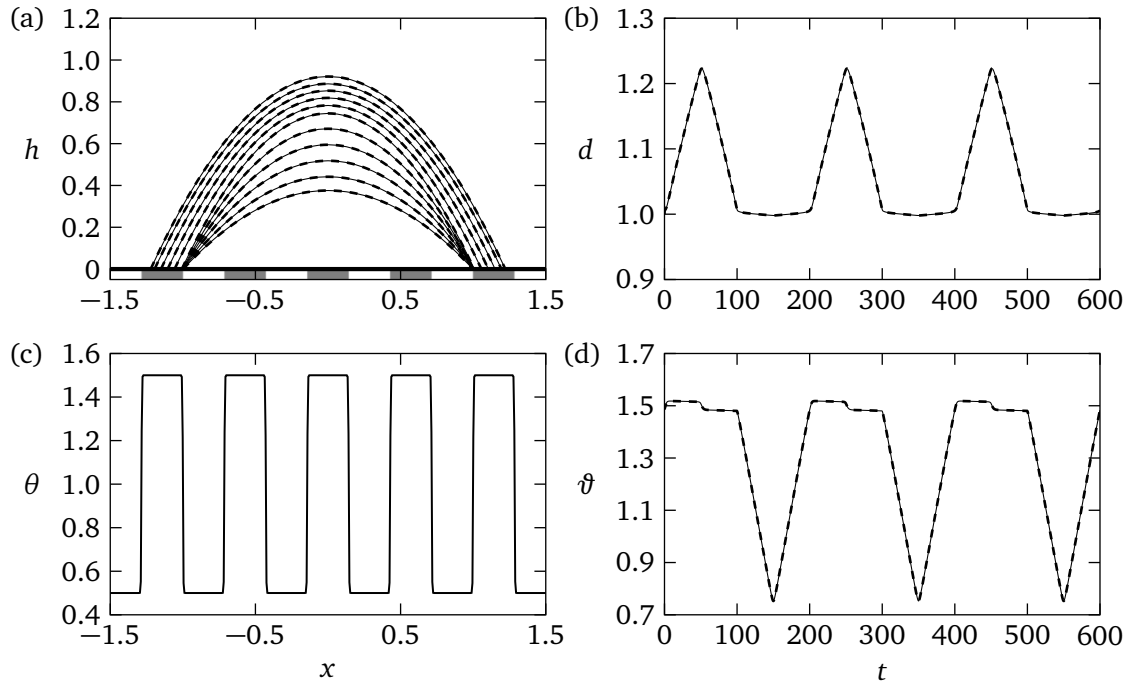
Figure 5.2: Alternating constant-angle and constant-radius modes on a substrate of alternating wettability patches with profile $\theta(x) = 1 + 0.5\tanh[30\cos(11x)]$. The mass flux is prescribed by (3.36) and $A(t)$ by (5.1) with $\mathcal{A} = 1$, $\tilde{\mathcal{A}} = 0.5$ and $\mathcal{P} = 200$. (a) Droplet profiles from $t = 50$ to $t = 150$ during mass loss in increments of 10 time units. Plots (b) and (d) are evolutions of the the droplet half-width and apparent contact angle, respectively. The substrate in (a) is shaded according to the values of $\theta(x)$ (plotted in (c)), where $\theta \approx 1 \pm 0.5$ are represented by the dark and light shaded patches, respectively.

robust and is sensitive to the system parameters. To demonstrate this, the calculation of figure 5.2 is repeated in figure 5.3, only changing the wavenumber of the heterogeneities and showing the evolution of the half-width $d(t)$ over a period after the fronts appear to settle to a periodic state. We observe that a different wavenumber can ultimately detune the dynamics of $d(t)$ shown in figure 5.2(b) and the system is able to exhibit markedly different behaviours. However, in principle, one can retune to the same qualitative dynamics by modifying other system parameters accordingly, for example, the way at which mass transfer occurs.

A manifestation of contact angle hysteresis in experiments is that the fronts remain pinned whenever the apparent contact angle falls between the values of the so-called receding and advancing contact angles (see Bonn *et al.* [23]). The combined effects of surface heterogeneities and mass transfer are able to capture such behaviours as well, without imposing *a priori* contact angle hysteresis. This is demonstrated in figure 5.4, for a substrate of alternating wettability patches. Fronts appear to be macroscopically pinned where the static angle transitions abruptly between the minimum and maximum contact angles, with
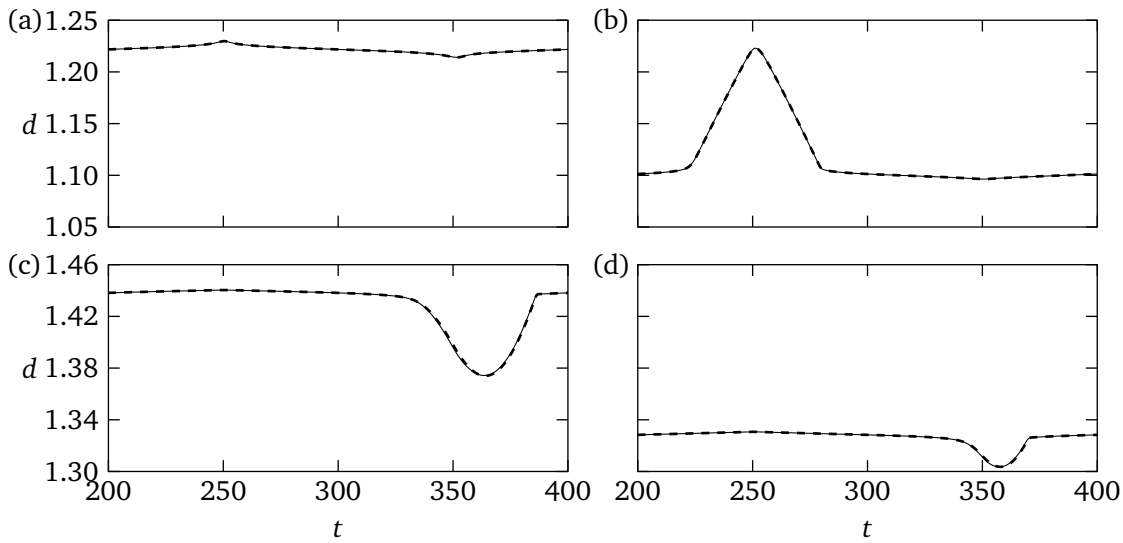
Figure 5.3:   Evolution of the half-width for the heterogeneity profile $\theta(x) = 1 + 0.5 \tanh[30 \cos(\omega x)]$ and different values of ω with all other parameters as in figure 5.2. (a) $\omega = 9$; (b) $\omega = 10$; (c) $\omega = 12$; (d) $\omega = 13$. Compare with figure 5.2(b) for which $\omega = 11$.
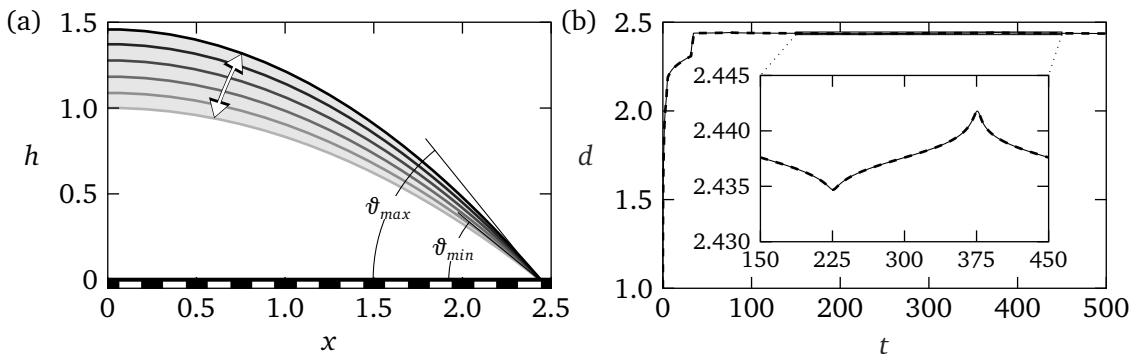
Figure 5.4: Macroscopic pinning on a substrate with profile $\theta(x) = 1 + 0.2 \tanh[20 \cos(8\pi x)]$. The mass flux is prescribed by (3.36) and $A(t)$ by (5.1) with $\mathcal{A} = 4$, $\tilde{\mathcal{A}} = 0.75$ and $\mathcal{P} = 300$. (a) Droplet profiles separated by 25 time units, over a period of liquid inflow/outflow. (b) Evolution of the droplet half-width, in which the contact points appears stationary macroscopically, but undergoes movements at the micro-scale (see inset).

the apparent contact angle varying approximately between these values. However, by zooming into the evolution of the half-width we observe that the fronts always exhibit movement, albeit at the micro-scale (for a millimeter-sized droplet, this would correspond to sub-micrometer motions along the substrate), a feature which is very accurately captured by the lower-dimensional system (3.35) (see inset of figure 5.4(b)). The use of heterogeneities as a plausible mechanism for hysteresis has also been invoked in the context of droplet motion on inclined surfaces to explain the pinning of the fronts as the inclination angle increased and the existence of a critical angle beyond which the substrate can no longer support the droplet
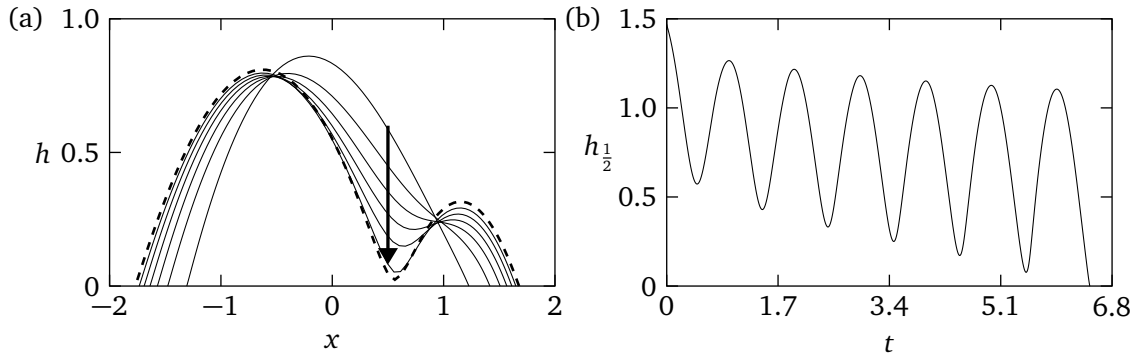
Figure 5.5: Droplet breakup due to a localised mass flux when $\theta(x) = 1$. Here fluid is injected/removed at $x_0 = 0.5$ and q is given by (5.2) with $S = 15$ and $A(t) = 2 + 0.6\cos(2\pi t)$. (a) Droplet profiles from $t = 0.5$ in increments of 1 time unit until $t = 5.5$ (direction of time indicated by the arrow). The dashed curve shows the profile when $t = 6.44$ where the computation was terminated. (b) Evolution of the droplet height at $x = 0.5$ showing the thinning of the profile where q is localised.

at equilibrium (see Savva & Kalliadasis [59]).

5.1.2 Localised Mass Flux

The simple flux distribution (3.36) previously revealed some of the qualitative features of the dynamics. For arbitrary spatio-temporal flux variations, the motion of the moving fronts is captured by (3.35) through the presence of $I_{\pm}$ terms, (3.27). In this section, the effects of localised mass transfer are explored, by representing $q(x,t)$ with the scaled Gaussian

$$q(x,t) = \frac{2\dot{A}(t)\sqrt{S}\,e^{-S(x-x_0)^2}}{\sqrt{\pi}\left\{\mathrm{erf}\left[\sqrt{S}(a_+ - x_0)\right] - \mathrm{erf}\left[\sqrt{S}(a_- - x_0)\right]\right\}}, \tag{5.2}$$

whose peak is located inside the droplet footprint at x_0, and the prefactor is chosen to satisfy (2.53e) (here 'erf' denotes the error function). When $S > 0$ is sufficiently large (in the limit $S \to \infty$, $q \to \dot{v}\delta(x - x_0)$), we can use (5.2) with $a_-(t) < x_0 < a_+(t)$ to argue that $q_{\pm} \approx 0$, so that we may use the reduced system (3.35) instead of the more complete system (3.34). As mentioned previously, the full model requires a considerably denser mesh to resolve the spatial variations of q prescribed according to (5.2). For this reason, we used only moderate values for S to achieve a satisfactory compromise between a fast decay of q towards zero, and computational efficiency.

It is worth noting that localised fluxes may lead to droplet breakup when $|\dot{A}| \gg |\dot{a}_{\pm}|$, which is beyond the quasistatic limit of applicability of our theory. In such cases, the full PDE needs to be considered. Such an example is shown in figure 5.5 where we observe that the rapidly changing localised flux creates a neck region in the vicinity of the fluid inlet/outlet,
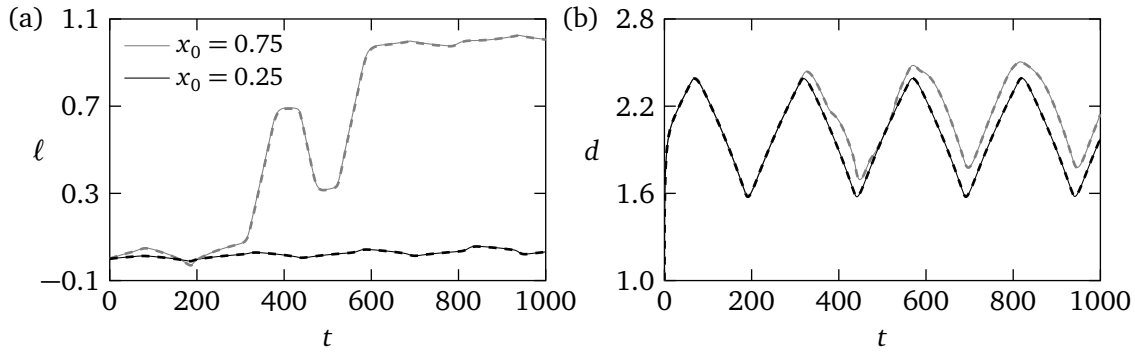
Figure 5.6: Effect of changing the position of the flux in over the substrate with profile $\theta(x) = 1 + 0.1\tanh[5\cos(\pi x)]$. The mass flux is given by (5.2) with $S = 20$ and $A(t)$ is prescribed by (5.1) with $\mathcal{A} = 3$, $\tilde{\mathcal{A}} = 1.25$ and $\mathcal{P} = 250$. Plots (a) and (b) are evolutions of the droplet midpoint and half-width for differently positioned fluxes.

which progressively becomes thinner and ultimately leads to breakup. In this example, the calculation was terminated just before the droplet height vanished at some point between the two contact points, thus avoiding the development of schemes to deal with the actual breakup and the resulting dynamics after it occurs.

Many of the interesting features reported previously for fluxes of the form (3.36) also pertain for the localised fluxes as well. However, if the mass flux is localised, more control may be exercised on how the droplets move on surfaces. If mass transfer occurs sufficiently slowly, it causes the droplet to move, to the extent permitted by heterogeneities, so as to centre around the inlet/outlet point. This, in turn, may require more time for the droplet to settle to periodic motion. This effect is highlighted in figure 5.6, showing that the droplet midpoint defined as $\ell = (a_+ + a_-)/2$ evolves very differently depending on where the inlet/outlet is located. Importantly, the excellent agreement of the reduced model with the full equations demonstrates the importance of including the $O(\dot{A}/|\ln\lambda|)$ terms in (3.35), which merely correspond to higher-order contributions to the leading-order terms at $O(1/|\ln\lambda|)$.

5.1.3   Transition to Periodic Dynamics

The previous examples demonstrate that the dynamics ultimately becomes periodic in the long-time limit if mass changes are also periodic. Apart from the cases shown in figure 5.6, we observe that the transition to periodic motion occurs around the first period of inflow and outflow, but it may be significantly prolonged depending on the heterogeneity profile. When $\theta(x)$ is suitably chosen it may allow for longer excursions away from the initial droplet position, which may violate the assumption for the flux to be localised somewhere between
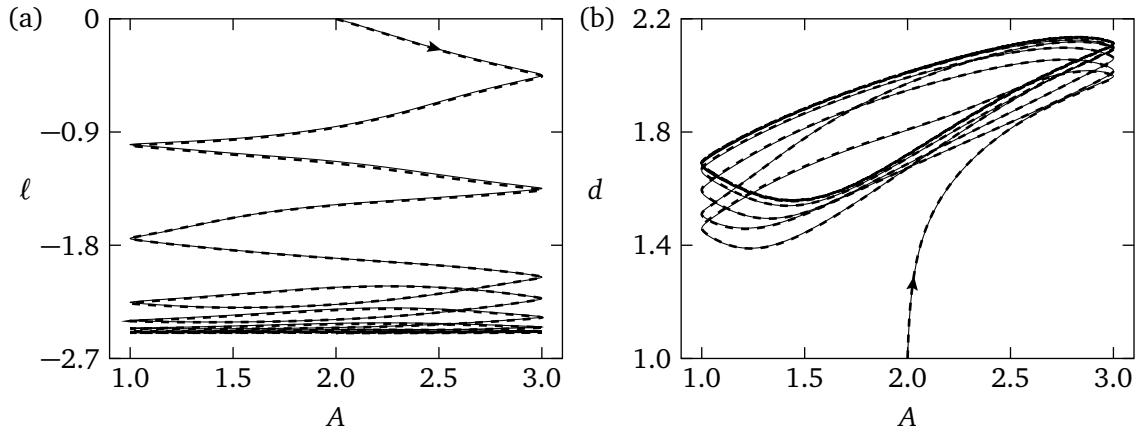
Figure 5.7: Slow settling to periodic dynamics when $\theta(x) = 1 + 0.1\cos(8\pi x/5) + 0.2\cos(\pi x/5)$. The mass flux is prescribed by (3.36) and $A(t)$ by (5.1) with $\mathcal{A} = 2$, $\tilde{\mathcal{A}} = 1$ and $\mathcal{P} = 100$. Plots (a) and (b) show the midpoint ℓ and half-width d as functions of the droplet area A, respectively.

the two contact points for (3.35) to hold. A remedy for this issue is to allow the location of the inlet/outlet to follow the droplet as time progresses. However, for studying these transitions, it suffices to just represent q by (3.36).

Such a calculation is depicted in figure 5.7, where a shorter period of mass transfer and a combination of harmonics for $\theta(x)$ is used, plotting how the half-width d and midpoint ℓ evolve with the droplet area $A(t)$. We readily observe that the droplet requires several more cycles to settle to a periodic motion, where, once more, the reduced model (3.35) excellently captures the dynamics predicted by the full model. For this choice of $\theta(x)$ the wettability contrasts are not as pronounced compared to, say, those of figure 5.2, which allows the droplet fronts to move more freely. As a result, pinning effects are weaker, which appear to prolong the transition to periodic dynamics.

Hence, it is important to acknowledge that the dynamics is strongly influenced by the interplay between mass flux and substrate features. In figure 5.8, we compare the mid-point dynamics for two different periods of inflow/outflow using (3.36) for a droplet moving over the same substrate. For the shorter period, the droplet settles to a periodic state within the first period of inflow/outflow (figure 5.8(a)); for the longer period the droplet undergoes multiple mass flux cycles before settling to the periodic state, while it is being shifted an order unity distance to a different region of the substrate (figure 5.8(b)). This example highlights that more slowly varying mass fluxes are more strongly influenced by substrate heterogeneities, thus suggesting that the effects of surface heterogeneities can be mitigated by increasing the
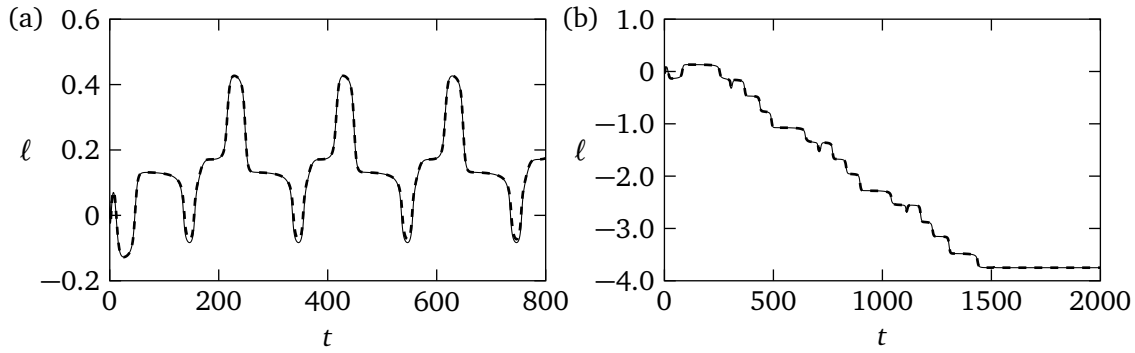
Figure 5.8: Delayed transition to periodic motion by changing the period of mass flux. Heterogeneities are prescribed through $\theta(x) = 1 + 0.1\cos(8\pi x/5) + 0.3\sin(10\pi x/3)$. The mass flux is prescribed by (3.36) and $A(t)$ by (5.1) with $\mathcal{A} = 2.5$, $\tilde{\mathcal{A}} = 1.5$ and different values for $\mathcal{P}$. Evolution of ℓ for (a) $\mathcal{P} = 200$ and (b) $\mathcal{P} = 400$.

mass flux rates, and that we can afford more control on droplet motion by coupling slowly varying fluxes with appropriately tuned surface heterogeneities.

5.1.4 Snapping Droplets

We have seen thus far that stick-slip events occur on typically faster time scales if the contact line is temporarily trapped on sharp wettability contrasts. In a recent study, Wells *et al.* [150] reported that for a sufficiently slowly evaporating droplet a different mode can be observed, which is marked by a series of distinct snapping events, during which the droplet shifts over a short time scale towards a different location on the substrate. Specifically, Wells *et al.* considered sinusoidal surface topographies both experimentally and numerically and observed that droplets can break the left-right symmetry as their contact line retracts due to evaporation, allowing them to move as a whole to a new location, but at a slower time-scale than typical stick-slip jumps. Similar effects may be observed with chemically heterogeneous surfaces as well. This is depicted in figure 5.9 for droplets of linearly decreasing mass and a substrate with heterogeneities prescribed according to

$$\theta(x) = 1 - \frac{1}{5}\tanh[50\cos(\pi x)] + \tilde{\theta}(x), \tag{5.3}$$

where $\tilde{\theta}(x)$ corresponds to band limited white noise represented by a superposition of harmonics of wavenumbers up to 10π, whose amplitudes are normally distributed with zero mean and standard deviation of 0.005. This profile has a lower wettability contrast to that of figure 5.2, whereas the low amplitude random features introduced by $\tilde{\theta}(x)$ promote the breaking of symmetry (see figure 5.9(c)). A comparison of figures 5.9(a) and 5.9(b) shows
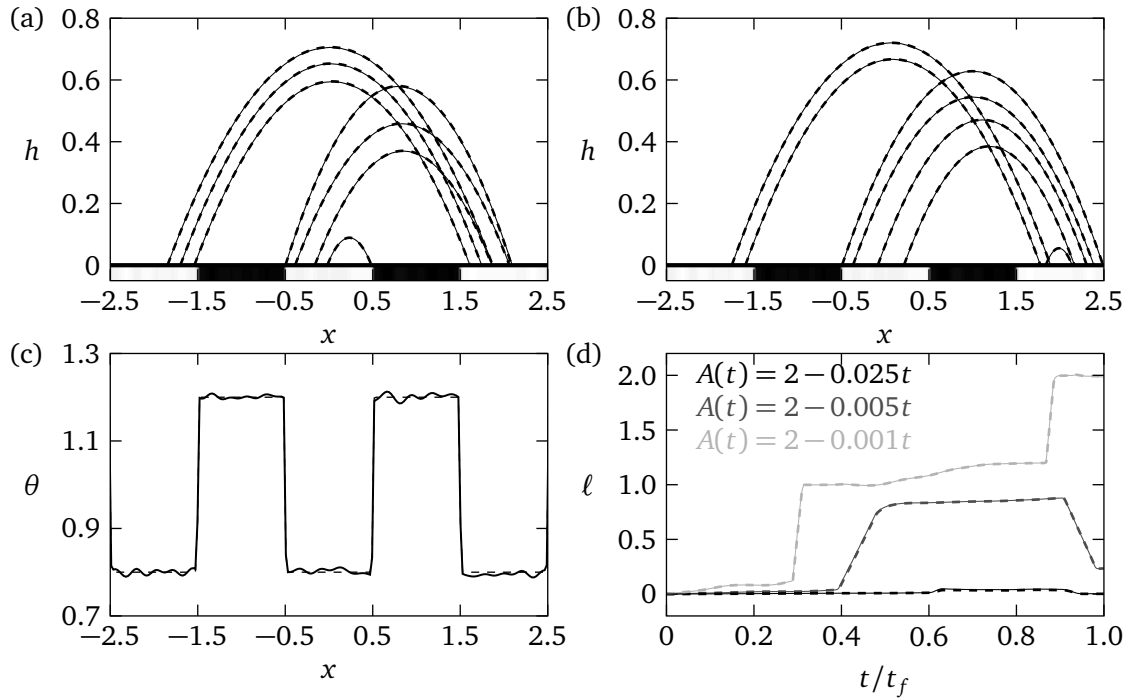
Figure 5.9: Snapping mode dynamics using (3.36) for the mass flux and linear mass loss according to $A(t) = 2 - \omega t$ (a) Droplet profiles when $\omega = 0.005$ plotted at times $t = 50$ to $t = 300$ in increments of 50 time units with the last profile at $t = 395$. (b) Profiles for area when $\omega = 0.001$ at times $t = 250$ to $t = 1500$ in increments of 250 time units and the last profile at $t = 1990$. (c) The realisation of the heterogeneity profile which is used in simulations (solid curve) and its noise-free counterpart given by $\theta(x) = 1 - 0.2 \tanh[50 \cos(\pi x)]$ (dashed curve). (d) Evolution of the mid-point as function of the normalised time t/t_f, where $t_f = 79$ for $\omega = 0.025$, $t_f = 399$ for $\omega = 0.005$, and $t_f = 1999$ for $\omega = 0.001$.

that the rate at which mass is lost plays a key role in the underlying motion. In both cases we initially have symmetrically receding fronts, until a snapping event occurs which shifts both droplets to the right. Depending on the rate of mass loss, a second snapping event occurs prior to extinction pushing the droplet to the left (faster mass loss, figure 5.9(a)) or to the right (slower mass loss, figure 5.9(b)). Figure 5.9(d) shows the evolution of the droplet mid-point in normalised time units and clearly demonstrates that the faster rate of mass loss completely suppresses the snapping event, whereas the snapping transitions for the slowest rate become more abrupt. This further corroborates our earlier assertion that, for heterogeneities to play a more predominant role, the rate at which fluid inflow/outflow occurs needs to be sufficiently slow. Similar observations can also be made with dynamics of mass gain as well, or even if mass transfer occurs periodically.

(a)   (b)
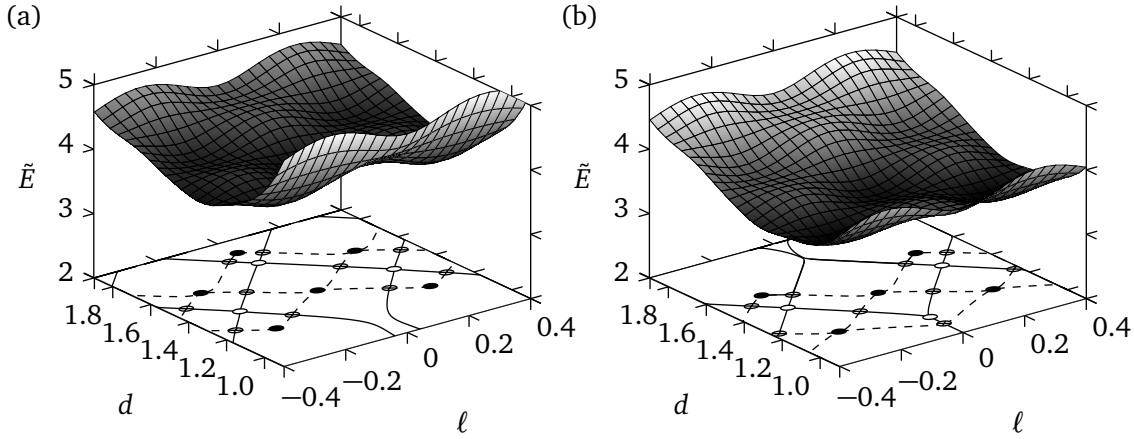
Figure 5.10: Interfacial energy for surfaces with heterogeneities prescribed according to $\theta(x) = 1 + 0.5\cos(4\pi x)$ when (a) $A = 1$, and (b) $A = 1.25$. Solid, open and crossed circles correspond to the stable, unstable and saddle points, respectively. Solid and dashed lines show the stable and unstable manifolds for the saddle nodes, respectively.

5.1.5 Bifurcation Analysis

To better understand the mechanisms for the behaviors observed as the system parameters vary, an alternative approach involves recording the nature and location of the resulting equilibria for different values of A. Hence, by treating A as a bifurcation parameter, we can trace how the location, nature and stability of these equilibria vary, which can then be contrasted with time-dependent simulations. For fixed A, the equilibria and their nature can be determined from the interfacial energy of the system defined in dimensionless long-wave form as (see Vellingiri *et al.* [55])

$$\tilde{E}(\ell, d) = \int_{\ell-d}^{\ell+d} \left[(\partial_x h_0)^2 + \theta(x)^2 \right] dx. \tag{5.4}$$

The extrema of $\tilde{E}$ correspond to the equilibria of the system, whose nature and stability can be assessed straightforwardly from the determinant of the Hessian matrix of $\tilde{E}(\ell, d)$. Figure 5.10 shows such an example for a specific heterogeneity profile and two nearby values of A. The figure also shows the equilibria projected on the $\ell - d$ plane together with the stable and unstable manifolds of the saddle points, which were computed from the IDE system (3.35) for $q \equiv 0$ and demarcate the basins of attraction of the stable equilibria. We see that changes in A result into bifurcations that alter the structure of the corresponding phase plane. By comparing figures 5.10(a) and 5.10(b), we observe the formation and destruction of equilibria, which ultimately reveal that dynamic changes in A can lead to appreciable changes in the motion of the droplet fronts. For example, compare the two phase portraits in figure 5.10
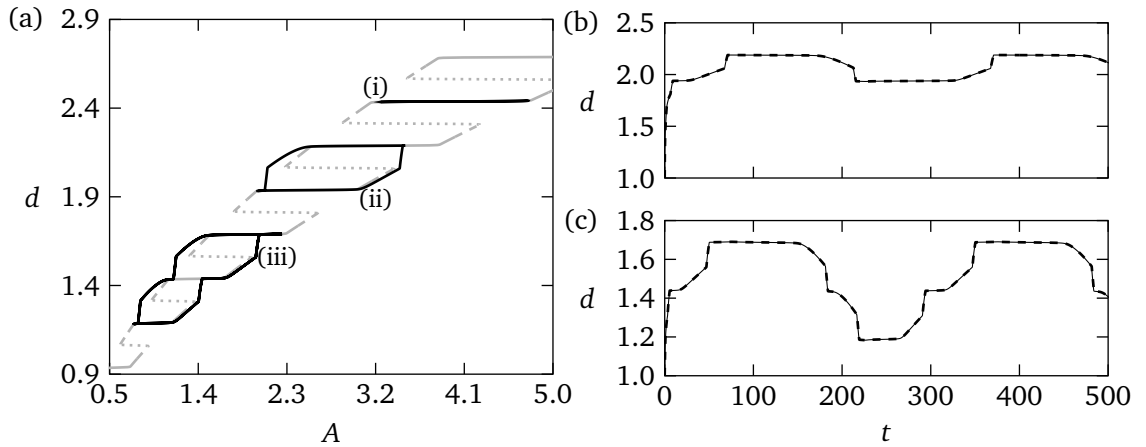
Figure 5.11: (a) Bifurcation diagram projected on the $A - d$ plane when $\theta(x) = 1 + 0.2 \tanh[20 \cos(8\pi x)]$ with overlaid dynamic simulations. Grey solid, dashed and dotted curves correspond to stable, saddle and unstable branches of the bifurcation diagram, respectively. Black curves are solutions to the reduced system (3.35), obtained with the same parameters as in figure 5.4 but with different values for $\mathcal{A}$: (i) $\mathcal{A} = 4$; (same as in figure 5.4) (ii) $\mathcal{A} = 2.75$ and (iii) $\mathcal{A} = 1.5$. Plots (b) and (c) are evolutions of the droplet half-width corresponding to curves (ii) and (iii) in (a), respectively, as obtained from the full (solid curves) and reduced (3.35) models.

in the close vicinity of $\ell = 0$; equilibria disappear when they collide as A is increased (for $d \approx 1.7$), or new equilibria form when previously non-intersecting manifolds meet (for $d \approx 1$). When such topological changes/bifurcations occur for sufficiently slow variations in A, the droplet responds to these changes by appreciably altering its motion. In other words, the droplet fronts are expected to closely trace how the corresponding equilibria evolve had A been treated as a bifurcation parameter, and the observed de-pinning events, such as stick-slip, the snapping mode or the transition from the constant-radius to the constant-angle modes are merely manifestations of the dynamics that arise due to the topological changes in the basins of attraction of nearby equilibria.

Similar work has been undertaken by Pradas *et al.* [125] using diffuse interface simulations in 2D. Unlike the work in [125], our work is limited to small contact angles, but our asymptotic analysis allows for a more efficient exploration of the parameter space, as well as a longer simulation of the system over many cycles of mass gain and loss to capture the transition to periodic motion. The remainder of this section is devoted to uncovering these bifurcation structures in the 3D space spanned by ℓ, d and A, when A is treated as a bifurcation parameter. The equilibrium branches were obtained by pseudo arc-length numerical continuation techniques for carefully chosen conditions to trace each branch (see
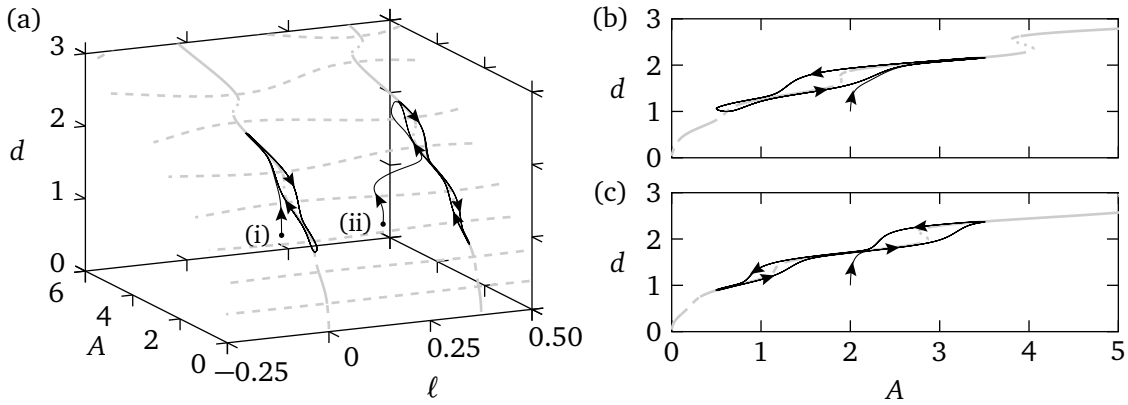
Figure 5.12: (a) Bifurcation structure for the substrate defined by $\theta(x) = 1 + 0.15\cos(8\pi x/3)$ in the $A-\ell-d$ plane (grey curves) with two overlaid calculations of the reduced model (black curves labelled (i) and (ii)). The styles of the grey curves are as in figure 5.11(a). Curves (i) and (ii) are obtained from equations (3.35) and (3.36); A is given by (5.1) with $\mathcal{A} = 2$, $\tilde{\mathcal{A}} = 1.5$ and $\mathcal{P} = 250$, using $a_\pm(0) = \pm 1$ for curve (i) and $a_+(0) = 0.5$ and $a_-(0) = -1.5$ for curve (ii). Plots (b) and (c) are slices of the bifurcation diagram in (a) showing, respectively, curves (i) and (ii) projected on the $A - d$ plane.

Allgower & Georg [216]).

One of the most interesting features shown in this work, which is not discussed by Pradas *et al.* [125] and is worthy of further investigation is the apparent contact angle hysteresis in figure 5.4, namely that the droplet appears to be pinned as liquid is pumped in and out of the droplet, but moves at smaller spatial scales. Figure 5.11(a) shows an overlay of the data in figure 5.4 (plot (i)) and the bifurcation diagram projected on the $A - d$ plane. For this example, A varies between 3.25 and 4.75, and is able to trace one of the stable branches of the bifurcation diagram for which d is nearly constant. Had A oscillated with a sufficiently larger amplitude beyond the span of the stable branch, de-pinning of the fronts and a transition to another stable branch with different d would have occurred. This is shown by plotting the evolution of the half-width for droplets of smaller mean size in figure 5.11(b) (plot (ii) in (a)) and figure 5.11(c) (plot (iii) in (a)), where the corresponding pinning/de-pinning events are clearly distinguished.

When substrates are decorated with strong wettability contrasts, the dynamics described above undergo abrupt transitions as the stable branches of the bifurcation diagram are traversed (see figure 5.11). In reality, the moving fronts only remain close to the bifurcation branches, but do not exactly trace them. This is a consequence of the fact that the bifurcation diagrams describe droplet equilibria for fixed values of A, whereas simulations describe dynamic phenomena and it is the quasi-steady character of the dynamics that allows us to
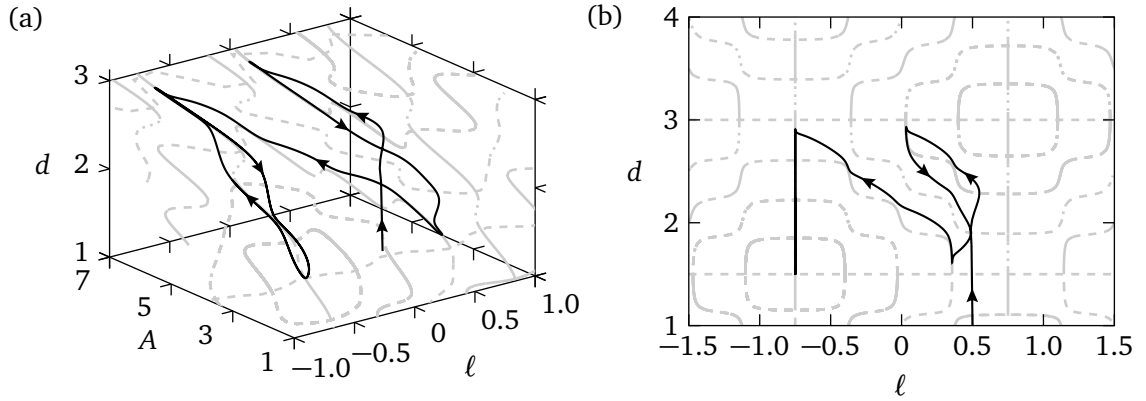
(a)

(b)

Figure 5.13: Delayed transition to periodic dynamics for the substrate $\theta(x) = 1 + 0.15\cos(8\pi x/3) + 0.05\sin(2\pi x)$ as visualised on a bifurcation diagram. (a) Bifurcation structure in the $A - \ell - d$ plane with an overlaid ODE trajectory obtained from equations (3.35) and (3.36); A is given by (5.1) with $\mathcal{A} = 4$, $\tilde{\mathcal{A}} = 2.5$ and $\mathcal{P} = 200$, using $a_+(0) = 1.5$ and $a_-(0) = -0.5$. (b) Projection of the plots in (a) on the $\ell - d$ plane. The style of the various curves are as in figure 5.11.

make meaningful visual comparisons between dynamic behaviors and these diagrams. If the heterogeneity features are represented by a single harmonic, the resulting equilibrium branches will contain more readily identifiable pitchfork bifurcations, as shown in figure 5.12. Like before, the droplet dynamics closely follows the stable branches of the system away from bifurcation points. Close to a bifurcation point, where typically a stable branch becomes unstable as A is varied, the dynamics of the system is slower to respond to this change and tends to overshoot away from the bifurcation points before approaching a nearby stable branch shortly afterwards. This overshooting has also been observed by Pradas *et al.* [125], and, generally, the departure of the actual dynamics away from the bifurcation curves becomes more pronounced if the contact lines become more mobile, which may result from more rapidly changing mass fluxes and stronger slip effects.

A more realistic representation of the heterogeneities of an actual substrate is expected to consist of many more harmonics than the simple harmonic of the profile considered in figure 5.12 due to typically unavoidable randomness in its features (see Savva *et al.* [84]). Such representations, however, make the investigation of the corresponding bifurcation structures unwieldy. To demonstrate this, figure 5.13 shows how the complexity of the bifurcation structure of figure 5.12 increases with the inclusion of an additional, low-amplitude harmonic in the heterogeneity profile of figure 5.12. For such a profile and depending on the initial state of the system, we can anticipate delayed transitions to periodic motion as the droplet fronts

navigate the space of nearby quasi-steady states until they reach a limit cycle in the long-time limit (see, e.g., the overlaid trajectory in figure 5.13).

Although the outcomes we have given here cannot be easily scrutinised by experiments, in this exploratory work we elucidated some of the key behaviours that arise in experimental settings. Through a number of cases we have demonstrated an intricate interplay between the various effects, showing how the dynamics can appreciably change if small changes are introduced to the chemical heterogeneities or fluid flow properties. In the coming sections we will extend the discussion and consider the more realistic 3D scenario where qualitative comparisons will be made to experimental observations.

5.2   3D Droplets on Chemically Heterogeneous Surfaces with Constant Mass

Throughout this section we consider 3D droplets spreading over flat and horizontal substrates. Unless otherwise stated, from this point onwards we fix $a(\phi, 0) = 1$, $(x_c(0), y_c(0)) = (0, 0)$, simulate with $\lambda = 10^{-3}$, and plot solutions to the full, hybrid and reduced models by solid, dashed and dotted curves, respectively. We choose λ to take a larger value simply because 3D simulations require significantly more computational time and resources, which become even more troublesome if we simulate up to higher values of t (which occur in upcoming sections exploring variable mass).

We start by discussing a small selection of the findings reported in [61] in the case of constant mass ($q = 0$). As explained in section 3.2 the reduced model for this situation is easily obtained by setting $\dot{v}(t)$ terms to zero in (3.98). The results shown here are chosen to highlight the merits of the analysis performed, and present the reasoning behind including the full expansion (3.44) rather than (3.46).

5.2.0.1   Complex Patterns and Higher-Order Effects

Here we show two examples involving complex patterned substrates. The first example is that of a dartboard pattern defined by the equation

$$\theta(x, y) = \frac{6}{5} + \frac{4}{5} \tanh \left\{ 10 \sin \left[6 \arctan \left(\frac{y}{x} \right) \right] \right\} \tanh \left[10 \sin \left(\pi \sqrt{x^2 + y^2} \right) \right], \qquad (5.5)$$
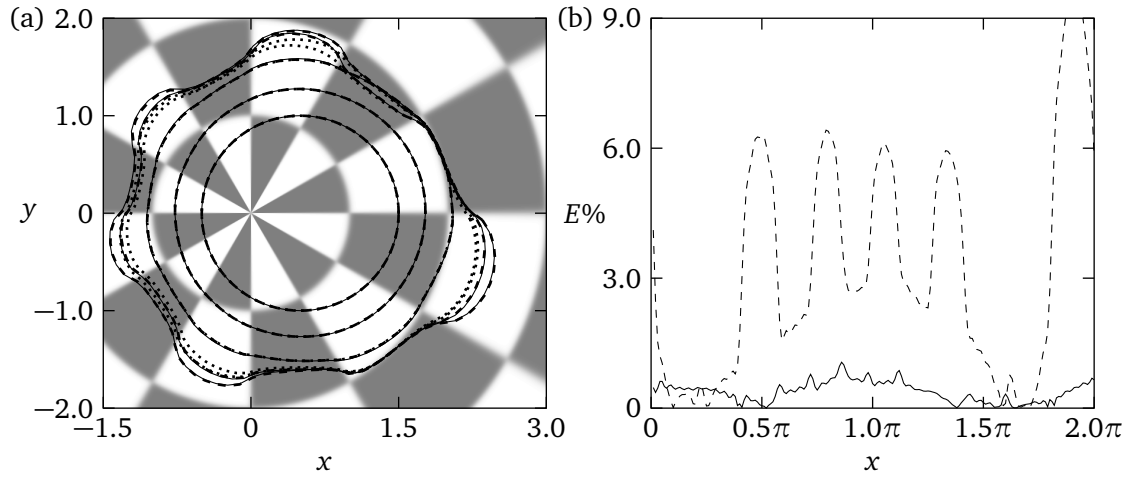
Figure 5.14: Spreading on the dartboard pattern given by (5.5) with $\lambda = 10^{-4}$, $x_c(0) = 0.5$, $y_c(0) = 0$ and $a(\phi, 0) = 1$. (a) Snapshots of the contact line when $t = 0$, 0.05, 0.5, 5 and 40. Solid, dashed and dotted lines correspond to the full, hybrid and reduced models, respectively. The substrate is shaded according to (5.5) where light patches are areas of higher wettability than darker ones. (b) The relative change in the values of $a(\phi, t)$ obtained from the full model compared to the reduced model (dashed curve) and the hybrid approach (solid curve) when $t = 30$.

where the values of θ vary between roughly 0.4 and 2. The results of the calculations using (5.5) are shown in figure 5.14 and demonstrate the excellent agreement of the hybrid approach with the full problem, where at all times the predictions of the contact line locations differ by less than 1% (see figure 5.14(b)). In contrast, the reduced model exhibits excellent agreement at the early stages of the dynamics, but as the droplet approaches equilibrium we see differences of up to 10% from the full model (see also the profiles in figure 5.14(a) when $t = 5$ and 40). This is to be expected given that the droplet develops pronounced protrusions as the contact line fronts invade the more wettable regions of the substrate, so the assumption that the contact line is nearly circular ceases to be valid.

The second example where we compare the calculations of the full model and the predictions of our theory concerns a more contrived setting where we superimpose a chequerboard pattern and a chemical gradient inducing a directional motion towards the more hydrophilic regions of the substrate. More specifically, the spatial variations of the contact angle are prescribed according to

$$\theta(x, y) = \frac{11}{5} + \frac{1}{\pi}\left\{1 - \frac{1}{4}g_1(x, y)\right\}g_2(x, y)\arctan\left(\frac{y}{x}\right) + \frac{1}{3}g_1(x, y), \qquad (5.6)$$

where the inverse tangent provides the gradient

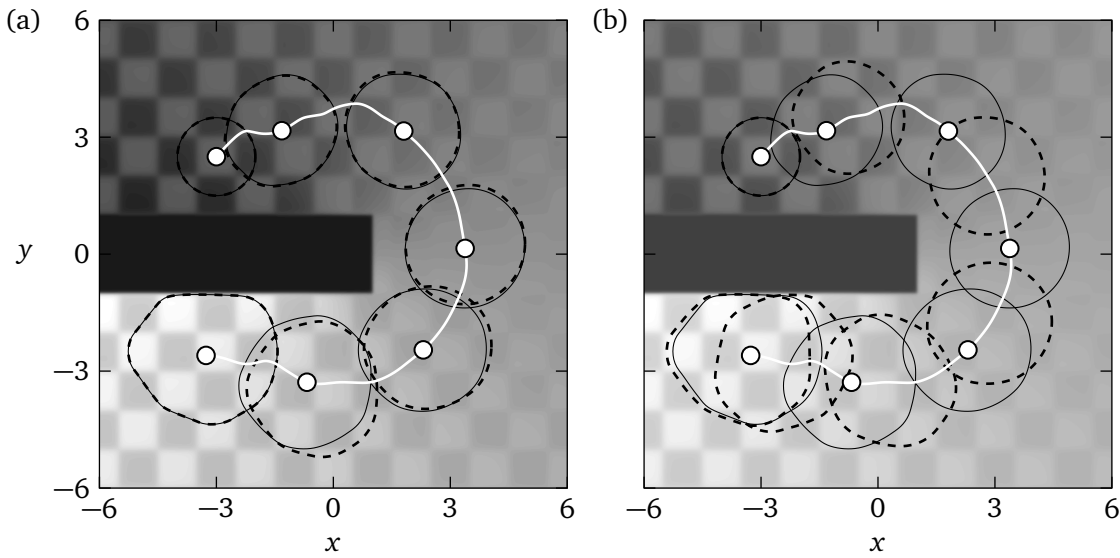$$g_1(x, y) = [1 - \tanh[20(y + 1)]\tanh[20(y - 1)]]\{1 - \tanh[20(x - 1)]\}, \qquad (5.7)$$

Figure 5.15: Snapshots of the contact line for a droplet moving on a substrate with $\theta(x,y)$ given by (5.6), $x_c(0) = -3$, $y_c(0) = 2.5$ and $a(\phi, 0) = 1$. The droplet migrates from the less hydrophilic region (top) to the more hydrophilic region (bottom). Snapshots correspond to times $t = 0, 20, 60, 100, 140, 200$ and 400. The white curve tracks the motion of the centroid of the contact area; white circles show the centroid locations corresponding to each of the snapshot shown. The solid curves correspond to the solution to the full problem. The dashed curves in (a) and (b) correspond, respectively, to the solutions to the hybrid problems using the expansion (3.46) and Lacey's result, (1.6).

is roughly equal to 4 when $|y| \leq 1$ and $x \leq 1$ and is used to mask the region where the inverse tangent is multivalued and

$$g_2(x,y) = 1 + \frac{3}{10} \tanh\left[3\cos(\pi x)\right] \tanh\left[3\sin(\pi y)\right], \tag{5.8}$$

provides a chequerboard pattern. For this choice of θ, the contact angle is about 3.5 when $|y| \leq 1$ and $x \leq 1$, so that it poses essentially a wettability barrier, which the droplet avoids. The minimum contact angle is roughly unity.

The reason for this choice is basically to test our theory in the case when the droplet undergoes a long excursion from its original position. Snapshots of the contact line are shown at different times in figure 5.15, where we see how the droplet evolves as it seeks an equilibrium towards the more hydrophilic region of the substrate. Interestingly this is not the only equilibrium, noting that there can also exist equilibria in the less hydrophilic region, near the initial droplet location (not shown here).

Although the contact line remains nearly circular at all times, the discretisation in the azimuthal direction requires a dense mesh because the value of the contact angle along the contact line exhibits sharp variations due to the chequerboard pattern. However, we
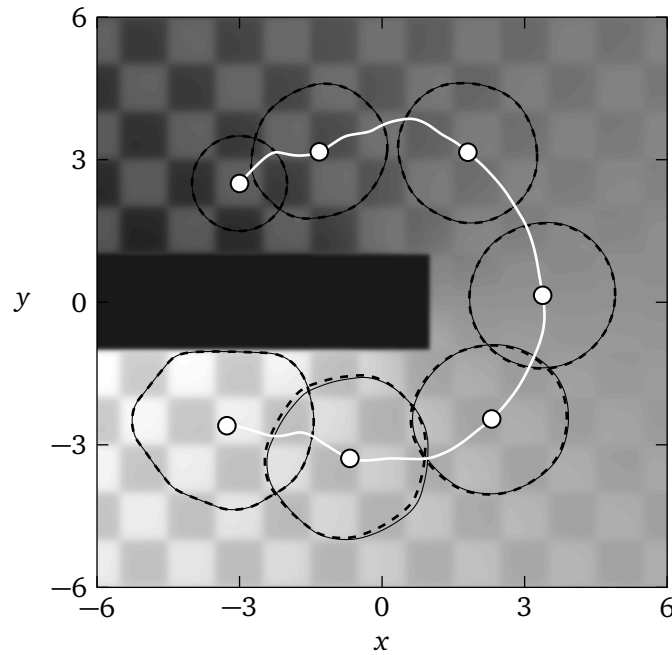
Figure 5.16: Repetition of the calculation of figure 5.15 using the improved hybrid method (i.e. (3.98)). Refer to figure 5.15 for the description of the various curves.

see appreciable deviations from the predictions of the hybrid and full problems (see figure 5.15(a)). The reduced problem gives very similar results as the hybrid one, but the comparison of the full problem with the leading-order asymptotic result from Lacey, (1.6), is rather poor (see figure 5.15(b)), illustrating the importance of going beyond the leading-order terms in the asymptotic analysis.

The discrepancy, which becomes more prominent at intermediate times, can be attributed, at least in part, to the logarithmically-singular terms omitted when considering the expansion (3.46). This can be alleviated by the analysis presented in section 3.2 where the full expansion (3.44) is considered. Although the full expansion yields more involved models, the simulation times were not appreciably affected. In figure 5.16 we repeat the calculations of the hybrid model using the system of equations which account for the additional terms. Although the contributions of these additional terms are expected to be generally small, it is clear that the agreement with the hybrid method improves appreciably. The small discrepancies that still remain at intermediate times may be attributed to various, perhaps equally valid factors, such as errors introduced by the spatial and/or time discretisation or the fact that our theory is based on more stringent assumptions than those required for such a computation to be accurately captured. For these reasons we did not deem necessary to pursue this further, especially given that the agreement we observe is generally very good considering also the very short

computation time with the hybrid (under 7 minutes) and reduced models (about 30 seconds), which is order of magnitudes faster compared to the simulation of the full model which took about 28 hours to complete and required significantly more computational resources (16 cores working in parallel compared to single-core computations with the other methods).

5.3   3D Prescribed Variable Mass

In this section we consider droplets of variable mass, where the flux changes occur in the droplets footprint and disappear at the contact line, like in section 5.1.

Generally, we investigate cases where the chemical heterogeneities $\theta(x, y)$ do not vary too sharply to avoid issues with retracting contact lines. In such cases the contact line tends to develop sharp localised features where the spatial discretisation under resolves such shapes. This could be resolved by introducing an adaptive meshing technique that places collocation points towards the position of greatest curvature. However, we did not pursue the intricacies of such cases since we are mainly interested in exploring in general the balance between liquid flux and chemical heterogeneity.

Just like the 2D case we consider $\mathcal{P}$-periodic fluctuations in the droplet mass, using the slightly modified version of (5.1)

$$v(t) = \mathcal{V} + \frac{\tilde{\mathcal{V}}}{\tan^{-1}(20)} \tan^{-1} \left[\frac{20 \sin(2\pi t/\mathcal{P})}{\sqrt{1 + 400 \cos^2(2\pi t/\mathcal{P})}} \right], \tag{5.9}$$

noting the change from $\mathcal{A}$ and $\tilde{\mathcal{A}}$ to $\mathcal{V}$ and $\tilde{\mathcal{V}}$, respectively, so that we can denote volumes rather than areas.

5.3.1   Random Substrates

In the first example for droplets with variable mass we consider a case motivated by the experimental results recorded by Dietrich *et al.* [217] who investigate stick-slip behaviours with droplets undergoing mass loss by dissolution. Specifically, the authors track droplets which enter a series of pinning/de-pinning events as the droplet loses mass, and record the stick-slip transitions that occur in consequence to the de-pinning events. While the analysis presented in section 3.2 does not account for evaporation, which is more prominent in the inner-region analysis (see section 3.3 and Saxton *et al.* [164] for further details), one can in principle emulate such a situation by considering a simple linear decrease in mass with
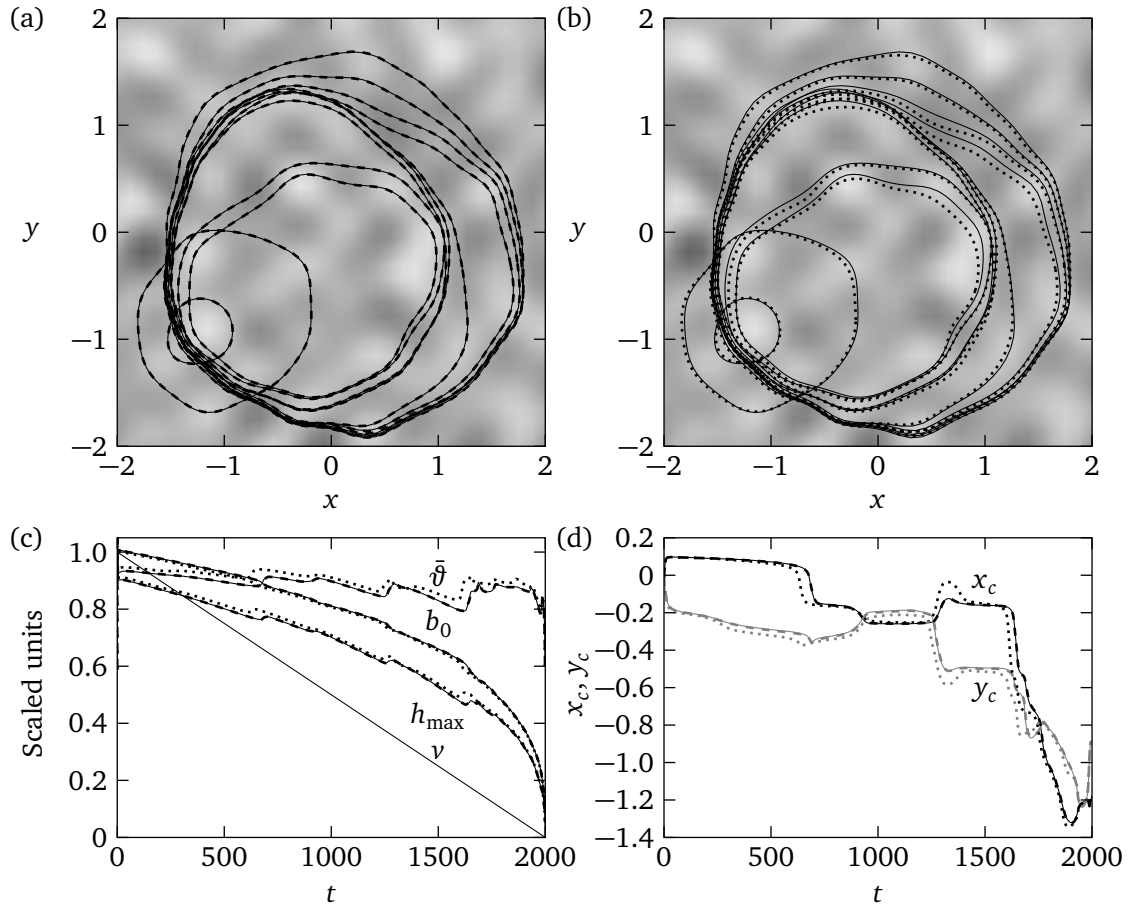
Figure 5.17: Stick slip events similar in appearance to the observations of Dietrich *et al.* [217]. The droplet loses mass according to $v(t) = \pi(2 - 0.001t)$ (using the flux distribution (3.105)) over a substrate generated with randomly distributed features (see text for the substrate generation). Plots (a) and (b) are droplet contact line profiles at various times. (c) The mean radius b_0, mean macroscopic angle $\bar{\vartheta}$, maximum height $h_{\max}$, and volume v which are scaled by 1.7, 1.7, 1.5 and 2π, respectively. (d) The centroid evolutions where x_c is plotted in black, and y_c is plotted in grey.

the distribution of flux (3.105). To mimic realistic based scenario where substrates typically exhibit spatial noise in the wettability, we generate heterogeneous surfaces of the form

$$\theta(x,y) = \hat{\theta}(x,y) + \tilde{\theta}(x,y). \tag{5.10}$$

Here $\hat{\theta}(x,y)$ is a prescribed function and gives the predominant structure of the substrate, and $\tilde{\theta}(x,y)$ corresponds to band limited noise. In the 2D study similar substrates were considered and gave rise to the snapping mode observed experimentally by Wells *et al.* [150] (see figure 5.9), here, they are used to view if realistic dynamics arise naturally from simulations.

Figure 5.17 shows a case where we consider a substrate of the form (5.10) where we set $\hat{\theta}(x,y) = 1.5$ and $\tilde{\theta}(x,y)$ is represented by a superposition of 75 harmonics with wavenumbers up to 3π and whose amplitudes are normally distributed with zero mean and
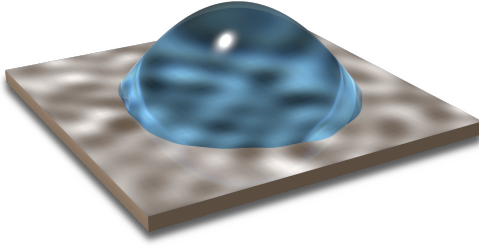
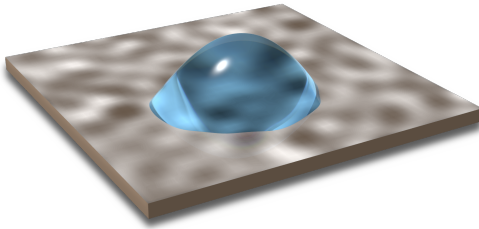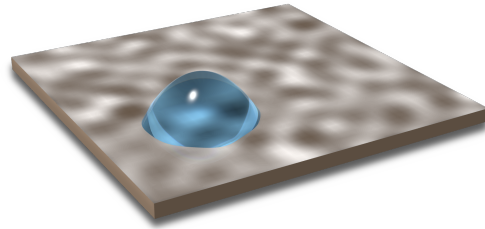(a)   (b)
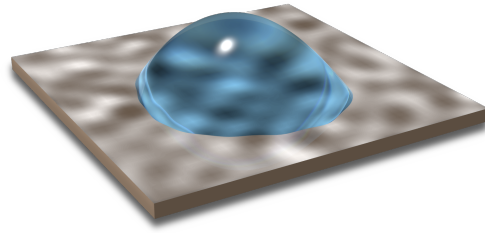
(c)   (d)

Figure 5.18: Droplet profiles for the simulation in figure 5.17 at times $t = 100$, $t = 800$, $t = 1390$, and $t = 1790$ for plots (a) - (d), respectively.

unit variance. By tracking the mean values of $a(\phi, t)$ and the apparent contact angle ϑ we observe a qualitatively similar comparison to the observations recorded in figure 2 of [217], noting the height is given at the maximum point, i.e. $h_{\max} = b_0 \bar{\vartheta}/2$. Although measurements in experiments are usually taken from a 2D slice coming from images, the purpose of the measurements recorded in figure 5.17 is to show that such features can naturally arise. Besides, recording the mean values can be viewed as reasonable for fluctuating contact lines which do not deviate too drastically from a circular radius (see the contact line profiles in figure 5.17(a) and the height profiles in figure 5.18).

As the droplet loses mass, the mean radius exhibits a series of jumps which is also marked with a temporary increase in the droplet height $h_{\max}$ and the mean contact angle $\bar{\vartheta}$. Usually in these circumstances the contact line will remain pinned at one location of lower wettability, therefore causing the rest of the contact line, and the corresponding motion of the centroid to shift to that point of the substrate (see figure 5.17(a), (b) and (d)). This also corroborates the observations of Dietrich *et al.* [217] which are here attributed to surface heterogeneities which may become difficult to account for in experiments. Noteworthy also is the excellent agreement between the predictions offered by the full and hybrid models which shows nearly
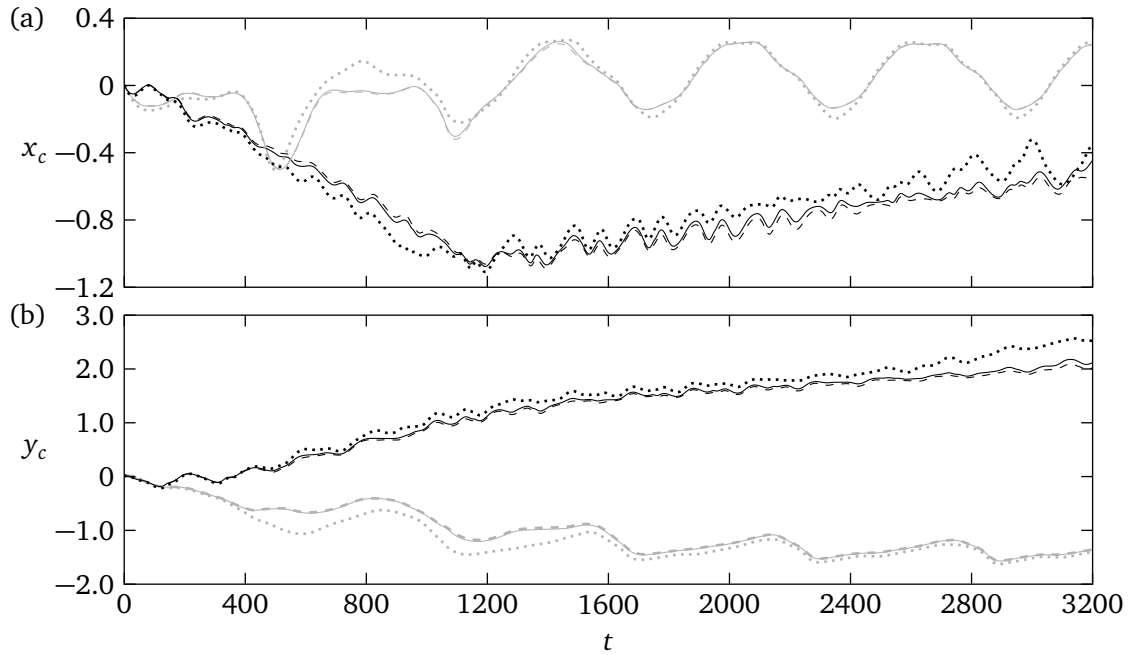
Figure 5.19: Multiple periods of liquid flux over a substrate with randomised heterogeneous features (see text for the substrate generation). Plots (a) and (b) depict motions of x_c and y_c, respectively, where mass is altered using the flux distribution (3.105). Volume changes are dictated using (5.9) with parameters $\mathcal{V} = 2\pi$, $\tilde{\mathcal{V}} = 1.5\pi$ where black and grey plots correspond to the flow periods $\mathcal{P} = 200$ and $\mathcal{P} = 600$, respectively. In both cases solid, dashed, and dotted lines correspond to the full, hybrid, and the low-order model (1.6), respectively.

indistinguishable results. The reduced model on the other hand shows some disagreement, but captures the generic features rather well.

One of the observations recorded in the 2D study was that periodic cycling of the droplet mass led to periodic spreading motions after initial transients decay. Here, we simulate for multiple flow periods over the randomised substrate (5.10) with $\hat{\theta}(x,y) = 1$ and where $\tilde{\theta}(x,y)$ is a superposition of 10 harmonics with wavenumbers up to 2π, whose amplitudes are normally distributed with zero mean and variance set to 0.3. These parameters give smoother transitions between the wettability patches in comparison to the substrate used for figure 5.17, meaning simulating the full model requires fewer collocation points in the azimuthal direction, thus allowing us to simulate for longer times with less computing resources. The outcome is shown in figure 5.19, and highlights this simulation by plotting the motions of the centroid for two different values of the flow period, namely one at $\mathcal{P} = 200$ and one at $\mathcal{P} = 600$. Remarkably, the dynamics do not become periodic within the simulated time frame for the case of the shorter period of inflow/outflow, noting that the agreement of the asymptotic model and the full equation worsens as we simulate further in time. Generally, by

removing the random noise from the substrate features we recover periodic spreading motions just like the observations made previously, which will be returned to in later sections. Hence, this result points to the possibility of having a transition to quasi-periodicity induced by the nonlinear coupling of random features and the period of inflow/outflow.

This case also presents us with an ideal opportunity to compare the predictions of the full model, the hybrid model, and solutions of the lower-order model (1.6). Qualitatively all models give similar predictions, noting that the best agreement is obtained with the hybrid model for the slower period of liquid flux, which is an observation that appeared to persist with other cases tested. For the shorter period of liquid flux there appears to be a gradual deterioration in the agreement between the full model and the solution obtained by the hybrid models, which is particularly pronounced in the case of the low-order model (1.6). While the disagreement in the centroid motion is not too dramatic it corroborates the findings of figure 5.15 where it is shown that the next-order correction is indeed essential to capture accurate solutions. However, we do remark that this disagreement could occur due to a variety of reasons. Firstly, the substrate features could be under-resolved by our spatial discretisation scheme which may nevertheless be fixed by increasing the resolution. In this case, however, solving for such high values of t would require significantly more time and resources. Likewise, small correction terms that possibly arise from the random features accumulate so that pinning/de-pinning events can possibly be mistimed across the models, thus ultimately causing the droplet to exhibit different dynamics.

5.3.2 Localised Mass Flux

Highlighted in section 5.1 was the possibility to use the reduced model to explore additional distributions of liquid flux provided that they occur within the droplet footprint and vanish at the contact line (or contact points for the 2D case). Particular attention was placed on highly localised fluxes which gave rise to cases where the droplet may move to a new region of the substrate (see figure 5.6), or where the droplet can split into two bodies (see figure 5.5). Using the reduced model (3.98) we can likewise explore such mass flux distributions, here considering the form

$$q = \frac{\dot{v}(t)\exp\left\{-\alpha\left[(x-x_0)^2+(y-y_0)^2\right]\right\}}{\displaystyle\int_{\Omega(t)}\exp\left\{-\alpha\left[(x-x_0)^2+(y-y_0)^2\right]\right\}\,\mathrm{d}\boldsymbol{x}} \tag{5.11}$$
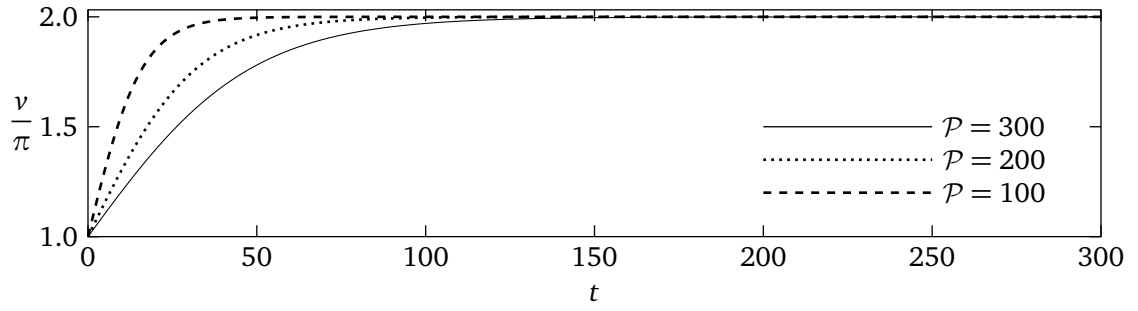
Figure 5.20: Plots of the volume function (5.12) for different values of $\mathcal{P}$ (see inside the plot). In each case $\mathcal{V} = \tilde{\mathcal{V}} = \pi$.
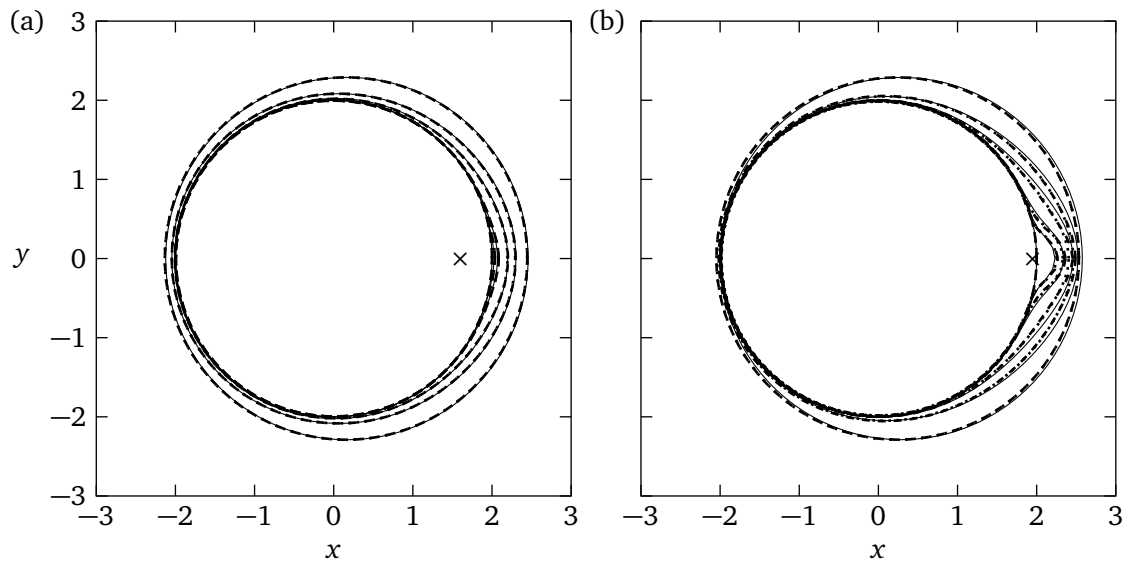

Figure 5.21: The effect of localised flux on contact line using (5.11) with parameters $S = 20$, $(x_0, y_0) = (1.6, 0)$ and $(1.95, 0)$ for (a) and (b), respectively (localisation depicted by crosses). The initial contact line shape is prescribed at $a(\phi, 0) = 2$ so that the droplet is at equilibrium for the starting volume $v(0) = 2\pi$. Both plots show droplet profiles at times $t = 0, 0.3, 1, 5$, 10 and 100 over the homogeneous substrate $\theta(x, y) = 1$. In both cases volume changes are governed using (5.12) with $\mathcal{V} = 2\pi$, $\tilde{\mathcal{V}} = \pi$ and $\mathcal{P} = 100$.

which prescribes a scaled Gaussian whose peak is located at $(x_0, y_0) \in \Omega(t)$ with $S > 0$, noting that the denominator is calculated with numerical quadrature. Just like before we only consider moderate values of S to gain a satisfactory compromise between q being practically zero at the contact line and resolving the sharp features in q with a relatively small number of collocation points. The choice of S is arguably more crucial in this part, since here we discretise in two spatial dimensions, meaning we are solving for significantly more unknowns than for 2D droplets. Therefore using a moderately large value for S is desirable to limit the number of collocation points required so that solutions can be computed within a shorter time.
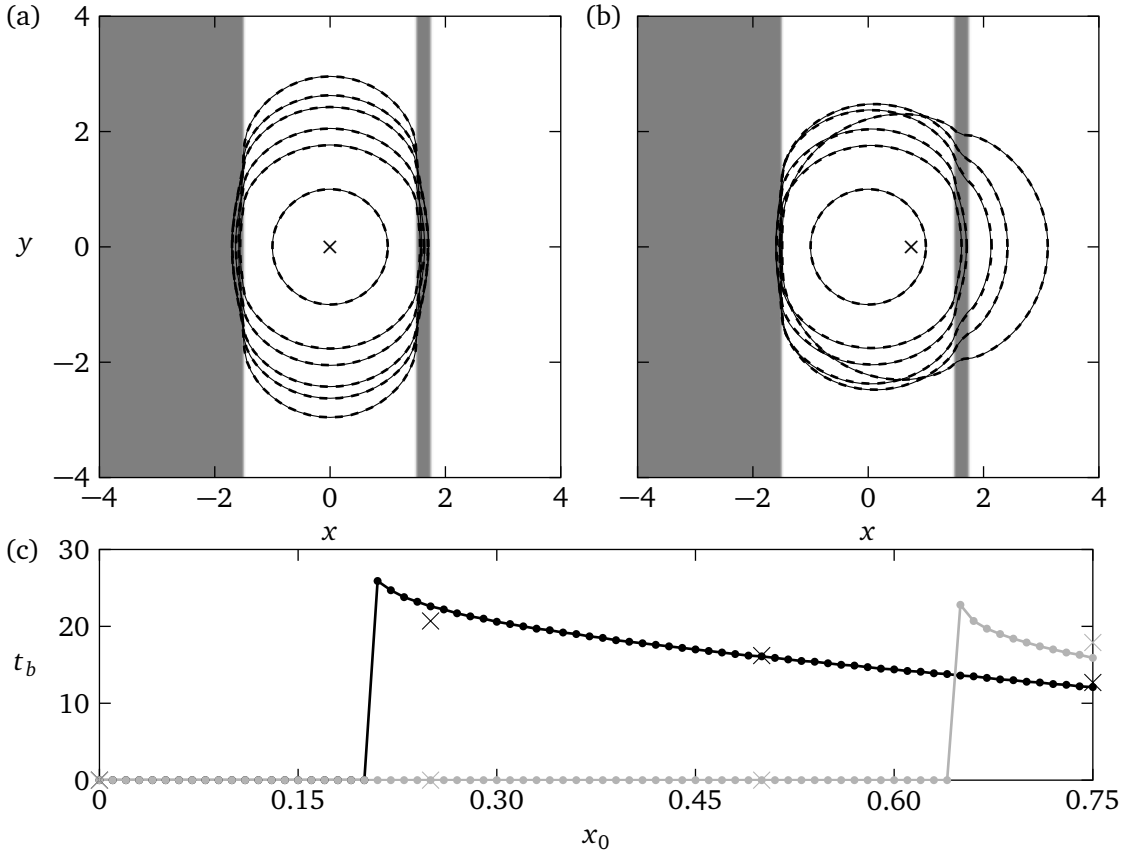
(a)

(b)

(c)

Figure 5.22: Localising the flux from $(x_0, y_0) = (0,0)$ to $(0.75, 0)$ with the heterogeneous barriers $\theta(x, y) = 1.2 + \tilde{g} \{\tanh[50(x - 1.5)] - \tanh[50(x + 1.5)] - \tanh[50(x - 1.75)]\}$. Plots (a) and (b) are droplet profiles at times $t = 0, 5, 10, 20, 30$ and 300 for localisation at $x_0 = 0$ and $x_0 = 0.75$, respectively (localisation depicted by crosses). The substrate in (a) and (b) is shaded according to the choice of θ where dark and light patches correspond to $\theta \approx 1.2 \pm \tilde{g}$ for $\tilde{g} = 0.25$, respectively. (c) The time the point $x_c(t) + a(0, t)$ breaks the heterogeneous barrier (t_b) against x_0, where black and grey plots are for $\tilde{g} = 0.25$ and $\tilde{g} = 0.275$, respectively, and crossed denote solutions from the full model. In all plots volume changes are given by (5.12) with $\mathcal{V} = \pi$, $\tilde{\mathcal{V}} = 2\pi$ and $\mathcal{P} = 100$.

In the examples that follow, we assume that the volume varies according to

$$v(t) = \mathcal{V} + \tilde{\mathcal{V}} \tanh\left(\frac{2\pi t}{\mathcal{P}}\right), \tag{5.12}$$

which gives either liquid injection or removal depending on the sign of $\tilde{\mathcal{V}}$, and monotonically increases/decreases until $v = \mathcal{V} + \tilde{\mathcal{V}}$ (see figure 5.20). In figure 5.21 we use (5.11) with (5.12) to investigate the effect of localised flux on the contact line. Here we consider a homogeneous substrate with $\theta(x) = 1$ and a droplet of volume $v = 2\pi$ centred at the origin and having an initial radius of $a(\phi, 0) = 2$, which corresponds to the equilibrium radius at this volume. The mass flux is prescribed according to (5.11) in two cases of liquid injection which occur at $(x_0, y_0) = (1.6, 0)$ (figure 5.21(a)) and $(x_0, y_0) = (1.95, 0)$ (figure 5.21(b)), where in both

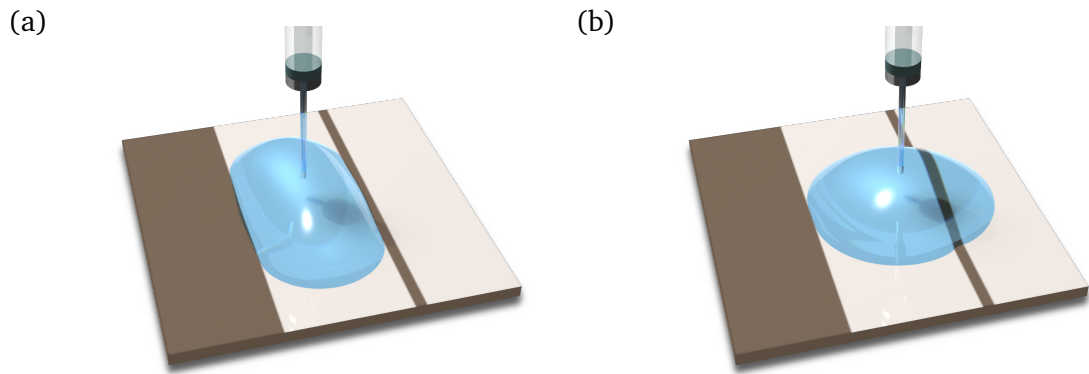(a)   (b)

Figure 5.23: Droplet profiles for the final stage of figure 5.22(a) and (b).

we kept identical volume changes. In both figures 5.21(a) and (b) there is a distortion in the contact line along the positive x axis which occurs due to the localisation of the flux, noting that more appreciable protrusions are obtained as the flux is moved closer to the contact line. In both cases this protrusion takes place in the initial stages and dies out rather quickly, so that in the long time limit where volume changes decay the droplet will assume a circular contact line, as expected. We also remark on the levels of agreement obtained by using the reduced and hybrid models, noting the best agreement is obtained in figure 5.21(a) solely because less fluid is transferred through the contact line. Despite the caveat of assuming $q(1, \phi, t) = 0$ in the analysis, the reduced and hybrid models capture the protrusion observed in figure 5.21(b) rather well.

The results in section 5.1 indicated that the dynamics is a tight interplay between liquid flux and heterogeneity, showing that small changes to either could cause significant changes in the droplet dynamics. In figure 5.22 we investigate this interplay by considering a droplet confined between two parallel heterogeneous stripes, where multiple positions of fluid entry are considered by using (5.11). This case is reminiscent to figure 4 in Kusumaatmaja & Yeomans [218] where the authors provide insights on sorting droplets using wettability patterns by using lattice Boltzmann simulations. For the case considered here two scenarios can arise depending on the position of fluid entry (see the height profiles of figure 5.23). In one case the droplet remains inside the heterogeneous barriers and elongates parallel to the stripes (see figure 5.22(a)), which is a feature observed in related works in the case of constant mass (see, e.g. [219–221]). In the second case the droplet overcomes the heterogeneous barrier and shifts to the right while remaining pinned to the boundary of the leftmost stripe (see figure
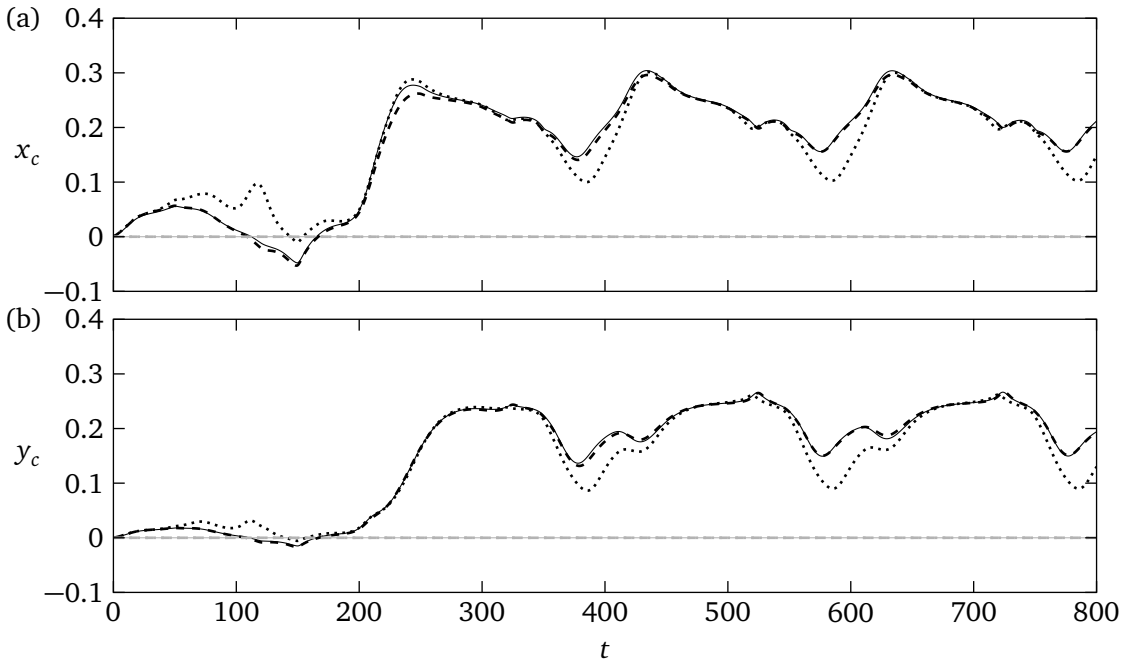
Figure 5.24: Transition to periodic motion over the substrate $\theta(x, y) = 1 - 0.15 \{\cos[2\pi(x + y)] + \cos[2\pi(x - y)]\}$ where the localised flux distribution (5.11) is used with parameters $(x_0, y_0) = (0.75, 0.25)$ for black curves, and $(x_0, y_0) = (0, 0)$ for grey curves, using $S = 50$ for both. Volume changes are governed with (5.9) by using $\mathcal{V} = 2\pi$, $\tilde{\mathcal{V}} = \pi$ and $\mathcal{P} = 200$. Plots (a) and (b) are evolutions of x_c and y_c, respectively.

5.22(b)). These two distinct regimes, however, are highly dependent on the position where the flux is localised as shown in figure 5.22(c). Interestingly, changing the strength of the heterogeneous stripes by a rather small amount (a 1.72% increase) drastically changed the point of localisation required to break the barrier, moving $x_0 = 0.21$ to $x_0 = 0.65$. Although some small disagreements can be observed between the predictions of the full and hybrid models in figure 5.22(c), the spreading is generally captured rather well. It is worth noting that the insights obtained in figure 5.22(c) were based on 150 simulations of the hybrid model, which were completed in a much shorter time-frame than a single simulation of the full model, which is precisely why the agreement is only tested for 8 distinct cases.

Contrary to cases shown in section 5.1, the example presented in figure 5.19 shows a case where the transition to periodic motion did not occur within the simulation window explored. Previously it was remarked that the removal of the randomised substrate features would yield periodic spreading when coupled with periodic cycling of the droplet volume. In figure 5.24 it is clear to see that this is indeed the case, since periodic spreading motion is obtained practically within 2 cycles of inflow and outflow. Let us also mention that other examples considered (not included here for brevity) also exhibit similar behaviours, giving
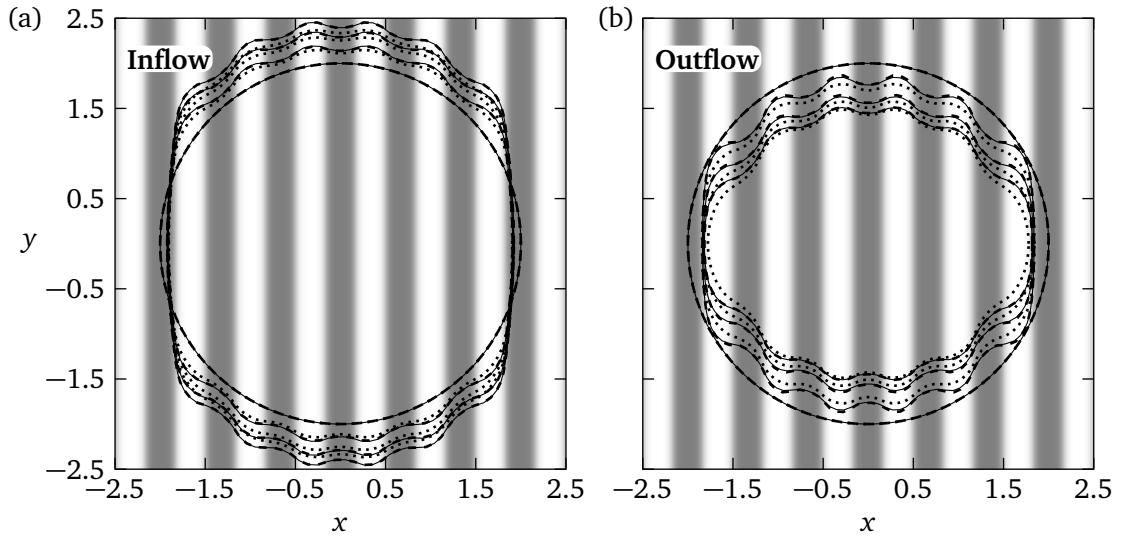
Figure 5.25: Fluid inflow/outflow over the striped substrate $\theta(x,y) = 1 + 0.35\tanh[2\cos(3\pi x)]$. The volume is changed using (5.12) where $\mathcal{V} = 2\pi$, $\mathcal{P} = 200$ and $\tilde{\mathcal{V}} = \pm\pi$ in (a) and (b), respectively. Contact line profiles are plotted at times $t = 0$, 20, 40 and 100. In both plots dark and light patches correspond to $\theta \approx 1 \pm 0.34$, respectively.

periodic spreading motions over substrates with periodic features after the initial transients. Likewise consistent with section 5.1 on 2D droplets is that the droplet considered here is expected to ultimately centre itself around the inlet and outlet of the liquid flux (see figure 5.6). However, for this to occur, the heterogeneities need to be sufficiently weak. Noteworthy also is that the hybrid model again yields the best comparison with the full model, whereas the reduced model only captures the qualitative features which further corroborates the findings in figure 5.17.

5.3.3 Striped Substrates

Perhaps the most commonly studied configurations with chemical heterogeneities is that of alternating wettability patterns whereby droplets tend to align themselves to the features of the surface (see Bliznyuk *et al.* [219]), preferentially moving along the more wettable regions, and for sufficiently strong wettability contrasts the droplet may also split into satellite bodies [222]. Noteworthy also are the studies by Jansen *et al.* [192, 193] who consider the shape of droplets over stripes of alternating wettability by using a lattice Boltzmann approach. This numerical method, as previously explained, is popular in the literature to describe mesoscopic fluid motion due to its flexibility in describing complicated geometries [68, 189, 190, 223], although, it is also worth noting that such settings can also be investigated with other

numerical means, for example, using a disjoining pressure model with a finite-difference approach as shown by Schwartz & Eley [41].

In figure 5.22(a) we saw that during liquid inflow the drop will elongate and conform to striped features across the substrate, consistently with the findings of studies that consider droplets of constant mass. Various studies also investigate droplet dynamics over substrates comprised of multiple parallel stripes, finding that the contact line can become distorted due to the substrate heterogeneity (see Léopoldès *et al.* [224] and Jansen *et al.* [193]). Jansen *et al.* [192] study tuning the droplet kinetics to control the equilibrium shape after deposition. For smaller droplet initial diameters they observe an elongation to conform to the parallel stripes, however, for larger droplet initial diameters the equilibrium shape becomes more spherical. In figure 5.25 we observe similar dynamics can arise by varying the droplet volume while maintaining identical initial conditions. For liquid inflow the contact line advances along the parallel stripes like before, whereas for liquid outflow the contact line recedes and becomes more spherical in shape.

Noteworthy is that in both cases the hybrid model performs most optimally in capturing the contact line variations, which is consistent with our findings reported in [61] where results with striped substrate features for droplets of constant mass are shown. Should the receding case be simulated for further loss of mass, a stick-slip event will be initiated whereby the contact line will quickly recede in the x direction and remain pinned on a new stripe. For the stripe strengths considered here the stick-slip event will cause the full and hybrid methods to fail due to the spatial discretisation issues described previously. It is worth noting that the reduced model does not suffer from this issue and therefore the stick-slip event can be captured, although, perhaps less accurately.

5.3.4 Small-Scale Features

In this final example we consider another substrate formed with randomly distributed heterogeneous features, this time using the formula

$$\vartheta(x,y) = 1 + \sum_{j=1}^{800} \tilde{\theta}\left(\sqrt{(x-\bar{x}_j)^2 + (y-\bar{y}_j)^2}, d_j\right), \qquad (5.13\text{a})$$

where we define

$$\tilde{\theta}(x,d) = \frac{1}{2}\left\{\tanh\left[200(x+d)\right] - \tanh\left[200(x-d)\right]\right\}. \qquad (5.13\text{b})$$

Equation (5.13a) gives 800 localised features of radius $d = 0.05$ with positions $(\bar{x}_j, \bar{y}_j)$ which were chosen to lie uniformly in the square $(-3, 3) \times (-3, 3)$ so that the features are at least 0.15 dimensionless units apart. We have previously used (5.13a) in [61] for the case of constant mass to examine stick-slip behaviours with advancing contact lines; here, we are interested in the dynamic phenomena that arise from cycling the volume through periodic inflow and outflow of mass. To properly resolve the contact line variations which emerge due to the rather complicated heterogeneity, we simulate using the reduced model alone. This is purely due to the rather large amount of collocation points required azimuthally, which makes solving the full model infeasible with our current implementation and the hybrid model rather challenging due to the solution of large dense matrix-vector equations at each time-step. However, since the reduced model works generally well for other cases considered, we can use this to gather a qualitative outlook on the dynamics that arise. Besides, in this regime $\partial_\phi a$ may become $O(1)$ and therefore strictly speaking it violates the assumptions put forth in the analysis. The purpose of this example is to demonstrate that the models presented can capture qualitative features that arise in experimental settings.

The result of the computation is shown in figure 5.26 where dynamically cycling the droplet volume gives rise to a number of features present in previous examples. Firstly, it is easy to see from figure 5.26(a) and (b) that pinning/de-pinning events emerge throughout both the inflow and outflow stages. The constant-radius and angle modes also appear as a consequence of the pinning events which suggests, like in section 5.1, that such behaviours may arise in experimental settings due to substrate features which may become difficult to track (see figure 5.26(c) and (d)). Interestingly the dynamics here share qualitative appearance to figure 10 in [113] where the authors experimentally analyse cycling the droplet's volume through a needle at its base. Like the results here, Lam *et al.* [113] show that the constant-radius mode is rather brief and occurs shortly after the flow conditions switch, giving predominately the constant-angle mode.

Although the localised flux distribution (5.11) could have been used for this example, we opted against this solely to reduce the computational complexity by bypassing the evaluation of the integrals $I(m, t)$. Nonetheless, in this example we expect that both the flux distributions (3.105) and (5.11) will yield similar behaviours. Noteworthy also is that the stick-slip and pinning behaviours resemble that of Cubaud & Fermigier [63] (see also Cubaud *et al.* [87]), although, no direct comparisons can be made since Cubaud & Fermigier consider
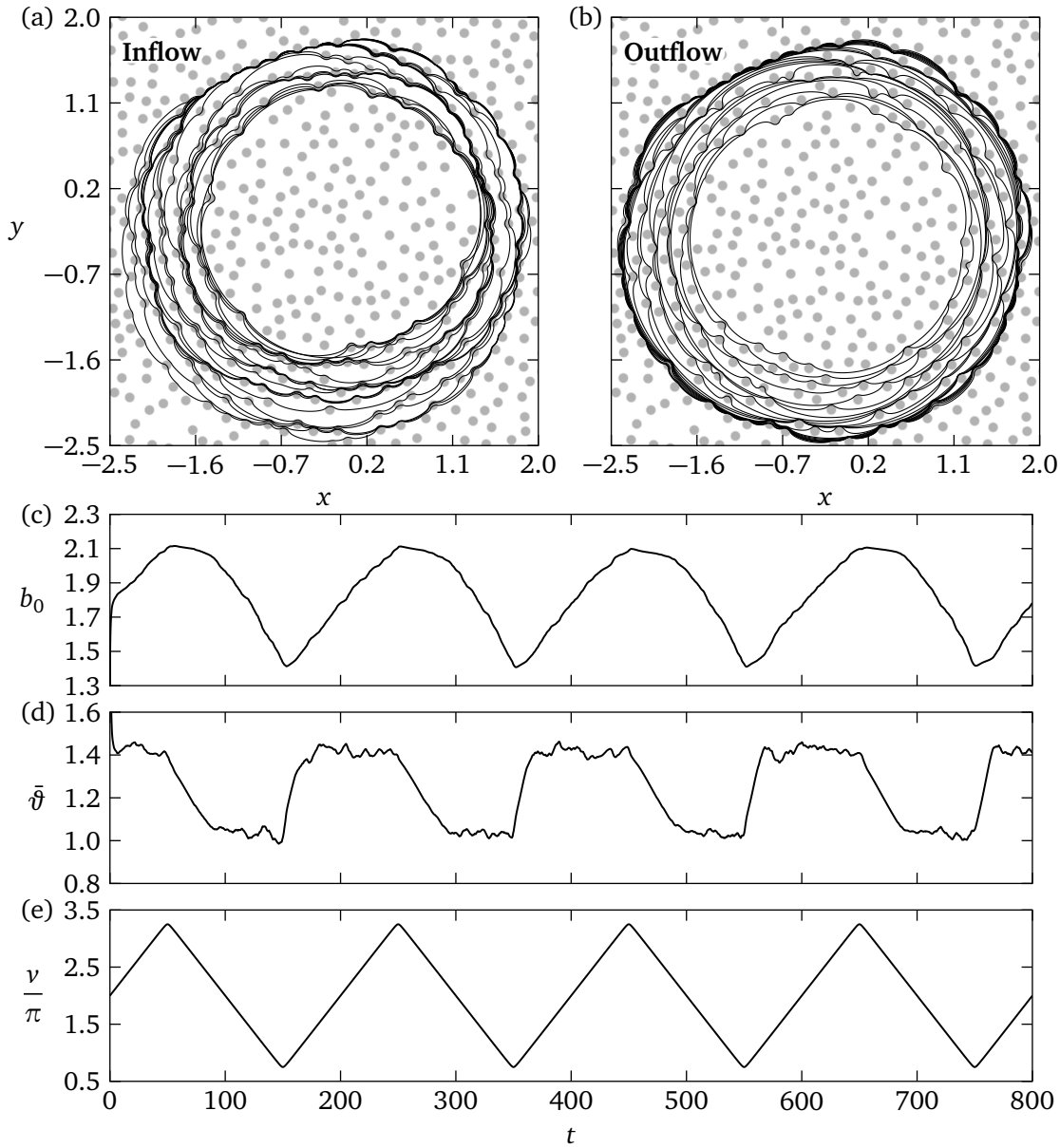
Figure 5.26: Dynamic volume cycling over a substrate comprised of small scale features (see text for generation of the substrate). Volume is fluctuated using (5.9) using parameters $\mathcal{V} = 2\pi$, $\tilde{\mathcal{V}} = 1.25\pi$ and $\mathcal{P} = 200$ where we consider the flux distribution (3.105). (a) Droplet profiles during inflow from $t = 150$ to $t = 250$ in increments of 5. (b) Droplet profiles during outflow from $t = 250$ to $t = 350$ in increments of 5. (c) The mean radius b_0, (d) the mean apparent contact angle $\bar{\vartheta}$ and (e) the scaled volume v/π.

larger droplets where gravitational effects become appreciable, which, in the present case are neglected in favour of analytical tractability.

Throughout previous cases the coupling between surface heterogeneity has given rise to a large array of interesting phenomena, showing how many of the results obtained for 2D cases (see section 5.1) also arise in 3D simulations. While no quantitative comparison with experiments was undertaken here, qualitative comparisons were offered for a few cases. This

is primarily due to the fact that no experimental studies come with the time evolution of the contact line fully recorded. However, we are confident at least that the models we present can capture the generic features rather well, and thus, can be used as a tool to further explore the interesting interplay between liquid flux and chemical heterogeneity. In this manner, we extend the results in the next section to include mass loss through evaporation to assess the dynamics that arise once fluid loss is maximised close to the contact line, rather than through the bulk as considered here.

5.4   Evaporation Dynamics

In this section we consider droplets that are losing mass through evaporation, rather than the processes discussed previously in both the 2D and 3D scenarios. The asymptotic analysis undertaken in section 3.3 indicates that evaporation and surface heterogeneity are tightly entwined, since extraction of the inner region variables θ_e, β_{in} and $\tilde{\beta}_{\text{in}}$ relies on both the flux and chemical heterogeneity. Therefore, effects such as droplet pinning, stick-slip, and deformed contact lines could be eradicated by simply increasing the effect evaporation has on the micro-scale dynamics, as suggested by figures 3.3, 3.4 and 3.5.

Here, the theoretical predictions of section 3.3 will be contrasted to numerical solutions of the full equations (2.51) for a number of cases. Unless otherwise stated we set the initial droplet volume to $v(0) = 2\pi$ and as in section 5.2 we use $a(\phi, 0) = 1$ and $(x_c(0), y_c(0)) = (0, 0)$. To mitigate the numerical issues with stiffness that arise during the final stages as the collocation points get crammed closer and closer together, all simulations were paused once $b_0 \leq 0.1$. After pausing, the obtained solution was interpolated to a sparser mesh and the solver was restarted, which was ultimately terminated at time $t = t_e$ at which the stopping criterion $b_0 \leq 0.01$ is met. At this stage the volume becomes $O(10^{-6})$ and beyond the scope of the macroscopic analysis presented, therefore, we did not pursue further the numerical intricacies of the extinction stage, since, for the most part, the numerical tools are used to validate the theory (which is applicable for macroscopically large droplets and for a sufficient separation of scales). The main interest of the present study is to analyse droplets through the evaporation stage, rather than the extinction stage which occurs on a much smaller time scale.

We elucidate the impact of the various parameters of the problem through the dynamics

of simulations, offering where appropriate comparison of the reduced model (3.98) to the full equations (2.51) to assess the validity of the analysis. Due to the aforementioned restriction on λ, we modify the impact of evaporative flux on the microscopic behaviours by varying $\mathcal{E}$ and mostly maintaining $\mathcal{K} = 10^{-4}$ so that the evaporation formulas (3.144) and (3.147) hold. The main purpose of this study is to analyse the interplay between evaporation and chemical heterogeneities, rather than studying in more detail the role of $\mathcal{E}$ and $\mathcal{K}$ on the dynamics, which was highlighted partially in chapter 3 and discussed at length by Savva *et al.* [53]. Thus, varying $\mathcal{E}$ and keeping $\mathcal{K} = 10^{-4}$ does not limit the view on the dynamics we wish to uncover, since, we can explore the balance between the flux and chemical heterogeneity by simply considering a range of $\mathcal{E}$.

5.4.1   Striped Substrates

In the first example we consider a substrate comprised of striped features similar to that investigated previously for cases of liquid flux through the bulk (see figure 5.25 and the surrounding discussion). As seen in figures 3.3, 3.4 and 3.5 evaporation dominates the dynamics for large values of E and/or small values of K, essentially weakening the influence of substrate heterogeneity. This is also demonstrated in figures 5.27 and 5.28, where we also see that decreasing E allowed for the droplet to spread more and assume a non-circular shape (see also figure 5.29). Importantly, this suggests that stick-slip and pinning events in experiments are as much attributed to the substrate features as the flux, since, for dynamics more strongly modified by evaporation these features disappear entirely (as perhaps better shown by the logarithmic plots in figure 5.27).

Furthermore, this case allows us to examine the applicability of the theoretical methods including the various formulas derived to determine the droplet volume during the first three evaporation stages. As theorised in section 3.3, the higher distortions in the contact line given by simulating with lower values of E render (3.147) inapplicable. This is not entirely surprising since the theory used to derive this formula is based on the caveat of nearly circular contact lines, and thus, serves as a leading-order approximation which nevertheless works well for strong evaporation effects. Yet, using (3.144) which relaxes the assumptions of the analysis provides a better model for the volume evolution, by improving the agreement with the full PDE when there are larger contact line distortions. Moreover, in alignment with Savva
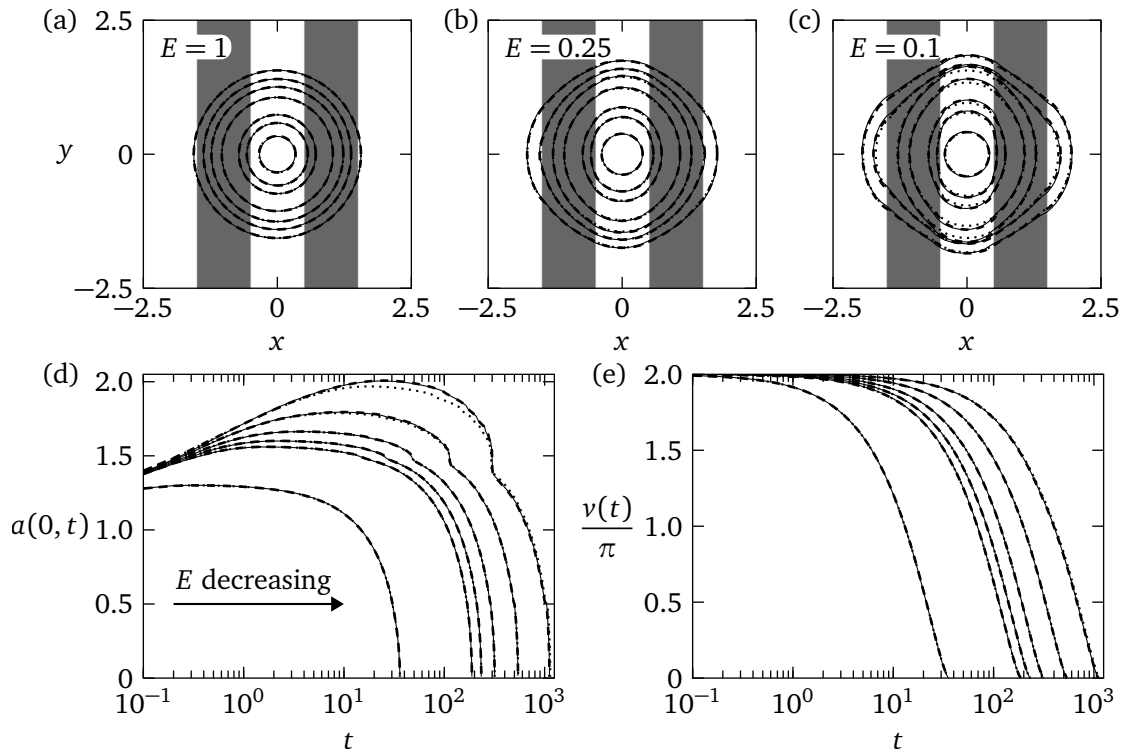
Figure 5.27: Droplets evaporating over the striped substrate $\theta(x,y) = 1 - 0.4\tanh[50\cos(\pi x)]$ where $K = 0.1$ and $E = 10$, 1, 0.75, 0.5, 0.25 and 0.01. Plots (a) - (c) show droplet profiles for select cases of E when the droplet is at 99%, 70%, 50%, 30%, 10%, 5% and 1% of the initial volume. The substrate is shaded according to the choice of θ where dark and light patches correspond to $\theta_{\text{max,min}} \approx 1 \pm 0.4$, respectively. Plots (d) and (e) show $a(0,t)$ and $v(t)$ evolutions on a logarithmic time axis. In all plots solid, dashed and dotted lines are solutions of the full, hybrid and reduced models, respectively, where the evaporation formula (3.144) was used.

et al. [53] we see that there is no appreciable mass loss through the spreading stage, even for higher values of E, which is perhaps best viewed in the log plots of figure 5.27. In essence, this implies that using $\vartheta \approx \theta_e$ to describe the dynamics through the first three stages in the evolution of the volume is reasonable, meaning a more intricate analysis to account for the second stage is not necessarily required. Also notable is that for $E = 0.25$ and $E = 0.1$ the full problem required stopping and remeshing to capture the final stick-slip event which occurs when $t \approx 500$ and $t \approx 1000$ for each case, respectively (see figure 5.28). This is essentially a manifestation of the spatial discretisation struggling to resolve the sharp transition between the contact angles of striped features, causing the problem to become increasingly stiff (which was resolved by restarting the solver with a sparser mesh). Perhaps this stage would be more appropriately captured with an adaptive mesh that places more collocation points at the positions of greatest curvature, however, since the full model is used predominately to
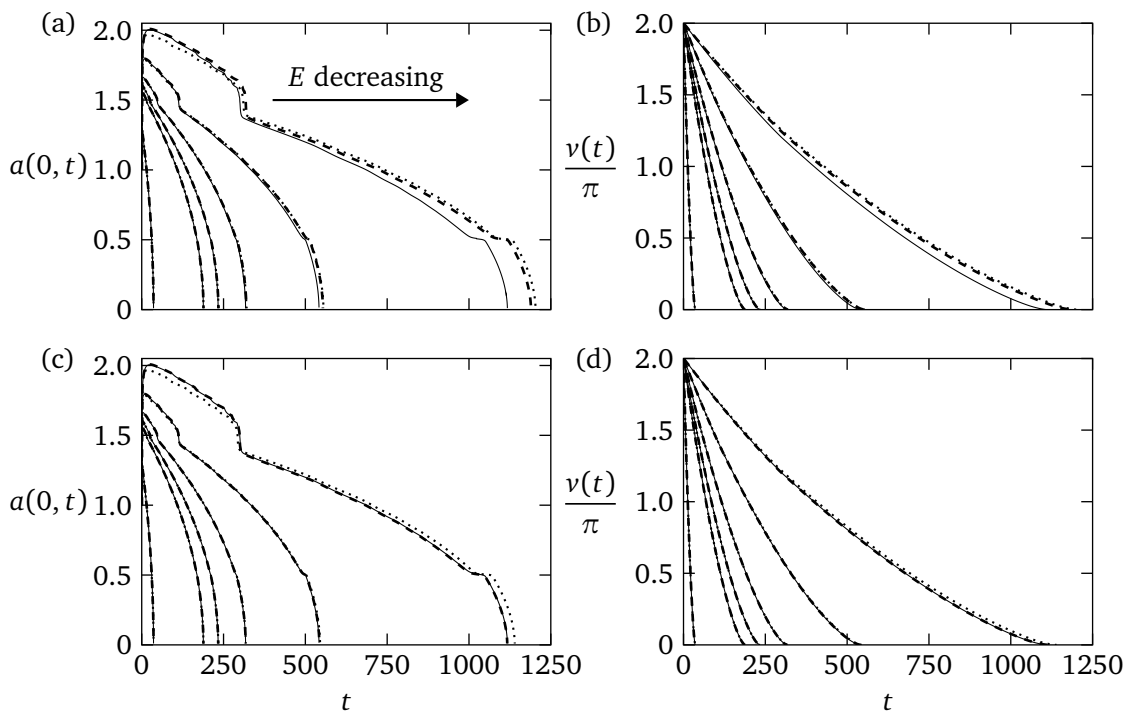
Figure 5.28: Plots (a)-(d) show the evolutions of $a(0, t)$ and $v(t)$ for the cases inside figure 5.27. In (a) and (b) the leading-order evaporation formula (3.147) is used, whereas (3.144) is used for (c) and (d). The styles of the curves are as in figure 5.27.
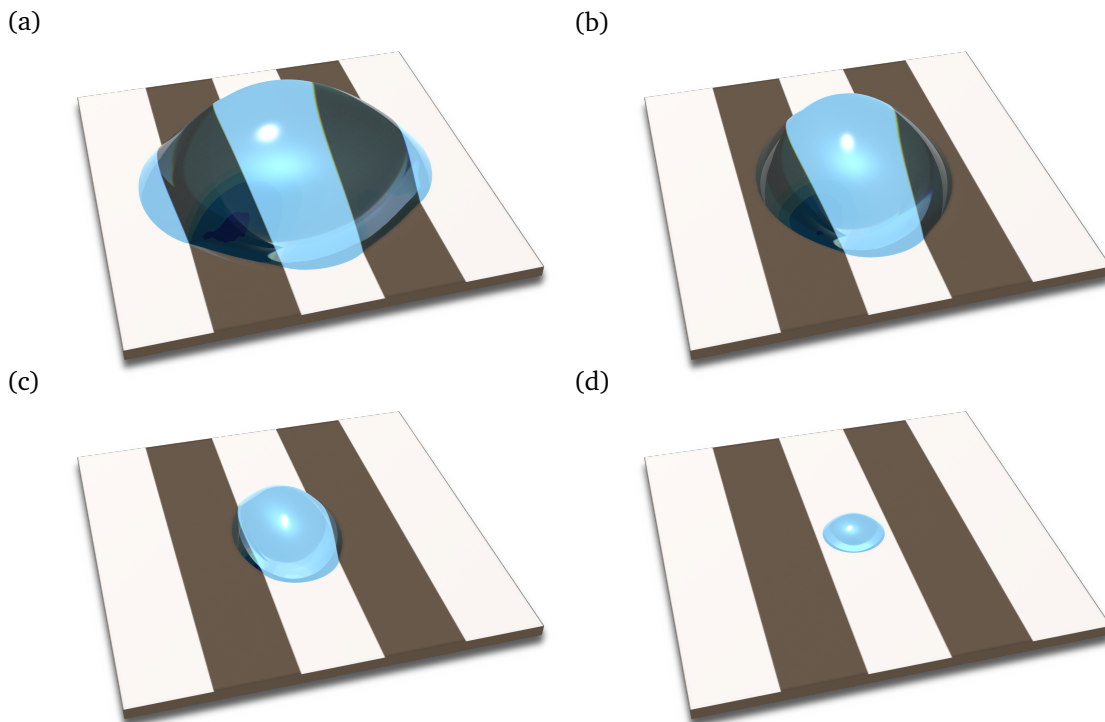

Figure 5.29: Droplet profiles for figure 5.27(c) at 99%, 50%, 10%, and 1% of the initial volume.
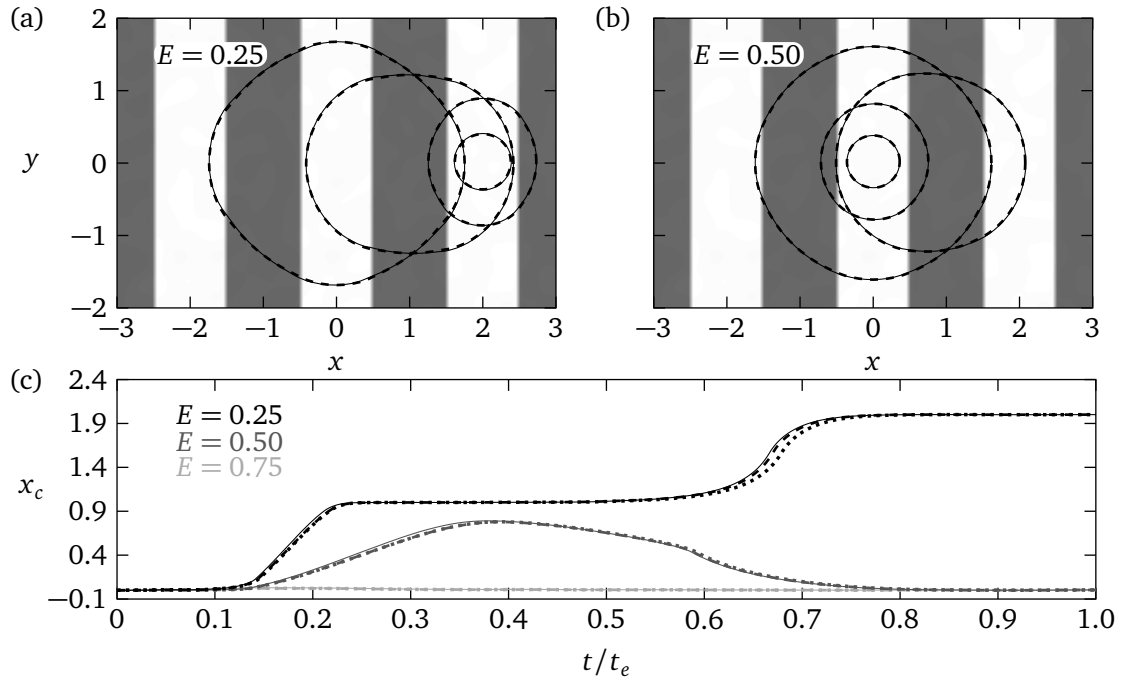
Figure 5.30: The snapping mode of evaporation reported by Wells *et al*. [150]. Plots (a) and (b) are droplet profiles at 90%, 45%, 10% and 1% of the starting volume for $E = 0.25$ and $E = 0.5$, respectively. The substrate in both (a) and (b) is shaded according to the choice of θ (see text for a description of the substrate). Plot (c) shows x_c evolutions for $E = 0.75$, $E = 0.5$ and $E = 0.25$ where $t_e = 233.9$, 308.9 and 509.2, respectively. In all plots $K = 0.1$, solid lines correspond to the full model, and dashed and dotted correspond to the hybrid model with evaporation formulas (3.144) and (3.147), respectively.

validate the theory we chose not to pursue it further. In contrast, no numerical stiffness issues were observed when simulating the reduced model, and only marginal stiffness was observed with the hybrid model.

5.4.2 Snapping Droplets

Previous results indicate that for substrates that are relatively simple in appearance, complicated behaviours can arise. However, the prescribed functional forms for the substrate profiles may be viewed as too contrived and unrealistic since there always exists a small amount of random noise in the surface features, be they topographical and/or chemical. Therefore, we use the striped substrate considered in figures 5.28 and 5.27 and include a small amount of random noise using (5.10) with $\hat{\theta}(x, y) = 1 - 0.4 \tanh [50 \cos(\pi x)]$, and $\tilde{\theta}(x, y)$ being band limited white noise with 50 harmonics, wavenumbers up to 4π and normally distributed amplitudes with zero mean and variance set to 0.1. This circumstance was previously considered in section 5.1 for the case of linear outflow of mass in 2D through
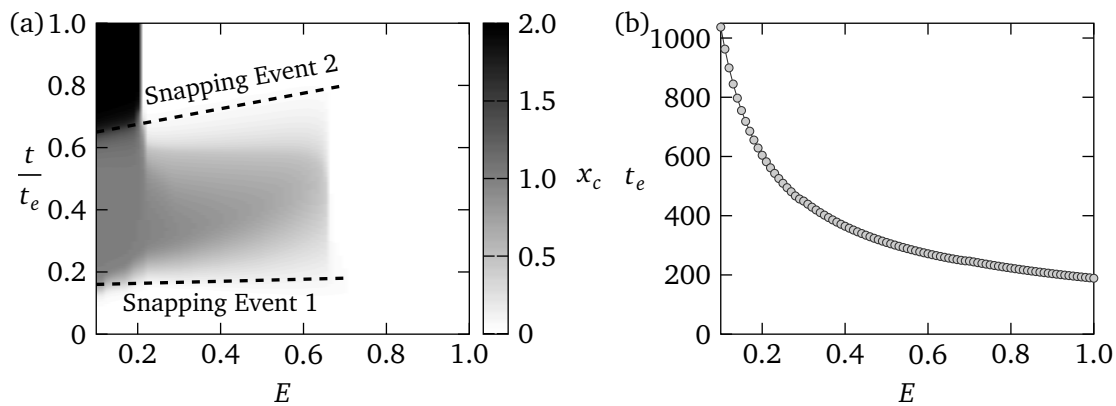
Figure 5.31: Distribution of x_c and the total evaporation time for 90 simulations using the hybrid method and evaporation formula (3.144). (a) The location of x_c for varying E on a scaled time axis. (b) The evaporation time t_e against E where the discrete values were joined for clarity. In both plots the substrate and remainder of the parameters are identical to figure 5.30.

the bulk, and gave rise to the snapping mode of evaporation observed by Wells *et al.* [150] (see figure 5.9 and the surrounding discussion). In figure 5.30 we observe that such events also arise in the 3D model with chemical heterogeneities. Crucially, the snapping events are highly dependent on the strength at which the inner region features are modified, noting that if they are sufficiently strong then the snapping events are bypassed entirely. This agrees with the findings of the 2D case where we observed that faster linear outflow of mass likewise eliminated the presence of snapping transitions.

Since the hybrid approach can be simulated very efficiently compared to the full PDE without compromising the accuracy of the results, we simulated for a larger range of values of E in order to understand better how transitions to different behaviours can occur. In figure 5.31 we show the outcome of 90 simulations of the hybrid method for $E = 0.1$ to $E = 1$ in increments of 0.01, plotting in figure 5.31(a) the values of x_c obtained for varying E and on a time axis scaled by the evaporation time t_e. It is easy to see that indeed the three scenarios highlighted in figure 5.30 arise as we vary E are the only possibilities that arise in this setting. It should be noted that other snapping transitions could exist if different types of substrate noise are considered, such as the droplet snapping to the left side of the substrate, rather than the right as seen here. Noteworthy is that if snapping events exist (for $E < 0.7$ here), we see that the first event occurs roughly around 20% of the droplet's lifespan, and that the second transition appears between 60% and 70% which suggests that the droplet must have to be at a critical mass for the transitions to occur, irrespective of the value of E. Also notable is that for
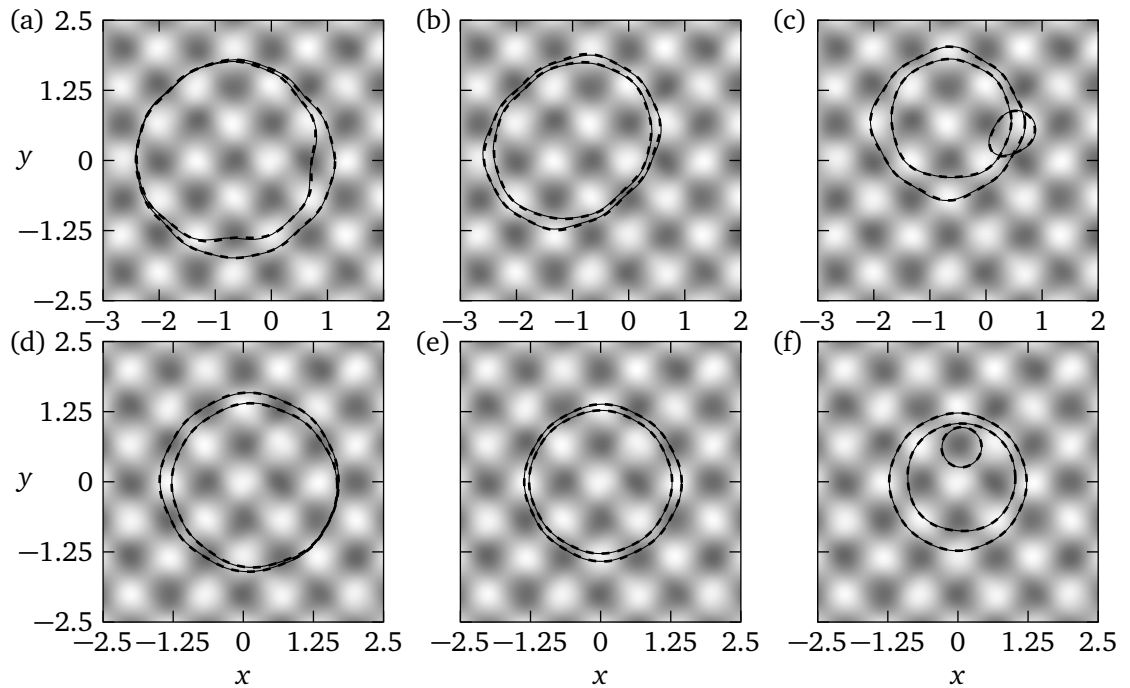
Figure 5.32: Snapping events over the eggbox-like pattern as reported by Wells *et al.* [150] where the droplet will cycle between diamond-like and rectangular shapes. In plots (a)-(e) the substrate is shaded according (5.10) with $\hat{\theta} = 1.2 - 0.25\cos[1.5\pi(x + y)] - 0.25\cos[1.5\pi(x - y)]$, and $\tilde{\theta}$ being band limited white noise with 50 harmonics, wavenumbers up to 4π and normally distributed amplitudes with zero mean and variance set to 0.05. (a)-(c) Show contact line profiles for 90%, 70%, 60%, 45%, 40%, 20% and 1% of the starting volume for $E = 0.1$. Plots (d)-(f) repeat these curves for $E = 0.5$. In all plots $K = 0.1$, and the appearances of the curves are the same as figure 5.30.

the case where $E = 0.25$ we have $t_e = 509$ whereas for its noiseless counterpart in figure 5.28, $t_e = 543$ which suggests that small-scale features $(\tilde{\theta} = O(10^{-2}))$ can appreciably change the lifetime of a droplet (here by 7%).

Also reported by Wells *et al.* [150] is the possibility for the droplet to undergo snapping transitions on substrates with an eggbox-like topography, changing its contact line shape from diamond-like, to one of a more rectangular appearance. Interestingly, such features can also arise with chemical heterogeneities as depicted in figure 5.32 where these distinct shapes can be observed through the evaporation process. We note, however, that in this case the swap between the two distinct shapes occurs only once, rather than the several times reported by Wells *et al.* [150], which could be a manifestation of the fact we consider chemical heterogeneities here, rather than topographical substrate variations. However, this effect is sensitive to the strength and density of the features, as well as the substrate noise. Just like the case presented in figures 5.30 and 5.31, this can be eliminated entirely by increasing the
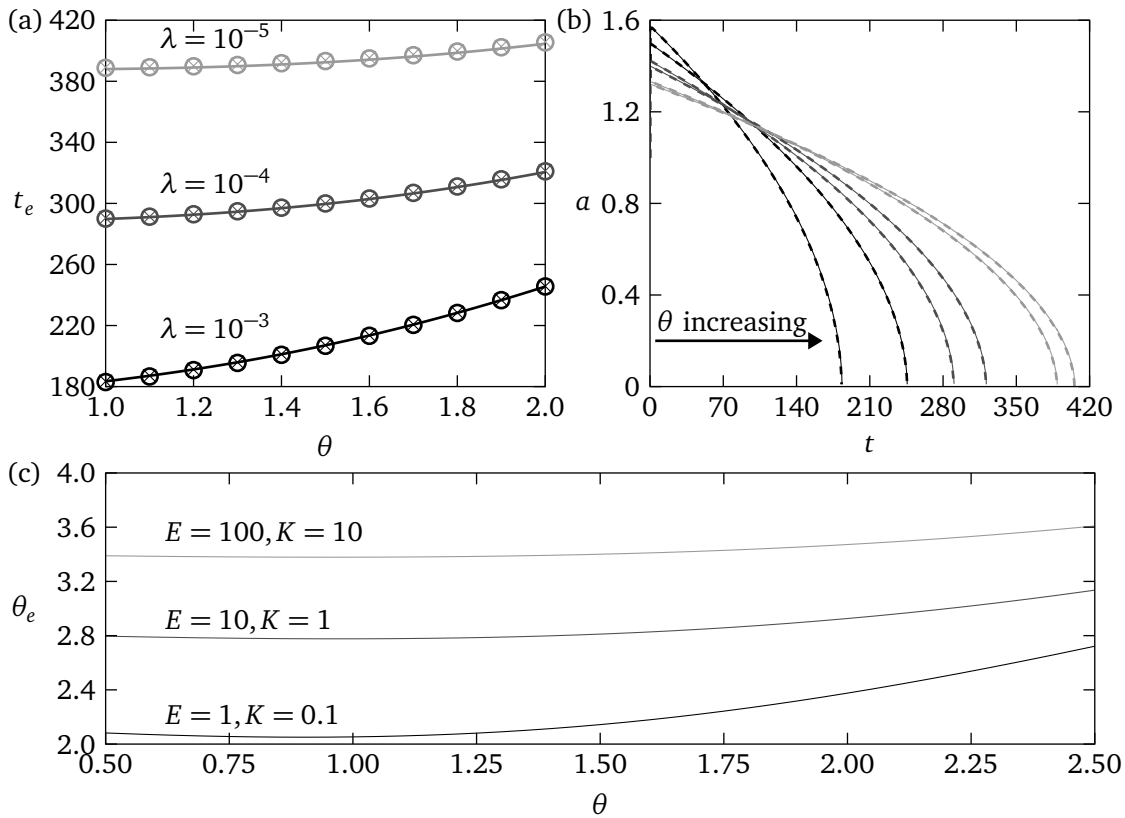
Figure 5.33: A case highlighting the effect of slip for $\mathcal{E} = 10^{-3}$ and $\mathcal{K} = 10^{-4}$. (a) The evaporation time in the same style as figure 3.7. (b) Radius evolutions for $\theta = 1$ and $\theta = 2$ where solid lines denote solutions to the full model, and dashed lines are solutions of the reduced model with (3.147). (c) Plots of the modified angle θ_e for varying θ. In (a) - (c) black, dark grey, and light grey curves correspond to simulations with $\lambda = 10^{-3}$, 10^{-4}, and 10^{-5}, respectively.

strength of evaporation, as depicted by figures 5.32 (d)-(f) which show nearly circular contact lines with small variations in the centroid motion.

5.4.3   The Effect of Slip

It is evident from the analysis presented in section 3.3 that the parameter controlling slip, λ, is of high importance. Cases explored here were based for somewhat larger values of λ to alleviate the numerical stiffness issues associated with simulating for lower slip, while extracting generic features on the coupling between evaporation and heterogeneity by varying E. Here we partially relax this restriction and consider fixing $\mathcal{E} = 10^{-3}$ and $\mathcal{K} = 10^{-4}$ and vary λ, noting that this was also considered previously by Savva *et al.* [53] for homogeneous substrates.

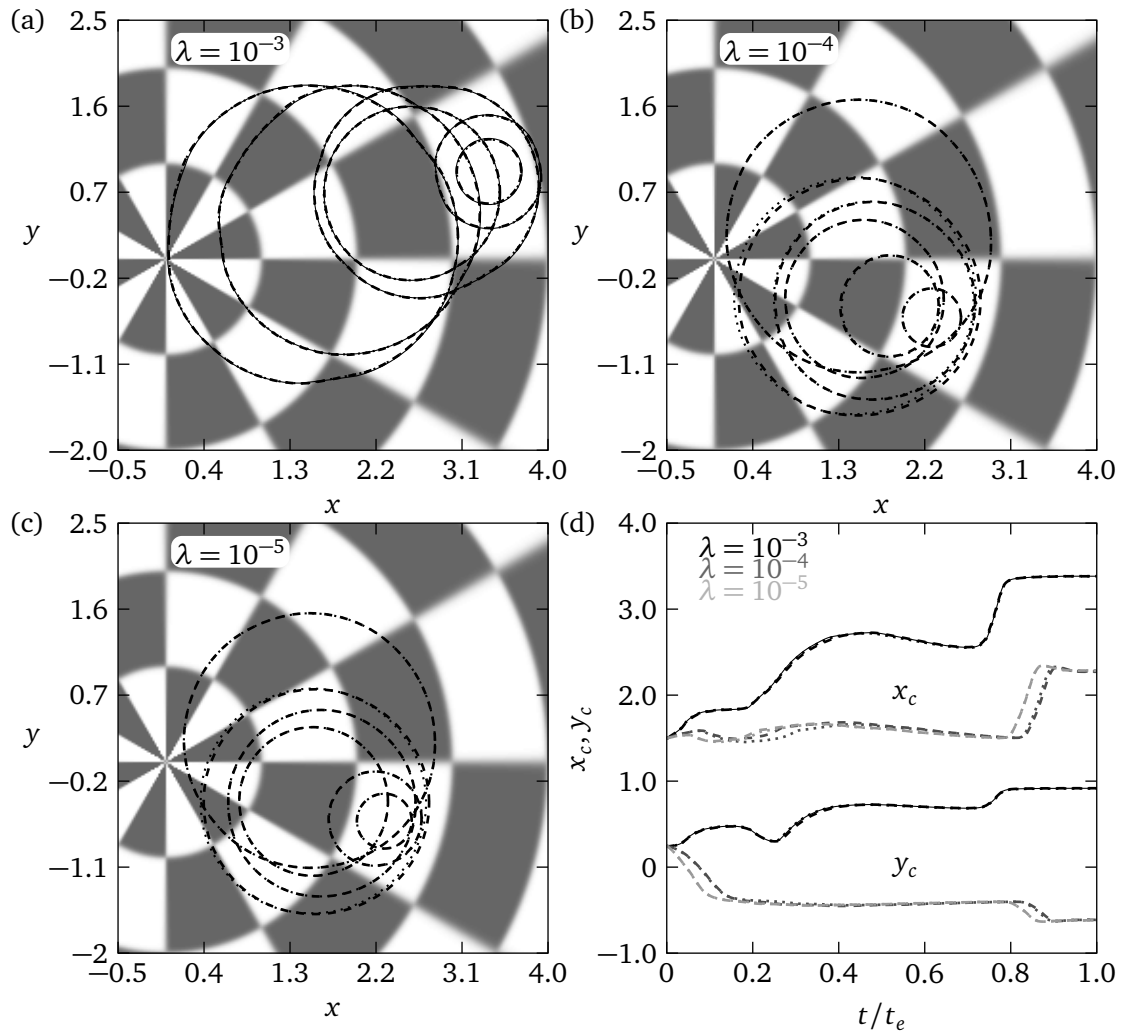To extend upon the work of Savva *et al.* we first consider axisymmetric droplets and vary

Figure 5.34: Droplets evaporating over the dartboard pattern substrate (5.5) for $\mathcal{E} = 10^{-3}$ and $\mathcal{K} = 10^{-4}$ with initial placement at $(x_c(0), y_c(0)) = (1.5, 0.25)$. Plots (a), (b) and (c) show contact line profiles at 99%, 70%, 40%, 20%, 5%, and 1% of the initial volume for $\lambda = 10^{-3}$, $\lambda = 10^{-4}$, and $\lambda = 10^{-5}$ respectively. (d) The centroid evolution for (a) - (c) where the time axis was scaled by $t_e = 181.1$, 295.7, and 394.1 for decreasing λ. In all plots, solid, dashed and dotted lines correspond to the full, hybrid and reduced models, respectively, where the evaporation formula (3.144) was utilised.

the surface heterogeneity to extract some generic features of how slip impacts the dynamics. Consistently with Savva *et al.* we observe in figure 5.33(b) that longer slip lengths cause the droplets to spread more, and in doing so evaporate at faster rates. Arguably the dynamics is more strongly impacted by larger slip lengths, since, figure 5.33(a) highlights a more dramatic increase in the total evaporation time as heterogeneity is increased: for $\lambda = 10^{-3}$ there is a 33.8% increase in the evaporation time between $\theta = 1$ and $\theta = 2$, whereas for $\lambda = 10^{-4}$ the change is 10.6%, and for $\lambda = 10^{-5}$ only 4.3%. Besides, this is not entirely surprising since plots of θ_e in figure 5.33(c) show that heterogeneity has a weaker impact on the dynamics for

higher values of E and K.

The differences between the values of slip become more apparent once we consider spatial variations in the substrate features. For this circumstance we use the substrate with a dartboard pattern (5.5) which has previously been used in figure 5.14. Arguably, using this substrate is also good approach to view the differences in slip since figure 5.33 indicates that the dynamics is more appreciably affected by heterogeneity as slip is increased.

In figure 5.34 we present simulations for the values of λ considered in figure 5.33, noting that simulating the full equations becomes increasingly difficult for lower values of λ, which is why comparison is only given for $\lambda = 10^{-3}$. Consistently with the results presented in figure 5.33 we observe that the case where $\lambda = 10^{-3}$ (figure 5.34(a)) behaves markedly differently compared to the other two cases. Here, the droplet moves to a different region of the substrate which is a direct consequence of the droplet being more mobile because of larger λ, and the evaporative effects becoming weaker (the values of E and K become smaller, since in all simulations we kept $\mathcal{E}$ and $\mathcal{K}$ constant), which, as alluded to earlier, more strongly impact the dynamics.

5.4.4 Stick-Slip Events

Contrary to the previous cases depicting the snapping mode of evaporation (see figures 5.30, 5.31 and 5.32), substrate transitions can occur at much faster time-scales by what is commonly referred to as stick-slip motion (or alternatively, stick-jump motion). While this effect has naturally emerged in 2D (see figures 5.6 and 5.11) and 3D (see figures 5.17 and 5.26) simulations, the evaporative flux dynamics behave slightly differently since the inner region parameters rely on both the flux and heterogeneous terms, contrary to before when the flux terms did not enter the inner region dynamics. In previous simulations, the effects of heterogeneity were mitigated by increasing E, and thus, enhancing θ_e so that it attains increasingly larger values than θ (meaning the dynamics are more strongly influenced by the flux, and less by the heterogeneity). Primarily motivated by the experimental work of Dietrich *et al.* [217] we repeat the simulations of figure 5.17, but instead of a linear mass loss, we prescribe evaporative effects for different values of E. The results are shown in figure 5.35, where we observe that stronger evaporation effects weaken pinning events, to the extent of essentially removing stick-slip dynamics for the larger values of E. At the same
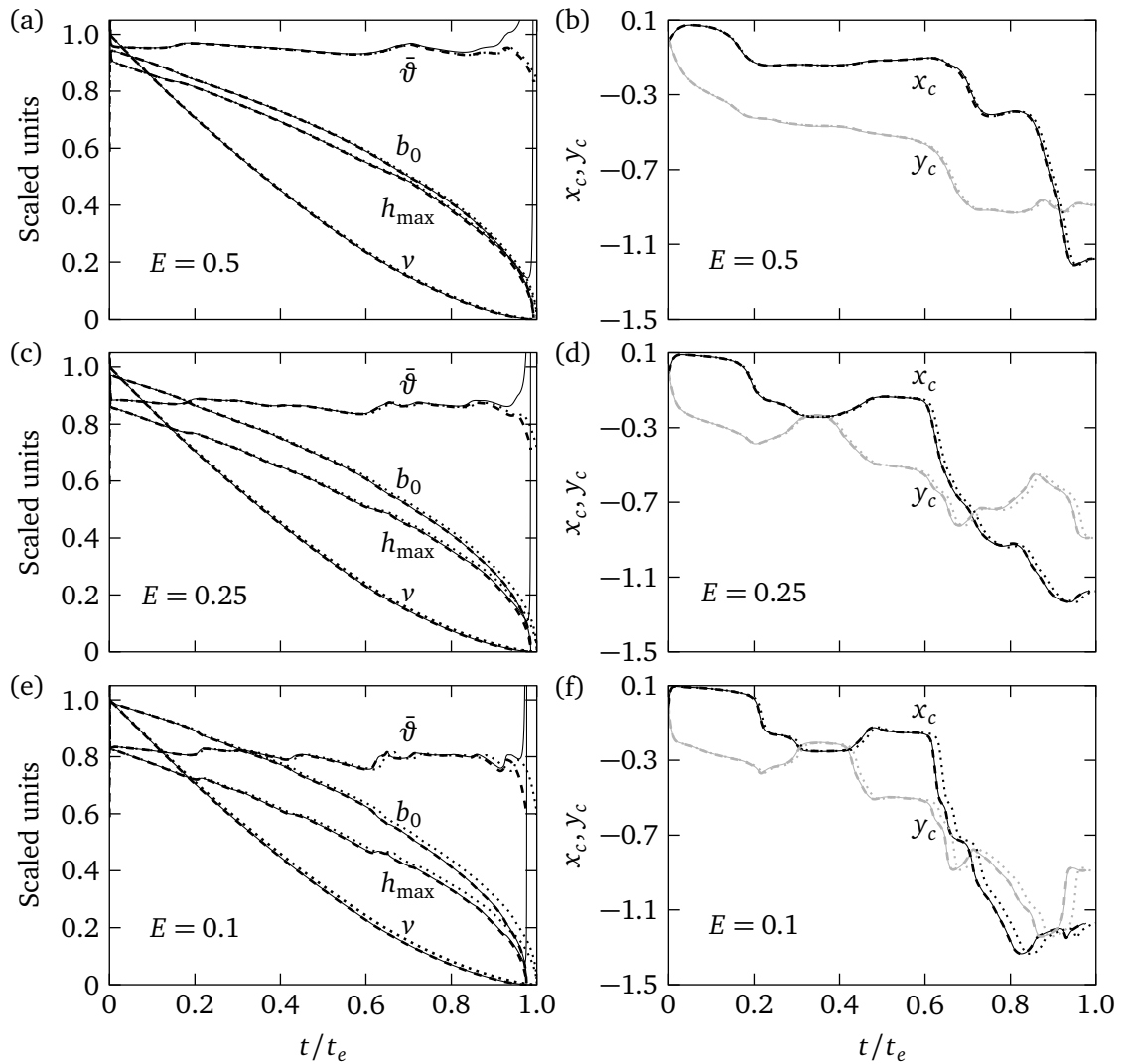
Figure 5.35: Stick-slip events similar to that reported by Dietrich *et al.* [217] for $E = 0.5$, 0.25 and 0.1 over the substrate used in figure 5.17. Plots (a), (c) and (e) depict the evolution of the mean radius b_0, mean apparent contact angle $\bar{\vartheta}$, maximum height $h_{\max} = b_0\bar{\vartheta}/2$, and volume v where each variable was scaled with 1.7, 2, 1.7 and 2π respectively. Plots (b), (d) and (f) are the centroid evolutions in time, where black curves are plots of x_c and grey of y_c. The time axis was scaled by $t_e = 364$, 665.4 and 1545 for decreasing E, which is the value taken from the simulation of the hybrid model with (3.147). In all plots $K = 0.1$, and the styles of the curves are the same as figure 5.30.

time, we observe that the apparent contact angle in the final stages (and consequently $h_{\max}$) predicted by the full equations undergo an abrupt increase, which is a product of the fronts receding quickly so that the apparent contact angle increases to prevent this from happening. We do note, however, that properly resolving these final moments would require more radial collocation points which would nevertheless increase numerical stiffness and computational time. Therefore, this sharp increase may also be attributed to inaccurately capturing the droplet extinction stage. However, since the analysis we present does not account for this stage
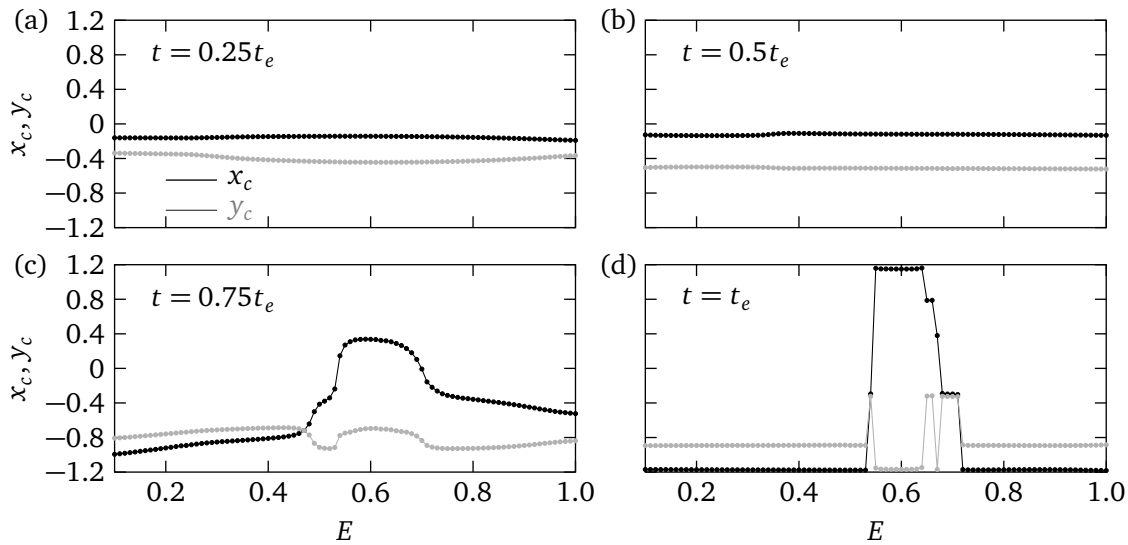
Figure 5.36: Centroid positions for varying E from 90 simulations of the hybrid method with (3.144), $K = 0.1$, and the substrate used in figure 5.35. Plots (a)-(d) indicate the x_c (black) and y_c (grey) positions for 25%, 50%, 75% and 100% of the droplets lifespan, respectively.

we chose not to pursue further the numerical intricacies that would be required to properly resolve droplet extinction. We only desire to capture solutions during the evaporation stage to properly assess how heterogeneity impacts the overall dynamics, rather than the final stage where heterogeneity does not impact the evaporation too appreciably.

Unlike the snapping case reported in figures 5.30 and 5.31, it appears as if the randomised features of the substrate in figure 5.35 have not altered appreciably the motion of the centroid. However, using the hybrid method, we can again extract some generic features by simulating for a range of E. Figure 5.36 presents the result of this approach, showing that for a range of E between roughly 0.55 and 0.7 the droplet follows a different path along the substrate, showing rather appreciable changes in x_c and y_c. Once again, like figure 5.31 we see that the centroid motion is indeed rather sensitive to the parameters controlling the flux, showing how different behaviours can arise by slight modifications in the flux.

5.4.5   Constant-Radius and Angle Modes

As highlighted in section 1.4, as well as examples shown in this section (see, e.g. figure 5.35), surface heterogeneity often leads to pinning events where the droplet can remain localised for a period of time. This creates the constant-radius mode in which the contact angle of the droplet fluctuates along the contact line while the radius remains mainly fixed. This mode, and the corresponding constant-angle mode have previously been discussed in both the 2D
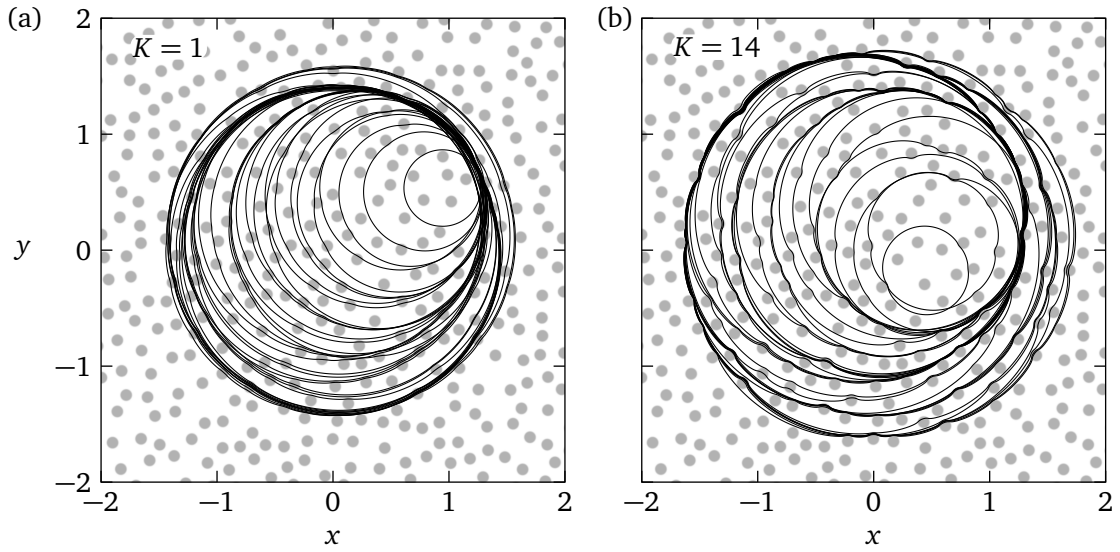
Figure 5.37: Contact line profiles for evaporating droplets at various times over the substrate used in figure 5.26. Plots (a) and (b) depict cases for $K = 1$ and $K = 14$, respectively, where $\lambda = 2 \times 10^{-5}$ and $E = 4$. In both cases, solutions are obtained with the reduced model and the evaporation formula (3.144).

(see figure 5.2) and 3D (see figure 5.26) geometries with prescribed mass flux, where the switch between these modes can naturally occur when chemical heterogeneities are present. These previous cases, however, concerned mass changes through the macro-scale, and thus, the micro-scale details were not affected by the mass flux.

To view in which situations such modes can arise we perform simulations with substrates that are comprised of randomly distributed wettability features, and consider fairly weak evaporative flux so that heterogeneity effects become more apparent. Here we proceed with simulating the reduced model only, since resolving the substrate features with either the full or hybrid methods would require a rather large number of azimuthal collocation points, as described in section 5.3.4. Rather than presenting data concerning the droplet mean radius and apparent contact angle as previously done in the thesis, we trace the evolution of the radius and angle when the droplet shape is viewed in the x and y planes in direct analogy of how experimental measurements are taken (see, e.g. Dietrich *et al.* [217] for methods used in related experiments). Thus, we locate all x and y coordinates of the contact line using (2.55) and consider

$$d_x = \frac{\max(x) - \min(x)}{2} \quad \text{and} \quad d_y = \frac{\max(y) - \min(y)}{2}, \tag{5.14}$$

(a)   (b)

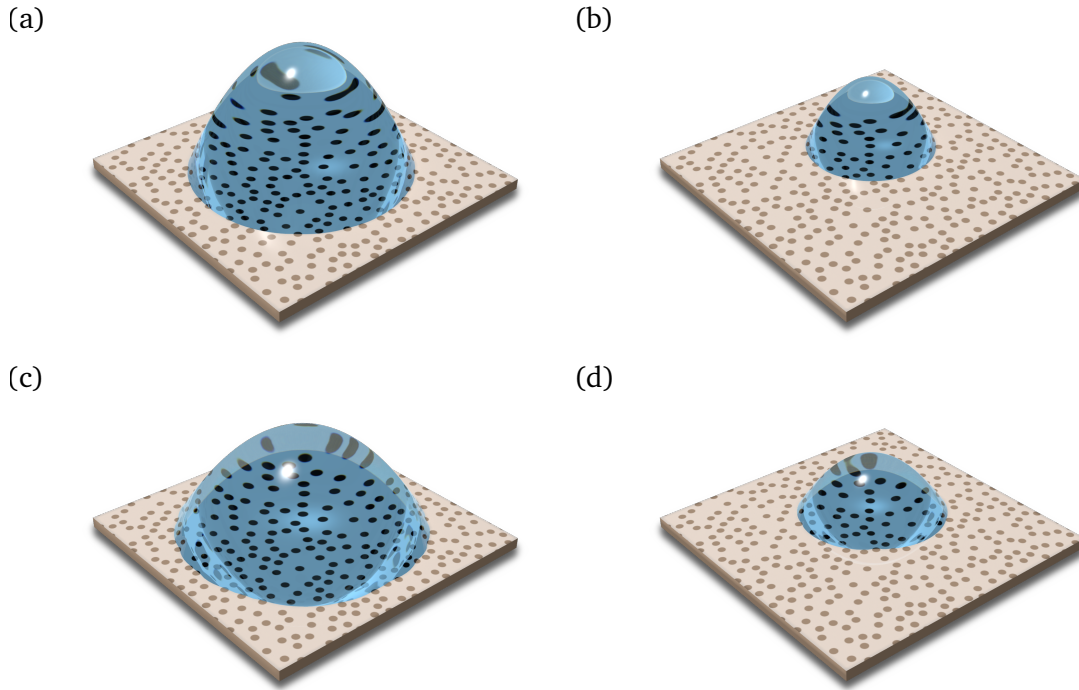(c)   (d)

Figure 5.38: Plots (a) and (b) are droplet profiles for figure 5.37(a) at 99% and 20% of the initial volume. Plots (c) and (d) show profiles at the same volumes for the droplet considered in figure 5.37(b).

as a measurement of the droplet half-width alongside

$$\vartheta_x = \frac{4v}{\pi d_x^3} \quad \text{and} \quad \vartheta_y = \frac{4v}{\pi d_y^3}, \tag{5.15}$$

as the corresponding apparent contact angles in the x and y planes, respectively.

In the first case we consider the same substrate used for figure 5.26 where the constant-radius and angle modes were observed for the cases of fluid transfer through the bulk. In figure 5.37 we investigate two cases of evaporating droplets where K is varied to highlight dynamics that are modified by slightly weaker or stronger evaporation effects. It is easy to see that in the case where kinetic resistance is greater (figure 5.37(b)) the contact line becomes more distorted and the influence of heterogeneity is felt more strongly. However, the influence of heterogeneity still appears for lower kinetic resistance (figure 5.37(a)) since pinning events still occur. Figure 5.39 depicts the angle and half-width evolutions as described previously, and indeed show that the constant-radius and angle modes arise naturally through the heterogeneities present across the substrate, although, they are more noticeable, once again, when evaporation is weaker. Let us also remark in the differences in evaporation times. For $K = 14$ we have $t_e \approx 2079$, whereas $t_e \approx 2400$ for $K = 1$ which is a 15.44% increase.
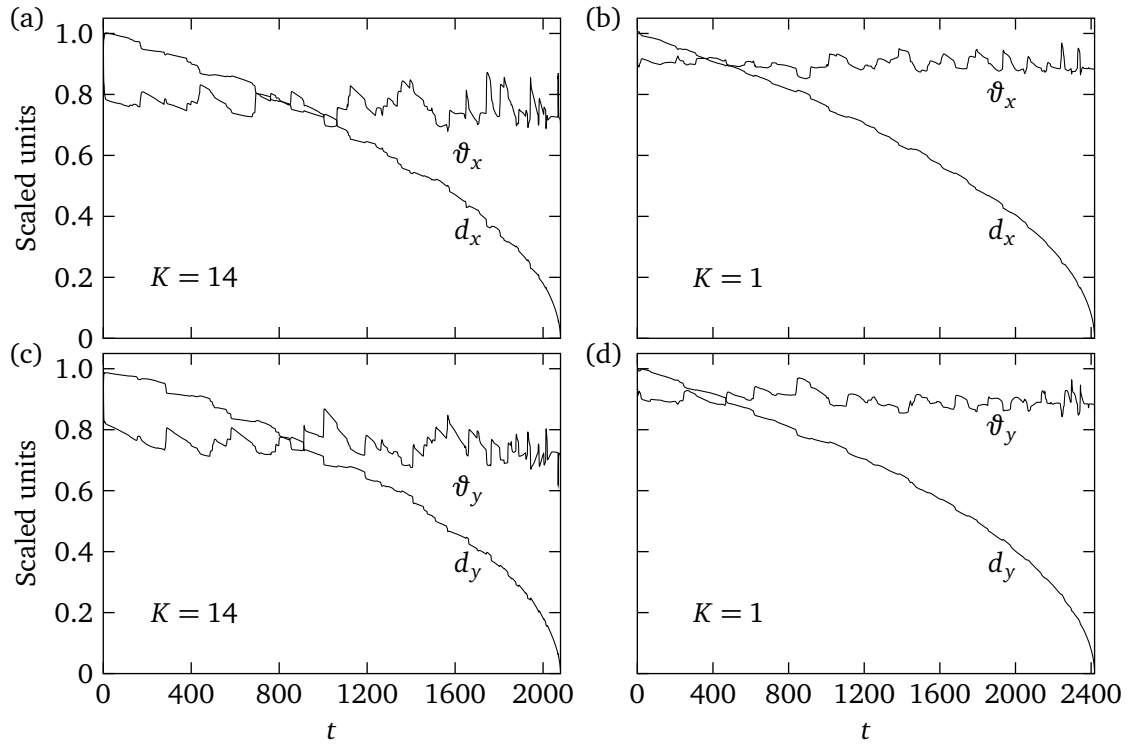
Figure 5.39: Radius and angle evolutions for the case presented in figure (5.37). Plots (a) and (c) highlight the $K = 14$ case for evolutions in the x and y planes, respectively. Plots (b) and (d) likewise show the evolutions in the x and y planes for when $K = 1$ (see text for how $d_{x,y}$ and $\vartheta_{x,y}$ are found). For the $K = 14$ cases the angles and half-widths were scaled by 2.05 and 1.7, respectively. Likewise for $K = 1$ the angles and half-widths were scaled by 2.5 and 1.52, respectively.

This can be explained by the overall larger radii achieved in the higher kinetic resistance case, which consequently flattens the free surface which allows more molecules to escape through evaporation (see the droplet profiles in figure 5.38).

Noteworthy from figure 5.37 is that the evaporation parameters were chosen to match figure 8 in [53] (i.e. $E = 4$, $K = 14$ and $\lambda = 2 \times 10^{-5}$) which are loosely based on having a water droplet (see also section 3.3). During their computation the evaporation time is predicted at $t_e \approx 2000$ dimensionless units, here, the inclusion of surface heterogeneity has delayed the total evaporation time, noting that if we retained a homogeneous substrate as in [53] the evaporation time reduces to $t_e \approx 1984$, which is roughly in the same ballpark as in [53] which uses the Navier-slip model.

To conclude the investigation of evaporating droplets, we consider a random superposition of features. Namely, in figure 5.40 we simulate for a droplet evaporating over a substrate similar in appearance to the one used in figure 5.17, noting that in this circumstance changes in surface wettability occur on much shorter length-scales than previous cases, which means that
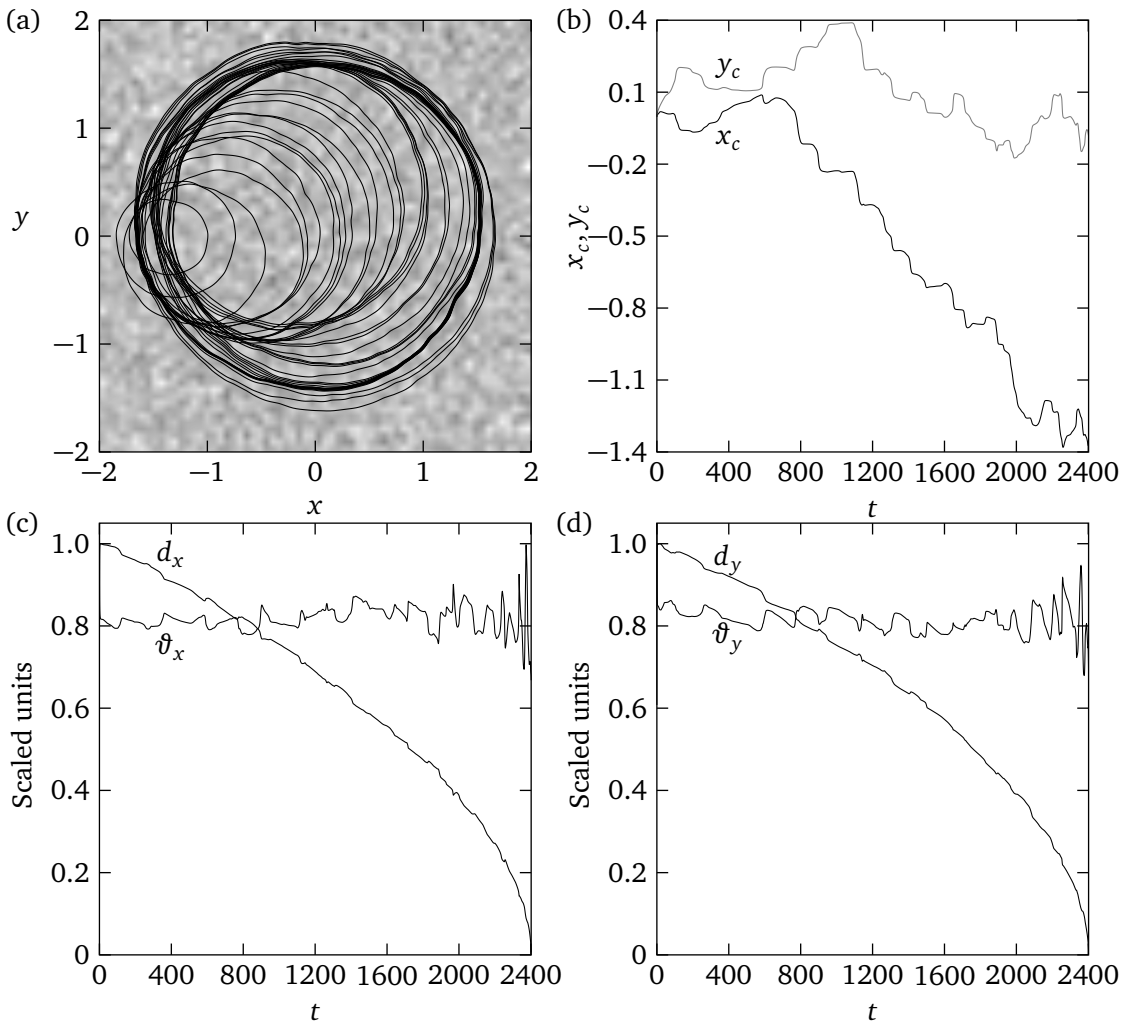
Figure 5.40: Evaporating droplet over a noisy-type substrate described by (5.10) where $\hat{\theta} = 1.5$, and $\tilde{\theta}$ is band limited noise comprised of 90 harmonics, wavelengths up to 13π and normally distributed amplitudes with zero mean and unit variance. (a) Depicts contact line profiles at various times. (b) The x_c (black) and y_c (grey) centroid evolutions. Plots (c) and (d) depict radius and angle evolutions in the x and y planes, respectively, where the half-widths was scaled by 1.65 and the angles by 2.11. In all plots, solutions were obtained with the reduced model and the evaporation formula (3.144) by using $\lambda = 2 \times 10^{-5}$, $E = 4$ and $K = 14$.

just as the calculation of figure 5.37 their resolution requires a greater amount of azimuthal collocation points, rendering the full and hybrid models difficult to resolve with the current numerical tools. The main purpose behind using such a substrate is to emulate qualitatively how pinning events may arise in randomly heterogeneous surfaces. As depicted in figure 5.40(b) we certainly see this is the case, where the droplet will frequently encounter pinning events, leading to their associated de-pinning and stick-slip behaviours. Like figures 5.37 and 5.39, this leads to the appearance of both the constant-radius and angle modes in the x and y planes, once more showing these features can arise due to variations in the surface wettability,

which in this case are rather noisy. Figure 5.40 also shows an increase in evaporation time as compared to figure 5.39(a) and (c), which is due to the larger average contact angle in figure 5.40 ($\theta_{\text{avg}} \approx 1.5$) compared to figure 5.37 ($\theta_{\text{avg}} \approx 1.17$), which in turn cases the heat transfer from the substrate to the droplet to become less efficient.

5.5 3D Droplets on Rough Surfaces with Constant Mass

In this section we further the discussion by considering substrates with changes in its topography, contrary to previous sections where the substrate was perfectly flat. As highlighted in the analysis of section 3.4 we consider substrate features that are rather small in amplitude to avoid the surface features perforating the free surface of the droplet, and also so that we can use the reduced model (3.98) with an appropriate change of the apparent contact angle. Therefore, in the cases that follow we use (3.98) by considering a change of ϑ either using the boundary integral approach as described in chapter 4 (the hybrid model) or using equation (3.163) (the reduced model).

Unless otherwise stated, we maintain the initial parameters $(x_c(0), y_c(0)) = (0, 0)$ and $a(\phi, 0) = 1.01$, to avoid the so-called *gamma contour* that occurs at radius $a(\phi, 0) = 1$ which causes the ill-conditioning in the boundary integral formulation with logarithmic kernels (see Jaswon [225] for more discussion on the gamma contour). This issue has previously been dealt with by rescaling the droplet radius and volume to avoid the unit circle, however choosing $a(\phi, 0) = 1.01$ also suffices and allows us to bypass rescaling topographical features, which may become difficult if they are generated numerically. Thus, with $\lambda = 10^{-3}$, $v(t) = 2\pi$, and surface heterogeneity $\theta(x, y) = 1$ we simulate spreading on topographically varying substrates, contrasting where appropriate with the solutions of the full problem, and that of the model derived by Lacey [52] (equation (1.6)).

5.5.1 Corrugated Surfaces

We first consider a substrate of corrugated topographical features analogously to the striped chemical heterogeneities seen in sections 5.3.3 and 5.4.1. Previously the striped substrates considered had rather sharp changes between the high and low contact angles, here, we consider substrate transitions that are smoother to avoid the droplet becoming trapped at the striped features, which is also in alignment with the long-wave assumption. Such substrates
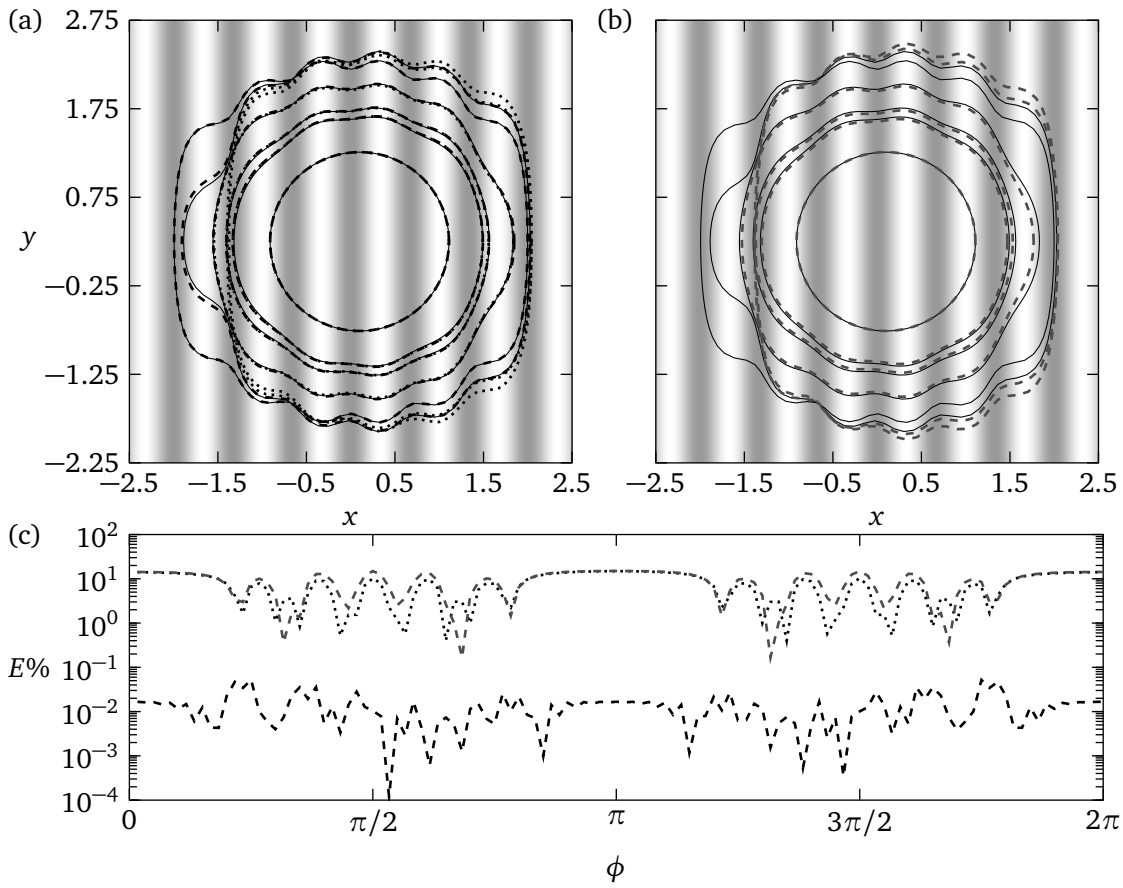
Figure 5.41: Spreading over a substrate of striped topographical features prescribed by $\eta(x, y) = 0.05 \cos(3\pi x)$ with initial placement at $(x_c(0), y_c(0)) = (0.1, 0.25)$. Plots (a) and (b) are contact line profiles at $t = 0, 0.1, 0.2, 1, 15$, and 100 where solid, dashed, and dotted black lines correspond to the full, hybrid and reduced models, respectively. Dashed grey profiles in (b) correspond to solutions of Lacey's leading-order model (1.6). The substrate is shaded corresponding to the choice of η where dark and light patches correspond to the high and low regions, respectively. (c) The percentage error in $a(\phi, t)$ for the equilibrium shape predicted by the hybrid model (dashed black), reduced model (dotted black), and Lacey's prediction (dashed grey) as compared to the solution from the full equations.

have been considered with evaporating droplets by Wells *et al.* [150] and gave rise to the snapping transitions which have been discussed at length in previous sections.

In figure 5.41, this case is presented where the droplet is initialised so that it exhibits asymmetric behaviours as the contact line expands so that we can assess the merits of the theory presented. In fact we observe through figures 5.41(a) and (b) that two equilibria emerge due to the off-centre initial placement. While Lacey's equation (1.6) and the reduced method fail in predicting the equilibria of the full equations they are indeed in agreement with each other, nevertheless, the hybrid model provides the most satisfactory agreement with a rather low percentage error in the final contact line shape (see figure 5.41(c)). This points
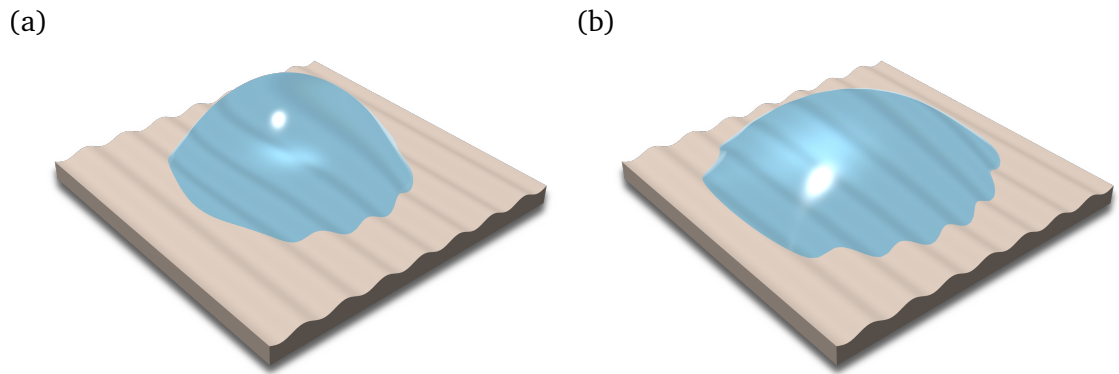
(a) (b)

Figure 5.42: Droplet profiles for figure 5.41 at times $t = 1$ and $t = 100$ in (a) and (b), respectively.

to the presence of multiple equilibria induced through the surface topographies, which is also alluded to from the phase plane analysis presented by Savva & Kalliadasis [56] who considered the 2D case. Noteworthy also is that similar to the chemical heterogeneity study, the droplet elongates and conforms to the parallel grooves, even though the surface features are rather small in comparison to the height during spreading (see figure 5.42 for two height profiles).

Importantly, the disagreement in solutions further highlights the importance of considering the hybrid approach coupled with the next-order correction derived in the current analysis. Especially since both the hybrid model and Lacey's equation (1.6) use the boundary integral method, and yet, give two different results. Interestingly, the initial spreading stages predicted by the reduced model appear to agree better than Lacey's equations also. While we expect that Lacey's equations will work more favourably as $\lambda \to 0$ we again emphasise that simulating the full equations become infeasible in this limit, as the increase in numerical stiffness causes longer simulation times. Still, the hybrid method performs rather well in the value of λ considered, noting that only small discrepancies appear in the intermediate spreading stages which is likely attributed to the neglected surface roughness corrections.

5.5.2 Periodic Features

Leading from the previous example we increase the complexity of the substrate by considering corrugations in both the x and y directions. Figure 5.43 shows this result in the style presented in figure 5.41 to compare with the corrugated substrate earlier to highlight that the presence of more dense substrate features causes a more irregularly-shaped contact line. In contrast to the previous example, figure 5.43 shows that the reduced model predicts the correct equilibria,
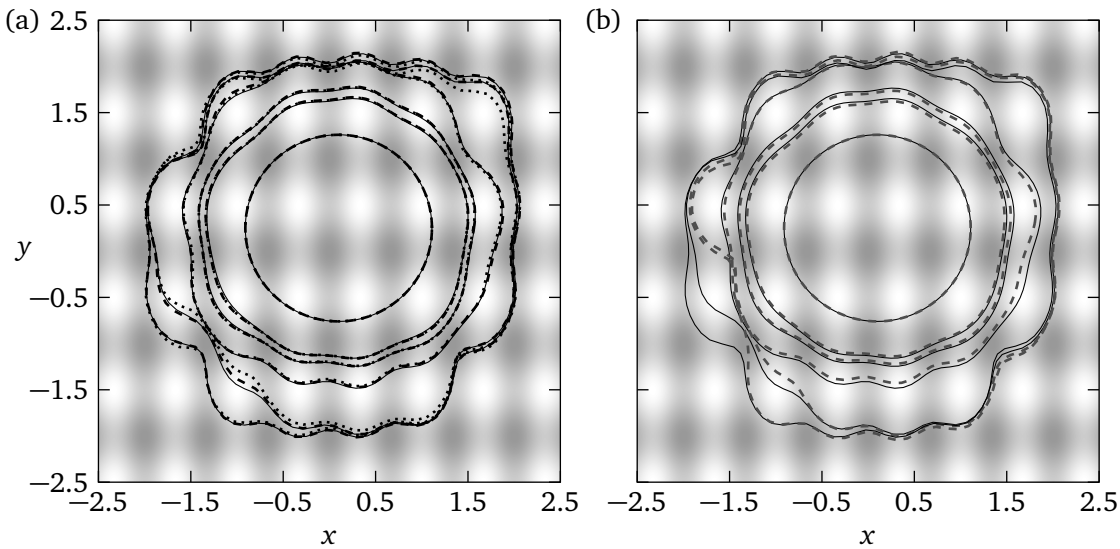
Figure 5.43: Spreading over a surface with more densely populated features prescribed by $\eta(x,y) = 0.05\cos(2\pi y) + 0.05\cos(3\pi x)$. Plots (a) and (b) depict contact line snapshots using the same styles, times, and initial parameters as figure 5.41.

however, Lacey's equations predict this incorrectly since a final stick-slip event is not captured (around $(-1.5, 0)$). It is worth mentioning that incorrectly capturing equilibria from Lacey's equation (1.6) does not persist for all cases tested. Generally (1.6) does predict the correct equilibria with disagreement manifesting through the intermediate spreading stages which is also sometimes observed with the reduced model. The purpose of these examples was merely to highlight the importance of the next-order correction retained in this analysis, which appears to perform well throughout.

Interestingly, as in Cubaud & Fermigier [226] with chemical features, we can also obtain droplets whose contact lines assume geometric shapes. This is presented in figure 5.44(a) where the contact line assumes an octagonal-like shape and in figure 5.44(b) where it appears to have a hexagonal-like shape. In the limit as the wavelength of the asperities decreases, the contact line will resemble, respectively, a rotated square and a rhombus. The change in contact line shapes is a manifestation of altering the parameters controlling the number of features in each direction, noting also that the final equilibrium is rather sensitive on the substrate as well as the initial input parameters, since in some tested cases breaking of the symmetry occurred and skewed droplet shapes were ultimately obtained.
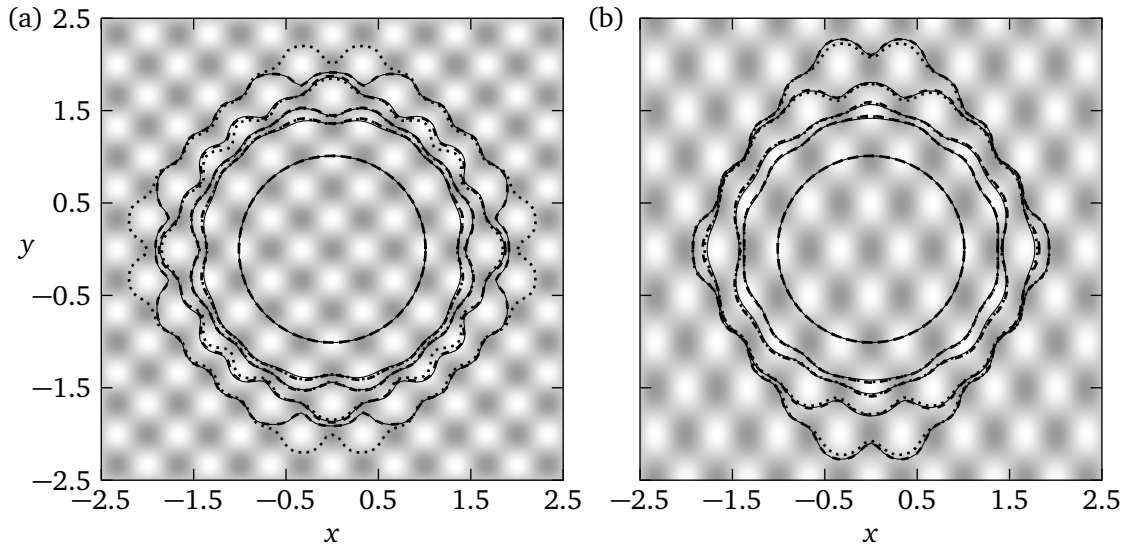
Figure 5.44: Spreading over periodically structured substrates which promote different final equilibria by slightly modifying the features. Plots (a) and (b) show contact line snapshots for times $t = 0$, 0.1, 0.2, 1 and 100 over the surfaces $\eta(x,y) = 0.1\cos(3\pi x)\cos(3\pi y)$ and $\eta(x,y) = 0.1\cos(3\pi x)\cos(2\pi y)$, respectively. Refer to figure 5.41 for a description of the various curves.

5.5.3 Random Features

Motivated by previous cases explored with chemical heterogeneity (e.g. figures 5.17, 5.19, 5.35 and 5.40) we likewise consider substrates with randomly distributed features in the form

$$\eta(x,y) = \hat{\eta}(x,y) + \tilde{\eta}(x,y). \qquad (5.16)$$

where $\hat{\eta}(x,y)$ denotes the predominant structure of the substrate, and $\tilde{\eta}(x,y)$ is band limited white noise.

In figure 5.45 we examine two cases, each where $\hat{\eta}(x,y) = 0$, and $\tilde{\eta}(x,y)$ is generated with 10 harmonics, wavelengths up to 2π and normally distributed amplitudes with zero mean and variance set to 0.15 so that topographical features vary at long length scales, meaning comparison with the full equations is possible. In both figures 5.45(a) and (b) similar spreading behaviours emerge as the contact line grows increasingly non-circular to account for the substrate features. Although the substrate amplitudes vary on a larger scale than previously considered, the hybrid and reduced models cope rather well, showing only minor discrepancies during the spreading stages and equilibrium shape. Besides, as better viewed from figure 5.46 the substrate features are still rather small as compared to the droplet size, like figure 5.42.
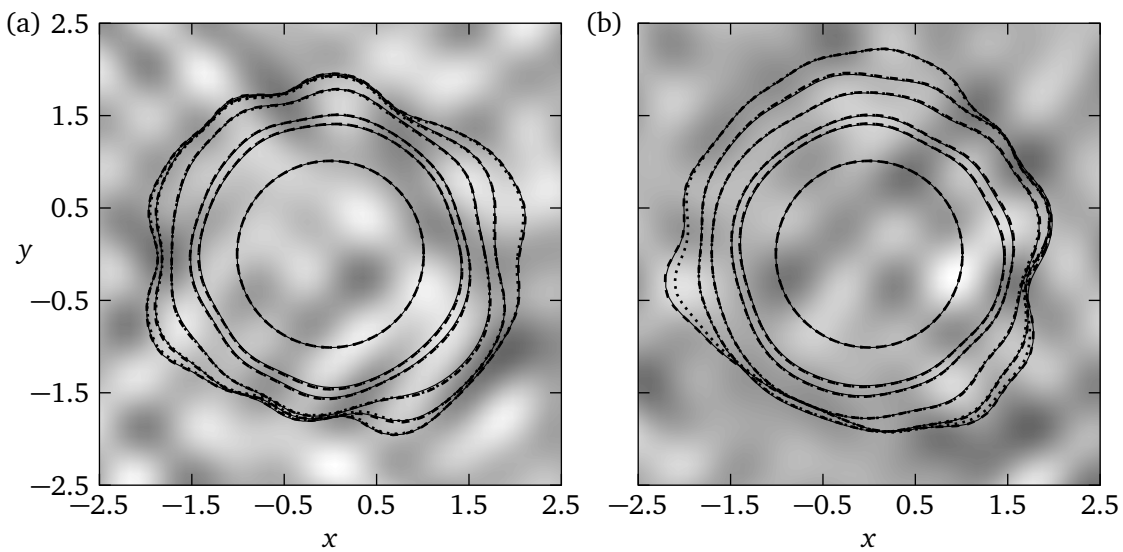
Figure 5.45: Contact line motion over two substrates characterised by randomly distributed features where $\eta_{\mathrm{min/max}} \approx \pm 0.15$ in both (a) and (b) (see text for generation of the substrate). Contact line profiles are given at times $t = 0, 0.1, 0.2, 1, 3$ and 50, and the various curves are in the same style as figure 5.41.
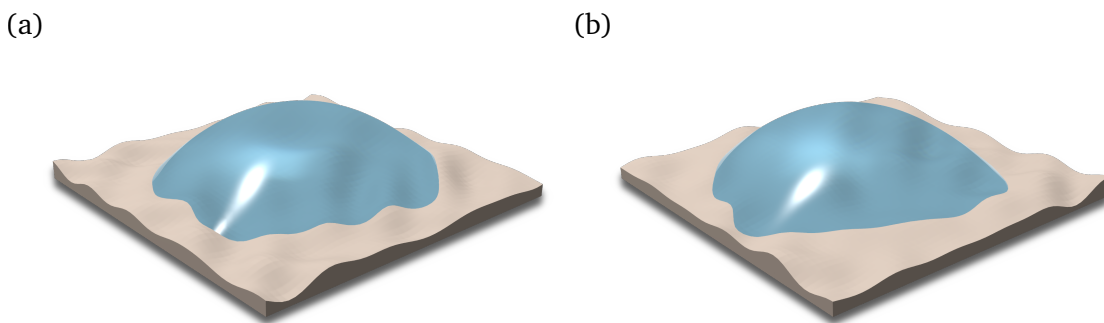
Figure 5.46: Droplet profiles for the equilibrium shapes in figures 5.45(a) and (b).

5.5.4 Stick-Slip Events

Throughout previous cases we have shown rather compelling numerical evidence to highlight the validity of using the reduced model to calculate droplet spreading behaviours. Therefore, similar to cases performed previously (see section 5.3.4) we can confidently use the reduced model to investigate situations that are too computationally demanding for the full or hybrid models while remaining mostly within the regime of validity to ensure accurately depicted solutions.

As shown in the 2D setting by Savva & Kalliadasis [56] even small amplitude features can cause the droplet to undergo stick-slip transitions during the spreading stages, and indeed this has been observed through cases presented here, for example with figure 5.44. Arguably, these
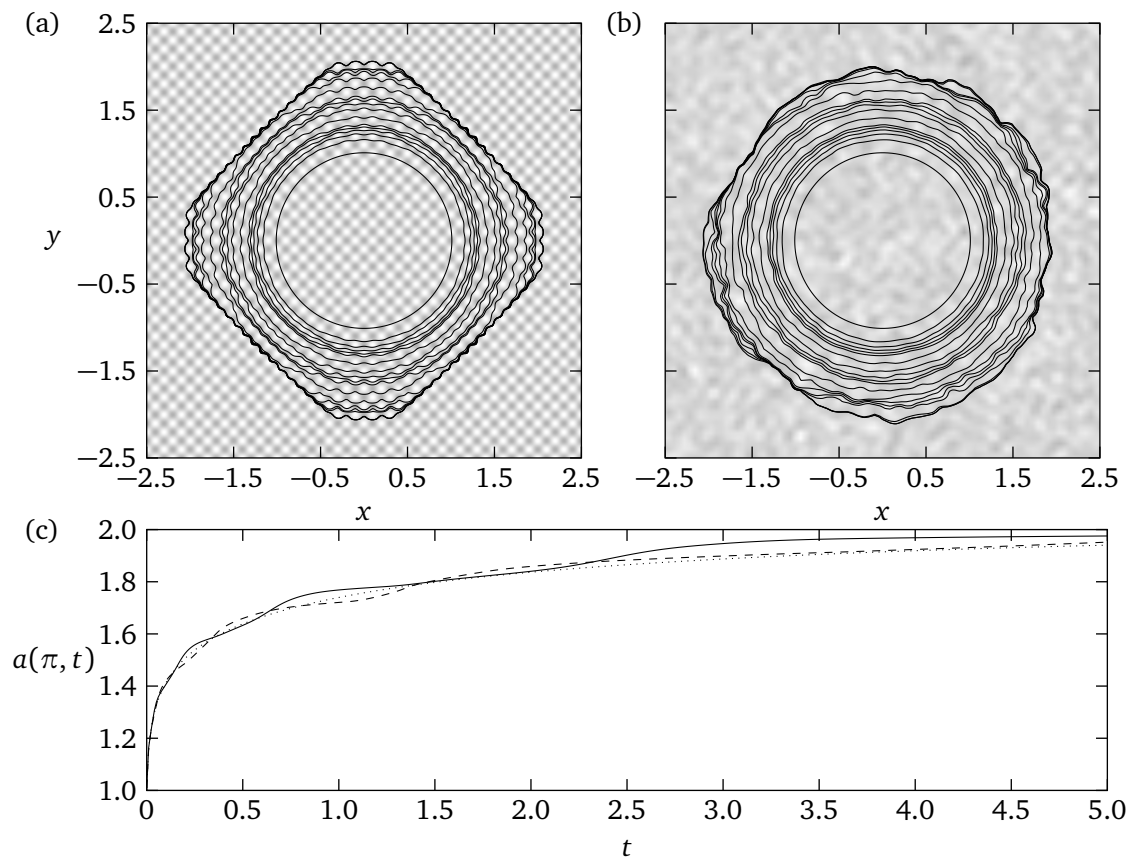
Figure 5.47: Stick-slip effects induced through features of small amplitudes and wavelengths using $\eta(x,y) = 0.025\cos(10\pi x)\cos(10\pi y)$ in (a) and one comprised of random noise in (b) (see the text for a more detailed description). Plots (a) and (b) depict contact line snapshots at various times where solutions are given by the reduced model only. (c) The initial spreading stages along the negative x axis where solid lines correspond to (a), dashed lines to (b), and dotted lines to the rate of spreading on $\eta(x,y) = 0$.
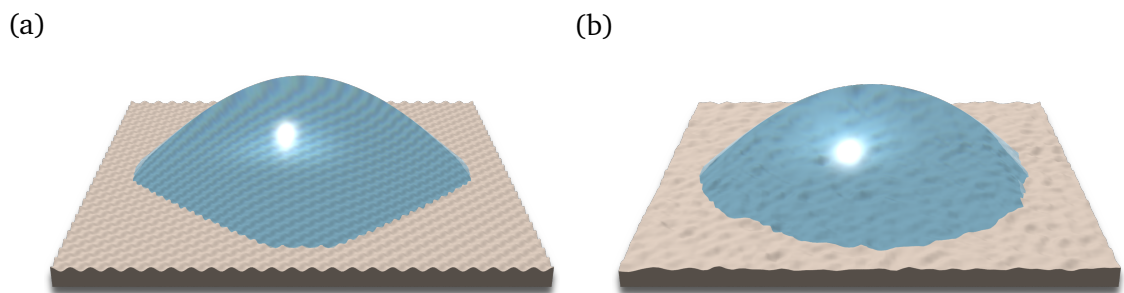
Figure 5.48: Droplet profiles at the equilibrium stages seen in figure 5.47.

transitions more easily occur once the substrate is more densely populated with topographical features. Thus, in figure 5.47 we investigate two such cases, one with a structured substrate similar in appearance to figure 5.44(a), and one comprised of random spatial features using

(5.16) where $\tilde{\eta}(x, y)$ is formed with 75 harmonics, wavelengths up to 10π and normally distributed amplitudes with zero mean and variance set to 0.05. While both situations exhibit similar spreading behaviours, it is worth noting that figure 5.44(b) is arguably more reminiscent of an actual contact line, since in reality all substrates will contain small variations in the surface topography, as better visualised in figure 5.48. In these cases, the amplitudes of the substrate features have been enhanced to emphasised the stick-slip events, however, it is worth noting that stick-slip behaviours can also occur to a lesser degree on substrates with smaller amplitude topographies. Therefore, stick-slip events can be attributed to either chemical heterogeneity, or changes in the surface topography, where even small changes can give large variations in the spreading behaviours.

5.5.5   A Miscellaneous Example

A final example to test the limits of the theoretical analysis concerns a case of a wrinkled substrate generated through an equilibrium solution to the Swift-Hohenberg equation

$$\partial_t \eta = \tilde{\epsilon}\eta - \left(\nabla^2 + 1\right)^2 \eta + \tilde{g}\eta^2 - \eta^3, \tag{5.17}$$

which is a non-linear PDE noted for its pattern forming behaviours, originally derived to study convective instabilities in fluid flows (see Swift & Hohenberg [227] for its derivation, and [228] for the numerical solution used). To generate the substrate we consider the parameters $\tilde{\epsilon} = 3$, $\tilde{g} = 0$ and a random initial condition which forms a pattern on the doubly periodic $(0, 2\pi) \times (0, 2\pi)$ grid , where amplitudes are scaled so that the features lie in the range $\eta_{\text{max/min}} \approx \pm 0.043$.

Such a substrate consists of irregularly shaped grooves and was used to examine how the liquid manages to impregnate its features. Here we observe that the contact line favours motion along the shallower parts of the substrate, but we also observed a discrepancy that is more pronounced at intermediate times, whereby both the hybrid and reduced models failed to capture on time a de-pinning event that occurred at the lower left part of the contact line, resulting in about an 11% error in the contact line shape. Note that this disagreement is most likely attributed to the higher-order corrections accounting for the surface roughness terms, which, for the sake of analytical tractability have been neglected in the present treatment. Therefore this case motivates a more detailed future analysis which can capture such events with better accuracy.
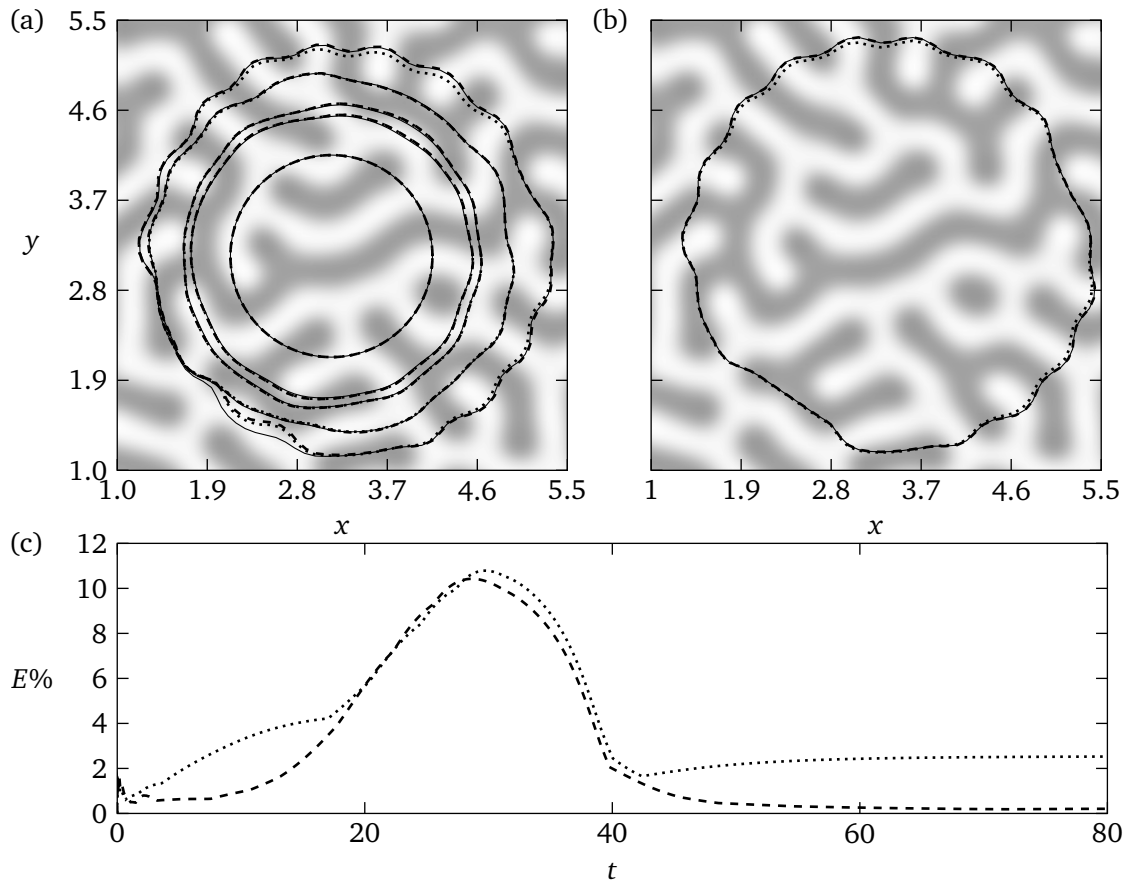
Figure 5.49: Spreading over a substrate generated through a numerical solution of the Swift-Hohenberg equation (5.17) with initial droplet placement at $(x_c(0), y_c(0)) = (\pi, \pi)$. (a) Contact line snapshots at times $t = 0, 0.1, 0.2, 1.5$ and 20. (b) The equilibrium contact line snapshot at time $t = 80$. (c) Evolution of the percentage error in the contact lines between the hybrid and full models (dashed), and the reduced and full models (dotted). The styles of the curves in (a) and (b) are the same as figure 5.41.

5.6   Summary

In this chapter we have presented an array of results to highlight the merits and applicability of the theory, as well as to extract some generic features of the dynamics observed in experiments. Particular attention was placed upon droplets that are subjected to changes in mass which is either lost in the macroscopic features or by evaporation where the flux is maximised near the contact line. Importantly, these results highlighted the presence of hysteresis arising through the chemical heterogeneity which is not assumed to be present *a priori*, it arises directly in simulations. Therefore, features such as stick-slip and pinning events occur naturally through the majority of the cases considered, and also arose in section 5.5 where we considered substrates which vary topographically, rather than chemically.

Through all cases presented we observe excellent agreement between the outcomes of

the theoretical analysis and computations of the full equations, noting that the most optimal agreement was obtained with the hybrid method which combines the merits of the theory with the boundary integral method. The analysis presented here gives more satisfactory agreement as compared to an equation which retains the leading-order term only, showing that obtaining the non-trivial higher-order corrections is indeed essential to accurately capture the dynamics.

— Chapter 6 —

Concluding Remarks and Future Outlook

6.1 Conclusions of the Thesis

The motion of a liquid drop on solid surfaces is a process that is rather easy to conceptualise, however, the governing physics behind this situation is inherently complex, rendering their study highly non-trivial. The dynamics is governed by an interplay between macro-scale effects such as gravity and capillarity, and micro-scale features such as slip at the moving contact line. Therefore numerical and analytical frameworks were devised which consider both scales and encapsulate all the relevant effects. While the numerical frameworks were easy to generalise and account for a variety of problems, the drawback is that they are computationally demanding and require lengthy simulation times. The analytical descriptions mitigated these but, on the other hand, they apply for specific parameter regimes and are not easily generalisable to other settings. However we showed that obtaining simplified models through the analytical investigation is crucial so that a variety of scenarios can be investigated with considerably fewer computational resources.

6.1.1 Derivation of the Model

In chapter 2 we reviewed the derivation of the governing model (2.51) which describes the motion of a thin droplet moving down an inclined, rough, and chemically heterogeneous substrate. In the regime where inertial effects are negligible, we performed a long-wave (or thin-film) approximation of the Navier-Stokes equations which was coupled with the appropriate boundary conditions to form a single evolution equation for the liquid thickness, noting that the stress singularity at the moving contact line was removed through the use of a slip condition. To supplement the non-dimensional thin-film equation (2.30), we derived the locally varying contact angle condition (2.41), and the moving boundary condition (2.50),

which when coupled with the vanishing thickness (2.31) and volume condition (2.51e) gave the full model (2.51). Simplifications to (2.51) were also proposed by reducing to the 2D geometry and considering horizontal and flat substrates where gravity effects are negligible, yielding (2.53). Noteworthy is that different slip schemes were used for both (2.51) and (2.53) which consider the inverse linear slip model, and the Navier slip model, respectively. While the Navier slip scheme is perhaps the more popular model used in the literature, the pressure exhibits logarithmic singularities at the contact line, which makes its numerical implementation rather non-trivial, whereas the pressure is regularised with the inverse linear slip model (see chapter 4). In this thesis, we considered both slip models to highlight the differences in their numerical implementations whilst maintaining a consistent approach with related works. Besides, the asymptotic analysis for each slip model is identical provided that variations in the contact line occur at length-scales much longer than slip.

6.1.2   Analytical Methods

In chapter 3 we developed new asymptotic models that approximate (2.51) and (2.53) by assuming that the motion of the contact line, and rate of liquid flux is slow. The analytical descriptions were initialised by considering a 2D droplet to gather some important physical insights, and obtain understanding on how to combat the full 3D problem which is arguably more difficult to treat. The 2D analysis extended on the work of Vellingiri *et al*. [55] by considering droplets which undergo mass changes due to a form of liquid flux which occurs at the free surface of the drop, or through the substrate. Although the evolution equations we obtained apply for arbitrary mass fluxes, we opted to limit the discussion to cases where it vanishes at the contact points, primarily to avoid any implementation difficulties that would have arisen had we solved for the evolution of the droplet fronts using the transcendental equations (3.34). In this particular limit, the simpler set of IDEs (3.35) was obtained, which can essentially be viewed as an augmented Cox-Voinov law which accounts for mass transfer effects. Although these models are not valid at early times, or when $\dot{a}_\pm \to 0$, the results presented suggest that we may confidently use them at all times, without compromising the general excellent agreement with the predictions of the full equations. To investigate some of the generic features of the dynamics in further detail, we considered two kinds of distributions for the liquid flux, namely one that scales with the droplet thickness according to (3.36) and

one that mimics a more localised flux distribution, as described by (5.2). While the former does not correspond to physically motivated scenario, it allows for further simplifications of the IDE system (3.35) so that it reduces to a system identical to that derived by Vellingiri *et al.* [55] who consider the case of constant mass (here, area changes appear through the apparent contact angle). For more general flux distributions, the spatial dependence on q enters (3.35) through the integral terms $I_\pm$. Although they appear as higher-order corrections to the analysis, their presence is needed in order to accurately capture the dynamics.

The 2D analysis was generalised to the arguably more realistic 3D setting. We have reported some preliminary findings for the case of constant mass in [61] which we have extended here to include changes in the droplet volume, analogously to the 2D case. To simplify the analysis based on the observations made in section 3.1, the assumption that mass flux vanishes along the contact line was applied so that explicit equations could be extracted for the Fourier coefficients of the contact line (3.98). These equations, like their analogous 2D counterpart (3.35), contained additional integral corrections $I(m, t)$ which incorporate the spatially varying flux term q into the dynamics.

In a related asymptotic analysis, we have also tackled the case of a droplet evaporating into a pure vapour atmosphere which differed from the previous case in that the mass flux is maximised close to the contact line. More specifically, the outcomes of the outer region analysis in section 3.2 were reused, neglecting $\dot{v}(t)$ terms which are $O(\lambda|\ln(\lambda)|)$ as $\lambda \to 0$. However, in this case the inner-region dynamics are markedly different and required a separate treatment which was analogous to that utilised by Savva *et al.* [53], where the equivalent inner-region dynamics of the Navier slip model were investigated. The analysis resulted in additional parameters that were extracted from solutions to certain boundary value problems, which were precomputed and stored. The equations obtained from matching were coupled with an evolution equation for the droplet volume in the limit when $a_0 \ll \mathcal{K}$ and $\theta \approx \theta_e$ which allowed us to couple the finer micro-scale details with the macroscopic terms. We found that the equation arising from a strict application of the linearisation about a nearly circular contact line was unable to capture more strongly deformed contact lines. Therefore a second equation, (3.144), was considered in which the contact line and angles remain unexpanded, which was found to more accurately capture the evolution of the droplet volume.

Finally, the analysis was concluded by relaxing the assumption that the substrate is flat so that changes surface topography emerge providing they occur at length-scales much longer

than λ, and that the substrate features are sufficiently small so that they do not perforate the free surface of the drop. Importantly, as a first investigation we assumed that the terms of $O(\dot{b}_0 \eta_m)$ were smaller than the terms at $O(\dot{b}_m)$, which implied that the surface roughness terms only appear in the leading-order dynamics. In this distinguished limit the analysis simplifies considerably, enabling us to re-use (3.98) as the reduced system of equations by appropriately changing the apparent contact angle to incorporate the effects of substrate topography.

6.1.3   Numerical Methods

In chapter 4 we developed numerical frameworks to solve for the motion of the contact line. To resolve the sharp boundary layers in $\partial_\nu h$ as $\lambda \to 0$, we discretised the thin-film PDE using the Chebyshev collocation method which allowed us to resolve these layers with a comparatively smaller number of collocation points compared to, say, a finite difference method with an equispaced grid. Numerical schemes were developed for both 2D and 3D droplets which were based upon the ideas presented in [56]. Specifically, in the 2D scenario we assumed flat and horizontal substrates in the gravity-free regime to contrast with the asymptotic models of section 3.1. The 3D scheme, which is a key novel contribution of the present thesis is rather general, and accounts for gravitational effects, surface heterogeneities, substrate inclination and mass transfer effects.

While the Chebyshev collocation method is able to resolve the dynamics in the vicinity of the contact line with comparatively fewer collocation points, simulation times can grow rather lengthy since numerical stiffness increases as $\lambda \to 0$. Therefore, to offer an attractive alternative between full-scale computing and low-order theoretical models, a hybrid numerical scheme was developed based around the boundary integral method presented by Glasner [153]. While Glasner limited his investigation to inclined surfaces and chemically heterogeneous effects, we have combined this scheme with the asymptotic theory presented here, unlike Glasner who evolved the contact line based on the leading-order theory, which as we have demonstrated in chapter 5 can be inadequate for a number of scenarios.

6.1.4 Simulations

To assess the validity of the theory presented in chapter 3 and to explore some interesting physical phenomena associated with droplet spreading, we discussed a number of representative cases in chapter 5 that contrasts the results of the previous chapters. In the majority of the cases considered we observed excellent agreement between the outcomes of the analysis and the numerical solutions of the full equations, noting that the most optimal agreement was obtained with the hybrid model. While the reduced models performed rather well in the regime of their applicability, disagreement emerged for cases with more strongly deformed contact lines, which nevertheless was rectified by considering the hybrid approach. Typically speaking for cases involving 3D droplets, the reduced model simulations would require no longer than a minute on a standard laptop, whereas the hybrid approach sometimes took a few minutes longer due to the large number of linear system solves (see chapter 4). Despite the increased simulation times of the hybrid approach, they are still orders of magnitude shorter than the times required to solve the full equations.

In the 2D scenario, we presented a number of cases that highlight the intricate interplay among the various effects, demonstrating how droplet behaviour can drastically change even when small changes are introduced to the surface chemistry or fluid flow properties. Crucially, some of the key contributions of the present work include complementing related works in 2D [55, 107, 125], showing that it is indeed possible to view hysteresis-like effects without explicitly assuming *a-priori* the presence of hysteresis (see figures 5.2 and 5.4), as well as demonstrating how the various modes observed for evaporating droplets naturally emerge if the presence of heterogeneities is accounted for. In all simulations performed, periodic mass fluxes led to periodic dynamics in the long-time limit, although the time required for the fronts to settle to periodic motion is highly dependent on the structure of the heterogeneities as well as the choice of the initial conditions (see section 5.1.5). Although the outcomes of a 2D model cannot be straightforwardly scrutinised by experiments, the combined analytical and computational work we have undertaken made looking into the complicated bifurcation structure of the dynamics possible. Therefore, gaining further insights into how hysteresis-like effects and transients to periodic motion occur by following the topological changes that take place as the nature and stability of the droplet equilibria evolve with the changing droplet area.

By using the more realistic 3D model, we examined the interaction between droplets and heterogeneous substrates for cases involving constant mass. While the full set of results are reported in [61], a few examples are included here to highlight the applicability of the theory performed. We further examined the balance between liquid flux and chemical heterogeneity by considering cases motivated by experimentally observed scenario. Let us note that in section 5.3 no quantitative comparison with experiments was sought, since no study in the literature reported the time evolution of the contact line. However, we were able to demonstrate that features commonly observed in the experimental setting naturally arose through the dynamic simulations, including stick-slip events, pinning/de-pinning behaviours, and the constant-radius and constant-angle modes. Notably, qualitative comparison between the experimental studies of Dietrich *et al.* [217] who consider evaporating droplets (see figure 5.17), and Lam *et al.* [113] who consider liquid inflow/outflow with a needle (see figure 5.26), were demonstrated. These comparisons were performed with substrates decorated with random heterogeneities. In other words, these features emerged due to the substrate heterogeneities, which are generally difficult to explore in experiments as well as with full-scale direct numerical simulations. Just like section 5.1, we noticed that the dynamics is quite sensitive to the parameters controlling the flux and chemical heterogeneity, showing how small changes can yield large differences in the subsequent behaviours. Nevertheless, (3.98) was able to predict these behaviours excellently, showing a more favourable agreement, as opposed to solutions based on the leading-order equation (1.6), which only accounts for mass flux effects through the apparent contact angle (see figure 5.15 for a case of constant mass, and figure 5.19 for a case of variable mass).

The balance between mass changes and chemical heterogeneity was further expanded on by simulating for evaporating droplets, where features like stick-slip, pinning events and the constant-radius and constant-angle modes naturally arose. By modifying the parameters controlling the mass flux, the influence of evaporation on the micro-scale dynamics weakened and therefore the effects of surface heterogeneity grew stronger, meaning that the aforementioned effects can be mitigated entirely by simply increasing the strength of evaporation. Just as before, we have also explored cases with random substrate features, replicating the so-called snapping mode reported by Wells *et al.* [150] and stick-slip jumps similar in appearance to Dietrich *et al.* [217]. Crucially, these simulations allowed us to assess the assumptions put forth in the analysis, specifically those used to derive the evaporation

formulas (3.144) and (3.147). While (3.147) worked rather well for contact lines that are nearly circular, (3.144) outperformed (3.147) in each case considered, especially for circumstances where substrate variations caused larger deformations in the contact line. Strictly speaking, a few assumptions put forth do not formally hold asymptotically, such as using the time-scale for the second stage of evaporation to describe the first three stages, and using (3.144) to determine the droplet volume. However the rather convincing numerical evidence we obtained suggests that such assumptions can be used without impacting the excellent agreement observed from all cases presented, allowing us to bypass a more intricate analysis.

Using appropriate changes to the apparent contact angle appearing in (3.98), we considered droplets of constant mass spreading over substrates that exhibit small changes in its topography, rather than being ideally flat like all previously considered cases. Again, features such as droplet pinning and stick-slip naturally arose from this configuration, even though the substrate features were rather small in comparison to the droplet size. Importantly, the acceptable level of accuracy obtained through all cases considered justified the step of treating $O(\dot{b}_0 \eta_m)$ terms as higher-order corrections to the analysis. From an analytical point of view such terms should be retained to supply a more complete model, however, the analysis to include them grows rather unwieldy, and therefore as a first investigation they were neglected. Besides, these terms most likely account for the finer details during the spreading stage, since, in all cases considered the droplet equilibrium was predicted excellently by the hybrid model. This is evident from figure 5.41 whose equilibrium is incorrectly predicted by the low-order model (1.6) and the reduced model; whereas the hybrid model performs excellently, showing only minor disagreements during the spreading stages. Hence, this study may be viewed as a starting point for future exploration where the higher-order corrections will be retained, which we expect that they will alleviate the discrepancies during the spreading stage.

6.2 Future Outlook

Whilst the methodologies presented in this thesis can, at least in principle, be extended to examine other complexities (e.g. body forces), the analysis becomes more cumbersome to tackle. Therefore, the most clear direction for future work is to consider the full analytical treatments of these scenarios to generate models which can assist in the intelligent design of

new experimental studies. In this sense, parameter regimes of interest can be explored prior to experimental fabrication, or perhaps optimisation tools can be created for the design and improvement of modern technologies.

Here we test the limits of applicability of the reduced model (3.98) in conjunction with the boundary integral method by examining gravitational effects. Although in the derivation of (3.98) body forces were not accounted for, the discussion in this section contains some exploratory work which we endeavour to pursue in the future. Specifically, we will investigate the influence of gravity for droplets on heterogeneous substrates both horizontal and inclined, comparing (3.98) and the leading-order result (1.6) with solutions to the full PDE, which can be more straightforwardly adapted to tackle such cases. Unless stated otherwise, we run simulations using the same initial parameters such as those given in section 5.5.

6.2.1   Horizontal Surfaces

To start the investigation we restrict our attention to the regime of horizontal ($\alpha = 0$) substrates with the aim of partially illustrating the impact of the Bond number in the spreading dynamics. As mentioned in the introductory chapter, gravitational effects become appreciable once the characteristic length-scale L is larger than the capillary length l_c, in which regime the macro-scale dynamics become a competition between gravity and capillarity. For increasing Bo, flattening of the free surface forces the droplet to spread to increasingly larger radii (see also Hocking [54] and Savva & Kalliadasis [58]). Consistently with this observation in figure 6.1 we observe that this occurs even when surface topographies are present to inhibit the spreading of the contact line. Specifically, as Bo increases larger overall radii are achieved with different equilibrium shapes attained at each case. Besides the analysis used to derive (3.98) neglecting completely the presence of the Bond number, the hybrid method performs rather well. However, we expect that the intermediate spreading stages would be better captured should a full asymptotic treatment be performed which properly accounts for the effects of gravity and surface roughness.

6.2.2   Inclined Surfaces

Using the generalised boundary integral formulation we can make extensions upon the previous result by considering substrates that have been inclined. This has been explored in
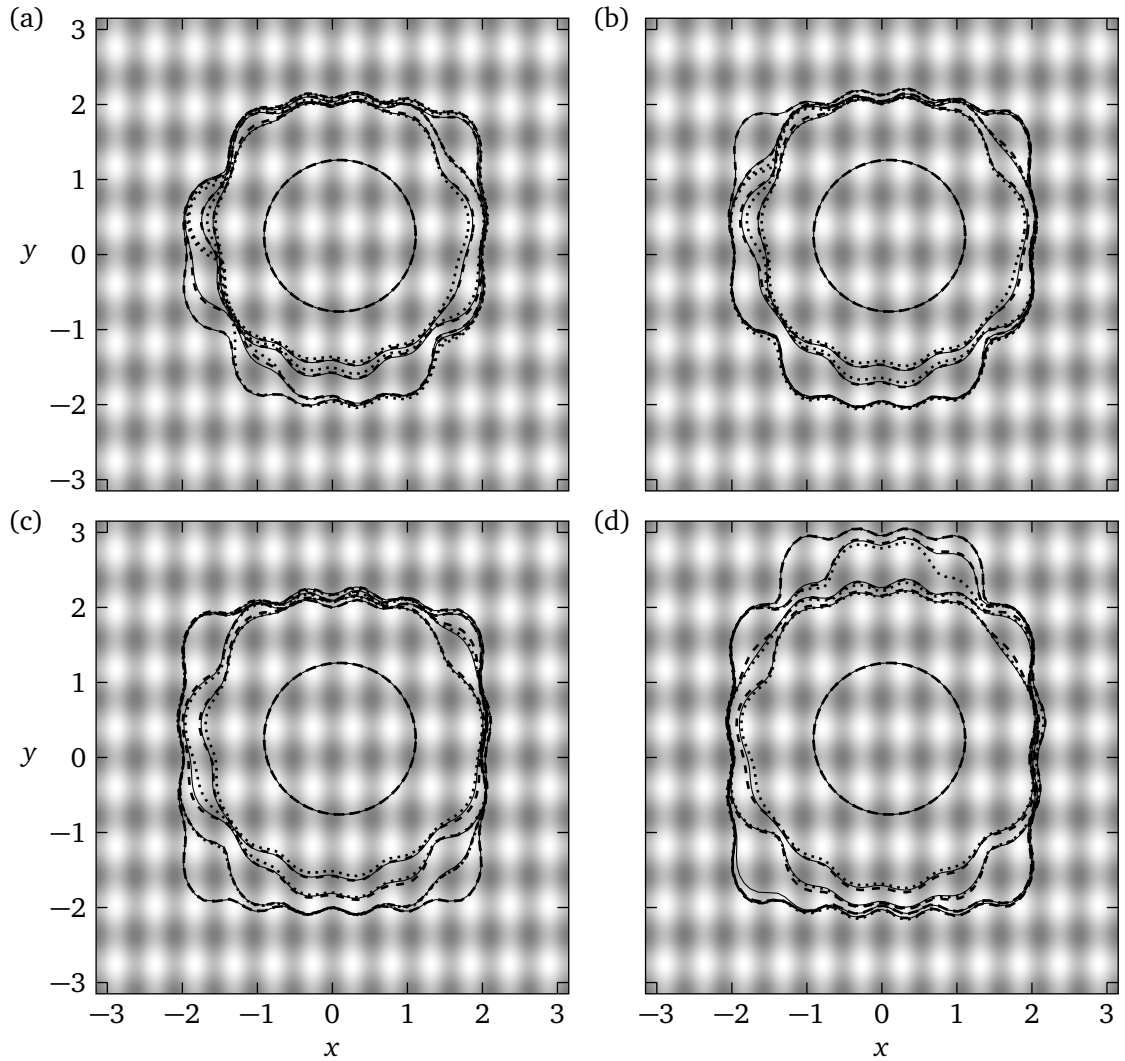
Figure 6.1: The impact of gravity on droplet equilibria. Plots (a) - (d) are droplet contact line profiles at times $t = 0, 1, 2.5, 15$ and 100 for Bo $= 0, 1, 2.5$ and 5, respectively. The substrate and initial parameters are the same as figure 5.43. Solid, dashed and dotted lines correspond to solutions from the full model, (3.98) and (1.6), respectively.

the 2D setting by Savva & Kalliadasis [59], whereas here we provide some preliminary work which will form the basis for future explorations upon completion of full analytical treatment. To ensure fair comparison between the solutions obtained from the full equations and the analysis which neglects the presence of gravity and substrate inclination, we consider the regime of small Bo and α to form a better idea of the applicability of the theory. Also, in this regime we can reduce the chance of the droplet forming cusps at the rear, which frequently become unstable and split the droplet into smaller satellite bodies (see, e.g. Podgorski *et al.* [229]).

In figure 6.2 we consider a few cases of small inclination angles, where chemical and
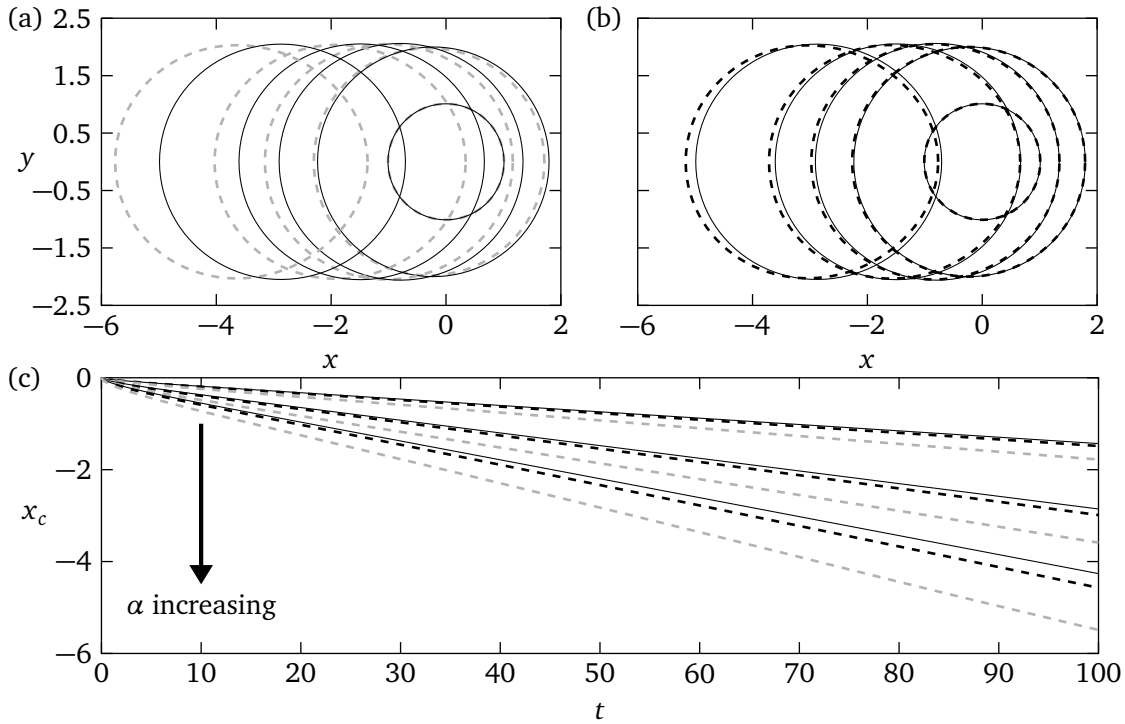
Figure 6.2: Effect of surface inclination on the centroid motion $x_c(t)$ for $\alpha = 2.5°$, $5°$ and $7.5°$ where $\alpha_s = 15°$ and Bo $= 0.75$. Plots (a) and (b) show contact line snapshots for $\alpha = 5°$ at times $t = 0, 5, 25, 50$ and 100 comparing the leading-order result (a) and the model with the higher-order corrections included (b). (c) The motion of the centroid x_c for all values of α. In all plots solid lines correspond to solutions of the full model, dashed black are solutions of (3.98) and dashed grey are solutions of (1.6).

topographical substrate changes are not present to gather an idea of how the reduced model (3.98) performs. As expected, the agreement between the hybrid method and full problem degrades as α increases. However, the key observation in this result is that the leading-order theory performs worse throughout, which supports our previous assertions that deriving the next-order correction is indeed essential to accurately predict the dynamics. While strictly speaking the theory derived here does not apply for inclined slopes, it nevertheless performs far more satisfactorily than the simulations with (1.6).

Importantly, a full asymptotic treatment will provide a sufficiently accurate prediction so that the speeds of descend of droplets can be optimised for a large array of applications featuring droplet transport, as well as to further elucidate some of the interesting effects that occur in experiments. One such configuration is the possibility for a droplet to move uphill against gravity in the presence of a favourable chemical gradient, which has been studied experimentally by Chaudhury & Whitesides [230]. Using the rather small inclination angle $\alpha = 2.5°$ in figure 6.3 we can replicate this effect, also highlighting the importance of fine
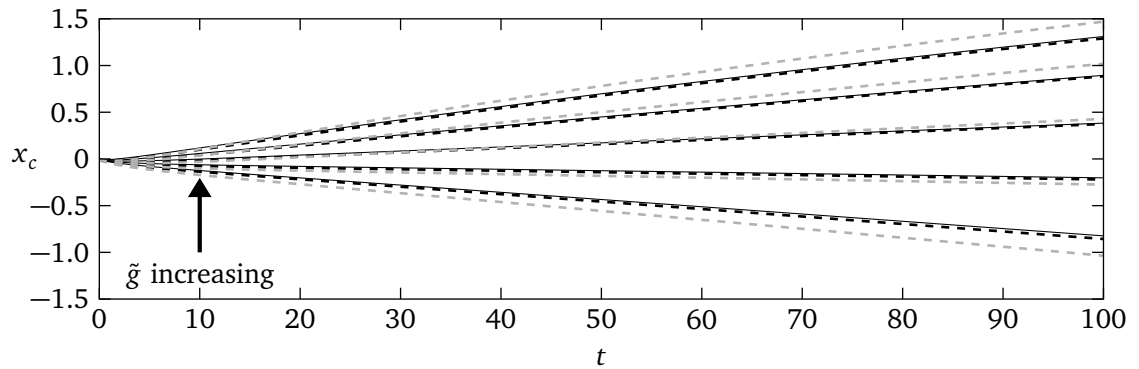
Figure 6.3: Tuning a linear chemical gradient to make a droplet move uphill. The centroid position $x_c(t)$ is plotted against time for $\theta(x, y) = 1 - \tilde{g}x$ where $\tilde{g}$ takes values from 0.025 to 0.125 in increments of 0.025. Here we maintain the parameters $\alpha = 2.5°$, $\alpha_s = 15°$, and Bo $= 0.75$ for all cases. The styles of the curves are the same as figure 6.2.
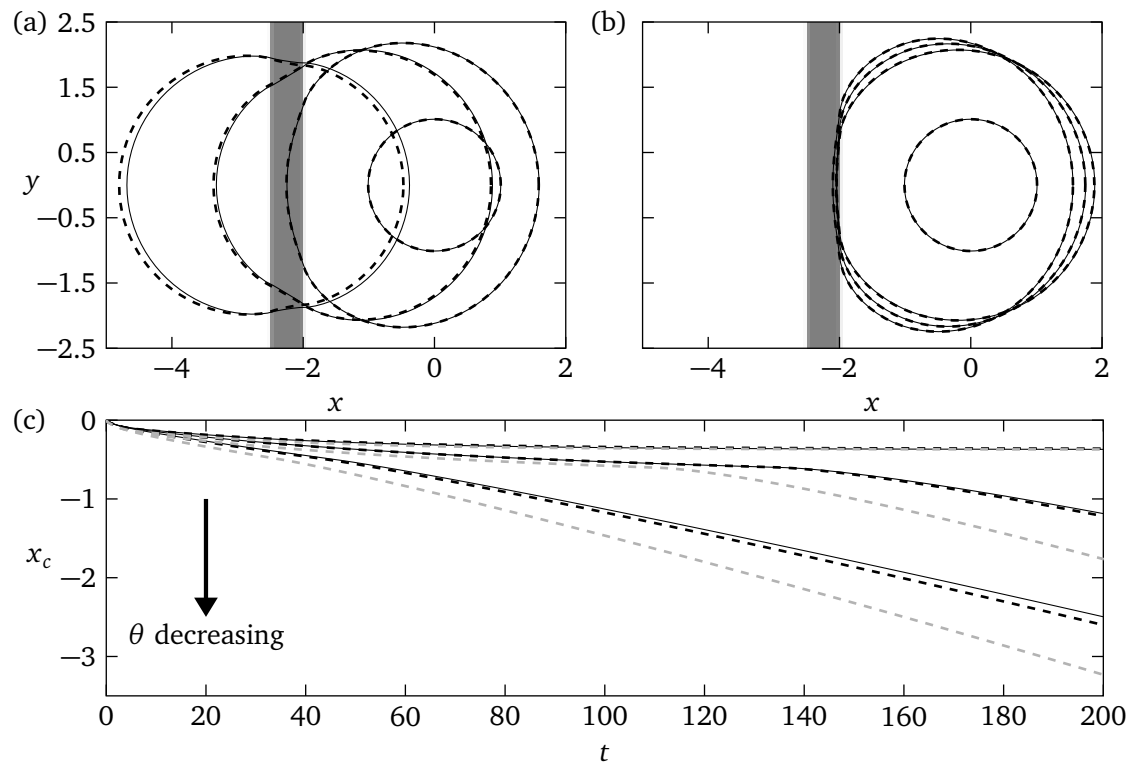
Figure 6.4: Preventing a droplet from moving downhill using the chemical barriers of the form $\theta(x, y) = 1 + \tilde{g}\{\tanh[50(x + 2.5)] - \tanh[50(x + 2)]\}$. Plots (a) and (b) are droplet profiles at times $t = 0$, 50, 200 and 300 for $\tilde{g} = 0.1$ and $\tilde{g} = 0.15$, respectively. (c) The evolution of x_c for $\tilde{g} = 0.05$, 0.1 and 0.15. In all plots the styles of the curves, Bo, α and α_s are the same as figure 6.2.

tuning the features to achieve the desired droplet motion and prevent the droplet from moving downhill. Crucially, we must emphasise that no quantitative comparison can be made with Chaudhury & Whitesides [230] who consider the larger angle of $\alpha = 15°$, deferring this work to a future effort.
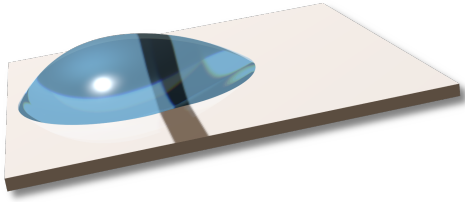
(a)   (b)
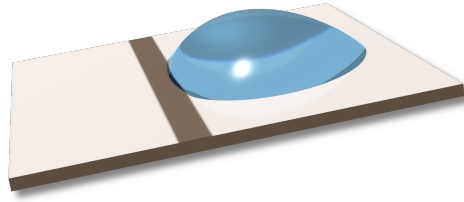
Figure 6.5: Droplet profiles for figure 6.4(a) and (b) at $t = 300$.

Noteworthy is that it is also possible for a droplet to remain pinned on an inclined surface by appropriately modifying the substrate features. This occurs frequently in the natural world, for instance, with raindrops on plant leaves or on a car wind shield (see chapter 1), and can be attributed to contact angle hysteresis arising through the substrate features. Such circumstances have been investigated in the 2D setting by Savva & Kalliadasis [59], here, we present a basic case to show that such configurations can be explored in the present theoretical framework. In figure 6.4 we use a basic heterogeneous strip where the contact angle of the strip is increased for each simulation, noting that if the strip is sufficiently weak, the descend is only delayed and not stopped (see also figure 6.5). Just like previous examples, the dynamics are captured rather well by the theory presented here, noting that discrepancies grow as the descend speed is increased. Crucially, models like (3.98) and the leading-order one (1.6) can be solved on a much more realistic time-scale than that of the full problem, highlighting how such methods can adequately be used for optimisation tools to determine, say, the strength of heterogeneity required to pin droplets for a variety of inclination angles.

6.2.3   Other Directions

Interest also lies in exploring into configurations that may be too computationally expensive when solving the full equations. One avenue is to consider the dynamics of multiple droplets by computing in parallel simulations of (3.98) for each droplet and capturing where appropriate the coalescence dynamics when droplets merge. Considering the time-frames required for solutions of the reduced models, thousands of droplets could be simulated in the same time-frame as the full problem for a single drop, especially if supercomputing clusters with GPUs are used. This could further assist in the optimisation of applications in technology, such as spray cooling processes, and the design of hydrogen fuel cells that

rely on efficient transport of water for optimal conductivity. By appropriately modifying the surface features, the optimisation of water collecting materials can also be explored to develop more efficient materials for arid regions across the planet (see, for example, Zhu *et al*. [12]). Since the dynamics for droplet coalescence occur on smaller time-scales than that of, say, evaporation, one can approximate this scenario like in Sikarwar *et al*. [231] who consider it an instantaneous event. In this sense, upon coalescence they prescribe a new droplet with a circular contact line whose volume is the sum of the coalescing droplets, and is positioned at the centre of mass of the droplets.

As noted in chapter 4, the numerical scheme presented here which is based upon a slip model is limited in the sense that we cannot consider topological changes. Therefore, events such as droplet coalescence and splitting could not be investigated, deferring this to a future effort where a precursor film model is considered. A precursor film model requires more intricate meshing techniques to account for the moving contact line, however, this would allow for multiple droplets to be tracked more naturally than the methodologies presented here, meaning some assessment between the parallel ODE simulations previously mentioned could be considered.

Another avenue of research is to extend the current theory into the branch of non-Newtonian fluids to investigate the spreading dynamics of droplets of blood. Naturally, the study of non-Newtonian fluids is highly non-trivial, however, progress can be made analytically by modelling blood as a simple power law fluid to account for the shear thinning behaviours blood exhibits (see, e.g. [232–234]). Understanding the interaction of blood with a variety of substrates can assist in the development of microfluidic devices where optimal transport of blood is required for a variety of medical applications.

Also important is going beyond the long-wave theory used here. The true thermodynamic equilibrium is not captured with the long-wave theory as the curvature term is merely approximated, meaning the current model is limited to small slopes. Should the full curvature term be included, then the small-slopes restriction can be lifted provided that the slope is slowly varying (see e.g. Snoeijer [235]). As described in the recent work by Thiele [198], long-wave models have been improved by modifying the curvature term, and therefore it would be interesting to explore this avenue in the future and develop more efficient models that capture the full thermodynamic equilibrium.

— Appendix A —

Derivations in the Polar Geometry

To formulate a numerical scheme using the pseudospectral collocation method and solve (2.51) for contact line motion, we moved the free boundary problem to one on fixed intervals using (2.54). Consequently, the time derivative $\partial_t(\cdot)$, gradient operator $\nabla(\cdot)$, Laplacian operator $\nabla^2(\cdot)$, the full governing PDE (2.51a) and its conditions required transformation to the new coordinate system. In chapter 2 many of the details were bypassed, however, in this appendix we highlight the basic principles which are based on the tensor calculus techniques presented by Battaglia & George [236].

These techniques are based on the *Einstein summation* rules, which allow for operations such as the dot product between two n dimensional vectors $\boldsymbol{A}$ and $\boldsymbol{B}$ to be defined concisely as

$$A_a B_a = \boldsymbol{A} \cdot \boldsymbol{B} = A_1 B_1 + A_2 B_2 + \ldots + A_n B_n. \tag{A.1}$$

In this sense $A_a B_a$ is formulated with the summation implied, where the following rules are considered:

1. Repeated indices are implicitly summed over.
2. Each index can appear at most twice in one term.
3. Each term must contain identical non-repeated indices.

In our case this notation allows us to calculate the transformed operators straightforwardly, where summations are considered over two coordinates, in other words

$$\boldsymbol{x}' = (x, y) = \left(x^{1'}, x^{2'} \right) \to \boldsymbol{x} = (r, \phi) = \left(x^1, x^2 \right), \tag{A.2}$$

where primes denote the variables in the Cartesian geometry with basis vectors $\boldsymbol{e}_x = (1, 0)^{\mathrm{T}}$ and $\boldsymbol{e}_y = (0, 1)^{\mathrm{T}}$.

Central to discussing any transformation of variables is the Jacobian matrix, which is defined in [236] as (where x and y are transformed using (2.54))

$$\left[R_b^{a'}\right] = \left[\partial_{x^b}x^{a'}\right] = \begin{pmatrix} \partial_r x & \partial_\phi x \\ \partial_r y & \partial_\phi y \end{pmatrix} = \begin{pmatrix} a\cos\phi & r\left(\partial_\phi a\cos\phi - a\sin\phi\right) \\ a\sin\phi & r\left(\partial_\phi a\sin\phi + a\cos\phi\right) \end{pmatrix}, \tag{A.3}$$

and allows us to determine the basis vectors in the new polar geometry by multiplying the Cartesian basis against the Jacobian matrix, namely

$$\boldsymbol{e}_r = R_b^{a'}\boldsymbol{e}_x = \begin{pmatrix} a\cos\phi \\ a\sin\phi \end{pmatrix}, \quad \text{and} \quad \boldsymbol{e}_\phi = R_b^{a'}\boldsymbol{e}_y = r\begin{pmatrix} \partial_\phi a\cos\phi - a\sin\phi \\ \partial_\phi a\sin\phi + a\cos\phi \end{pmatrix}. \tag{A.4}$$

However, to determine the expression for the gradient we require the dual basis vectors, $\boldsymbol{e}^r$ and $\boldsymbol{e}^\phi$, that satisfy the Kronecker delta property $\boldsymbol{e}^a \cdot \boldsymbol{e}_b = \delta_b^a$ which is zero if $a \neq b$, or 1 if $a = b$. This basis is found using the formula

$$\boldsymbol{e}^a = g^{ab}\boldsymbol{e}_b \tag{A.5}$$

where g^{ab} is a symmetric tensor defined by the dot products of the basis vectors, in other words $\boldsymbol{e}^a \cdot \boldsymbol{e}^b = g^{ab}$, and has inverse $[g_{ab}]^{-1} = [g^{ab}]$. Therefore, we can determine g_{ab} through the dot products $\boldsymbol{e}_a \cdot \boldsymbol{e}_b = g_{ab}$ and thus arrive with

$$[g_{ab}] = \begin{pmatrix} a^2 & ra\partial_\phi a \\ ra\partial_\phi a & r^2\left[a^2 + (\partial_\phi a)^2\right] \end{pmatrix}, \tag{A.6}$$

finally yielding

$$[g^{ab}] = \begin{pmatrix} \dfrac{a^2 + (\partial_\phi a)^2}{a^4} & -\dfrac{\partial_\phi a}{ra^3} \\ -\dfrac{\partial_\phi a}{ra^3} & \dfrac{1}{r^2a^2} \end{pmatrix}, \tag{A.7}$$

as the inverse. The gradient and Laplacian operators are formulated using

$$\boldsymbol{\nabla}(\cdot) = \partial_a(\cdot)\boldsymbol{e}^a, \tag{A.8}$$

$$\nabla^2(\cdot) = \frac{\partial_a\left[\sqrt{G}g^{ab}\partial_b(\cdot)\right]}{\sqrt{G}}, \tag{A.9}$$

where $G = r^2a^4$ is the determinant of $[g_{ab}]$, therefore giving (2.59) and (2.60) for the gradient and Laplacian operators, respectively.

Finding the time derivative $\partial_t(\cdot)$ in the polar geometry is a simple application of the chain rule

$$\partial_t(\cdot) \rightarrow \partial_t(\cdot) - \dot{x}\partial_x(\cdot) - \dot{y}\partial_y(\cdot) \tag{A.10}$$

where we use the gradient operator (2.59) to obtain

$$\partial_x(\cdot) \to \frac{a\cos\phi + \partial_\phi a \sin\phi}{a^2}\partial_r(\cdot) - \frac{\sin\phi}{ra}\partial_\phi(\cdot), \tag{A.11a}$$

$$\partial_y(\cdot) \to \frac{a\sin\phi - \partial_\phi a \cos\phi}{a^2}\partial_r(\cdot) + \frac{\cos\phi}{ra}\partial_\phi(\cdot), \tag{A.11b}$$

and therefore giving the full expression

$$\partial_t(\cdot) \to \partial_t(\cdot) - \frac{1}{a}\left[\dot{x}_c\cos\phi + \dot{y}_c\sin\phi + r\partial_t a + \frac{\partial_\phi a}{a}(\dot{x}_c\sin\phi - \dot{y}_c\cos\phi)\right]\partial_r(\cdot)$$
$$+ \frac{\dot{x}_c\sin\phi - \dot{y}_c\cos\phi}{ar}\partial_\phi(\cdot). \tag{A.12}$$

The final component in our transformations is to determine $\boldsymbol{\nabla}\cdot\left[h\left(h^2 + \lambda^2\right)\boldsymbol{\nabla}P\right]$ which is used in the PDE (2.51a), and can be determined using the expression for the gradient with the divergence, which is given as

$$\boldsymbol{\nabla}\cdot\boldsymbol{A} = \frac{\partial_a(\sqrt{G}A^a)}{\sqrt{G}}, \tag{A.13}$$

where $A^a = \boldsymbol{A}\cdot\boldsymbol{e}^a$ for $\boldsymbol{A} = Q\boldsymbol{\nabla}P$ with $Q = h\left(h^2 + \lambda^2\right)$. Therefore, we find that

$$\boldsymbol{\nabla}\cdot\boldsymbol{A} = \frac{1}{\sqrt{G}}\left\{\partial_r\left[Q\sqrt{G}\left(g^{1,1}\partial_r P + g^{1,2}\partial_\phi P\right)\right] + \partial_\phi\left[Q\sqrt{G}\left(g^{1,2}\partial_r P + g^{2,2}\partial_\phi P\right)\right]\right\}, \tag{A.14}$$

which simplifies to yield the expression seen in (2.57) and (2.58).

— Appendix B —

Boundary Value Problems Arising in Section 3.3

For evaporating droplets we require the parameters θ_e, β_{in} and $\tilde{\beta}_{\text{in}}$ which arise through the inner region analysis (see section 3.3). In order to determine these parameters from the inner region equations, we opt for a numerical treatment similar to Savva *et al.* [53] who obtain these parameters for the case of homogeneous surfaces and use of the Navier-slip model. Therefore, the appropriate modifications need to be introduced to account for the different slip model and surface heterogeneities, so that given E and K we find the inner region parameters for a range of θ_*, which are stored and retrieved during calculation of the reduced model.

B.1 Determination of θ_e

Firstly, to extract the modified angle θ_e we change the independent variable in (3.117) from ξ to Υ_0 leading to the lower-order non-linear differential equation

$$F \partial_{\Upsilon_0} \left[\Upsilon_0 \left(\Upsilon_0^2 + 1 \right) F \partial_{\Upsilon_0} \left(F \partial_{\Upsilon_0} F \right) \right] = -\frac{E}{\Upsilon_0 + K}, \tag{B.1}$$

where the presence of heterogeneous terms have been incorporated into $F = \theta_* \partial_\xi \Upsilon_0$. Therefore, we are solving the above ODE for $F(\Upsilon_0)$ alongside the conditions that $\partial_{\Upsilon_0} F \to 0$ and $\partial_{\Upsilon_0}^2 F \to 0$ as $\Upsilon_0 \to \infty$, as well as the boundary condition $F(0) = \theta_*$. Using this change of variables, the modified angle θ_e is determined from the value of F at infinity. To solve this equation numerically, we opt for an approach based on the pseudospectral collocation method where we make the change of variables $\Upsilon_0 = \mathcal{L}(1+s)/(1-s)^2$ for $s \in [-1, 1]$ to obtain a discretisation on the semi-infinite interval $[0, \infty)$ which avoids the use of domain truncation of shooting methods to obtain the behaviours at infinity. Here $\mathcal{L} > 0$ is a mapping parameter

which is used to push more points towards infinity and better resolve the behaviours there (see Boyd [237] for more details). Typically, we found that using 150 collocation points and $\mathcal{L} \in [5, 15]$ suffices for resolving behaviours at both the origin and infinity. The resulting boundary value problem is solved by Newton iterations, with θ_e found from the value of F at $s = 1$.

B.2   Determination of β_{in}

The value of β_{in} is obtained using similar methodologies, where we change (3.120) to the independent variable to Υ_0 yielding

$$\partial_{\Upsilon_0} \left\{ \Upsilon_0 \left(\Upsilon_0^2 + 1 \right) F \partial_{\Upsilon_0} \left[F \partial_{\Upsilon_0} \left(F \partial_{\Upsilon_0} \Upsilon_1 \right) \right] + \left(3\Upsilon_0^2 + 1 \right) F \partial_{\Upsilon_0} \left(F \partial_{\Upsilon_0} F \right) \Upsilon_1 \right\}$$
$$- \frac{E\Upsilon_1}{F \left(\Upsilon_0 + K \right)^2} + 1 = 0, \quad \text{(B.2)}$$

which depends on the function F satisfying (B.1) and the conditions mentioned previously. Although the above equation appears to be more complicated than (B.1), (B.2) is a linear differential equation which can be solved by direct matrix inversion, unlike (B.1). Using Υ_0 as the independent variable gives the far field behaviour

$$\Upsilon_1 \sim \frac{\Upsilon_0}{\theta_e^3} \ln\left(\frac{\beta_{\text{in}} \theta_* \Upsilon_0}{\theta_e \text{e}} \right) \quad \text{as} \quad \Upsilon_0 \to \infty, \quad \text{(B.3)}$$

which is used to isolate the value of β_{in} by exploiting the linearity of (B.2); casting it as a problem for $\tilde{\Upsilon}_1$ with

$$\Upsilon_1 = (\Upsilon_0 + 1) \left[\tilde{\Upsilon}_1(\Upsilon_0) + \frac{\ln(\Upsilon_0 + 1)}{\theta_e^3} \right], \quad \text{(B.4)}$$

where $\tilde{\Upsilon}_1$ satisfies the conditions $\tilde{\Upsilon}_1(0) = 0$, $\partial_{\Upsilon_0} \tilde{\Upsilon}_1(0) = -1/\theta_e^3$, and $\partial_{\Upsilon_0} \tilde{\Upsilon}_1 = \partial_{\Upsilon_0}^2 \tilde{\Upsilon}_1 = 0$ as $\Upsilon_1 \to \infty$. Using this recasting we solve the fourth order linear problem for $\tilde{\Upsilon}_1$, and determine the value of β_{in} by considering the behaviour at the far field, so that

$$\beta_{\text{in}} = \frac{\theta_e}{\theta_*} \text{e}^{1 + \theta_e^3 \tilde{\Upsilon}_{1\infty}}, \quad \text{(B.5)}$$

where $\tilde{\Upsilon}_{1\infty}$ is the value of $\tilde{\Upsilon}_1$ as $\Upsilon_0 \to \infty$ (or equivalently at $s = 1$ in the computational domain).

B.3   Determination of $\tilde{\beta}_{\mathbf{in}}$

Finding the value of $\tilde{\beta}_{in}$ requires similar techniques, this time applied to (B.1). After solving for F (and consequently θ_e), we perform the substitution

$$F = \theta_e + \frac{\mathcal{G}(\Upsilon_0)}{1 + \Upsilon_0} - \frac{E}{2\theta_e^3 (1 + \Upsilon_0)} \ln(1 + \Upsilon_0), \tag{B.6}$$

which is used in (B.1) with the conditions $\mathcal{G}(0) = -\theta_e + \theta_*$ and $\partial_{\Upsilon_0} \mathcal{G} = \partial_{\Upsilon_0}^2 \mathcal{G} = 0$ as $\Upsilon_0 \to \infty$. Therefore we solve the non-linear equation for $\mathcal{G}$ using the techniques used previously for F, and then consider

$$F \sim \theta_e - \frac{E}{2\theta_e^3 \Upsilon_0} \ln(\tilde{\beta}_{in} \Upsilon_0) \quad \text{as} \quad \Upsilon_0 \to \infty, \tag{B.7}$$

to obtain the value of $\ln(\tilde{\beta}_{in})$ by using the value of $\mathcal{G}$ as $\Upsilon \to \infty$ (denoted as $\mathcal{G}_\infty$), namely

$$\ln(\tilde{\beta}_{in}) = \frac{-2\theta_e^3 \mathcal{G}_\infty}{E}. \tag{B.8}$$

— Appendix C —

Early Time Dynamics

In chapter 3 it was remarked that the analytical methods undertaken do not account for the initial time dynamics where the free surface evolves towards its quasistatic shape. This happens on a very short time-scale, usually occurring within $t = O(10^{-3})$ dimensionless time units, meaning that this stage is too brief to have a lasting impact on the overall dynamics (as indicated by the results in chapter 5).

To illustrate this point further, we initialise the PDE solver in 2D with more distorted initial conditions (ICs) than the shape (4.13), and compare to simulations of the reduced model (3.35). The ICs we consider are the 'dimpled' shape

$$h(s, 0) \approx 2 - 6s^4 + 4s^2, \tag{C.1}$$

and the 'flattened' shape

$$h(s, 0) \approx \frac{176}{75}\left(1 - s^{10}\right), \tag{C.2}$$

noting that we use $\approx$ to emphasise that the actual IC is chosen according to (4.13) with $\epsilon = 0.01$. The results of the computation is shown in figure C.1 where we see that by $t = 10^{-3}$ the ICs (C.1) and (C.2) relax to the quasistatic shape and are well described by the parabolic solution (3.15). It is also apparent that during this short time-span the contact line does not move too appreciably, which is also consistent with a similar calculation performed by Ren *et al.* [238].

From figure C.1(c) we see that the overall dynamics are not appreciably altered, since all cases considered transition to the same equilibrium in the long-time limit. Clearly, some differences persist during the very early stages (see the inset of C.1(c)), however, this is quickly rectified as the spreading motions are nearly indistinguishable from $t = O(10^{-1})$ onwards. However, it is easy to see that the initial condition considered in chapter 4, equation 4.13, provides the most optimal comparison with the theoretical analysis.
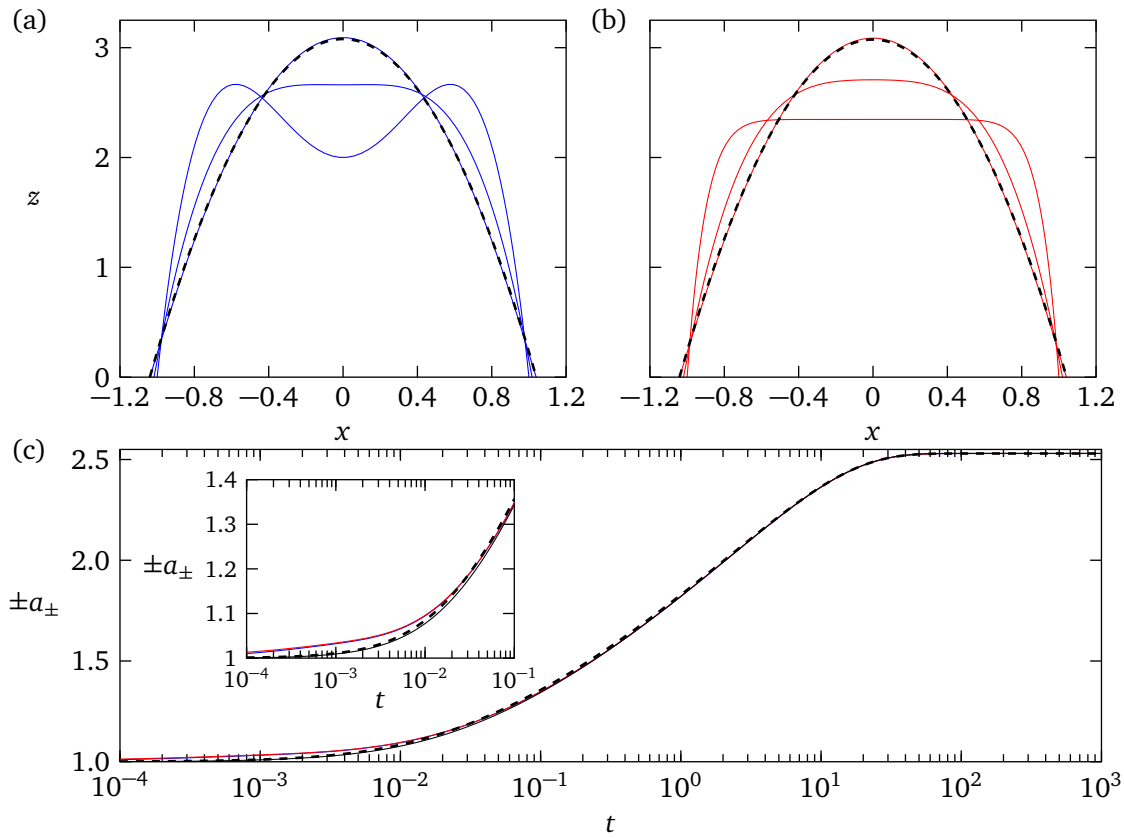
Figure C.1: Snapshots of the free surface when $t = 0$, 10^{-4} and 10^{-3} for (a) $h(s, 0) \approx 2 - 6s^4 + 4s^2$ and (b) $h(s, 0) \approx 176\left(1 - s^{10}\right)/75$. By $t = 10^{-3}$ the free surface is well-described by a parabola (dashed curve). (c) Evolution of the droplet contact points $\pm a_\pm$ showing the solution to the PDE using (4.13) and $\epsilon = 0.01$ (black solid curve), the 'flattened' IC (red curve), the 'dimpled' IC (blue curve), and the solution to the ODEs (3.35) (dashed black curve). The inset shows a magnified plot of into the early-stage dynamics.

Therefore we conclude that the accounting for the very early stages in the analysis, which primarily would require a numerical treatment, is not an essential step to take.

Bibliography

[1] X. Gao & L. Jiang. Biophysics: water-repellent legs of water striders. *Nature*, 432 (7013):36, 2004.

[2] D. Vella & L. Mahadevan. The "cheerios effect". *Am. J. Phys.*, 73(9):817–825, 2005.

[3] V. Dugas, J. Broutin, & E. Souteyrand. Droplet evaporation study applied to DNA chip manufacturing. *Langmuir*, 21(20):9130–9136, 2005.

[4] J. Park & J. Moon. Control of colloidal particle deposit patterns within picoliter droplets ejected by ink-jet printing. *Langmuir*, 22(8):3506–3513, 2006.

[5] P. Calvert. Inkjet printing for materials and devices. *Chem. Mater.*, 13(10):3299–3305, 2001.

[6] A. D. Eales, N. Dartnell, S. Goddard, & A. F. Routh. The impact of trough geometry on film shape. A theoretical study of droplets containing polymer, for P-OLED display applications. *J. Colloid Interface Sci.*, 458:53–61, 2015.

[7] E. P. Santangelo, M. A. Corticelli, & P. Tartarini. Experimental and numerical analysis of thermal interaction between two droplets in spray cooling of heated surfaces. *Heat Tran. Eng.*, 39(3):217–228, 2018.

[8] J. Breitenbach, I. V. Roisman, & C. Tropea. From drop impact physics to spray cooling models: A critical review. *Exp. Fluids*, 59(3):55, 2018.

[9] D. Y. Paithankar, E. V. Ross, B. A. Saleh, M. A. Blair, & B. S. Graham. Acne treatment with a 1,450 nm wavelength laser and cryogen spray cooling. *Laser Surg. Med.*, 31(2): 106–114, 2002.

[10] H. M. Al-Ahmadi & S. C. Yao. Spray cooling of high temperature metals using high mass flux industrial nozzles. *Exp. Heat Transfer*, 21(1):38–54, 2008.

[11] M. Al Qubeissi. Predictions of droplet heating and evaporation: An application to biodiesel, diesel, gasoline and blended fuels. *Appl. Thermal Eng.*, 136:260–267, 2018.

[12] H. Zhu, Z. Guo, & W. Liu. Biomimetic water-collecting materials inspired by nature. *Chem. Commun.*, 52(20):3863–3879, 2016.

[13] A. Ghosh, S. Beaini, B. J. Zhang, R. Ganguly, & C. M. Megaridis. Enhancing dropwise condensation through bioinspired wettability patterning. *Langmuir*, 30(43): 13103–13115, 2014.

[14] A. Lee, M.-W. Moon, H. Lim, W.-D. Kim, & H.-Y. Kim. Water harvest via dewing. *Langmuir*, 28(27):10183–10191, 2012.

[15] T. Pravinraj & R. Patrikar. A droplet actuation technique for a lab-on-chip device using partial wetting surface without external force. *Sensors and Actuators A: Physical*, 285: 482–490, 2019.

[16] W. Barthlott & C. Neinhuis. Purity of the sacred lotus, or escape from contamination in biological surfaces. *Planta*, 202(1):1–8, 1997.

[17] I. P. Parkin & R. G. Palgrave. Self-cleaning coatings. *J. Mater. Chem.*, 15(17):1689–1695, 2005.

[18] F. Mugele & J.-C. Baret. Electrowetting: from basics to applications. *J. Phys. Condens. Mat.*, 17(28):R705–R774, 2005.

[19] B. Berge & J. Peseux. Variable focal lens controlled by an external voltage: An application of electrowetting. *Eur. Phys. J. E*, 3(2):159–163, 2000.

[20] G. Beni, S. Hackwood, & J. L. Jackel. Continuous electrowetting effect. *Appl. Phys. Lett.*, 40(10):912–914, 1982.

[21] S. K. Cho, H. Moon, & C.-J. Kim. Creating, transporting, cutting, and merging liquid droplets by electrowetting-based actuation for digital microfluidic circuits. *J. Microelectromech. S.*, 12(1):70–80, 2003.

[22] T. Young. III. An essay on the cohesion of fluids. *Philos. T. R. Soc. Lond.*, (95):65–87, 1805.

[23] D. Bonn, J. Eggers, J. Indekeu, J. Meunier, & E. Rolley. Wetting and spreading. *Rev. Mod. Phys.*, 81(2):739, 2009.

[24] P. Yatsyshin, M.-A. Durán-Olivencia, & S. Kalliadasis. Microscopic aspects of wetting using classical density functional theory. *J. Phys. Condens. Mat.*, 30(27):274003, 2018.

[25] L. H. Tanner. The spreading of silicone oil drops on horizontal surfaces. *J. Phys. D. Appl. Phys.*, 12(9):1473, 1979.

[26] A. M. Cazabat & M. A. Cohen Stuart. Dynamics of wetting: effects of surface roughness. *J. Phys. Chem.*, 90(22):5845–5849, 1986.

[27] J.-D. Chen & N. Wada. Wetting dynamics of the edge of a spreading drop. *Phys. Rev. Lett.*, 62(26):3050, 1989.

[28] O. V. Voinov. Hydrodynamics of wetting. *Fluid Dyn.*, 11(5):714–721, 1976.

[29] H. K. Moffatt. Viscous and resistive eddies near a sharp corner. *J. Fluid Mech.*, 18(1): 1–18, 1964.

[30] D. N. Sibley, A. Nold, N. Savva, & S. Kalliadasis. A comparison of slip, disjoining pressure, and interface formation models for contact line motion through asymptotic analysis of thin two-dimensional droplet spreading. *J. Eng. Math.*, 94(1):19–41, 2015.

[31] C. Huh & L. E. Scriven. Hydrodynamic model of steady movement of a solid/liquid/fluid contact line. *J. Colloid Interface Sci.*, 35(1):85–101, 1971.

[32] C.-L. Navier. Mémoire sur les lois du mouvement des fluides. *Mem. Acad. Sci. Inst. Fr.*, 6(1823):389–440, 1823.

[33] Y. D. Shikhmurzaev. Singularities at the moving contact line. Mathematical, physical and computational aspects. *Physica D: Nonlinear Phenomena*, 217(2):121–133, 2006.

[34] P. A. Thompson & S. M. Troian. A general boundary condition for liquid flow at solid surfaces. *Nature*, 389(6649):360, 1997.

[35] G. He & N. G. Hadjiconstantinou. A molecular view of Tanner's law: molecular dynamics simulations of droplet spreading. *J. Fluid Mech.*, 497:123–132, 2003.

[36] T. Qian, X.-P. Wang, & P. Sheng. Molecular scale contact line hydrodynamics of immiscible flows. *Phys. Rev. E*, 68(1):016306, 2003.

[37] V. Dussan. The moving contact line: the slip boundary condition. *J. Fluid Mech.*, 77: 665–684, 1976.

[38] P. J. Haley & M. J. Miksis. The effect of the contact line on droplet spreading. *J. Fluid Mech.*, 223:57–81, 1991.

[39] E. Ruckenstein & C. S. Dunn. Slip velocity during wetting of solids. *J. Colloid Interface Sci.*, 59(1):135–138, 1977.

[40] P. G. de Gennes. Wetting: statics and dynamics. *Rev. Mod. Phys.*, 57(3):827–863, 1985.

[41] L. W. Schwartz & R. R. Eley. Simulation of droplet motion on low-energy and heterogeneous surfaces. *J. Colloid Interface Sci.*, 202(1):173–188, 1998.

[42] P. Colinet & A. Rednikov. On integrable singularities and apparent contact angles within a classical paradigm. *Eur. Phys. J. Spec. Top.*, 197(1):89–113, 2011.

[43] E. S. Benilov & M. Vynnycky. Contact lines with a contact angle. *J. Fluid Mech.*, 718: 481–506, 2013.

[44] P. Seppecher. Moving contact lines in the Cahn-Hilliard theory. *Int. J. Eng. Sci.*, 34(9): 977–992, 1996.

[45] D. N. Sibley, A. Nold, N. Savva, & S. Kalliadasis. On the moving contact line singularity: Asymptotics of a diffuse-interface model. *Eur. Phys. J. E*, 36(3), 2013.

[46] D. E. Weidner & L. W. Schwartz. Contact-line motion of shear-thinning liquids. *Phys. Fluids*, 6(11):3535–3538, 1994.

[47] Y. D. Shikhmurzaev. *Capillary Flows with Forming Interfaces*. Chapman and Hall/CRC, 2019.

[48] S. B. G. O'Brien & L. W. Schwartz. Theory and modeling of thin film flows. *Enc. Surf. Colloid Sci.*, pages 5283–5297, 2002.

[49] B. R. Duffy & S. K. Wilson. A third-order differential equation arising in thin-film flows and relevant to Tanner's law. *Appl. Math. Lett.*, 10(3):63–68, 1997.

[50] J. Eggers. Hydrodynamic theory of forced dewetting. *Phys. Rev. Lett.*, 93(9), 2004.

[51] J. H. Snoeijer & J. Eggers. Asymptotic analysis of the dewetting rim. *Phys. Rev. E,* 82 (5), 2010.

[52] A. A. Lacey. The motion with slip of a thin viscous droplet over a solid surface. *Stud. Appl. Math.*, 67(3):217–230, 1982.

[53] N. Savva, A. Rednikov, & P. Colinet. Asymptotic analysis of the evaporation dynamics of partially wetting droplets. *J. Fluid Mech.*, 824:574–623, 2017.

[54] L. M. Hocking. The spreading of a thin drop by gravity and capillarity. *Q. J. Appl. Math.*, 36(1):55–69, 1983.

[55] R. Vellingiri, N. Savva, & S. Kalliadasis. Droplet spreading on chemically heterogeneous substrates. *Phys. Rev. E.*, 84(3):036305, 2011.

[56] N. Savva & S. Kalliadasis. Two-dimensional droplet spreading over topographical substrates. *Phys. Fluids.*, 21(9):092102, 2009.

[57] N. Savva & S. Kalliadasis. Dynamics of moving contact lines: A comparison between slip and precursor film models. *Europhys Lett.*, 94(6):64004, 2011.

[58] N. Savva & S. Kalliadasis. Influence of gravity on the spreading of two-dimensional droplets over topographical substrates. *J. Eng. Math.*, 73(1):3–16, 2012.

[59] N. Savva & S. Kalliadasis. Droplet motion on inclined heterogeneous substrates. *J. Fluid Mech.*, 725:462–491, 2013.

[60] N. Savva & S. Kalliadasis. Low-frequency vibrations of two-dimensional droplets on heterogeneous substrates. *J. Fluid Mech.*, 754:515–549, 2014.

[61] N. Savva, D. Groves, & S. Kalliadasis. Droplet dynamics on chemically heterogeneous substrates. *J. Fluid Mech.*, 859:321–361, 2019.

[62] S. Brandon & A. Marmur. Simulation of contact angle hysteresis on chemically heterogeneous surfaces. *J. Colloid Interface Sci.*, 183(2):351–355, 1996.

[63] T. Cubaud & M. Fermigier. Advancing contact lines on chemically patterned surfaces. *J. Colloid Interface Sci.*, 269(1):171–177, 2004.

[64] H. B. Eral, J. M. Oh, & D. J. C. M. Mannetje. Contact angle hysteresis: a review of fundamentals and applications. *Colloid Polym. Sci.*, 291(2):247–260, 2013.

[65] R. E. Johnson & R. H. Dettre. *Wetting of low-energy surfaces*, volume 49. Marcel Dekker, Inc.: New York, 1993.

[66] E. Rio, A. Daerr, F. Lequeux, & L. Limat. Moving contact lines of a colloidal suspension in the presence of drying. *Langmuir*, 22(7):3186–3191, 2006.

[67] J. Y. Chung, J. P. Youngblood, & C. M. Stafford. Anisotropic wetting on tunable micro-wrinkled surfaces. *Soft Matter*, 3(9):1163–1169, 2007.

[68] H. Kusumaatmaja & J. M. Yeomans. Modeling contact angle hysteresis on chemically patterned and superhydrophobic surfaces. *Langmuir*, 23(11):6019–6032, 2007.

[69] G. Macdougall & C. Ockrent. Surface energy relations in liquid/solid systems I. The adhesion of liquids to solids and a new method of determining the surface tension of liquids. *P. Roy. Soc. Lond. A. Mat.*, 180(981):151–173, 1942.

[70] E. B. Dussan V. On the ability of drops or bubbles to stick to non-horizontal surfaces of solids. Part 2. Small drops or bubbles having contact angles of arbitrary size. *J. Fluid Mech.*, 151(-1):1, 1985.

[71] M. Miwa, A. Nakajima, A. Fujishima, K. Hashimoto, & T. Watanabe. Effects of the surface roughness on sliding angles of water droplets on superhydrophobic surfaces. *Langmuir*, 16(13):5754–5760, 2000.

[72] J. J. Bikerman. Sliding of drops from surfaces of different roughnesses. *J. Colloid Interface Sci.*, 5(4):349–359, 1950.

[73] C. W. Extrand & Y. Kumagai. Liquid drops on an inclined plane: The relation between contact angles, drop shape, and retentive force. *J. Colloid Interface Sci.*, 170(2): 515–521, 1995.

[74] P. Roura & J. Fort. Equilibrium of drops on inclined hydrophilic surfaces. *Phys. Rev. E*, 64(1), 2001.

[75] A. B. D. Cassie. Contact angles. *Discuss. Faraday. Soc.*, 3:11–16, 1948.

[76] R. Crawford, L. K. Koopal, & J. Ralston. Contact angles on particles and plates. *Colloid. Surface*, 27(4):57–64, 1987.

[77] G. Yamauchi, J. D. Miller, H. Saito, K. Takai, T. Ueda, H. Takazawa, H. Yamamoto, & S. Nislhi. Wetting characteristics of newly developed water-repellent material. *Colloid. Surface. A.*, 116(1-2):125–134, 1996.

[78] J. T. Woodward, H. Gwin, & D. K. Schwartz. Contact angles on surfaces with mesoscopic chemical heterogeneity. *Langmuir*, 16(6):2957–2961, 2000.

[79] R. N. Wenzel. RESISTANCE OF SOLID SURFACES TO WETTING BY WATER. *Ind. Eng. Chem.*, 28(8):988–994, 1936.

[80] S. J. Hitchcock, N. T. Carroll, & M. G. Nicholas. Some effects of substrate roughness on wettability. *J. Mater. Sci.*, 16(3):714–732, 1981.

[81] S. Shibuichi, T. Onda, N. Satoh, & K. Tsujii. Super water-repellent surfaces resulting from fractal structure. *J. Phys. Chem.*, 100(50):19512–19517, 1996.

[82] J. Bico, C. Tordeux, & D. Quéré. Rough wetting. *Europhys. Lett.*, 55(2):214–220, 2001.

[83] N. Savva, G. A. Pavliotis, & S. Kalliadasis. Contact lines over random topographical substrates. Part 1. Statics. *J. Fluid Mech.*, 672:358–383, 2011.

[84] N. Savva, S. Kalliadasis, & G. A. Pavliotis. Two-dimensional droplet spreading over random topographical substrates. *Phys. Rev. Lett.*, 104(8), 2010.

[85] J. F. Joanny & P.-G. de Gennes. A model for contact angle hysteresis. *J. Chem. Phys.*, 81 (1):552–562, 1984.

[86] J. F. Joanny & P.-G. de Gennes. Competition between wetting and adverse macroscopic forces. *Cr. Acad. Sci. II*, 299(10):605–608, 1984.

[87] T. Cubaud, M. Fermigier, & P. Jenffer. Spreading of large drops on patterned surfaces. *Oil & Gas Sci. Tech.*, 56(1):23–31, 2001.

[88] S. Varagnolo, D. Ferraro, P. Fantinel, M. Pierno, G. Mistura, G. Amati, L. Biferale, & M. Sbragaglia. Stick-slip sliding of water drops on chemically heterogeneous surfaces. *Phys. Rev. Lett.*, 111(6), 2013.

[89] J. F. Oliver, C. Huh, & S. G. Mason. The apparent contact angle of liquids on finely-grooved solid surfaces-a SEM study. *J. Adhesion*, 8(3):223–234, 1976.

[90] G. McHale, S. Aqil, N. J. Shirtcliffe, M. I. Newton, & H. Y. Erbil. Analysis of droplet evaporation on a superhydrophobic surface. *Langmuir*, 21(24):11053–11060, 2005.

[91] N. Anantharaju, M. Panchagnula, & S. Neti. Evaporating drops on patterned surfaces: Transition from pinned to moving triple line. *J. Colloid Interface Sci.*, 337(1):176–182, 2009.

[92] T. A. Duncombe, E. Y. Erdem, A. Shastry, R. Baskaran, & K. F. Böhringer. Controlling liquid drops with texture ratchets. *Adv. Mater.*, 24(12):1545–1550, 2012.

[93] S. R. Subramanian, N. Moumen, & J. B. McLaughlin. Motion of a drop on a solid surface due to a wettability gradient. *Langmuir*, 21(25):11844–11849, 2005.

[94] N. Moumen, S. R. Subramanian, & J. B. McLaughlin. Experiments on the motion of drops on a horizontal solid surface due to a wettability gradient. *Langmuir*, 22(6): 2682–2690, 2006.

[95] G. Fang, W. Li, X. Wang, & G. Qiao. Droplet motion on designed microtextured superhydrophobic surfaces with tunable wettability. *Langmuir*, 24(20):11651–11660, 2008.

[96] J. T. Yang, J. C. Chen, K. J. Huang, & J. A. Yeh. Droplet manipulation on a hydrophobic textured surface with roughened patterns. *J. Microelectromechanical S.*, 15(3):697–707, 2006.

[97] M. J. Hancock & M. C. Demirel. Anisotropic wetting on structured surfaces. *MRS Bulletin*, 38(5):391–396, 2013.

[98] K. Takeda, A. Nakajima, Y. Murata, K. Hashimoto, & T. Watanabe. Control of water droplets on super-hydrophobic surfaces by static electric field. *Jpn. J. Appl. Phys.*, 41 (Part 1, No. 1):287–291, 2002.

[99] S. Daniel & M. K. Chaudhury. Rectified motion of liquid drops on gradient surfaces induced by vibration. *Langmuir*, 18(9):3404–3407, 2002.

[100] S. Daniel, S. Sircar, J. Gliem, & M. K. Chaudhury. Ratcheting motion of liquid drops on gradient surfaces. *Langmuir*, 20(10):4085–4092, 2004.

[101] P. Brunet, J. Eggers, & R. D. Deegan. Vibration-induced climbing of drops. *Phys. Rev. Lett.*, 99(14), 2007.

[102] E. S. Benilov & J. Billingham. Drops climbing uphill on an oscillating substrate. *J. Fluid Mech.*, 674:93–119, 2011.

[103] F. Li & F. Mugele. How to make sticky surfaces slippery: Contact angle hysteresis in electrowetting with alternating voltage. *Appl. Phys. Lett.*, 92(24):244108, 2008.

[104] S. J. Lee, J. Hong, K. H. Kang, I. S. Kang, & S. J. Lee. Electrowetting-induced droplet detachment from hydrophobic surfaces. *Langmuir,* 30(7):1805–1811, 2014.

[105] N. Savva, G. A. Pavliotis, & S. Kalliadasis. Contact lines over random topographical substrates. Part 2. Dynamics. *J. Fluid Mech.*, 672:384–410, 2011.

[106] F. Xu & O. E. Jensen. Drop spreading with random viscosity. *P. R. Soc. A-Math Phy*, 472 (2194):20160270, 2016.

[107] J. M. Oliver, J. P. Whiteley, M. A. Saxton, D. Vella, V. S. Zubkov, & J. R. King. On contact-line dynamics with mass transfer. *Eur. J. Appl. Math.*, 26(5):671–719, 2015.

[108] H. P. Greenspan. On the motion of a small viscous droplet that wets a surface. *J. Fluid Mech.*, 84(1):125–143, 1978.

[109] H. P. Greenspan & B. M. McCay. On the wetting of a surface by a very viscous fluid. *Stud. Appl. Math.*, 64(2):94–112, 1981.

[110] C. Aydemir. Time-dependent behavior of a sessile water droplet on various papers. *Int. J. Polym. Mater.*, 59(6):387–397, 2010.

[111] L. Espín & S. Kumar. Droplet spreading and absorption on rough, permeable substrates. *J. Fluid Mech.*, 784:465–486, 2015.

[112] D. Arora, A. P. Deshpande, & S. R. Chakravarthy. Experimental investigation of fluid drop spreading on heterogeneous and anisotropic porous media. *J. Colloid Interface Sci.*, 293(2):496–499, 2006.

[113] C. N. C. Lam, R. Wu, D. Li, M. L. Hair, & A. W. Neumann. Study of the advancing and receding contact angles: liquid sorption as a cause of contact angle hysteresis. *Adv. Colloid. Interfac.*, 96(1-3):169–191, 2002.

[114] H.-Y. Kim, S. Jeon, M. Song, & K. Kim. Numerical simulations of water droplet dynamics in hydrogen fuel cell gas channel. *J. Power Sources*, 246:679–695, 2014.

[115] M. J. Cheah, I. G. Kevrekidis, & J. B. Benziger. Water slug formation and motion in gas

flow channels: the effects of geometry, surface wettability, and gravity. *Langmuir*, 29 (31):9918–9934, 2013.

[116] Y. H. Erbil. Evaporation of pure liquid sessile and spherical suspended drops: A review. *Adv. Colloid. Interfac.*, 170(1):67–86, 2012.

[117] D. Brutin. *Droplet wetting and evaporation: from pure to complex fluids*. Academic Press, 2015.

[118] D. Brutin & V. Starov. Recent advances in droplet wetting and evaporation. *Chem. Soc. Rev.*, 47(2):558–585, 2018.

[119] R. D. Deegan, O. Bakajin, T. F. Dupont, G. Huber, S. R. Nagel, & T. A. Witten. Capillary flow as the cause of ring stains from dried liquid drops. *Nature*, 389(6653):827, 1997.

[120] R. D. Deegan, O. Bakajin, T. F. Dupont, G. Huber, S. R. Nagel, & T. A. Witten. Contact line deposits in an evaporating drop. *Phys. Rev. E*, 62(1):756, 2000.

[121] G. Berteloot, A. Hoang, A. Daerr, H. P. Kavehpour, F. Lequeux, & L. Limat. Evaporation of a sessile droplet: Inside the coffee stain. *J. Colloid Interface Sci.*, 370(1):155–161, 2012.

[122] C. Seo, D. Jang, J. Chae, & S. Shin. Altering the coffee-ring effect by adding a surfactant-like viscous polymer solution. *Sci. Rep.*, 7(1):500, 2017.

[123] H. B. Eral, D. Mampallil Augustine, M. H. G. Duits, & F. Mugele. Suppressing the coffee stain effect: how to control colloidal self-assembly in evaporating drops using electrowetting. *Soft Matter*, 7(10):4954, 2011.

[124] K. B. Kiradjiev, C. J. W. Breward, & I. M. Griffiths. Surface-tension-and injection-driven spreading of a thin viscous film. *J. Fluid Mech.*, 861:765–795, 2019.

[125] M. Pradas, N. Savva, J. B. Benziger, I. G. Kevrekidis, & S. Kalliadasis. Dynamics of fattening and thinning 2D sessile droplets. *Langmuir*, 32(19):4736–4745, 2016.

[126] C. Poulard, G. Guéna, & A. M. Cazabat. Diffusion-driven evaporation of sessile drops. *J. Phys. Condens. Mat.*, 17(49):S4213, 2005.

[127] A. M. Cazabat & G. Guena. Evaporation of macroscopic sessile droplets. *Soft Matter*, 6 (12):2591–2612, 2010.

[128] W. D. Ristenpart, P. G. Kim, C. Domingues, J. Wan, & H. A. Stone. Influence of substrate conductivity on circulation reversal in evaporating drops. *Phys. Rev. Lett.*, 99(23): 234502, 2007.

[129] M. C. Lopes, E. Bonaccurso, T. Gambaryan-Roisman, & P. Stephan. Influence of the substrate thermal properties on sessile droplet evaporation: Effect of transient heat transport. *Colloid. Surface. A.*, 432:64–70, 2013.

[130] Y. Tsoumpas, S. Dehaeck, A. Rednikov, & P. Colinet. Effect of marangoni flows on the shape of thin sessile droplets evaporating into air. *Langmuir*, 31(49):13334–13340, 2015.

[131] F. Girard, M. Antoni, & K. Sefiane. On the effect of marangoni flow on evaporation rates of heated water drops. *Langmuir*, 24(17):9207–9210, 2008.

[132] B. Sobac & D. Brutin. Thermocapillary instabilities in an evaporating drop deposited onto a heated substrate. *Phys. Fluids*, 24(3):032103, 2012.

[133] S. J. Gokhale, J. L. Plawsky, & P. C. Wayner Jr. Experimental investigation of contact angle, curvature, and contact line motion in dropwise condensation and evaporation. *J. Colloid Interface Sci.*, 259(2):354–366, 2003.

[134] C. Sodtke, V. S. Ajaev, & P. Stephan. Dynamics of volatile liquid droplets on heated surfaces: theory versus experiment. *J. Fluid Mech.*, 610:343–362, 2008.

[135] S. Cioulachtjian, S. Launay, S. Boddaert, & M. Lallemand. Experimental investigation of water drop evaporation under moist air or saturated vapour conditions. *Int. J. Therm. Sci.*, 49(6):859–866, 2010.

[136] R. Raj, C. Kunkelmann, P. Stephan, J. Plawsky, & J. Kim. Contact line behavior for a highly wetting fluid under superheated conditions. *Int. J. Heat. Mass. Tran.*, 55(9-10): 2664–2675, 2012.

[137] J. P. Burelbach, S. G. Bankoff, & S. H. Davis. Nonlinear stability of evaporating/condensing liquid films. *J. Fluid Mech.*, 195:463–494, 1988.

[138] M. Dondlinger, J. Margerit, & P. C. Dauby. Weakly nonlinear study of marangoni instabilities in an evaporating liquid layer. *J. Colloid Interface Sci.*, 283(2):522–532, 2005.

[139] B. Haut & P. Colinet. Surface-tension-driven instabilities of a pure liquid layer evaporating into an inert gas. *J. Colloid Interface Sci.*, 285(1):296–305, 2005.

[140] M. Potash Jr & P. C. Wayner Jr. Evaporation from a two-dimensional extended meniscus. *Int. J. Heat. Mass. Tran.*, 15(10):1851–1863, 1972.

[141] S. Moosman & G. M. Homsy. Evaporating menisci of wetting fluids. *J. Colloid Interface Sci.*, 73(1):212–223, 1980.

[142] V. S. Ajaev. Spreading of thin volatile liquid droplets on uniformly heated surfaces. *J. Fluid Mech.*, 528:279–296, 2005.

[143] D. M. Anderson & S. H. Davis. The spreading of volatile liquid droplets on heated surfaces. *Phys. Fluids*, 7(2):248–265, 1995.

[144] L. M. Hocking. On contact angles in evaporating liquids. *Phys. Fluids*, 7(12):2950–2955, 1995.

[145] J. M. Stauber, S. K. Wilson, B. R. Duffy, & K. Sefiane. Evaporation of droplets on strongly hydrophobic substrates. *Langmuir*, 31(12):3653–3660, 2015.

[146] J. M. Stauber, S. K. Wilson, B. R. Duffy, & K. Sefiane. On the lifetimes of evaporating droplets with related initial and receding contact angles. *Phys. Fluids*, 27(12):122101, 2015.

[147] A. Amini & G. M. Homsy. Evaporation of liquid droplets on solid substrates. I. Flat substrate with pinned or moving contact line. *Phys. Rev. Fluids*, 2(4):043603, 2017.

[148] A. Amini & G. M. Homsy. Evaporation of liquid droplets on solid substrates. II. Periodic substrates with moving contact lines. *Phys. Rev. Fluids*, 2(4):043604, 2017.

[149] T. Pham & S. Kumar. Drying of droplets of colloidal suspensions on rough substrates. *Langmuir*, 33(38):10061–10076, 2017.

[150] G. G. Wells, É. Ruiz-Gutiérrez, Y. Le Lirzin, A. Nourry, B. V. Orme, M. Pradas, & R. Ledesma-Aguilar. Snap evaporation of droplets on smooth topographies. *Nat. Commun.*, 9(1):1380, 2018.

[151] J. Eggers & L. M. Pismen. Nonlocal description of evaporating drops. *Phys. Fluids*, 22 (11):112101, 2010.

[152] L. N. Trefethen. *Spectral methods in MATLAB*, volume 10. SIAM, 2000.

[153] K. B. Glasner. A boundary integral formulation of quasi-steady fluid wetting. *J. Comput. Phys.*, 207(2):529–541, 2005.

[154] J. P. Ward & J. R. King. Thin-film modelling of biofilm growth and quorum sensing. *J. Eng. Math.*, 73(1):71–92, 2011.

[155] H. E. Huppert & E. Simpson. The slumping of gravity currents. *J. Fluid Mech.*, 99(4): 785–799, 1980.

[156] H. Wong, I. Fatt, & C. J. Radke. Deposition and thinning of the human tear film. *J. Colloid Interface Sci.*, 184(1):44–51, 1996.

[157] A. Oron, S. H. Davis, & S. G. Bankoff. Long-scale evolution of thin liquid films. *Rev. Mod. Phys.*, 69(3):931–980, 1997.

[158] R. V. Craster & O. K. Matar. Dynamics and stability of thin liquid films. *Rev. Mod. Phys.*, 81(3):1131–1198, 2009.

[159] D. J. Acheson. *Elementary fluid dynamics*. Clarendon Press, 2003.

[160] D. Peschka. Thin-film free boundary problems for partial wetting. *J. Comput. Phys.*, 295:770–778, 2015.

[161] I. S. Kang & L. G. Leal. Orthogonal grid generation in a 2D domain via the boundary integral technique. *J. Comput. Phys.*, 102(1):78–87, 1992.

[162] E. Lauga, M. Brenner, & H. Stone. Microfluidics: the no-slip boundary condition. *Spr. Hdb. Exp. Fluid. Mech.*, pages 1219–1240, 2007.

[163] M. H. Holmes. *Introduction to perturbation methods*, volume 20. Springer Science & Business Media, 2012.

[164] M. A. Saxton, J. P. Whiteley, D. Vella, & J. M. Oliver. On thin evaporating drops: When is the d^2-law valid? *J. Fluid Mech.*, 792:134–167, 2016.

[165] J. Eggers. Toward a description of contact line motion at higher capillary numbers. *Phys. Fluids*, 16(9):3491–3494, 2004.

[166] D. N. Sibley, A. Nold, & S. Kalliadasis. The asymptotics of the moving contact line: cracking an old nut. *J. Fluid Mech.*, 764:445–462, 2015.

[167] A. Nold. *From the Nano-to the Macroscale: Bridging Scales for the Moving Contact Line Problem*. PhD thesis, Imperial College London, 2016.

[168] M. A. Saxton, D. Vella, J. P. Whiteley, & J. M. Oliver. Kinetic effects regularize the mass-flux singularity at the contact line of a thin evaporating drop. *J. Eng. Math.*, 106 (1):47–73, 2017.

[169] J. Eggers. Existence of receding and advancing contact lines. *Phys. Fluids*, 17(8): 082106, 2005.

[170] R. W. Schrage. *A theoretical study of interphase mass transfer*. Columbia University Press, 1953.

[171] P. C. Wayner, Y. K. Kao, & L. V. LaCroix. The interline heat-transfer coefficient of an evaporating wetting film. *Int. J. Heat. Mass Tran.*, 19(5):487–492, 1976.

[172] V. P. Carey. *Liquid vapor phase change phenomena: an introduction to the thermophysics of vaporization and condensation processes in heat transfer equipment*. CRC Press, 2018.

[173] A. Y. Rednikov, S. Rossomme, & P. Colinet. Steady microstructure of a contact line for a liquid on a heated surface overlaid with its pure vapor: parametric study for a classical model. *Multiphase Sci. and Tech.*, 21(3), 2009.

[174] I. W. Eames, N. J. Marr, & H. Sabir. The evaporation coefficient of water: a review. *Int. J. Heat. Mass Tran.*, 40(12):2963–2973, 1997.

[175] P. Davidovits, D. R. Worsnop, J. T. Jayne, C. E. Kolb, P. Winkler, A. Vrtala, P. E. Wagner, M. Kulmala, K. E. J. Lehtinen, T. Vesala, & M. Mozurkewich. Mass accommodation coefficient of water vapor on liquid water. *Geophys. Res. Lett.*, 31(22), 2004.

[176] W. Ren & W. E. Boundary conditions for the moving contact line problem. *Phys. Fluids*, 19(2):022101, 2007.

[177] N. G. Hadjiconstantinou. Combining atomistic and continuum simulations of contact-line motion. *Phys. Rev. E*, 59(2):2475, 1999.

[178] N. G. Hadjiconstantinou. Hybrid atomistic–continuum formulations and the moving contact-line problem. *J. Comput. Phys.*, 154(2):245–265, 1999.

[179] K. Bao, Y. Shi, S. Sun, & X.-P. Wang. A finite element method for the numerical solution of the coupled Cahn–Hilliard and Navier–Stokes system for moving contact line problems. *J. Comput. Phys.*, 231(24):8083–8099, 2012.

[180] L. Luo, X.-P. Wang, & X.-C. Cai. An efficient finite element method for simulation of droplet spreading on a topologically rough surface. *J. Comput. Phys.*, 349:233–252, 2017.

[181] K. N. Christodoulou & L. E. Scriven. Discretization of free surface flows and other moving boundary problems. *J. Comput. Phys.*, 99(1):39–55, 1992.

[182] M. Muradoglu & S. Tasoglu. A front-tracking method for computational modeling of impact and spreading of viscous droplets on solid walls. *Comput. Fluids*, 39(4): 615–625, 2010.

[183] K. L. Maki & S. Kumar. Fast evaporation of spreading droplets of colloidal suspensions. *Langmuir*, 27(18):11347–11363, 2011.

[184] Y. Sui, H. Ding, & P. D. M. Spelt. Numerical simulations of flows with moving contact lines. *Annu. Rev. Fluid Mech.*, 46(1):97–119, 2014.

[185] S. Afkhami & M. Bussmann. Height functions for applying contact angles to 2D VOF simulations. *Int. J. Numer. Meth Fl.*, 57(4):453–472, 2008.

[186] J.-B. Dupont & D. Legendre. Numerical simulation of static and sliding drop with contact angle hysteresis. *J. Comput. Phys.*, 229(7):2453–2478, 2010.

[187] R. Scardovelli & S. Zaleski. DIRECT NUMERICAL SIMULATION OF FREE-SURFACE AND INTERFACIAL FLOW. *Annu. Rev. Fluid Mech.*, 31(1):567–603, 1999.

[188] S. Afkhami, J. Buongiorno, A. Guion, S. Popinet, Y. Saade, R. Scardovelli, & S. Zaleski. Transition in a numerical model of contact line dynamics and forced dewetting. *J. Comput. Phys*, 374:1061–1093, 2018.

[189] A. J. Briant, A. J. Wagner, & J. M. Yeomans. Lattice Boltzmann simulations of contact line motion. I. Liquid-gas systems. *Phys. Rev. E*, 69(3):031602, 2004.

[190] A. J. Briant & J. M. Yeomans. Lattice Boltzmann simulations of contact line motion. II. Binary fluids. *Phys. Rev. E*, 69(3):031603, 2004.

[191] S. van der Graaf, T. Nisisako, C. G. P. H. Schroën, R. G. M. van der Sman, & R. M. Boom. Lattice Boltzmann simulations of droplet formation in a T-shaped microchannel. *Langmuir*, 22(9):4144–4152, 2006.

[192] P. H. Jansen, K. Sotthewes, C. Ganser, C. Teichert, H. J. W. Zandvliet, & S. E. Kooij. Tuning kinetics to control droplet shapes on chemically striped patterned surfaces. *Langmuir*, 28(37):13137–13142, 2012.

[193] P. H. Jansen, K. Sotthewes, C. Ganser, H. J. W. Zandvliet, C. Teichert, & S. E. Kooij. Shape of picoliter droplets on chemically striped patterned substrates. *Langmuir*, 30 (39):11574–11581, 2014.

[194] T. Inamuro, S. Tajima, & F. Ogino. Lattice Boltzmann simulation of droplet collision dynamics. *Int. J. Heat. Mass Tran.*, 47(21):4649–4657, 2004.

[195] K. Mahady, S. Afkhami, J. Diez, & L. Kondic. Comparison of Navier-Stokes simulations with long-wave theory: Study of wetting and dewetting. *Phys. Fluids*, 25(11):112103, 2013.

[196] M.-A. Y.-H. Lam, L. J. Cummings, & L. Kondic. Computing dynamics of thin films via large scale GPU-based simulations. *J. Comput. Phys.: X*, 2:100001, 2019.

[197] M. Wilczek, W. Tewes, S. Engelnkemper, S. V. Gurevich, & U. Thiele. Sliding drops: Ensemble statistics from single drop bifurcations. *Phys. Rev. Lett.*, 119(20), 2017.

[198] U. Thiele. Recent advances in and future challenges for mesoscopic hydrodynamic modelling of complex wetting. *Colloid Surf. A.*, 553:487–495, 2018.

[199] R. Baltensperger, J.-P. Berrut, & B. Noël. Exponential convergence of a linear rational interpolant between transformed chebyshev points. *Math. Comput. Am. Math. Soc.*, 68 (227):1109–1120, 1999.

[200] J.-P. Berrut & L. N. Trefethen. Barycentric Lagrange interpolation. *SIAM Rev.*, 46(3): 501–517, 2004.

[201] P. J. Davis & P. Rabinowitz. *Methods of numerical integration*. Courier Corporation, 2007.

[202] D. Gottlieb & S. A. Orszag. *Numerical analysis of spectral methods: theory and applications*, volume 26. SIAM, 1977.

[203] W. Huang & D. M. Sloan. Pole condition for singular problems: the pseudospectral approximation. *J. Comput. Phys.*, 107(2):254–261, 1993.

[204] H. Wang, D. Huybrechs, & S. Vandewalle. Explicit barycentric weights for polynomial interpolation in the roots or extrema of classical orthogonal polynomials. *Math of Comput*, 83(290):2893–2914, 2014.

[205] M. Abramowitz & I. A. Stegun. *Handbook of Mathematical Functions*. Dover Publications Inc., 1972.

[206] S. Hao, A. H. Barnett, P.-G. Martinsson, & P. Young. High-order accurate methods for Nyström discretization of integral equations on smooth curves in the plane. *Adv. Comp. Math.*, 40(1):245–272, 2014.

[207] R. Kress, V. Maz'ya, & V. Kozlov. *Linear integral equations*, volume 82. Springer, 1989.

[208] R. Kress. Boundary integral equations in time-harmonic acoustic scattering. *Math. Comput. Model*, 15(3-5):229–243, 1991.

[209] B. K. Alpert. Hybrid Gauss-trapezoidal quadrature rules. *SIAM J. Sci. Comp.*, 20(5): 1551–1584, 1999.

[210] C. W. Clenshaw & A. R. Curtis. A method for numerical integration on an automatic computer. *Numer. Math.*, 2(1):197–205, 1960.

[211] L. N. Trefethen. Is Gauss quadrature better than Clenshaw–Curtis? *SIAM Rev.*, 50(1): 67–87, 2008.

[212] L. Greengard & V. Rokhlin. A fast algorithm for particle simulations. *J. Comput. Phys*, 73(2):325–348, 1987.

[213] M. C. A. Kropinski & B. D. Quaife. Fast integral equation methods for the modified helmholtz equation. *J. Comput. Phys.*, 230(2):425–434, 2011.

[214] B. D. Quaife. *Fast integral equation methods for the modified Helmholtz equation*. PhD thesis, Simon Fraser University: Department of Mathematics, 2011.

[215] S. Kapur & V. Rokhlin. High-order corrected trapezoidal quadrature rules for singular functions. *SIAM J. Numer. Anal.*, 34(4):1331–1356, 1997.

[216] E. L. Allgower & K. Georg. *Numerical Continuation Methods*. Springer Berlin Heidelberg, 1990.

[217] E. Dietrich, E. S. Kooij, X. Zhang, H. J. W. Zandvliet, & D. Lohse. Stick-jump mode in surface droplet dissolution. *Langmuir,* 31(16):4696–4703, 2015.

[218] H. Kusumaatmaja & J. M. Yeomans. Controlling drop size and polydispersity using chemically patterned surfaces. *Langmuir*, 23(2):956–959, 2007.

[219] O. Bliznyuk, E. Vereshchagina, S. E. Kooij, & B. Poelsema. Scaling of anisotropic droplet shapes on chemically stripe-patterned surfaces. *Phys. Rev. E,* 79(4):041601, 2009.

[220] R. David & A. W. Neumann. Anisotropic drop shapes on chemically striped surfaces. *Colloid Surf. A.*, 393:32–36, 2012.

[221] V. G. Damle & K. Rykaczewski. Nano-striped chemically anisotropic surfaces have near isotropic wettability. *Appl. Phys. Lett.*, 110(17):171603, 2017.

[222] L. Zou, H. Wang, X. Zhu, Y. Ding, R. Chen, & Q. Liao. Droplet splitting on chemically striped surface. *Colloid Surf. A,* 537:139–148, 2018.

[223] L. Biferale, R. Benzi, M. Sbragaglia, S. Succi, & F. Toschi. Wetting/dewetting transition of two-phase flows in nano-corrugated channels. *J. Comput-Aided. Mater.*, 14(3): 447–456, 2007.

[224] J. Léopoldès, A. Dupuis, D. G. Bucknall, & J. M. Yeomans. Jetting micron-scale droplets onto chemically heterogeneous surfaces. *Langmuir*, 19(23):9818–9822, 2003.

[225] M. A. Jaswon. Integral equation methods in potential theory. I. *P. Roy. Soc. Lond. A. Mat.*, 275(1360):23–32, 1963.

[226] T. Cubaud & M. Fermigier. Faceted drops on heterogeneous surfaces. *Europhys Lett.*, 55 (2):239, 2001.

[227] J. Swift & P. C. Hohenberg. Hydrodynamic fluctuations at the convective instability. *Phys. Rev. A*, 15(1):319, 1977.

[228] K. Daniels. Numerical solution to the swift-hohenburg equation. URL `http://nile.physics.ncsu.edu/hon292a-f08/`. Accessed: 19/04/2019.

[229] T. Podgorski, J. M. Flesselles, & L. Limat. Corners, cusps, and pearls in running drops. *Phys. Rev. Lett.*, 87(3):036102, 2001.

[230] M. K. Chaudhury & G. M. Whitesides. How to make water run uphill. *Science*, 256 (5063):1539–1541, 1992.

[231] B. S. Sikarwar, N. K. Battoo, S. Khandekar, & K. Muralidhar. Dropwise condensation underneath chemically textured surfaces: Simulation and experiments. *J. Heat Transfer*, 133(2):021501, 2011.

[232] Z.-P. Liang, X.-D. Wang, D.-J. Lee, X.-F. Peng, & A. Su. Spreading dynamics of power-law fluid droplets. *J. Phys. Condens. Mat.*, 21(46):464117, 2009.

[233] S. S. Shibeshi & W. E. Collins. The rheology of blood flow in a branched arterial system. *Appl. Rheol.*, 15(6):398, 2005.

[234] J. R. King. The spreading of power-law fluids. In *IUTAM Symposium on Free Surface Flows*, pages 153–160. Springer, 2001.

[235] J. H. Snoeijer. Free-surface flows with large slopes: Beyond lubrication theory. *Phys. Fluids*, 18(2):021701, 2006.

[236] F. Battaglia & T. F. George. Tensors: A guide for undergraduate students. *Am. J. Phys.*, 81(7):498–511, 2013.

[237] J. P. Boyd. *Chebyshev and Fourier spectral methods*. Courier Corporation, 2001.

[238] W. Ren, P. H. Trinh, & W. E. On the distinguished limits of the Navier slip model of the moving contact line problem. *J. Fluid Mech.*, 772:107–126, 2015.